STUDIES OF TWO-PHASE GAS-LIQUID FLOW IN MICROGRAVITY

A Dissertation

Presented to

the Faculty of the Department of Chemical Engineering

University of Houston

In Partial Fulfillment

of the Requirements for the Degree

Doctor of Philosophy

in Chemical Engineering

by

William Scott Bousman

December, 1994

Abstract

Two-phase gas-liquid flows are expected to occur in many future space operations. Due to a lack of buoyancy in the microgravity environment, two-phase flows are known to behave differently than those in earth gravity. Despite these concerns, little research has been conducted on microgravity two-phase flow and the current understanding is poor.

This dissertation describes an experimental and modeling study of the characteristics of two-phase flows in microgravity. An experiment was operated onboard NASA aircraft capable of producing short periods of microgravity. In addition to high speed photographs of the flows, electronic measurements of void fraction, liquid film thickness, bubble and wave velocity, pressure drop and wall shear stress were made for a wide range of liquid and gas flow rates. The effects of liquid viscosity, surface tension and tube diameter on the behavior of these flows were also assessed. From the data collected, maps showing the occurrence of various flow patterns as a function of gas and liquid flow rates were constructed. Earth gravity two-phase flow models were compared to the results of the microgravity experiments and in some cases modified. Models were developed to predict the transitions on the flow pattern maps.

Three flow patterns, bubble, slug and annular flow, were observed in microgravity. These patterns were found to occur in distinct regions of the gas-liquid flow rate parameter space. The effect of liquid viscosity, surface tension and tube diameter on the location of the boundaries of these regions was small. Void fraction and Weber number transition criteria both produced reasonable transition models.

Void fraction and bubble velocity for bubble and slug flows were found to be well described by the Drift-Flux model used to describe such flows in earth gravity. Pressure drop modeling by the homogeneous flow model was inconclusive for bubble and slug flows. Annular flows were found to be complex systems of ring-like waves and a

substrate film. Pressure drop was best fitted with the Lockhart-Martinelli model. Force balances suggest that droplet entrainment may be a large component of the total pressure drop.

Table of Contents

Appendices

List of Figures

List of Tables

Chapter 1 Introduction

1.1 Two-Phase Gas-Liquid Flows in Microgravity

The simultaneous flow of gas and liquid in a pipe occurs in many situations of industrial importance such as natural gas pipelines, power generation systems, refrigeration systems and vaporizing and condensing systems. The behavior of these systems is poorly understood despite many years of research. As a result, the design and refinement of such systems often requires exhaustive experimentation and the use of purely empirical correlations. Over the course of many years, this approach has allowed for the design and operation of many useful two-phase flow systems but the results are not easily extended to new applications.

The advent of human space flight has seen a progression of increasingly complex spacecraft and space stations placed into earth orbit and on the lunar surface. Near-term plans include the construction of a permanently manned space station facility while longer term goals include a permanent lunar facility and a manned mission to Mars. Low gravity manufacturing facilities in earth orbit for the production of special semiconductors and medically useful proteins are also planned.

As larger and more complex facilities are placed into microgravity (the near-zero gravity environment found in earth orbit) and reduced gravity environments, the systems needed to operate these facilities must be developed for use in these environments. Two-phase gas-liquid flows are expected to occur in several reduced gravity applications including: thermal distribution and control systems, condensing and vaporizing operations, operation and control of two-phase power cycles, storage and transfer of cryogenic fluids, and safety and performance issues associated with space-based nuclear power systems.

Gas-liquid flows are strongly affected by the magnitude and orientation of gravity because there is usually a large difference in the density of the two phases. Even on earth, the behavior of gas-liquid flows in vertical tubes is very different from the behavior of the same flows in horizontal or inclined tubes (Dukler and Taitel, 1984, Barnea, 1986). Thus, with the lack of buoyancy between the gas and liquid phases in the microgravity environment, microgravity gas-liquid flows are expected to behave differently from those on earth. This implies that models and design correlations developed for earth-based two-phase flow systems may fail to predict the behavior encountered in microgravity. In addition, it may be difficult to verify the operation, safety and reliability of systems designed for the microgravity environment while these systems are in earth gravity. Therefore, in order to develop reliable two-phase flow systems for use in space, the behavior of two-phase gas-liquid flows in microgravity must be better understood.

The expense of on-orbit experimental investigations is generally prohibitive for preliminary studies such as the present one. However, drop tower and aircraft facilities exist within NASA which can produce up to 25 seconds of microgravity during which time, two-phase flow experiments can be performed. These unique facilities were used in the present study.

1.2 Flow Patterns in Microgravity Two-Phase Gas-Liquid Flows

Two-phase gas-liquid flows distribute themselves into one of several distinct flow patterns depending primarily on the flow rates of liquid and gas, the physical properties of the fluids and the magnitude and orientation of gravity. Numerous experiments conducted over the entire parameter space of practical interest have shown the existence of three flow patterns in microgravity. These are represented graphically in Figure 1.1 and a collection of photographs of these flow patterns is included as Appendix A. As shown in Figure 1.1,

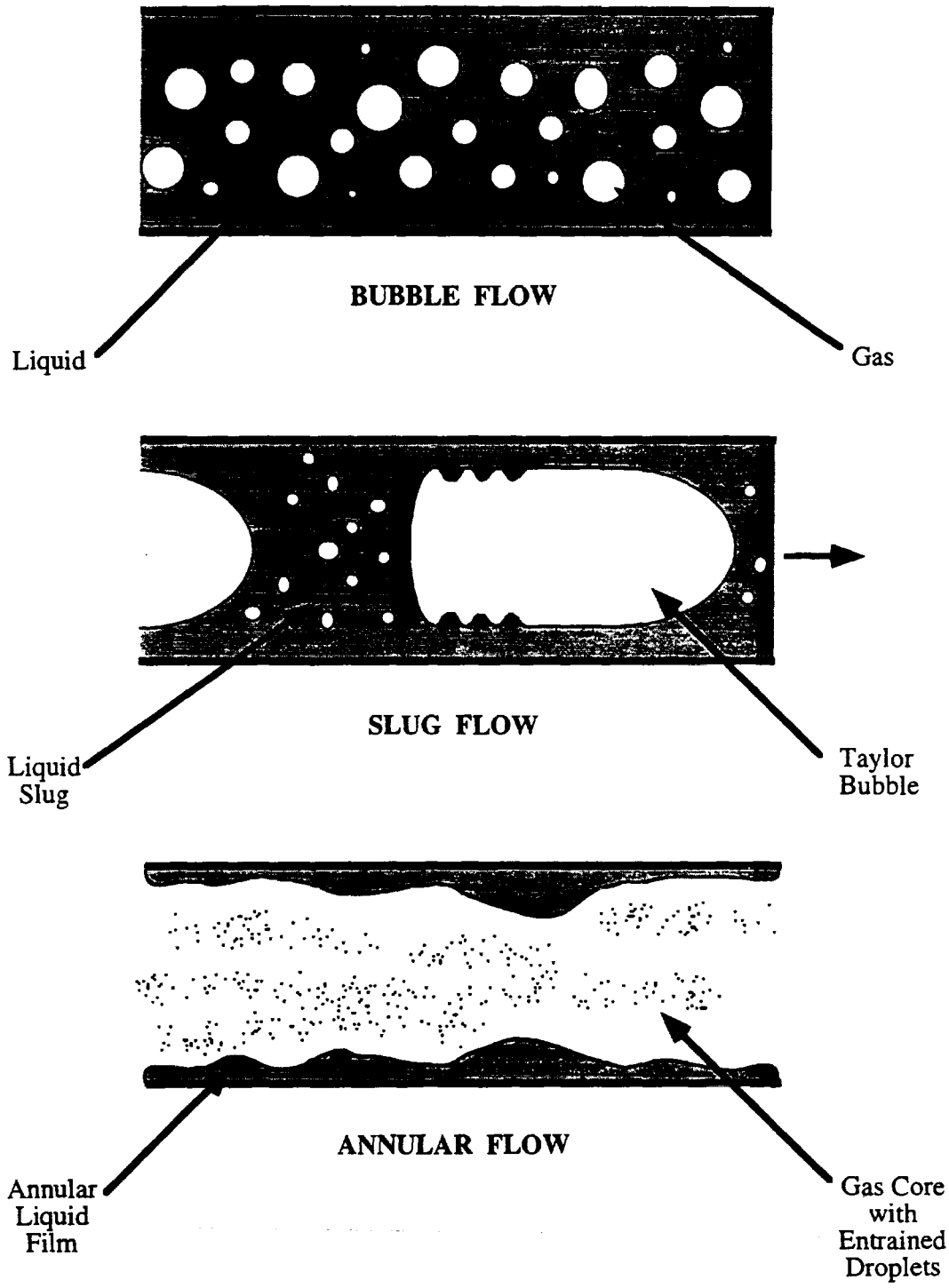

Figure 1.1 Two-Phase Flow Patterns Observed in Microgravity

the bubble flow pattern consists of discrete, nearly spherical gas bubbles surrounded by a continuous liquid phase. This flow pattern generally occurs when the flow rate of liquid is much larger than the flow rate of gas. When the gas flow rate of a bubble flow is sufficiently increased, the flow pattern will undergo a transition to the slug flow pattern which is also shown in Figure 1.1. This flow pattern is characterized by bullet-shaped Taylor bubbles separated by slugs of liquid. Finally, if the flow rate of gas is much larger than the flow rate of liquid, an annular flow pattern is formed, consisting of a rough wavy liquid film on the perimeter of the pipe surrounding a core of gas and entrained liquid droplets as shown in Figure 1.1.

The behavior of two-phase systems is strongly affected by the flow pattern. It is therefore possible for changes in the flow conditions which result in a flow pattern transition to cause large changes in important system characteristics such as pressure drop or heat transfer rates. Since changes in the magnitude and orientation of gravity can cause flow pattern transitions, the pattern which exists under a given set of conditions in microgravity must be known if the behavior of the system is to be predicted and understood.

Early research efforts in two-phase flows in normal gravity attempted to develop mostly empirical models which covered the entire parameter space of practical interest without regard to flow patterns. Such models were valid only within the parameter space studied and contributed little to a mechanistic understanding of the flow. As the field progressed, research began to focus on modeling individual flow patterns since the physics of each pattern is unique. This effort to develop flow-pattern-specific models has generally proven to be more successful than the earlier global models. In order for such models to be useful, the flow pattern must be known for any given set of flow conditions.

Flow pattern maps, showing the conditions under which each flow pattern exists, have been established for two-phase flows in normal gravity for a variety of orientations and geometries (Baker, 1954, Dukler and Taitel, 1984, Barnea, 1986). In contrast, since the microgravity environment has only recently become accessible for two-phase flow experiments, flow pattern maps for microgravity conditions of interest are in an earlier stage of development (Dukler et al., 1988, Bousman and Dukler, 1993, Reinarts, 1993, Zhao and Rezkallah, 1993). The first part of the present study was therefore focused on establishing microgravity flow pattern maps for a variety of flow conditions, liquid physical properties and tube sizes. Using experimental measurements and observations, flow pattern transition models were also developed to predict the occurrence of the flow patterns in microgravity.

1.3 Studies of Bubble, Slug and Annular Flow in Microgravity

Most previous microgravity two-phase flow investigations have focused almost exclusively on flow pattern identification. While this is a key issue in the understanding of these systems, a deeper knowledge of the processes occurring within a given flow pattern is also required for practical design and operation of two-phase flow systems. The quantities of interest to designers of two-phase systems as well as for researchers in the field include the void fraction, liquid film thickness, bubble and wave velocities, pressure drop, wall shear stress and the rate of droplet entrainment as a function of flow conditions and fluid physical properties. Development of mechanistic models to describe these and other factors as well as the eventual development of full flow simulations will likely require experimental measurements of these quantities so that the underlying mechanisms can be deduced.

In the course of this study, an experimental apparatus and techniques were developed which allowed for the accurate and precise measurement of key quantities of interest in each flow pattern. The validity of earth-based models in predicting these quantities was assessed and in some cases, new models suitable for the microgravity environment were proposed and tested.

1.4 Research Strategy

The goal of this research program is to first develop the experimental apparatus and techniques needed to make a number of two-phase flow measurements in the short duration microgravity environment provided by the NASA research aircraft. This effort is described in Chapter 2. The next phase of this study establishes flow pattern maps for three sets of liquid physical properties and two tube diameters across the gas and liquid flow rate parameter space of practical interest. This work is presented in Chapter 3. More detailed measurements of void fraction, bubble velocity and pressure drop are made for bubble and slug flow in Chapter 4. Efforts to model these quantities are also described. Since annular flow is of primary interest in most practical two-phase flow systems, a detailed study of this flow pattern is presented in Chapter 5 including the characterization of the waves and liquid film, as well as measurements of the pressure drop and wall shear stress. The measurements of bubble, slug and annular flow are used to develop and refine flow pattern transition models as described in Chapter 6. Finally, the results and conclusions which can be made from this study as well as recommendations for future work are summarized in Chapter 7.

Chapter 2 Experimental Apparatus

2.1 Microgravity Aircraft Facilities

Both the Learjet Model 25 aircraft based at the NASA Lewis Research Center and the KC-135 aircraft based at the NASA Johnson Space Center were used to conduct the microgravity experiments reported in this study. By following the parabolic flight path shown in Figure 2.1, these aircraft can produce periods of reduced gravity lasting 15-25 seconds (Lekan, 1989). By modifying the flight path, gravity levels of 0 g, 0.17 g (lunar) and 0.33 g (Martian) can be produced. This technique currently produces the longest period of reduced gravity available without resorting to space flight.

The Learjet can perform a maximum of six trajectories in a single flight before aircraft limitations require a return to the airport. The KC-135 aircraft can typically perform 40-50 trajectories in a single flight. Up to two flights per day can be performed by either aircraft.

To monitor the quality of the microgravity condition produced on the aircraft, three-axis accelerometers accurate to 0.001 g were mounted on the aircraft flow loops. A typical time trace of the z axis (floor to ceiling) acceleration measured during the microgravity trajectory is shown in Figure 2.2. This trace has a mean value of 0.008 g with a standard deviation of 0.017 g in the range of 7 - 18 s where the aircraft is considered to be in microgravity. The oscillations in the trace were caused by corrections to the trajectory, aircraft vibrations and atmospheric turbulence. Similar results are typically obtained for the x axis (nose to tail) and y axis (wing-tip to wing-tip) accelerations as well since these variables are also actively controlled by the pilots. Only data taken when the acceleration was within 0.02 g of zero in all three directions were used for the microgravity tests reported in this study. As a result, the duration of the experiments was typically 7-15 s.

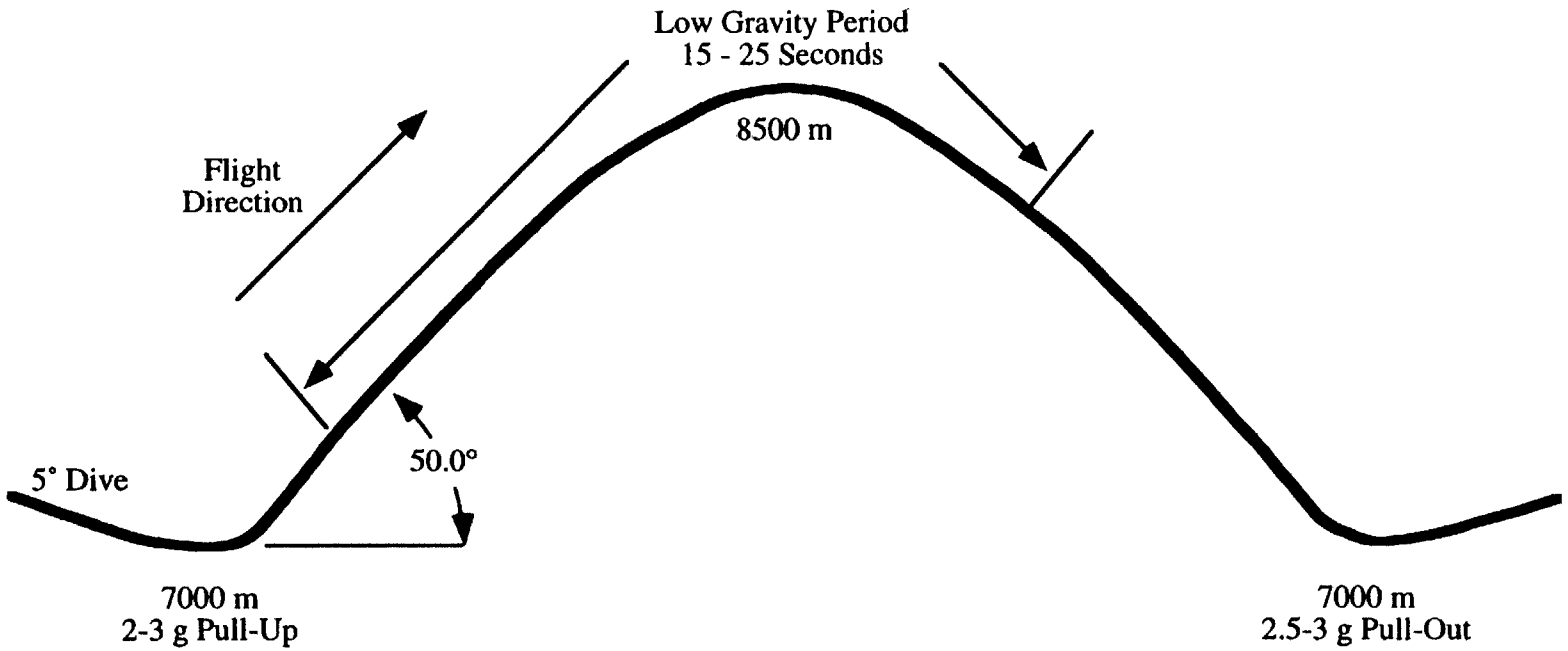

Figure 2.1 Typical Low Gravity Trajectory for NASA Learjet and KC-135 Aircraft

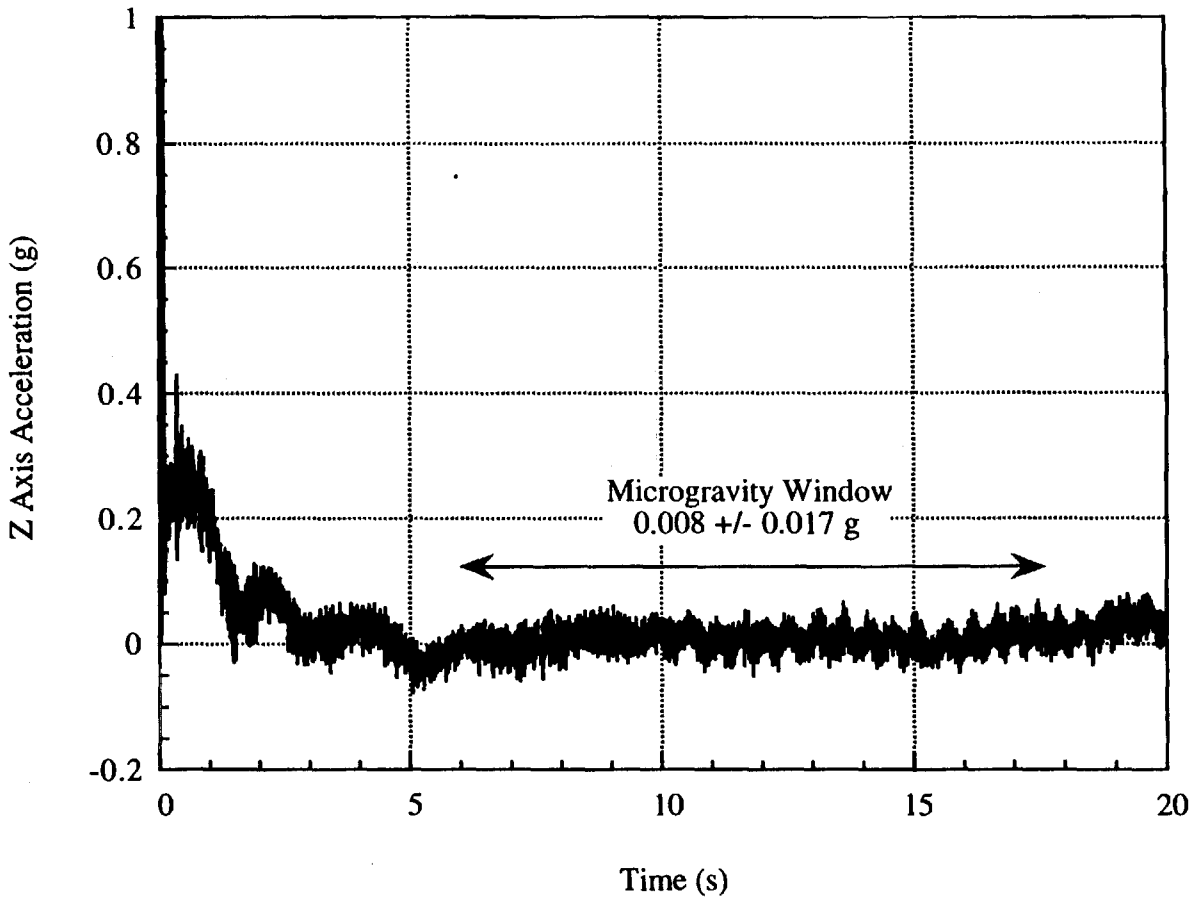

Figure 2.2 Typical Z Axis Accelerometer Trace Recorded on the NASA Learjet During a Microgravity Trajectory

2.2 Aircraft Flow Loops

The flow system used on board the Learjet to conduct experiments with the 12.7 mm ID test sections is shown schematically in Figure 2.3. The purpose of this system is to provide metered quantities of air and liquid to the mixer, collect the liquid for recycle and vent the air exiting the test section.

The air flow rate is controlled by passing the air through one of two choked orifices depending on the flow rate desired. The orifice plates are sized so that sonic velocity is achieved at the orifice for flow rates in the desired range. Once sonic velocity is achieved, the gas mass flow rate is a function only of the upstream pressure and temperature [Anderson, 1982]. This configuration eliminates the effect of downstream pressure changes on the gas flow rate. The upstream pressure is set prior to the experiment with a pressure regulator. During the experiment, the on-board computer records the upstream pressure and temperature (through a pressure transducer and thermocouple) at 1 Hz and calculates the gas mass flow rate and superficial velocity based on these measurements. The system is periodically calibrated so that accurate mass flow rates can be set and measured. Numerous experiments have shown that this system provides a steady mass flow rate of air to the system which is typically within 10% of the desired set point.

The liquid flow rate is controlled by a pair of metering valves on the discharge of the feed tank. In order to maintain a constant pressure in the feed tank during periods of reduced gravity and to prevent air bubbles from being ingested into the liquid system, the tank is equipped with an air pressure loaded piston. The liquid flow rate is a function of the pressure above the piston, the settings of the metering valves and the properties of the liquid being used. The turbine meter provides a digital readout of the flow rate via the computer system. The liquid system is periodically calibrated to provide set points for each liquid used and the liquid flow rate achieved is also typically within 10% of the desired set point. Both the liquid and gas supply systems contain solenoid activated on-off valves

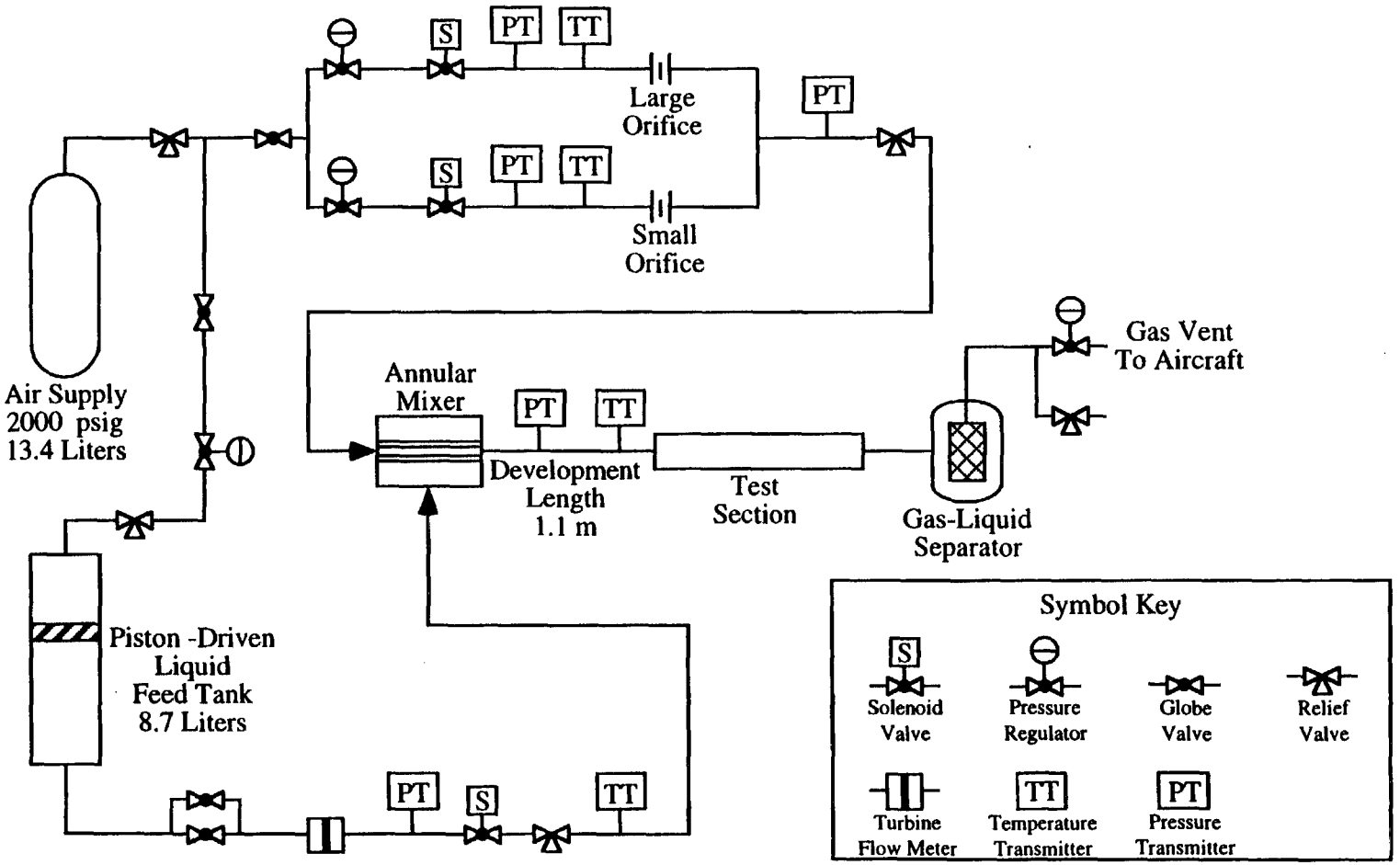

Figure 2.3 Flow Loop Used on the NASA Learjet for the 12.7 mm ID Test Sections

which allow the computer to start and stop the flow at the appropriate times during the trajectory.

In the mixer, the air is introduced axially into the tube while the liquid is introduced normal to the air stream. The body of the mixer is transparent so that details of the mixing dynamics can be observed and photographed. The internal tube in the mixer is interchangeable and two configurations were used in this study. During the flow mapping experiments to be described later, the liquid was introduced into the air stream through a series of small holes evenly distributed along the internal tube. Prior to the annular flow studies, the internal tube was replaced by a tube which introduced the liquid into the air stream as an annular film. While the dynamics inside the mixer were altered with the change in configuration, lab tests confirmed that the flow pattern observed at the end of the flow development section was unaffected by the changes in the mixer.

The two-phase air-liquid mixture exits the mixer into a 1.1 m length of smooth 11.2 mm ID stainless steel tubing which provides a flow development length of 86 pipe diameters upstream of the test section. The length of the development section is constrained by the available cabin space in the Learjet. Lab tests with a transparent development section in the concurrent upward, downward and horizontal flow configurations demonstrated that an unchanging flow pattern was achieved within 30 cm of the mixer outlet in all combinations of gas and liquid flow rates used during these studies. Based on these observations, and direct observation of unchanging flow pattern in the test section during microgravity, the flow development length used was deemed to be sufficient to provide a fully developed two-phase flow to the test section in all cases. The mixer, development section and test section are joined using Swagelock fittings which have been bored out to provide a constant internal diameter and a smooth connection between tubes.

Upon exiting the test section, the two-phase mixture passes into the gas-liquid separator. Since buoyancy cannot be used to separate the phases in microgravity, the

mixture is passed through a series of concentric stainless steel screen mesh cylinders. The liquid spreads across the mesh by surface tension and remains attached during microgravity. During the high gravity pull out portion of the flight trajectory, the liquid drains off the mesh to the bottom of the tank where it can be recycled. The air passes through the mesh unhindered and is vented through a pressure regulator to the aircraft cabin. While droplets of liquid are occasionally entrained in the vented gas when the highest flow rates are used, this technique provides a simple method for separating gas-liquid flows during short periods of reduced gravity.

The flow loop used on board the KC-135 aircraft with the 25.4 mm ID test section, shown schematically in Figure 2.4, was constructed after the Learjet flow loop studies were complete and thus incorporates many improvements based on experience gained from the Learjet flow loop. The KC-135 flow loop supplies metered flow rates of air and liquid to the mixer in the same method as the Learjet flow loop. The capacities of the gas and liquid supply tanks are much greater than those in the Learjet flow loop because the KC-135 performs many more trajectories in a single flight. The KC-135 flow loop also features a recycle system which pumps liquid from the gas-liquid separator to the liquid feed tank during the time between trajectories. The mixer is a venturi which provides a gas core and annular liquid film similar to the annular mixer used in the Learjet flow loop. The system is distributed across three racks which can be moved relative to each other and provide considerable flexibility in the lengths of test sections and flow development sections which can be used.

Since operations such as turning valves or activating switches can be difficult to perform in microgravity, many of the functions of the flow loop are controlled by a dedicated computer. Prior to entering the trajectory, the metering valves and regulators are set for a given experiment while the solenoid valves remain closed. When the operator feels the transition from the high gravity pull up to the microgravity portion of the

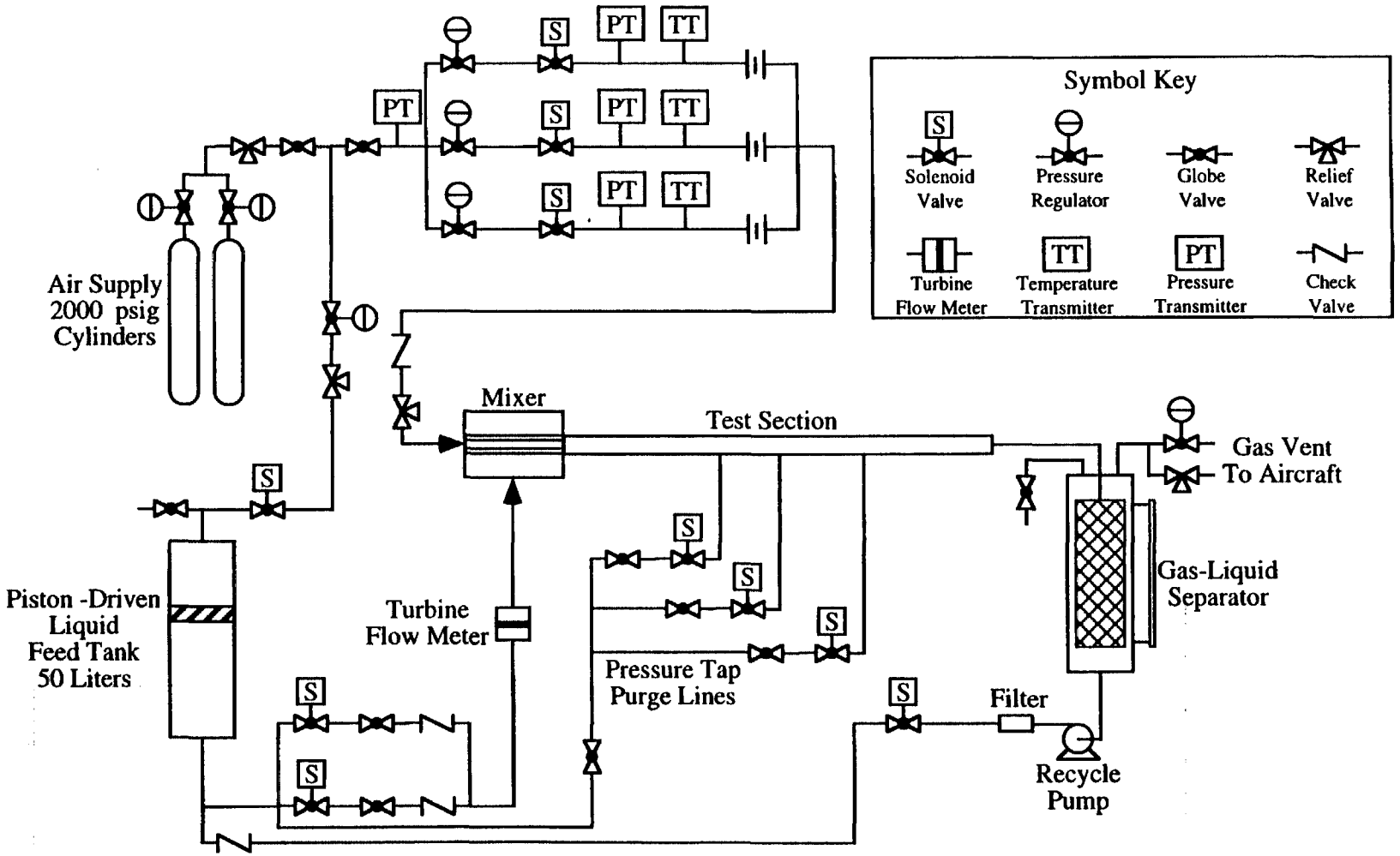

Figure 2.4 Flow Loop Used on the NASA KC-135 Aircraft for the 25.4 mm ID Test Section

trajectory, a single switch is activated which initiates all control functions on the computer. The computer first opens the solenoid valves, initiating the flows of gas and liquid. After a brief delay while the two-phase flow is allowed to develop, all probes and cameras are activated and the data are recorded in the computer random access memory. After 25 seconds, the computer shuts off the flows of gas and liquid and deactivates all instruments and cameras. During the brief period between trajectories, the data are written to a permanent storage device while cameras are reloaded and the flow rates for the next run are set. Both flow loops require only two operators to conduct the experiments.

2.3 Flow Visualization

During the course of this study, direct observation of the two-phase flow phenomena was central to the determination of flow patterns as well as the identification of potential mechanisms of transition. Flow features such as bubbles and waves may be less than 2 cm in length but can travel at velocities greater than 5 m/s. The human eye does not provide sufficient resolution to directly capture the details of such flows. Laboratory experiments have also demonstrated that standard video equipment, recording images at 30 frames per second, is inadequate for resolving two-phase flows in detail. Experience gained in this study has shown that high-speed photography or high-speed video recording is necessary to fully visualize the flow. High-speed photography was used in this study because of the prohibitive cost of high-speed video systems.

The movie films used in this study were taken with Milliken DBM5 high speed cameras using Kodak RAR2498 black and white film. The cameras had a shutter speed of 0.002 s and were calibrated to run at 400 frames per second. The cameras were fixed to the experiment racks and automatically activated by the computer 6 s after the flow started.

To avoid image distortion caused by the difference in refractive indices of the curved tube and the air, a viewing box was placed over the portion of the test section in view of the camera. This box presents a flat Plexiglass surface to the camera. The internal space between the viewing box and the test section tube was filled with water because the refractive index of the Plexiglass is much closer to that of water than that of air. A transparent millimeter scale attached to the box allows length scales to be determined from the images.

Lighting the viewing box from the back was found to give the best images. A lighting bar consisting of incandescent bulbs covered by a diffuser plate and placed against the back surface of the viewing box was used. An LED display showing the elapsed time is also in view of the camera so that the velocity of features in the flow can be computed from the images. The success of the photographic techniques used in this study is demonstrated by the photographic images in Appendix A, which show clear images of bubble, slug and annular flows.

2.4 Void Fraction Measurement Technique

A key design variable in multiphase flow systems is the void fraction (the ratio of the gas volume to the total volume) of the mixture. This quantity is useful in predicting two-phase physical properties, such as the mixture density, as well as in modeling heat transfer in vaporizing and condensing systems. It will be shown in later parts of this work that the gas void fraction of a two-phase mixture cannot simply be determined as the ratio of gas to gas-and-liquid flow rates as might be expected. Thus a local measurement of the void fraction is useful in correlating experimental results and in developing physically based two-phase flow models.

As will be discussed in detail in later sections, the void fraction measurement required for modeling is one which is axially local but averaged over the cross section of the tube. Early measurement techniques involved capturing a portion of the mixture in a holding vessel or in the pipe between fast-closing valves. These provide only overall averages (both axially and radially) and cannot measure void fraction in different regions of the flow such as in liquid slugs and across Taylor bubbles. A better technique uses flush mounted ring electrodes which measure void fraction by measuring the electrical conductivity of the mixture between the electrodes. This provides axially local measurements averaged over the cross section of the tube as required and does not disturb the flow. The output however is highly non-linear over the entire range of void fraction and the geometry of the electrodes must be matched to the range of void fractions to be measured (Colin, 1990). A variation of this technique involves measuring the electrical conductivity between parallel wires spanning the cross section of the tube. This idea was first proposed by Brown et al., 1978 for measuring liquid film thickness but was also adapted in this work to measure void fraction.

The configuration of the parallel-wire void fraction conductance probe is shown in Figure 2.5. Two 76 μm diameter thermocouple wires (13% Rh, 87% Pt) are stretched tightly across the tube cross-section separated by a 2.5 mm gap. The wires pass through 0.1 mm diameter holes in the tube wall which are sealed externally with O-rings. Accurate measurements require that the wires remain parallel, so the wire tension is maintained with external tensioning screws which are held fast with glue once the wires are in place.

The void fraction measurement is made by measuring the electrical conductance between the wires. The gas phase is essentially non-conductive while the liquid phase is made to be conductive using a small amount of sodium chloride (typically 0.5-1.5 g/L) to raise the specific conductance of the solution to approximately 0.002 mho/cm. The signal is therefore proportional to the fraction of conductive liquid between the wires. Since two-

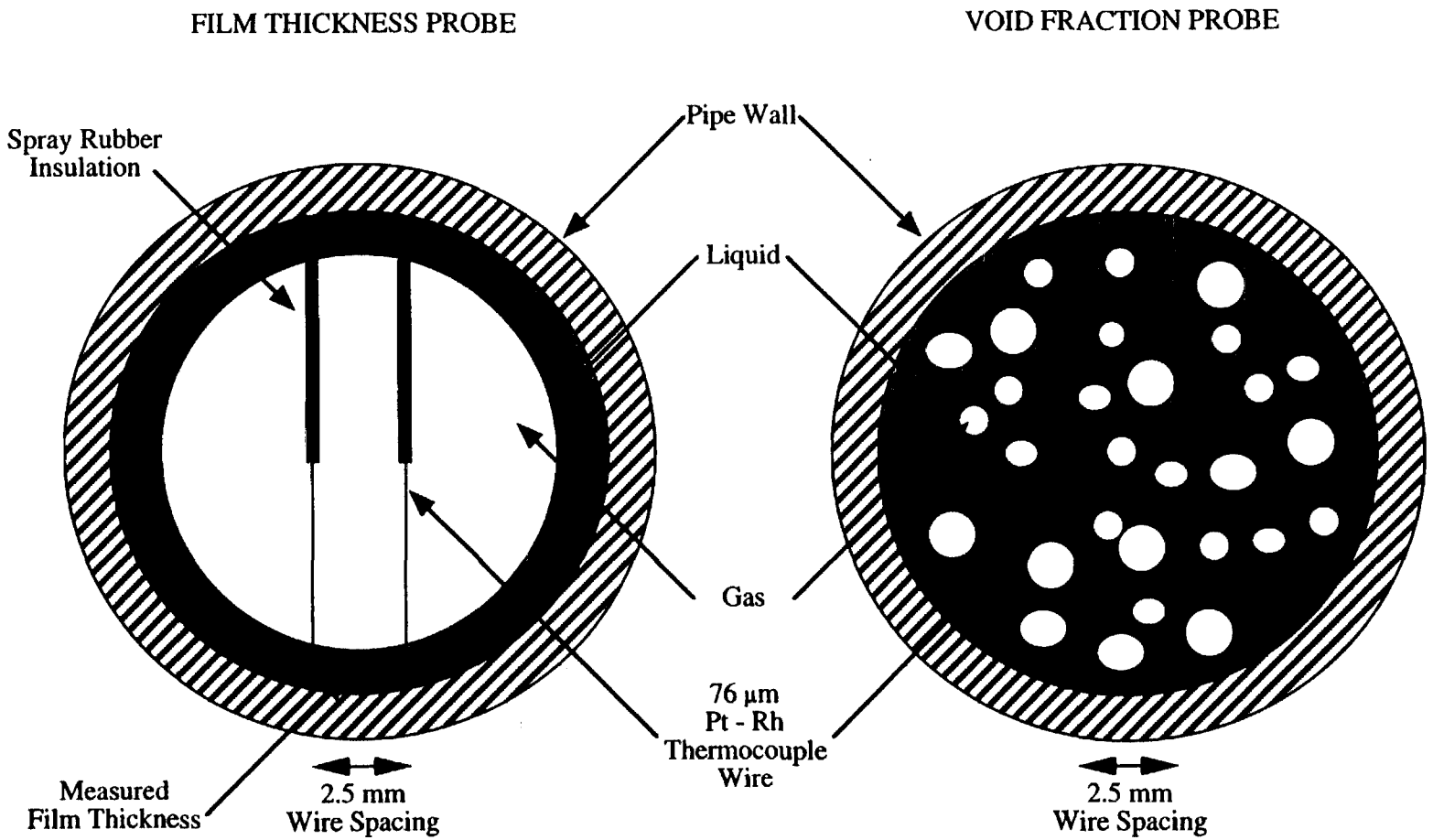

Figure 2.5 Parallel Wire Conductance Probes for Film Thickness and Void Fraction Measurement

phase flow features move quickly down the tube, a special high-speed conductance-measurement electronic system is required to obtain an axially local measurement. A prototype system was developed by the University of Houston and Circuit Concepts Inc. in the course of a previous study as described by Lacy, 1992. This system was modified by Circuit Concepts, Inc. and transferred to a printed circuit board using military-grade electronic components in order to provide accurate measurements in the high-vibration and high-electromagnetic noise environment of the aircraft.

To measure the conductance between the wires, a voltage must be applied between them. If a dc voltage were to be applied, migration of ionic species towards the wires would cause the signal to drift. The excitation of the wires must therefore occur at high alternating frequency. As mentioned by Brown, et al., 1978, the conductance between wires varies only as the log of the distance between them which can lead to significant interference between multiple probes operating in the same flow system. Measurements which are free of interference require that only one probe be active in any instant of time. Unfortunately, electronic systems which do not prevent this interference still appear in the literature (Paras and Karabelas, 1991).

The Circuit Concepts, Inc. system excites each of 16 conductance measurement channels in sequence by switching a 16 kHz square-wave voltage signal between them (Lacy, 1992). Each probe is active for 62.5 μs during which time, the other channels are inactive. After the channel is activated, the system is allowed to stabilize and the measurement is taken during the last 8 μs of the sampling window. This signal is stored in a sample-and-hold circuit for output. For this study, the system was configured to provide a 1 kHz output allowing frequencies of up to 500 Hz to be distinguished in the measurements.

The output signal from the conductance system is a function of the specific electrical conductance of the liquid solution, which can change with variations in the salinity and

temperature of the solution. To correct for small changes in the electrical conductance of the solution, the liquid was passed through a standard reference cell prior to entering the mixer. This cell is similar in construction to the void fraction probe shown in Figure 2.5 and is driven by the conductance measurement system. Since the offset voltage of all conductance channels is zero for a zero input, the output signals for the other conductance measurements can be corrected for changes in the solution conductivity by dividing the output signal by the reference cell output signal. During the microgravity experiments, the reference cell reading was recorded at 1 Hz and the results averaged over the run to produce a single reference voltage. Since the liquid solution was well-mixed prior to flight, the salinity and temperature were uniform throughout the liquid tank and only small deviations ($< 1\%$) from the average value were observed in the individual measurements.

The void fraction probe was calibrated using the apparatus shown in Figure 2.6. A two-phase mixture is passed upward through the vertically mounted test section containing the probe. The void fraction output signal from the conductance system was averaged for two minutes using a digital oscilloscope. At the end of the averaging period, the fast closing valves were shut and the height of liquid between the valves was measured. The time-averaged void fraction is determined from the ratio of the liquid height to the total height between the valves. The conductivity reference voltage was also recorded with every reading and used to correct the output signal for changes in conductivity. By varying the proportions of liquid and gas fed to the test section, the probe is calibrated over the entire range of void fraction. A typical void fraction calibration curve is shown in Figure 2.7 and the response is clearly linear over the entire range of void fraction. The probe was calibrated prior to flight and checked after flight to ensure that the calibration had not appreciably changed.

The uncertainty in the void fraction measurement is thought to be due primarily to the error in measuring the liquid height during calibration and in discretizing the analog

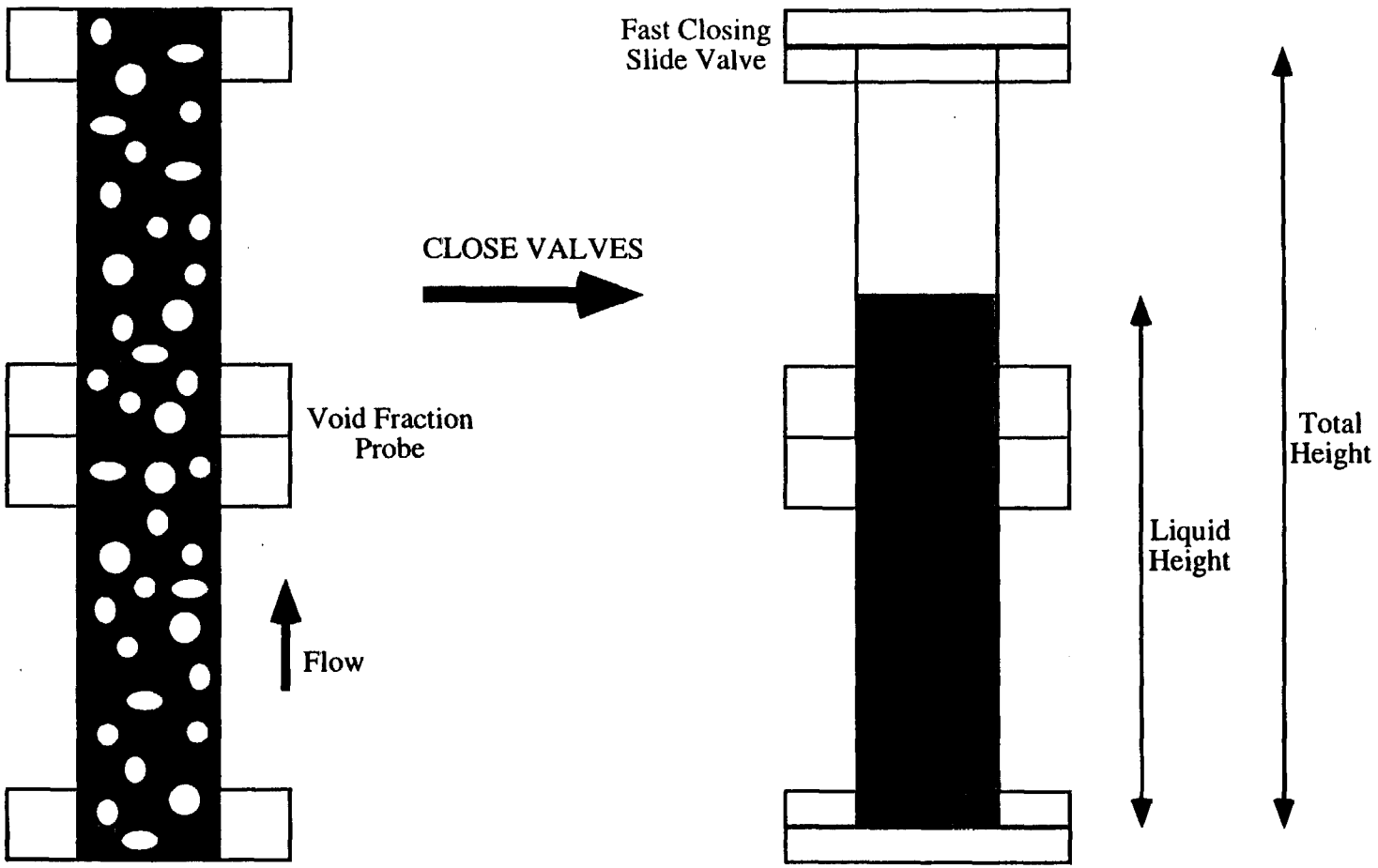

Figure 2.6 Void Fraction Probe Calibration Method

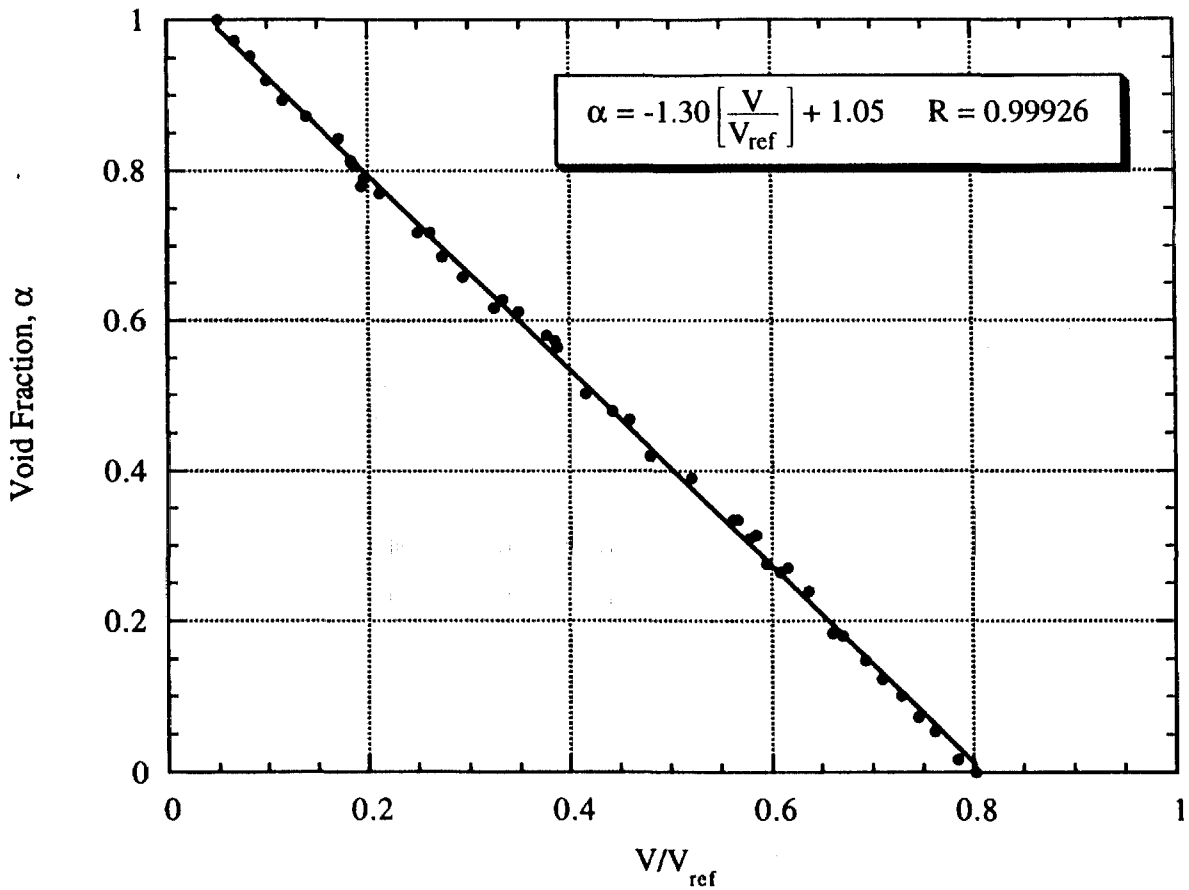

Figure 2.7 Typical Void Fraction Calibration Curve

output of the conductance system with the analog/digital converter in the data acquisition system. The void fraction, α, is determined from the height of liquid shown in Figure 2.6 by

$$\alpha = 1 - \frac{h_L}{h_T}. \tag{2.1}$$

Based on the equipment used during the calibration procedure, the uncertainty in the height measurements is estimated to be 0.5 mm. This yields a maximum uncertainty in the void fraction measurement of only ±0.4% for a void fraction of 0.75. As will be shown in later sections, for void fractions greater than 0.75, the flow pattern is annular and the void fraction probe was used only qualitatively in the annular flow regime. The discretization uncertainty caused by digitizing the signal in the 12-bit aircraft data acquisition system is only ±1.25 mV for the 0-10 V range of the system. With the typical full scale output (α = 0) of 7 V, the discretization produces an uncertainty of ±0.5%. Therefore, the uncertainty associated with the void fraction measurement are thought to be small, on the order of ±0.65%, in the range of $0 < \alpha < 0.75$.

The dynamic response of the void fraction probe is controlled by the response of the conductance system driving the probe. The output stage of the system is a low-pass filter with an RC time constant of 0.1 ms, producing a dynamic response of 10 kHz (Grob, 1977). However, since the conductance system is complex, the dynamic response to a step change was directly measured. A circuit was constructed which switched the input of the conductance measurement system between two resistance values in 4 μs. The response of the conductance system to this step change was recorded on a high speed digital oscilloscope and is shown in Figure 2.8. The results show no overshoot, indicating that the response of the conductance system is essentially first order (Tse and Morse, 1989). The normalized response of a first order instrument to a step response is given as

$$y = (1 - e^{-t/\theta}), \tag{2.2}$$

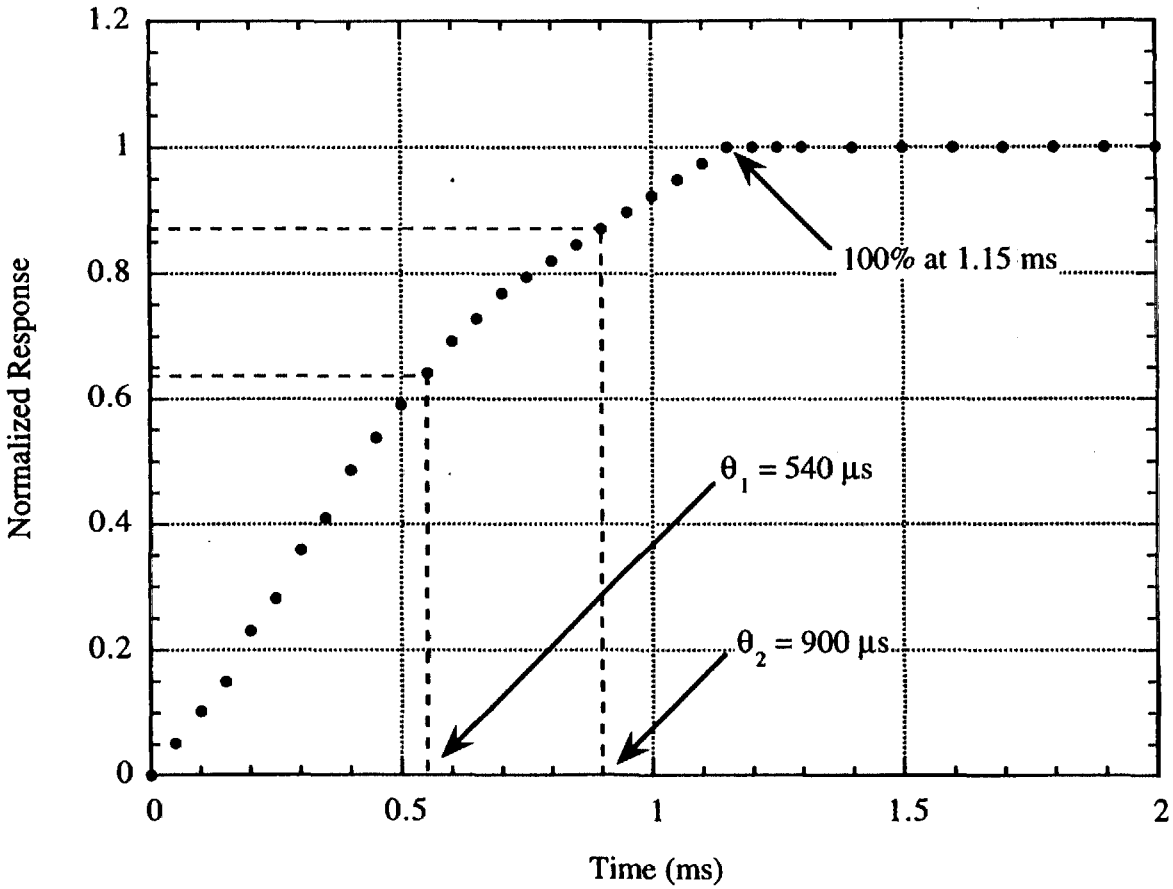

Figure 2.8 Conductance System Response to a 4 µs Step Change

where θ is the time constant of the system. For $t/\theta = 1$, (2.2) is solved to yield a value of 0.632. By determining the time needed for the response in Figure 2.8 to reach 63.2% of full scale, the time constant of the system was estimated to be 540 μs, leading to a dynamic response of 1850 Hz. Since the conductance measurements were acquired at 1000 Hz, the response was not limited by the conductance measurement system and frequencies of up to 500 Hz can be resolved in the void fraction measurement.

A typical void fraction time series trace of microgravity bubble flow is shown in Figure 2.9. The oscillations in the trace are individual bubbles passing between the wires as confirmed by comparing the trace with the high-speed movie films.

2.5 Film Thickness Measurement

A description of the shape of the gas-liquid interface is useful in understanding the nature of two-phase flows. The curvature of Taylor bubbles and the amplitude and shape of annular waves are closely related to phenomena such as pressure drop and entrainment of droplets which are of considerable practical interest. As will be shown in later sections, the shape of the interface is continuously changing and features such as bubbles and waves can travel at velocities greater than 5 m/s. In addition, the thickness of annular liquid films may be less than 0.2 mm with waves of only 0.5 mm in amplitude. Thus a non-intrusive probe which could measure the local thickness of very thin liquid films at a frequency sufficient to resolve the features in the flow was required.

Ideally, a film thickness probe should yield a point measurement at high frequency without disturbing the flow. This scenario has nearly been achieved using laser systems and related optical techniques in simple flow geometries such as large ducts and open channels. However, applying these techniques in small, closed pipes, such as those used

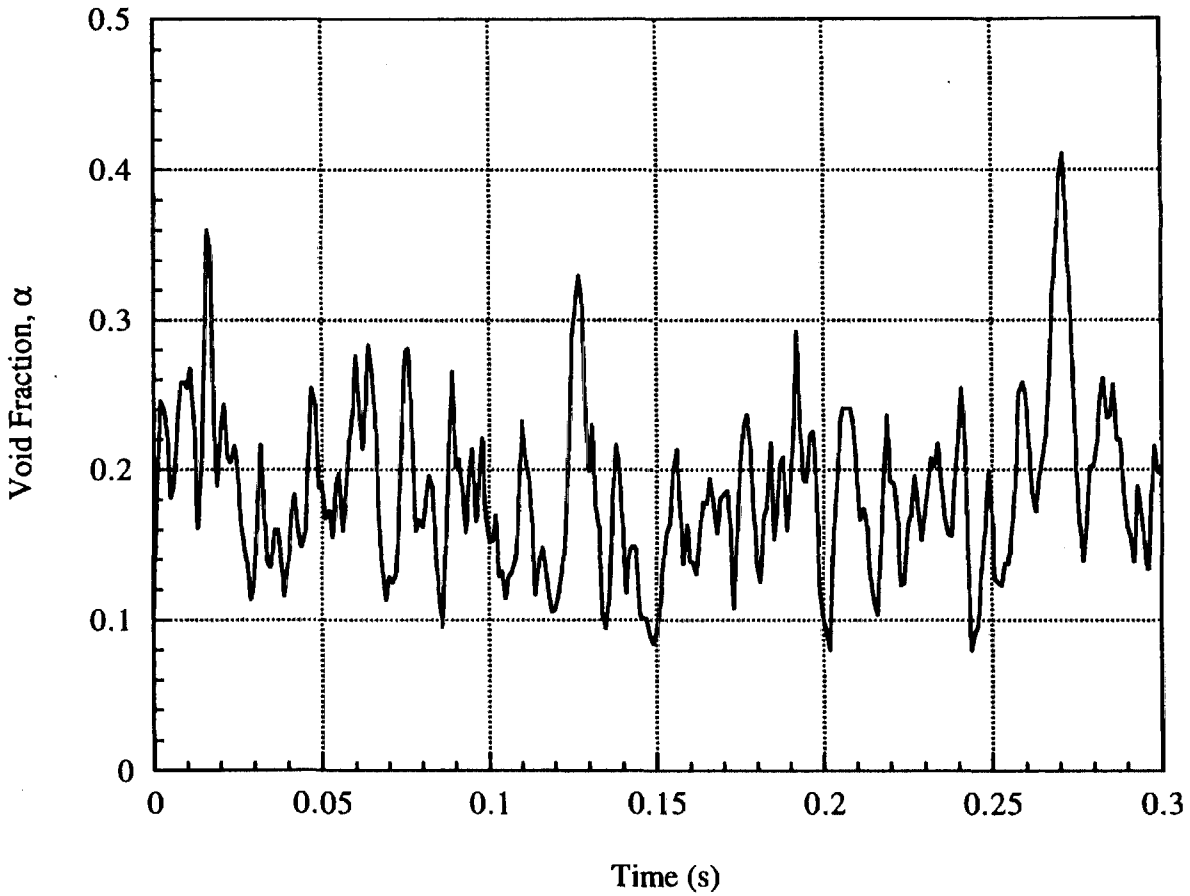

Figure 2.9 Typical Void Fraction Time Series for Bubble Flow in Microgravity

in this study, presents many problems related to maintaining a clear path for the laser (Jayawardena, 1993). An alternative technique is the parallel wire conductance probe as described by Brown, et al., 1978. The configuration of the probe is shown in Figure 2.5. The probe is identical to the void fraction probe described previously except that half of the length of the wires is insulated from the flow using thin coats of a spray rubber compound. The probe is driven by the conductance measurement system described previously and the output varies linearly with the height of the liquid film between the two wires.

Calibration of the film thickness probe requires special attention to precision because the liquid films in annular flow can be less than 0.2 mm in thickness. Traditionally, the test section containing the probe was laid horizontally with the wires positioned vertically and the liquid level raised while recording the output of the probe (Zabaras, 1985). This technique does not work well for small tubes (<1.5 cm ID) where the curvature of the pipe and surface tension of the liquid make producing very thin liquid films difficult. In addition, Lacy, 1992 presented evidence that this method produced erroneous results when compared to vertical falling films, although this could not be confirmed in the current study. For these reasons, an alternative calibration technique suitable for small tubes was developed in the course of this study.

A schematic representation of the film thickness calibration technique is shown in Figure 2.10. A Taylor bubble, injected into the section with a syringe, is held with a rod over the film thickness probe wires while liquid is pumped downward. A 50-50 wt% mixture of water and glycerin is used instead of water in order to reduce oscillations of the Taylor bubble. Various combinations of the rod position and the flow rate of liquid are used to produce liquid films over the wires ranging from 0.1 mm to 6.35 mm (pipe radius for the 12.7 mm ID test sections) in thickness. The thickness of the liquid film was measured using a needle gauge which was also connected to the conductance measuring system. After averaging the probe output for 30 s, the needle gauge was moved towards

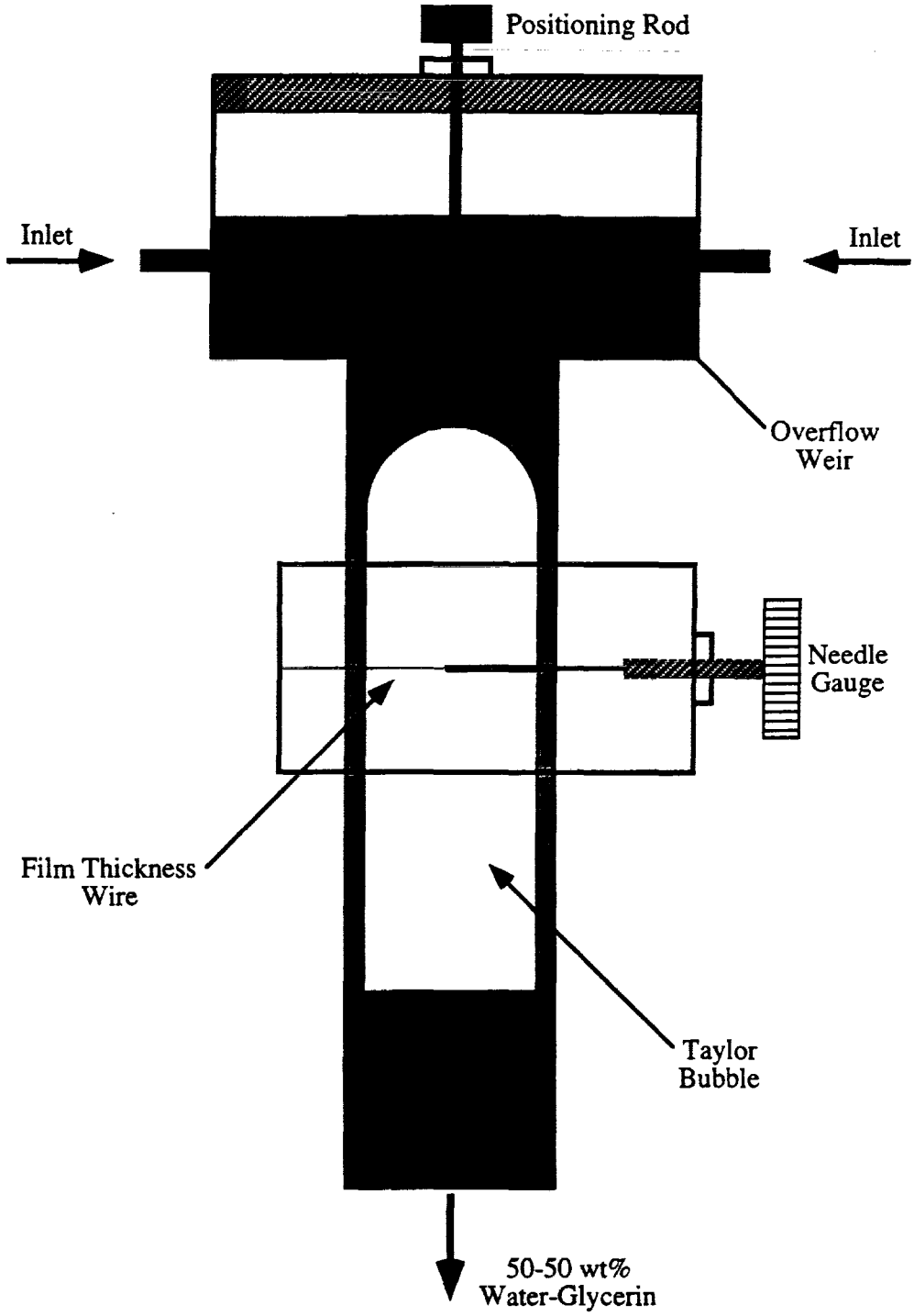

Figure 2.10 Film Thickness Probe Calibration Method

the liquid film until the needle contacted the liquid surface. When contact was made, a step change in the response of the conductance system would be observed on an oscilloscope. Once the surface was detected, the needle was stopped and the film thickness recorded. During the entire procedure, the reference cell reading was recorded and used to correct the results for changes in liquid temperature or salinity. A typical film thickness calibration curve is shown in Figure 2.11. The response is clearly linear over the entire range (0 - 6.35 mm) although nonlinearity was reported for this system for very large film thicknesses (> 20 mm) by Lacy, 1992.

The uncertainty in film thickness measurement is similar to that for the void fraction measurement with the largest uncertainties being attributed to the precision in measurement of the film thickness during calibration and in discretizing the output of the conductance measurement system. Based on the resolution of the needle gauge used for film thickness calibration, the calibration uncertainty is estimated at ±0.02 mm. This produces an uncertainty of ±4% for a film thickness of 0.5 mm (a typical value for annular flows). The discretization uncertainty of ±1.25 mV produces an uncertainty of only about ±0.6% for the same 0.5 mm annular film assuming a typical 5 V output for full pipe flow. Therefore the uncertainty in the film thickness measurements is estimated to be less than ±5% for film thicknesses of 0.5 mm or greater. The dynamic response of the film thickness probe is the same as that of the void fraction probe since both are limited by the response of the conductance measurement system.

Typical film thickness time traces for a Taylor bubble in slug flow and an annular wave are shown in Figures 2.12 and 2.13, respectively. The actual measurement points, acquired at 1000 Hz, are shown across a liquid slug and Taylor bubble for microgravity slug flow in Figure 2.14. A similar view of a microgravity annular wave is shown in Figure 2.15. As shown, the resolution is sufficient to define the curvature of the Taylor bubble and to completely describe the shape of the annular wave. Measurements of this

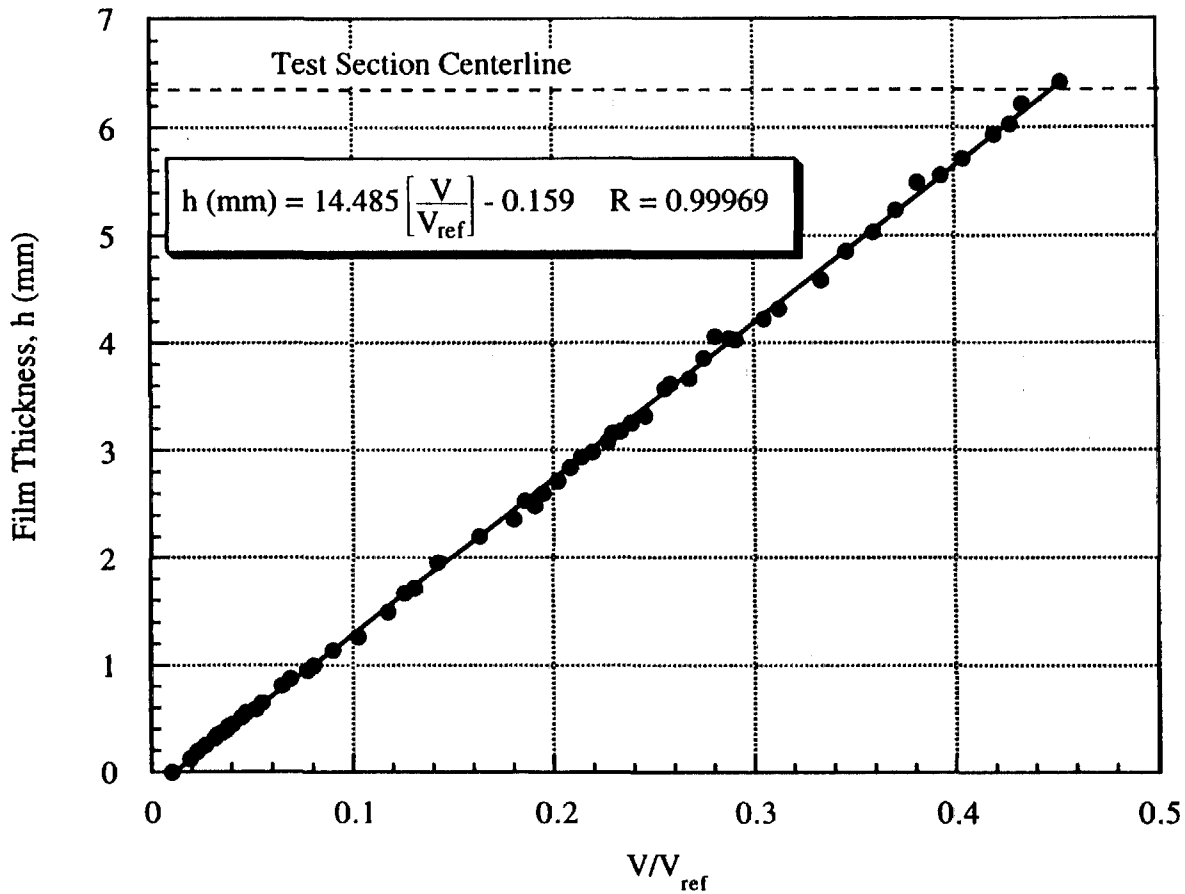

Figure 2.11 Typical Film Thickness Calibration Curve

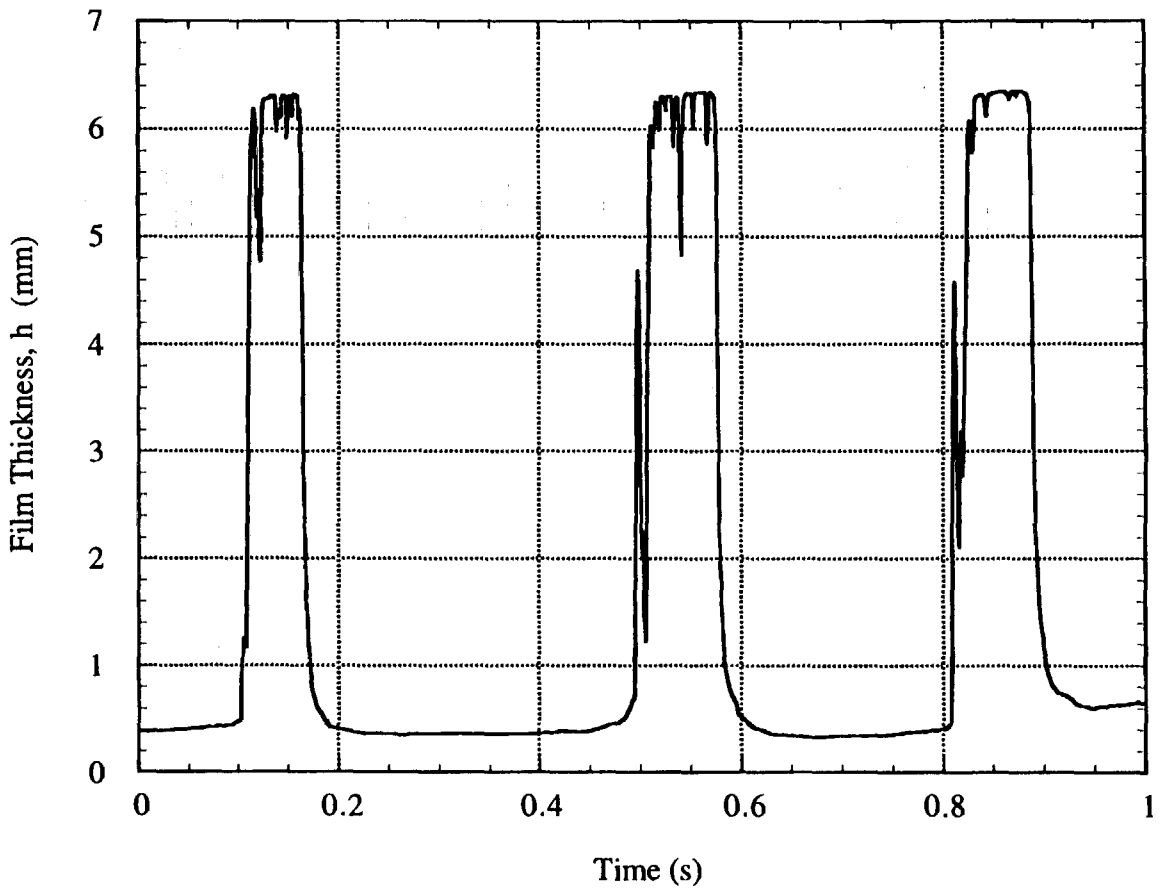

Figure 2.12 Typical Film Thickness Time Series Trace of Slug Flow in Microgravity

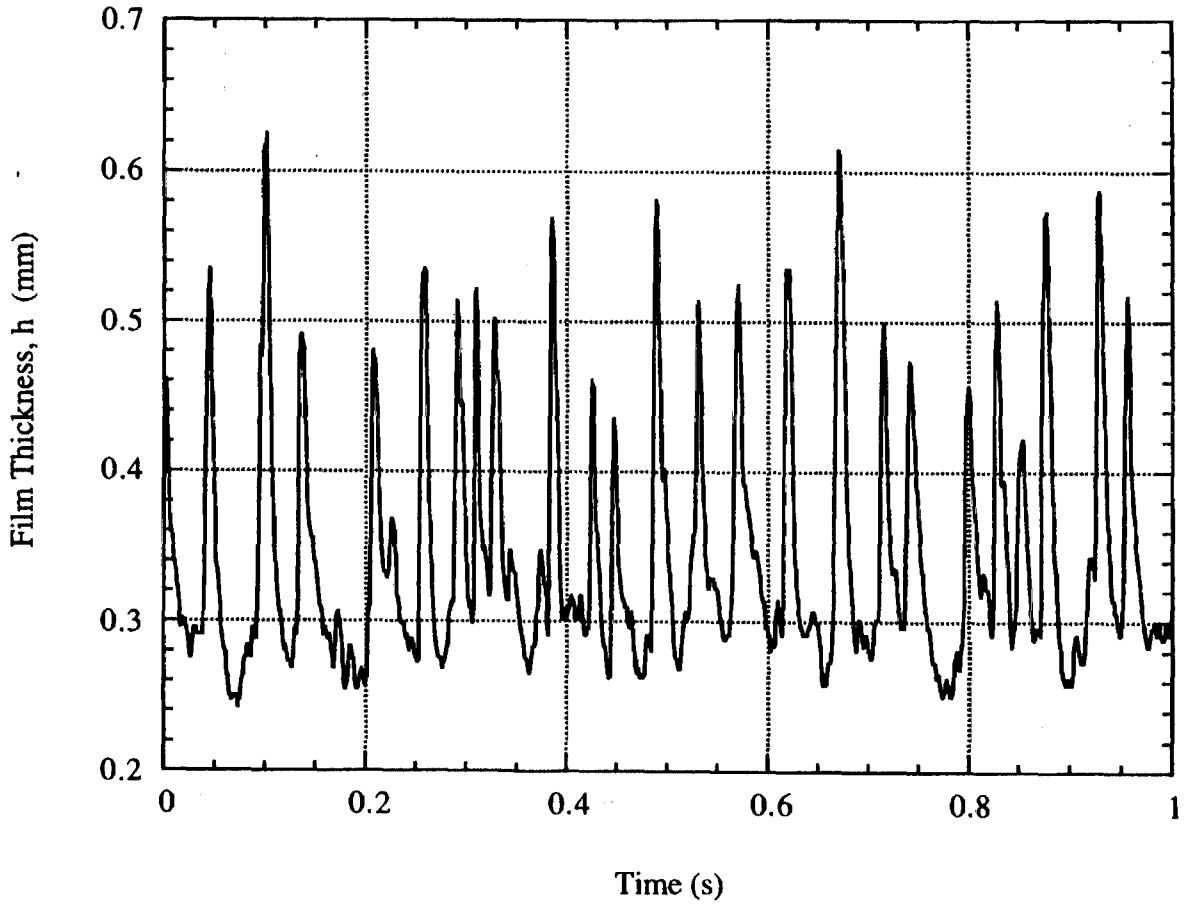

Figure 2.13 Typical Film Thickness Time Series Trace of Annular Flow in Microgravity

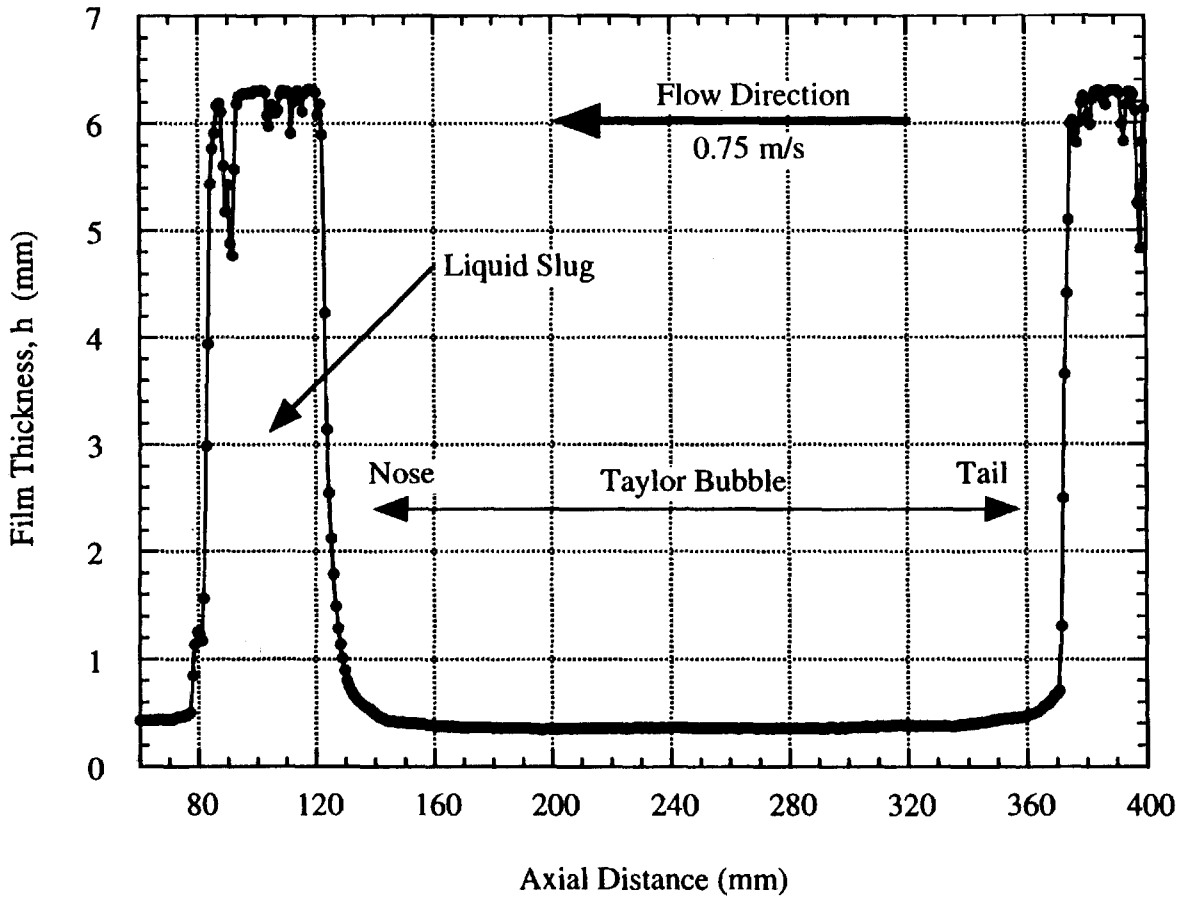

Figure 2.14 Resolution of Film Thickness Measurement Across a Liquid Slug and Taylor Bubble in Microgravity

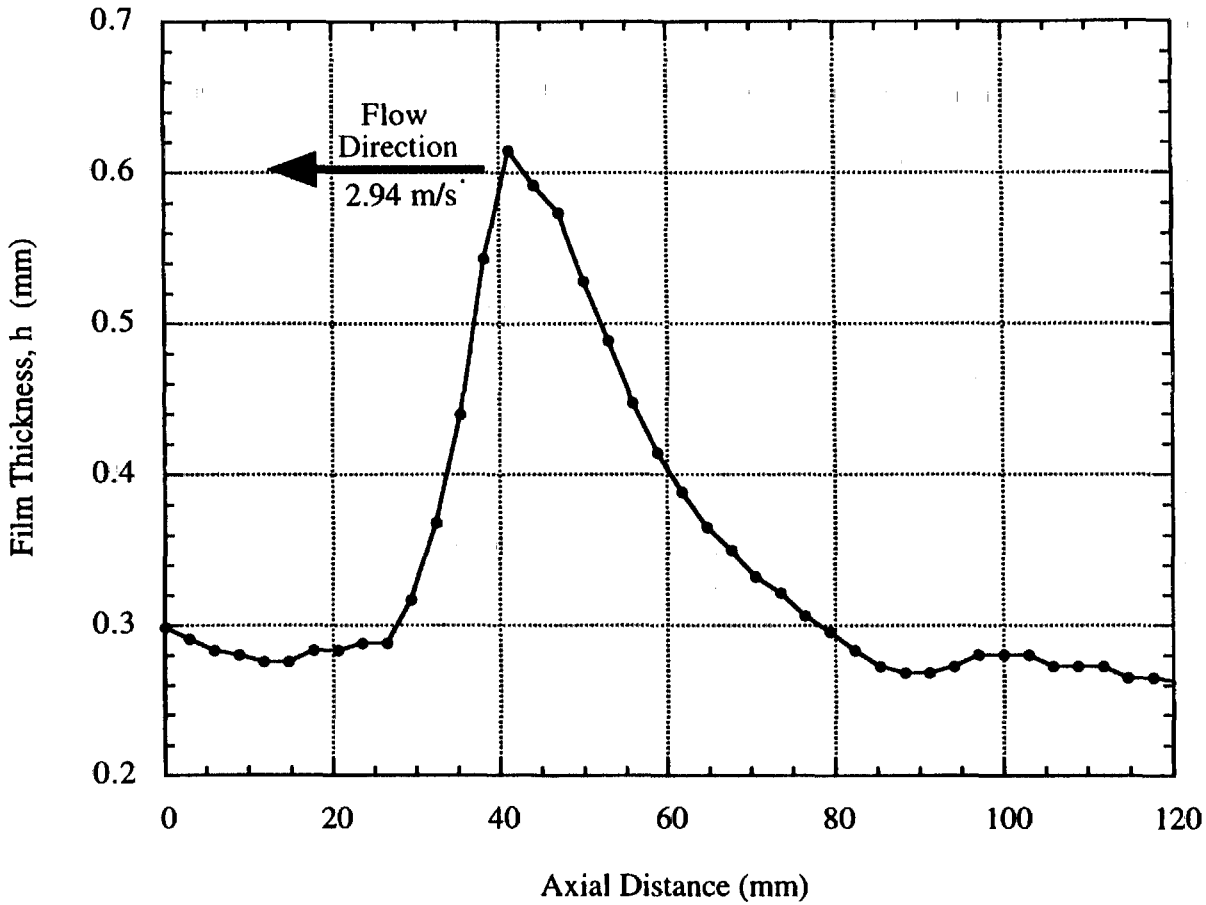

Figure 2.15 Resolution of Film Thickness Measurement Over an Annular Wave in Microgravity

detail will be required for accurate simulation of processes occurring at the gas-liquid interface.

2.6 Velocity Measurement

The velocity at which bubbles or waves travel is important to the understanding of the interaction between the gas and liquid in two-phase flows. In addition, the amplitude and frequency of vibrations induced by slug or annular flows on board spacecraft are of interest to designers. For these reasons, techniques were developed to measure the velocity of bubbles and waves in the flow.

Initial velocity determinations were made using high-speed movie film. A millimeter rule was attached to the camera viewing window mounted on the test section so that a bubble or wave front could be timed over a known distance. At a camera speed of 400 frames per second, this technique has a temporal resolution of 2.5 ms which is sufficient to track the features in the flow. The procedure is very time consuming however, requiring the velocity determination of many individual features in order to produce a reliable average velocity.

A more accurate and less time consuming approach uses the film thickness and void fraction measurements to determine the velocity from the time series of the conductance probes. In the test sections used in this study, the conductance probes (void fraction or film thickness) were a known distance apart. As a feature such as a bubble or wave front moves through the test section, it produces a signal first at the upstream probe and then at a downstream probe, separated by a distinct time lag. As long as the velocity of the feature is relatively constant and the shape of the interface does not change significantly, the velocity can be computed by taking the ratio of the probe separation distance to the measured time

lag. High speed photography confirmed that over short distances, the velocity and shape of the bubbles and waves are relatively constant.

The average time lag between any two probes can be computed from the normalized cross-correlation function given by Thomas, 1971 for processes X_1 and X_2 as

$$\rho_{12}(\tau) = \frac{R_{12}(\tau)}{[R_{11}(\tau)\, R_{22}(\tau)]^{1/2}}, \tag{2.3}$$

where ρ_{12} is the normalized cross-correlation function and τ is the time lag between probes. The cross-correlation function R is given by

$$R_{12}(\tau) = E\{X_1(\tau)\, X_2(t+\tau)\}, \tag{2.4}$$

where E represents the expectation value (mean). When the calculation was performed using a film thickness and a void fraction signal, the void fraction was converted to an equivalent film thickness by

$$\frac{h}{R} = 1 - \alpha^{1/2}, \tag{2.5}$$

where h is the local film thickness and R is the tube radius.

Using two conductance time series traces from a given experiment, the normalized cross-correlation is computed as a function of time lag. A typical result is shown in Figure 2.16. As shown, there is a well defined maximum in the normalized cross-correlation which occurs over a narrow range of time lag. This indicates that the features in the flow are traveling at a nearly uniform velocity, consistent with the photographic evidence. The modal value indicates the most common time lag which is used to calculate the average velocity.

The resolution of this technique is limited to 1000 Hz by the resolution of the conductance probes leading to a discretization uncertainty of ± 0.25 ms for the time lag.

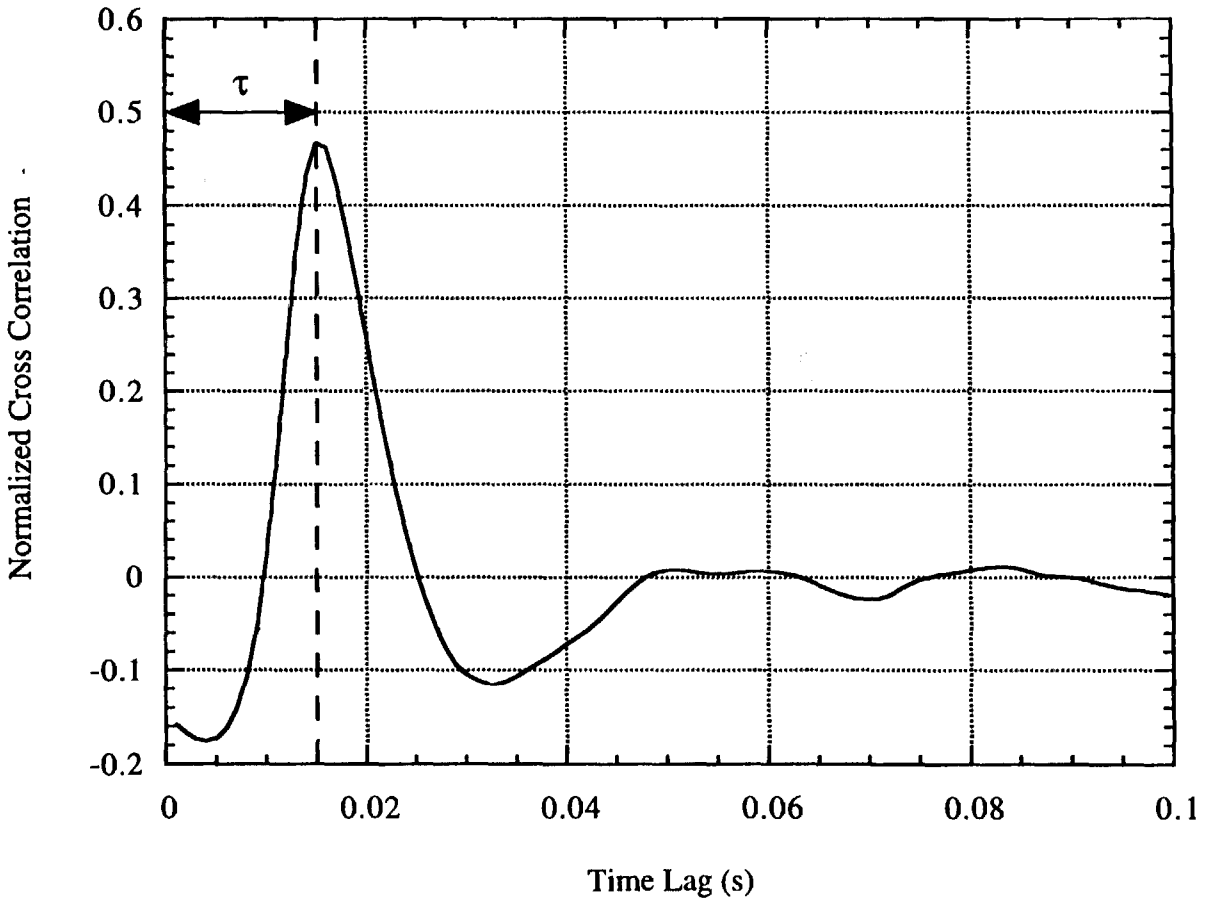

Figure 2.16 Typical Normalized Cross-Correlation for Annular Flow

This causes an uncertainty of ±3% at a velocity of 3 m/s typical of annular waves and an uncertainty of ±10% at 1 m/s typical of bubbles in bubble and slug flows. While these uncertainties are significant, this technique is more accurate than photographic determination, which only has a resolution of 1.25 ms.

To confirm the validity of the electronic velocity determination, the velocity determined in this way was checked against the velocity determined photographically. A strong correlation existed between the two techniques for bubble and slug flows. However there was a serious discrepancy between the techniques for annular flow due to the extreme difficulty in tracking wave fronts photographically. The electronic velocity determination technique was therefore judged to be superior.

2.7 Pressure Measurement

Gas-liquid flow often exhibits greatly enhanced pressure drop as compared to single-phase gas flows. The presence of even a small amount of liquid on the perimeter of a pipe in annular flow can result in a ten-fold increase in the gas-phase pressure drop (Bousman and McQuillen, 1994). The current knowledge of two-phase pressure drop in microgravity is very limited, consisting of a few empirical correlations and data sets confined to a relatively small region of parameter space (Colin, 1990, Miller, et al., 1993). A better understanding of the mechanisms leading to this pressure drop enhancement is important in determining the nature of momentum transfer between the two phases as well as for minimization and control of pressure drop in two-phase systems.

The accurate measurement of pressure drop in a two-phase system operating in the high vibration aircraft environment requires considerable attention to detail. A common problem in two-phase pressure measurements is the presence of gas bubbles in liquid filled lead lines between the test section and the pressure measuring apparatus. With a gas

bubble bridging the line, the pressure is offset by an amount equal to the surface tension at the gas-liquid interface. This effect often occurs intermittently and results in unreliable measurements. In the microgravity aircraft environment, errors in the pressure readings can also be generated by hydrostatic pressure in the lead lines due to the small, non-zero accelerations experienced by the aircraft. This effect is minimized by reducing the length of the path between the desired point of measurement and the pressure transducer.

Initially, standard Validyne DP15 differential pressure transducers were used but poor results were obtained. Despite the presence of a purging system, the liquid lead lines could not be kept free of gas bubbles. In addition, the transducers were subject to offsets as large as 20% of full scale caused by the severe aircraft vibration experienced prior to entering the microgravity trajectory. These results suggested that differential pressure transducers with external lead lines would not function properly in the microgravity aircraft environment.

The problems with pressure drop measurement were solved by using Druck PDCR 820 pressure transducers (1 psi full scale) with flush mounted diaphragms. These transducers use a silicon wafer as a pressure-sensitive diaphragm with the strain gauge doped directly onto the back side of the wafer. The transducer is unaffected by severe vibration and contains no internal dead volume where gas bubbles can collect.

The smallest-diameter diaphragm available was still too large to mount flush on the inside of the test section so a liquid-filled pressure transducer mount was developed. The details of this mount are shown in Figure 2.17. The mount holds the pressure transducer diaphragm in a liquid-filled cavity which is connected to the test section by a 1 cm long channel. The cavity is shaped so that air bubbles will rise out of the cavity into the test section when the test section is oriented horizontally (when the aircraft is in level flight). A purge connection at the bottom of the cavity allows the cavity to be filled with liquid while the air is pushed into the test section. The result is a liquid-filled path between the test

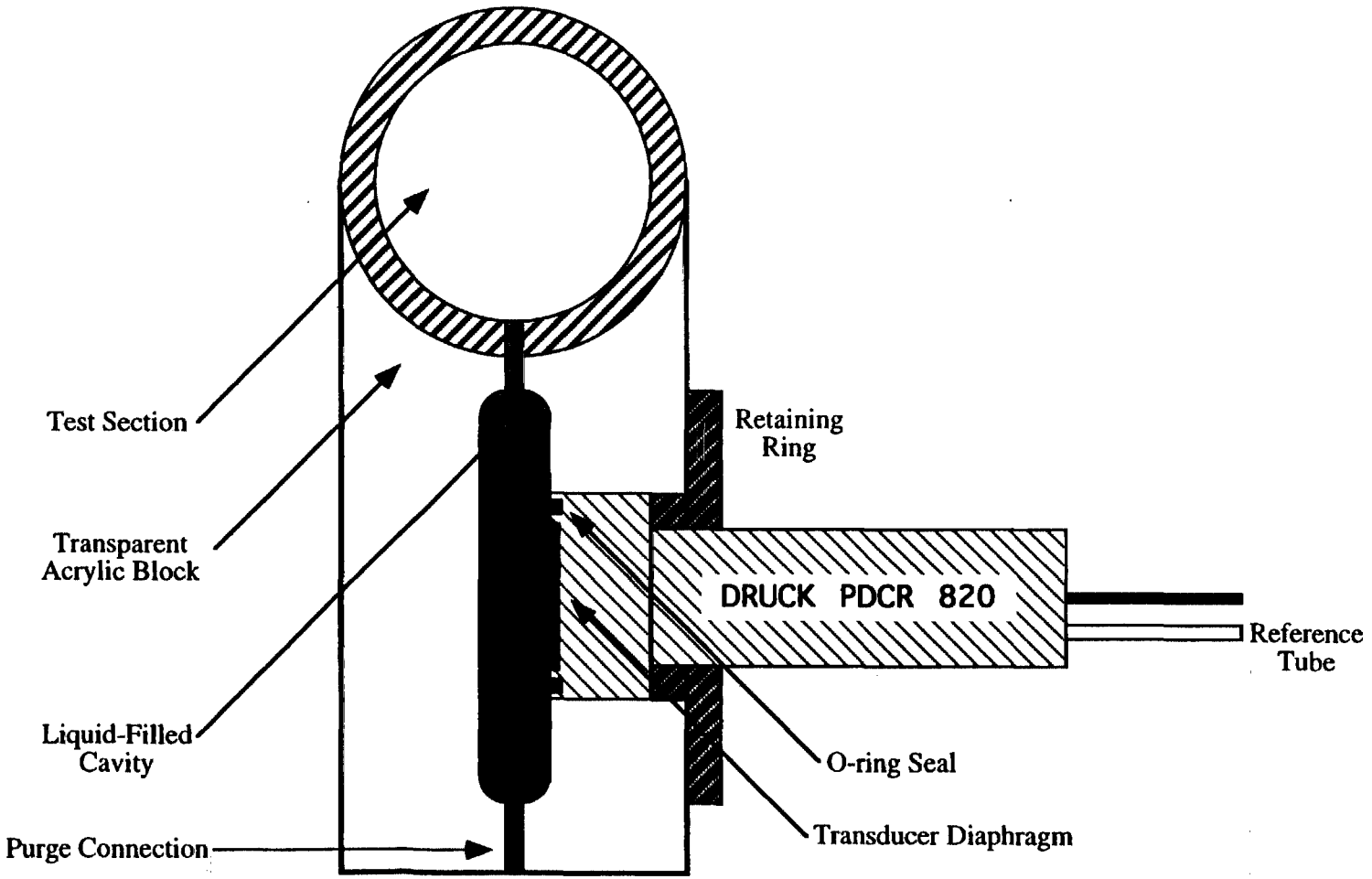

Figure 2.17 Liquid-Filled Pressure Transducer Mount

section and the transducer which is free of bubbles and too short for hydrostatic heads to alter the results. The mount is made of transparent Plexiglass so that purging of the cavity can be confirmed. The mounts are purged in flight and the purge flow is stopped just prior to entering the trajectory. Numerous observations have confirmed that the mounts remain free of gas bubbles throughout the trajectory.

The pressure inside the test section is controlled by the pressure regulator in the gas vent on the gas-liquid separator which holds the system pressure at about 2 psi above the aircraft cabin pressure. To prevent over-ranging of the pressure transducers, a version of the transducer with a pressure reference tube was used. In the Learjet flow loop, equal-length air-filled tubes connect the reference tube of each transducer to the gas space inside the gas-liquid separator upstream of the pressure regulator. On the KC-135 flow loop, a downstream-facing pitot tube was used as a reference system pressure. As the system pressure changes, the transducers are equally offset and remain in range. The pressure difference between transducers is then used to calculate the pressure drop.

The circuitry used to drive the pressure transducers and output the signals to the data acquisition system was developed at the University of Houston using military-grade electronics and hardware to minimize the effects of vibration and electromagnetic noise found in the aircraft environment. Multiple gains are provided so that a measurable output signal is produced even when the pressure drop is very low such as in bubble flow. The system provides individual transducer outputs as well as a differential output. Due to problems with precisely balancing the differential output, the individual outputs were subtracted point by point on a computer to obtain the differential pressure between transducers.

The pressure transducers and related electronics were calibrated by mounting the transducers in a air-tight test section. The pressure in the test section was set using mercury-filled and water-filled manometers equipped with indicating scales. A typical

calibration curve is shown in Figure 2.18. As shown, the response is linear even for pressures greatly exceeding the 1 psi full scale specification. The calibration was checked periodically but little deviation from previous calibration results was noted.

The accuracy of the pressure measurement is limited by the precision of the transducers, the uncertainty associated with calibration and the discretization uncertainty of the data acquisition system. The accuracy of the transducer is certified by the manufacturer to be 0.1% of full scale or 0.001 psi. The maximum error in pressure measurement from the mercury manometer used for calibration is estimated to be 0.03 psi. The ±1.25 mV discretization uncertainty leads to an uncertainty of only ±0.05% of full scale. Thus the estimated uncertainty is calculated to be about ±3% at 1 psi (typical for annular flow). For bubble flow experiments, where pressure gradients can be as low as 0.05 psi/m, the uncertainty in the measurement is considerable unless very long test sections are used.

The frequency response of the pressure measurement system is controlled by the response of the transducers and the electronics. According to the manufacturer, the pressure transducers have a -3 dB cutoff frequency of approximately 2000 Hz. The frequency response of the electronic circuit can be adjusted from 2 - 500 Hz by changing the values of the filter resistors. After much testing on the ground and in the aircraft, a cutoff frequency of 50 Hz was deemed to be optimal for these studies. As will be shown in later sections, the frequencies of slugs and waves are confined to < 30 Hz. While the pressure transducers did not respond to direct mechanical shocks, they did record pressure noise due to aircraft and camera induced vibrations transmitted through the liquid in the test section. Since most of this noise was in the 60 - 400 Hz frequency range, a cutoff frequency of 50 Hz was effective in reducing most of this noise. While this frequency response is adequate for determining the mean pressure drop in the test section, it may not be sufficient for measuring the precise pressure profile over the gas-liquid interface. To

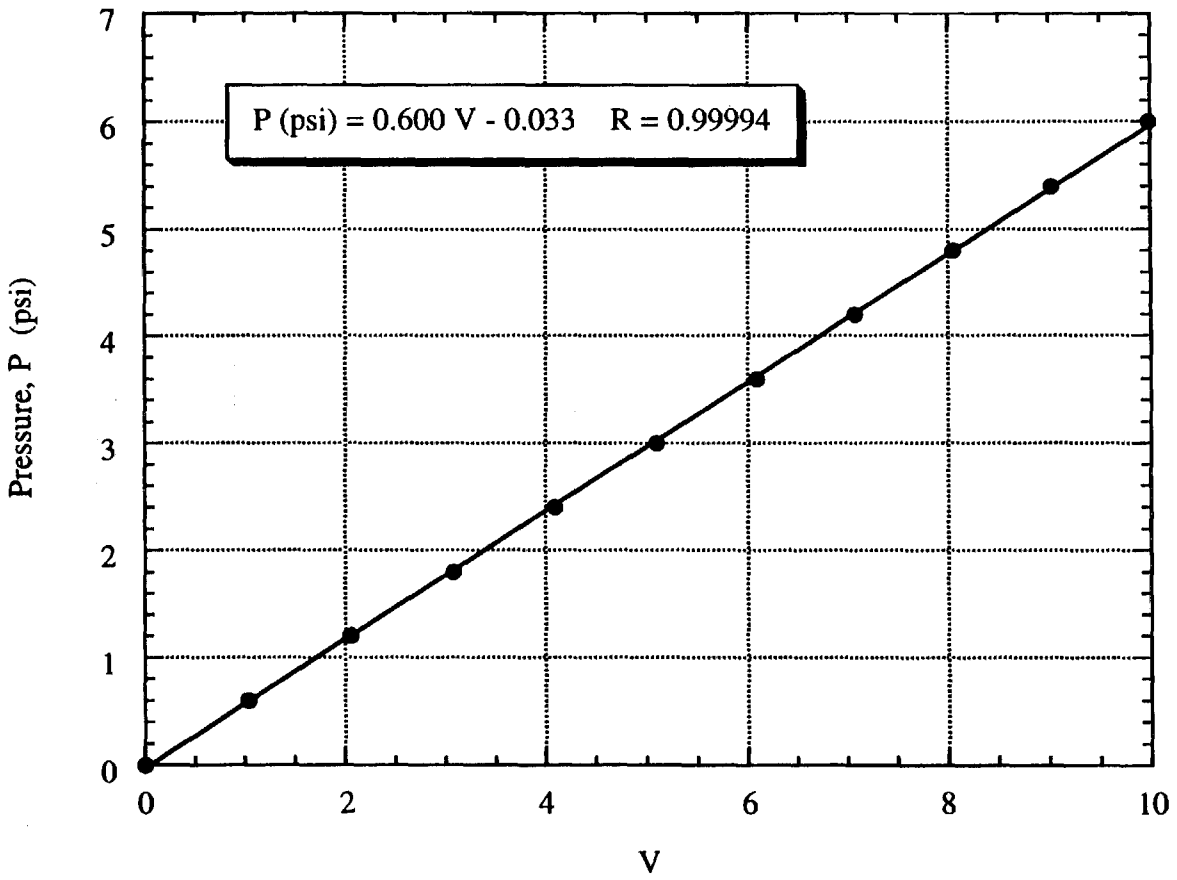

Figure 2.18 Typical Pressure Transducer Calibration Curve

accomplish this, higher-resolution measurements in a vibration-free environment such as in space flight may be required.

The typical pressure time-series traces for annular flow in microgravity are shown in Figure 2.19. The pressure transducers were separated by 0.5 m in this experiment and the change in mean value due to pressure drop across this distance is evident. The traces show a complex pattern of oscillations caused both by waves passing over the transducer and waves passing between the transducers and the gas-liquid separator where the pressure reference is located.

2.8 Wall Shear Stress Measurement

Wall shear stress measurements were made in a series of microgravity annular flow experiments so that the factors contributing to the total pressure drop could be better understood. The large pressure drop enhancement observed in annular flow as compared to single-phase gas flow is caused by a combination of wall friction, form drag across the wave and entrainment and deposition of liquid droplets. An independent measurement of the wall shear stress is useful in evaluating the relative importance of these contributions.

A comprehensive review of wall shear stress measurement techniques is given in Goldstein, 1983. Of the many techniques presented, only the hot film and electrochemical techniques, which are analogs of each other, have sufficient response to track the fast-moving annular waves. While the electrochemical technique is more sensitive, it involves the use of toxic compounds, such as potassium ferrocyanide, which are not permitted aboard NASA aircraft. For this reason, the hot film technique was selected to measure wall shear stress.

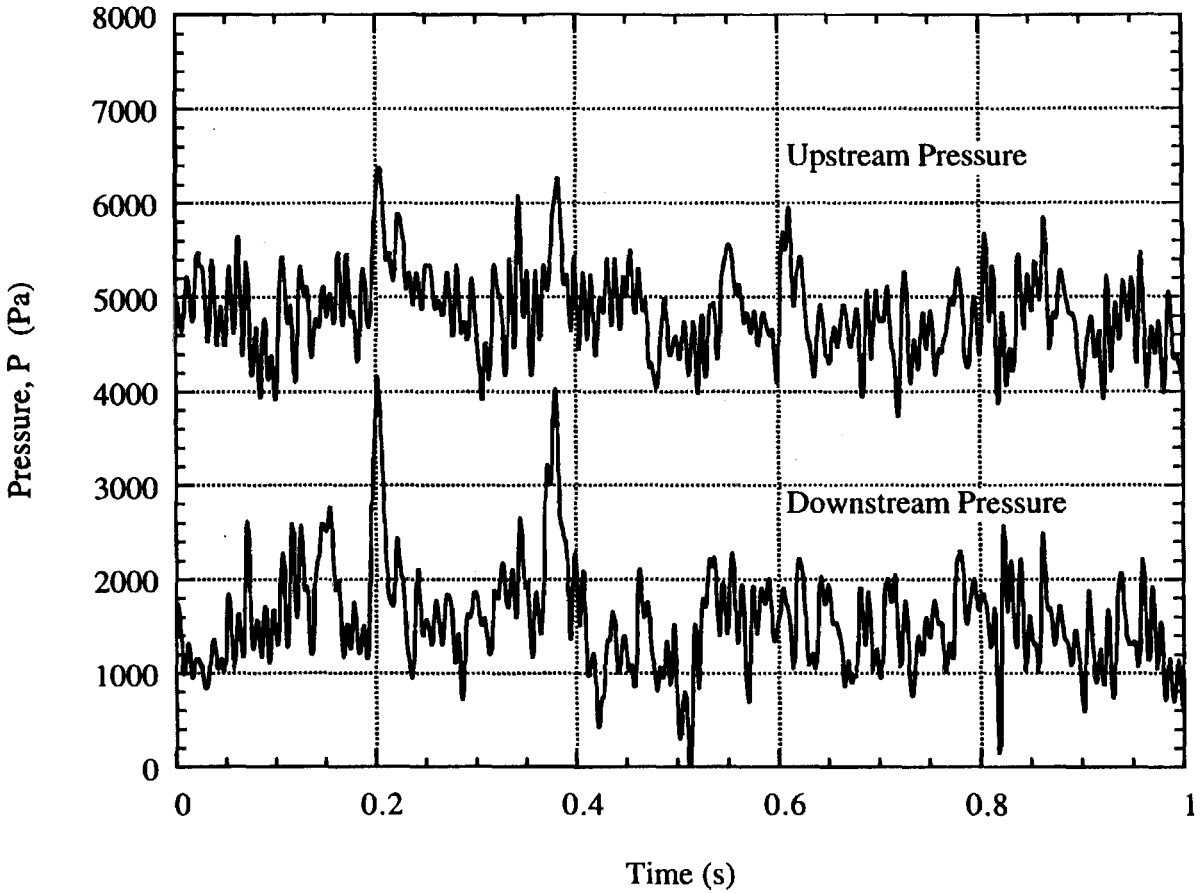

Figure 2.19 Typical Pressure Measurement Time Series for Annular Flow in Microgravity

The hot film probe used for these studies is shown in Figure 2.20. A set of these probes were manufactured for this project at the NASA Langley Research Center, although similar probes are available commercially. As shown, the probe consists of nickel hot film sensor and temperature compensator elements deposited on a 50 μm thick polyimide plastic film. The large copper pads are used to provide low-resistance connections to the elements. The wire leads connecting the copper pads to the instrumentation are located downstream of the elements so as to not disturb the flow. The entire probe is coated with a 5 μm layer of polyimide to electrically insulate the elements from the liquid. Since the probe is thin and flexible, it can be mounted flush to the inside wall of the test section. To minimize flow disturbances caused by a step at the leading edge of the probe, a shallow groove, approximately 125 μm in depth, was milled into the test section wall. The back side of the probe was coated with a thin layer of marine-grade epoxy, and laid into the groove. A small balloon was inflated inside the test section to push the probe flat against the wall while the epoxy cured. The result was a probe which was flush to the wall of the tube to within 20 μm, which is about the same as diameter tolerance of the test section Plexiglass tubing. The wire leads from the probes exited the test section immediately downstream of the probe and were insulated and sealed with polyester resin.

The idea of relating wall shear stress to the rate of heat transfer from a heated element was first used experimentally by Ludweig, 1949. The operating principle behind the hot film probe is shown in Figure 2.21. During operation, the sensing element is maintained at a constant temperature, approximately 40 C above the liquid temperature, using a Thermal Systems Inc. Model 1054A anemometer circuit. The electrical diagram of the circuit and the probe is presented in Figure 2.22. The anemometer circuit continuously adjusts the current to the element so that the resistance, and therefore the temperature, remains constant. The anemometer circuit also provides an output voltage which is proportional to the current required to maintain the element temperature. The output signal is therefore related to the rate of heat transfer from the hot film element. Since changes in

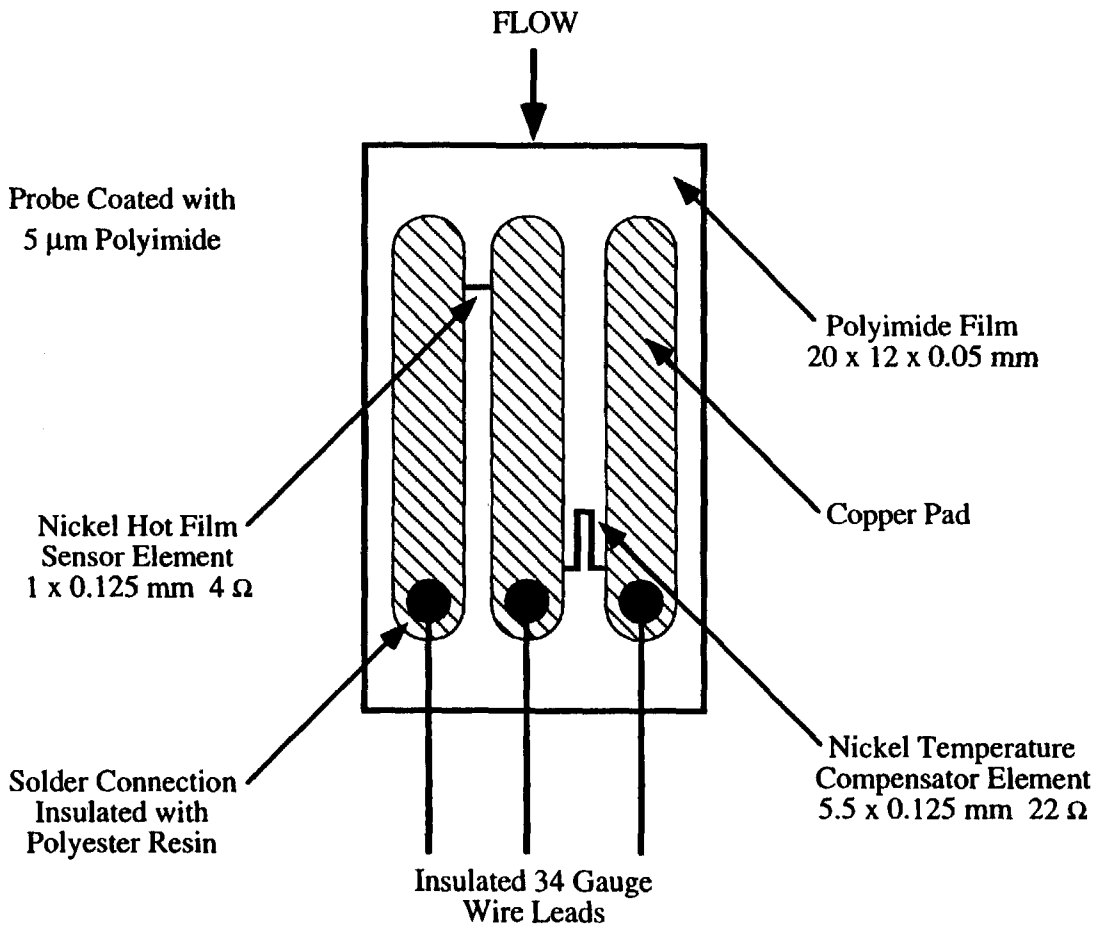

Figure 2.20 Flush Mounted Hot Film Wall Shear Stress Sensor

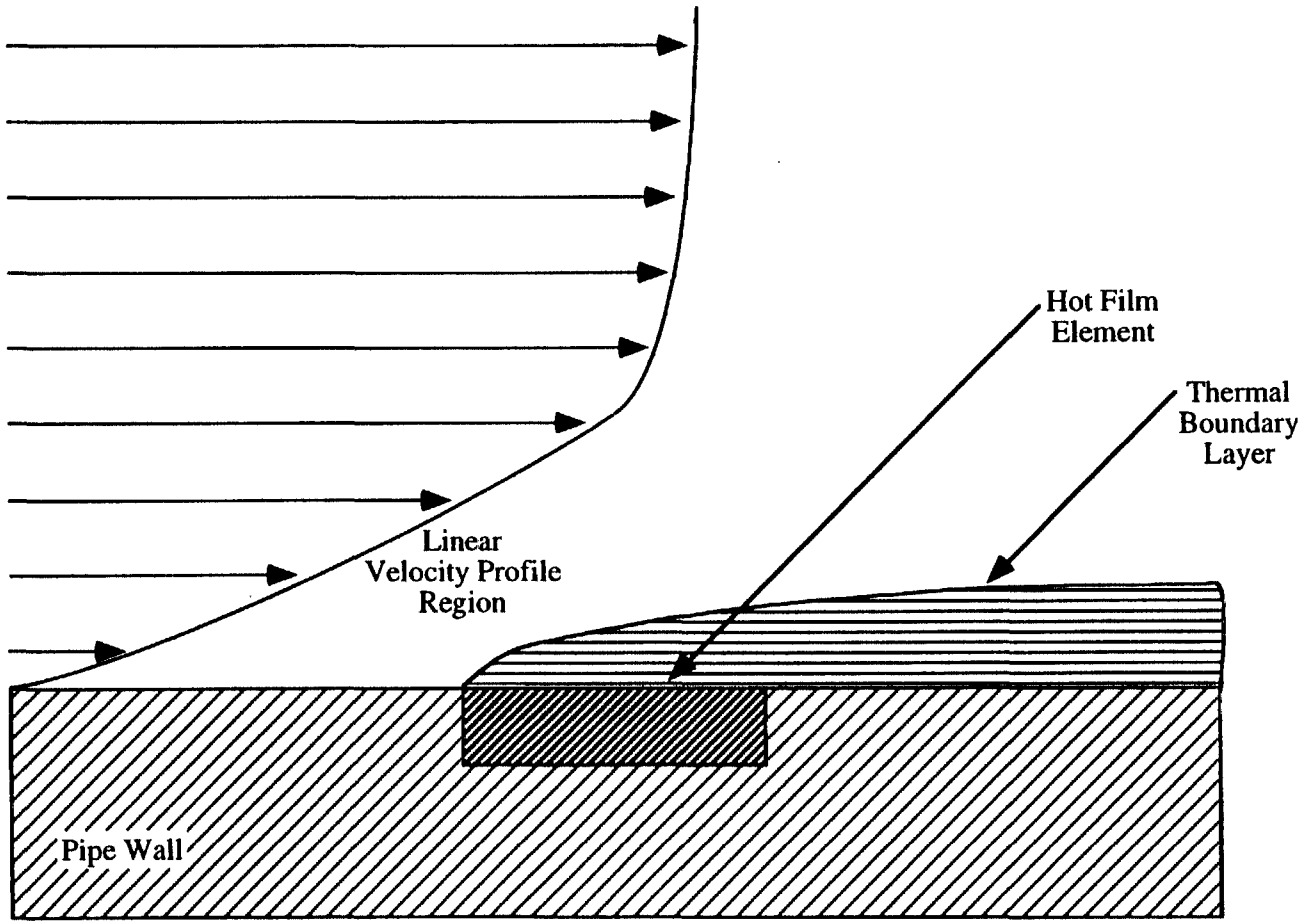

Figure 2.21 Representation of the Thermal Boundary Layer Formed Over the Hot Film Probe Element

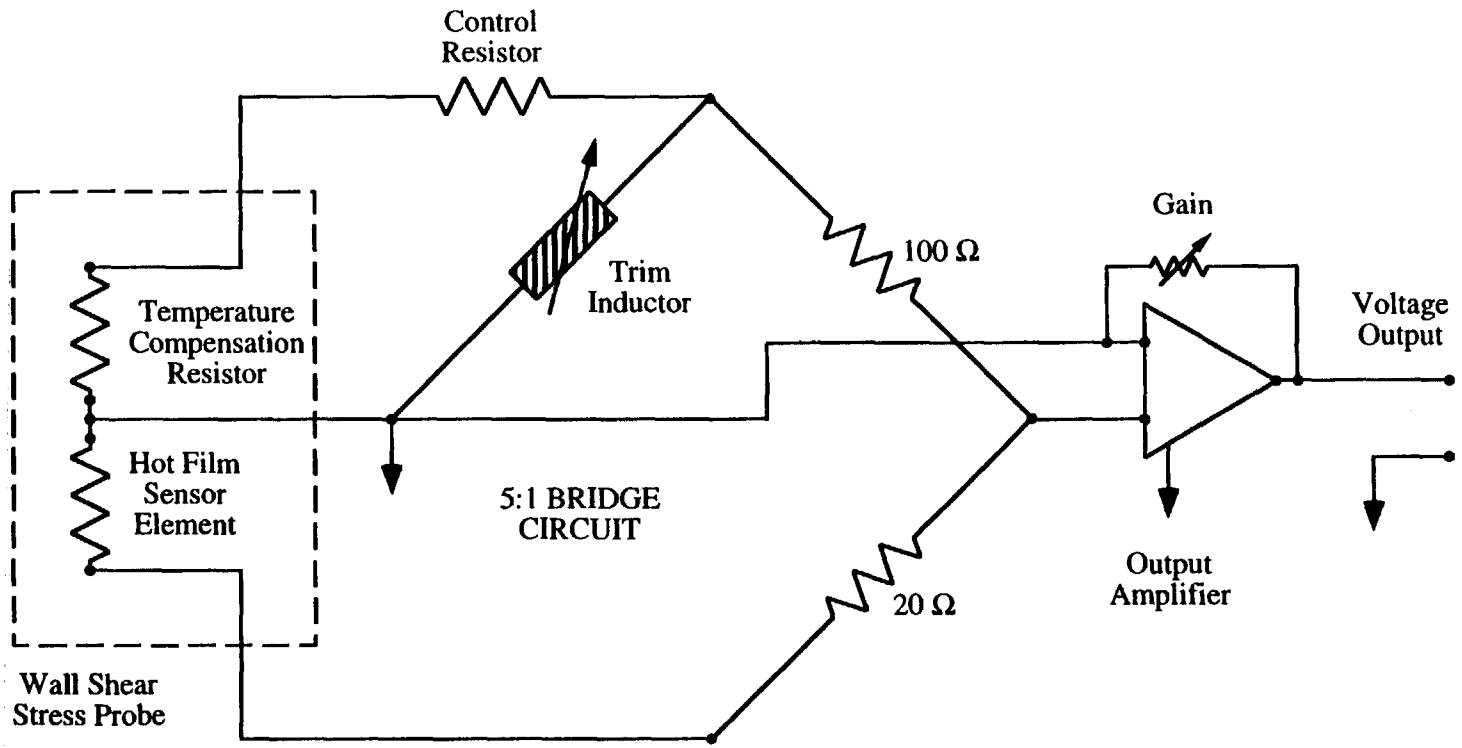

Figure 2.22 Electrical Diagram of Wall Shear Stress Probe and Anemometer Circuit

the fluid temperature would also lead to changes in rate of heat transfer which are not related to changes in the wall shear stress, a temperature compensating resistance element is also included on the probe. By including this resistance in the anemometer bridge circuit as shown in Figure 2.22, the voltage output is automatically adjusted for changes in fluid temperature. In practice, the compensation is effective only when the fluid temperature is within about 5 C of the calibration temperature. Fortunately, this condition was maintained in all flight experiments.

The element temperature is determined by the value of the temperature compensating resistance shown in Figure 2.22. As the sensing element temperature is increased, the sensitivity increases. However a point is reached when the element temperature becomes sufficient to cause the liquid to vaporize on the element surface. Operation in this mode results in erroneous results and excessive element temperature can lead to failure of the probe. The control resistance was adjusted when the probe was covered with a layer of stagnant liquid since vaporization is most likely to occur when the liquid velocity is low. The control resistance was raised until vaporization was observed and then the resistance was lowered slightly. This method maximizes probe sensitivity while protecting the element from thermal damage.

The relationship between the anemometer output and the wall shear stress is developed in Goldstein, 1983 from boundary layer theory. The development requires that the thermal boundary layer lie entirely within the wall region of the momentum boundary layer where the velocity gradient is approximately linear as shown in Figure 2.21. The development also assumes that natural convection effects are small making the technique unsuitable for extremely low velocities. When these assumptions are met, the relationship between wall shear stress and output voltage becomes

$$\tau_w^{1/3} = AV^2 + B, \tag{2.6}$$

where τ_W is the wall shear stress, V is the anemometer output voltage and A and B are constants. The constant A is related to the heat losses to the fluid while B is related to undesired heat losses to the substrate. The sensitivity of this method is limited as compared to electrochemical probes primarily because the heat loss to the substrate is often as large as the heat loss to the fluid (Goldstein, 1979).

In principle, the constants A and B in (2.6) can be derived from first principles but in practice, calibration is required. Since fluctuations in the flow due to turbulence and other effects cause fluctuations in the wall shear stress, proper time averaging of (2.6) leads to

$$\overline{\tau_w} = \overline{(AV^2 + B)^3}. \tag{2.7}$$

Since the fluctuations are small, a more convenient approximation,

$$\overline{(\tau_w)}^{1/3} = A\overline{V}^2 + B \tag{2.8}$$

can be used.

The choice of calibration method also requires careful consideration. A study of wall shear stress measurements in vertical annular flow by Govan et al., 1989 showed significant discrepancies in the results due to different calibration methods. The most prudent approach is to use a calibration technique which is as similar to the actual flow system as possible. For this reason, only in-situ calibration techniques were attempted.

The first calibration method to be attempted used single phase liquid flow since the relationship between wall shear stress and pressure drop is well understood. Based on pressure drop measurements, the level of wall shear stress encountered in annular flows was expected to be at least 30 Pa. Achieving such a high level of wall shear stress required very high liquid velocities which occasionally damaged void fraction and film thickness

wires in the test section. At low levels of wall shear stress (2 - 10 Pa), a calibration plot of $\tau_w^{1/3}$ vs V^2 yielded an approximately linear relation as predicted by (2.8). At higher levels however, the response of the system became increasingly insensitive to increases in wall shear stress and the calibration curve became highly non-linear. When this calibration was applied to annular flow data taken in the laboratory in normal gravity, the measured wall shear stress violated a force balance on the system, indicating that the calibration was faulty. A more detailed analysis of the turbulent pipe flow showed that at the velocities required to achieve high levels of wall shear stress, the linear region of the velocity profile became so thin that the thermal boundary layer would not lie within this region. Clearly, the single phase calibration technique was inappropriate for measuring wall shear stress in the range required for annular flow.

A more desirable calibration technique would be one in which the wall shear stress calibration is determined in annular flow. Nonidealities due to the nature of the flow would then most likely be accounted for in the calibration as well. An annular two-phase calibration technique is described by Govan et al., 1989 but few details are given so a two-phase method was developed during the course of this study. A force balance on an annular film provides the basis for the technique. As shown in Figure 2.23, under normal circumstances, the annular film is characterized by large disturbance waves on the film and a considerable amount of the liquid exists in the form of droplets which have been entrained from the crests of the waves. The presence of the waves and droplets leads to terms in the force balance which are difficult to measure and would lead to serious discrepancy in the calibration. However for very thin liquid films and very large gas velocities, the disturbance waves essentially disappear. Once the waves are suppressed, there is no mechanism for entrainment of droplets and the idealized annular film shown in Figure 2.23 is approached. With this arrangement, the magnitude of wall shear stress obtained in microgravity annular flows is easily produced during the calibration procedure.

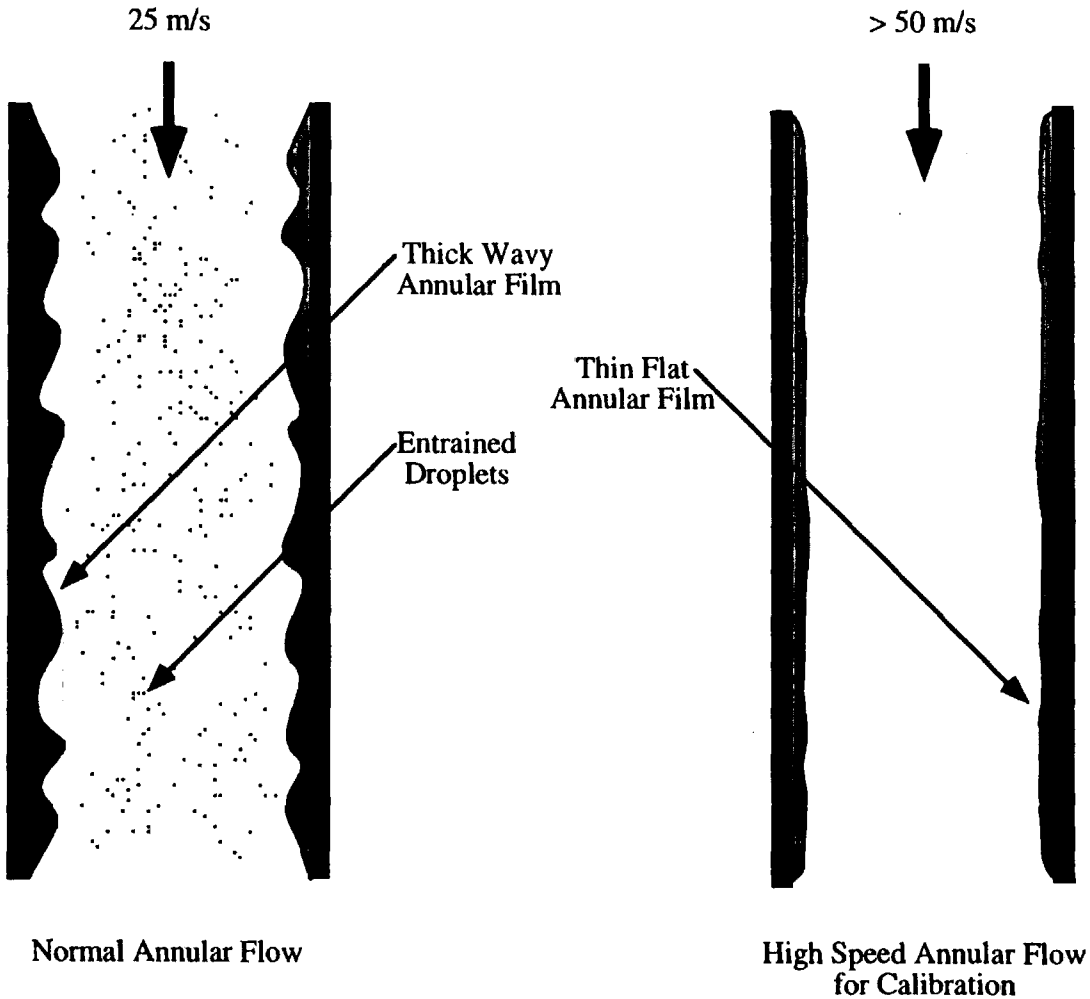

Figure 2.23 Creation of an Idealized Annular Film for Wall Shear Stress Calibration

A force balance on the tube wall with a steady, concurrent downward annular film without entrainment is given by

$$\bar{\tau}_w = \frac{D}{4}\frac{\overline{dP}}{dx} + \rho g \bar{h}. \tag{2.9}$$

This calibration technique requires measuring both the pressure drop and the liquid film thickness while recording the output of the anemometer. To begin the procedure, the smallest liquid flow rate which could be held constant was established in the test section and the gas flow rate was increased until the wave amplitude was less than 10% of the substrate thickness. Typically, superficial gas velocities exceeding 50 m/s were required to achieve this condition. Direct observation confirmed that entrainment was minimal once this state was achieved. Evaporative cooling effects were significant so the system was allowed to reach a temperature equilibrium prior to starting the calibration. The outputs of the pressure transducers, film thickness probe and anemometer were recorded for a one minute period and averaged electronically. The gas velocity was then raised slightly to take the next calibration point. A typical calibration curve is shown in Figure 2.24. As shown, when the data are plotted as suggested by (2.8), a linear relation is obtained in the range of 2 - 33 Pa for water. Calibrations repeated on different days or with moderately different fluid temperatures yielded the same results. When the gas velocity was lowered to obtain calibration points below a wall shear stress of 2 Pa, the waves became large and the calibration results were non-linear and non-reproducible, suggesting that the idealized annular flow no longer existed.

Since the physical properties which affect the heat transfer to the fluid are different for the water-glycerin solution also used in this study, the calibration procedure was repeated for this liquid. As shown in Figure 2.24, the output voltage is less for the water-glycerin solution but the linear relation is maintained.

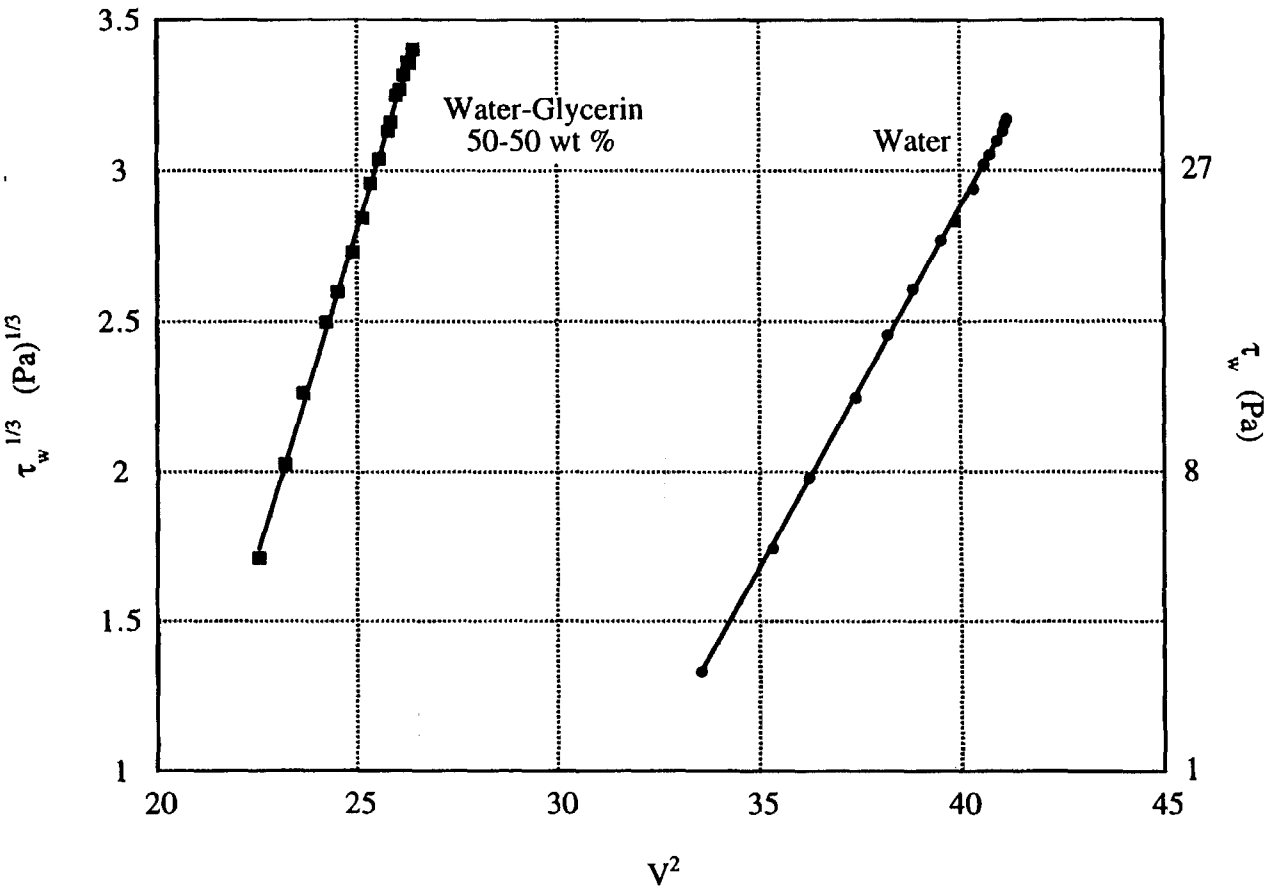

Figure 2.24 Typical Wall Shear Stress Calibration for Water and Water-Glycerin Solutions

The error in the wall shear stress measurement is difficult to estimate due to the many factors involved in the operation and calibration of the system. If the maximum uncertainty in pressure and film thickness measurement are used with (2.9), a maximum uncertainty of ±1.2 Pa is obtained at the midpoint of the calibration range. This ±7% uncertainty may be underestimated because uncertainty caused by the anemometer circuitry, changes in fluid properties and fouling of the sensor element were not included in the uncertainty analysis. Errors of ±10-15% may therefore be possible in the wall shear stress measurements.

Analysis of the dynamic response of hot film and hot wire anemometer probes is also complex. Estimates of the -3 dB cutoff frequency can be determined theoretically or experimentally. A theoretical approach to the frequency response of the probe was suggested by Fortuna and Hanratty, 1971. The temperature field within the thermal boundary layer was decomposed into mean and fluctuating quantities and the boundary layer equations were solved numerically. From this solution, a frequency response correction factor is calculated as a function of dimensionless frequency defined by Fortuna and Hanratty, 1971 as

$$\omega^* = \omega \frac{\nu}{U_*^2} N^{1/3}, \qquad (2.10)$$

where ω is the dimensionless frequency, $U*$ is the friction velocity and N is either the Prandtl or Schmidt number for heat transfer or mass transfer probes, respectively. The correction factor asymptotically approaches unity in the limit of zero frequency but rises sharply at higher frequency. The point where the sharp rise begins represents the practical upper limit of frequency response. For the probe used in this study, the frequency correction factor is nearly unity for $\omega^* < 0.2$. For a wall shear stress of 35 Pa (worst case), the predicted cutoff frequency is 19400 Hz for water (Pr = 7.0) and 1500 Hz for 50-

50 wt% water-glycerin (Pr = 49). Thus the frequency response of the wall shear stress probe is above the 1000 Hz sampling frequency in all cases.

The theoretical analysis estimates only the dynamic response of the probe without regard for the response of the anemometer system. The response of the probe and anemometer system together can be measured directly using a square-wave testing technique detailed by Freymuth, 1977 and the Thermal Systems Inc. operating manual for the anemometer. Using the 1000 Hz square-wave generator built into the anemometer system, the response of the system to the square-wave input was recorded on an oscilloscope. In accordance with the technique, the time delay is measured from the beginning of the pulse until the signal has decayed to 3% of the maximum value. This time was measured as 0.84 ms which corresponds to a frequency of 1190 Hz. This result suggests that the frequency response is limited by the anemometer system rather than the probe. These results also indicate that the 1000 Hz sampling frequency is nearly optimal.

A typical time series trace of the wall shear stress measurement taken for microgravity annular flow is shown in Figure 2.25. Such detailed measurements will be useful in simulation studies of annular waves.

2.9 Test Sections

Four test sections were constructed during the course of this study using combinations of the instruments previously described. Each was designed to provide the measurements required for a specific investigation.

The first test section constructed, shown if Figure 2.26, was one used to develop the flow pattern maps for a 12.7 mm ID tube. The test section consists of an acrylic Plexiglass tube to which the probes are attached. This flow pattern mapping test section

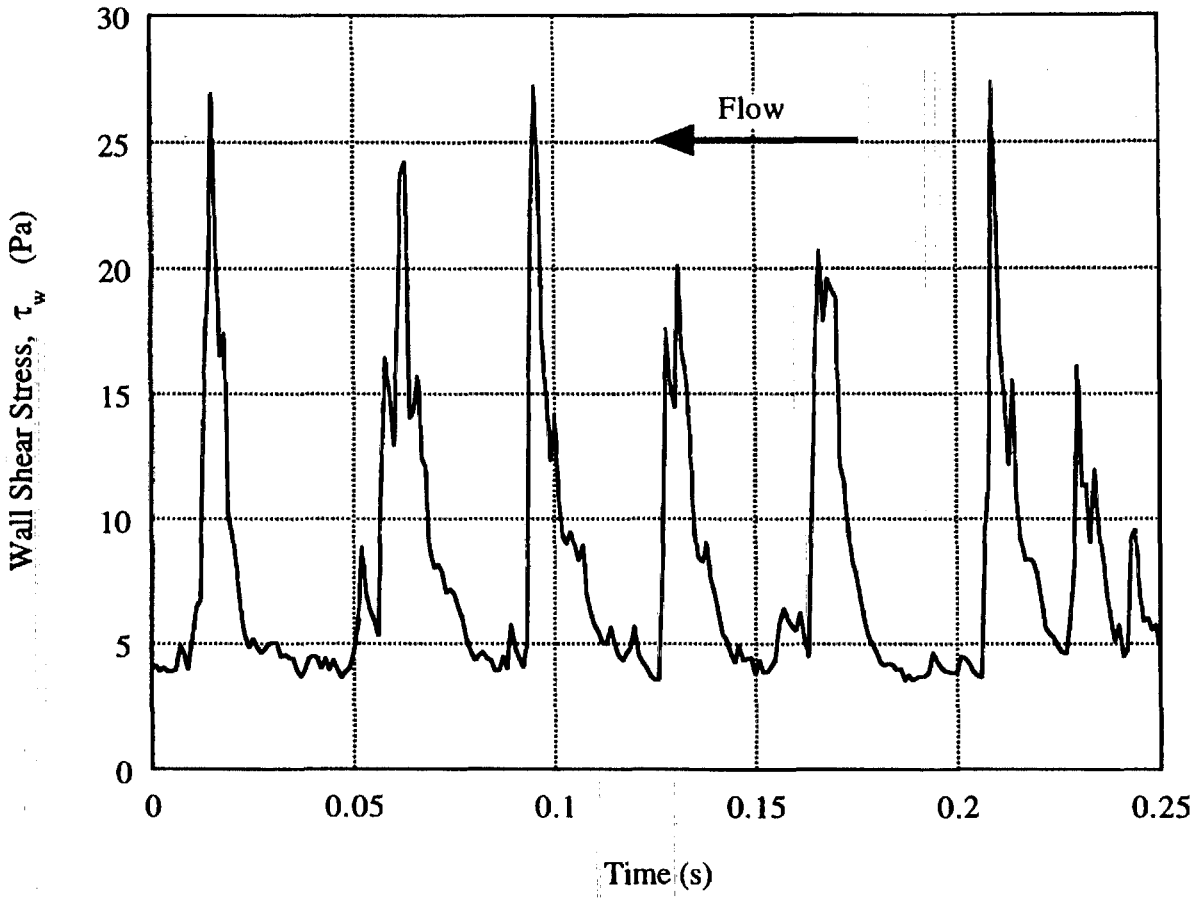

Figure 2.25 Typical Wall Shear Stress Time Series Trace for Microgravity Annular Flow

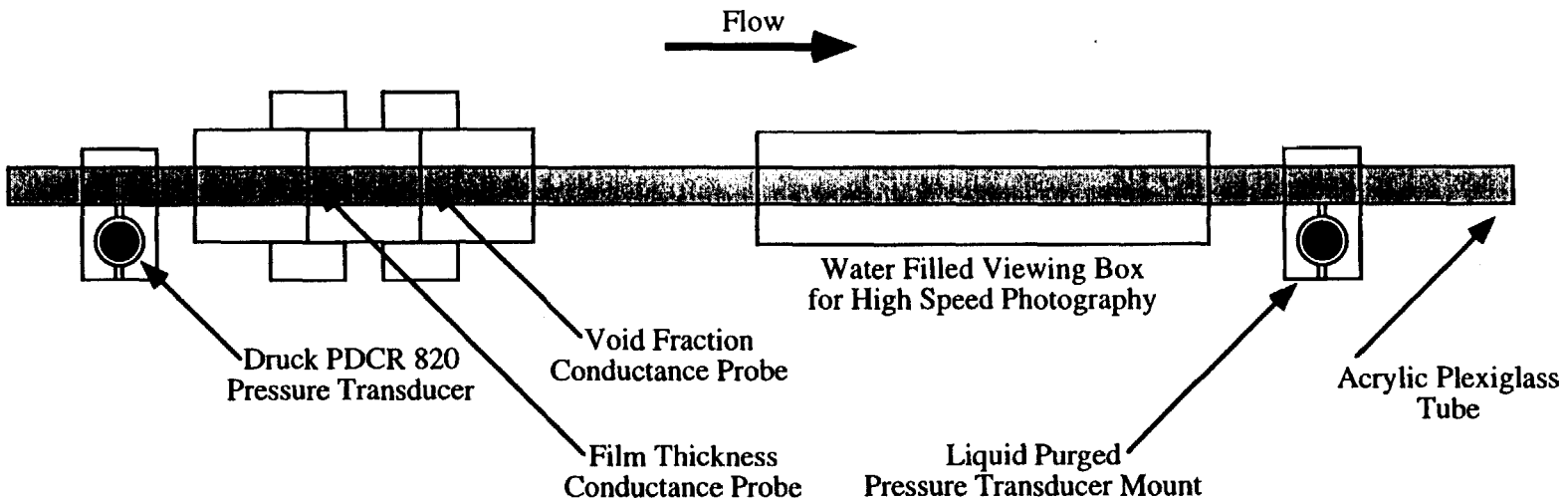

Figure 2.26 12.7 mm ID Flow Pattern Mapping Test Section

contains a void fraction and a film thickness probe separated by 50.8 mm. This allowed void fraction, film thickness and velocity to be determined. Two pressure transducer mounts and a viewing box allowed for pressure drop measurements and visualization of the flow patterns.

An improved version of the flow-pattern-mapping test section was later developed to incorporate the wall shear stress probe for use in annular flow measurements. This 12.7 mm ID annular flow test section, shown in Figure 2.27, has the same general design as the flow pattern mapping test section except that the locations of the void fraction and film thickness probes are reversed. The wall shear stress probe is located in the same cross-sectional plane as the film thickness probe but is offset 21° from the bottom of the tube where the film thickness measurement is made. This arrangement provides wave shape and wall shear stress measurements at nearly the same location. For annular studies, the void fraction probe is used only to provide a wave velocity measurement from cross-correlation.

A specialized test section was constructed to characterize the nature of microgravity annular films. This 12.7 mm ID test section, shown in Figure 2.28, contains five film thickness probes as well as pressure transducer mounts and a viewing box. The first four film thickness probes are offset axially from each other by 5 mm and offset angularly by 60°. Thus the film thickness is measured simultaneously at 0°, 60°, 120° and 180° (measured from the bottom of the tube) and at nearly the same axial location. This allows for the degree of axisymmetry in microgravity annular flows to be characterized. A fifth film thickness probe oriented at 0° is located 50 mm downstream from the first probe. This provides a qualitative measure of the evolution of the wave shape between the first and fifth probes. Only a few experiments were conducted with this test section before it was damaged and abandoned. However, the results obtained were sufficient to characterized the three-dimensional nature of the microgravity annular film as was intended. All three of

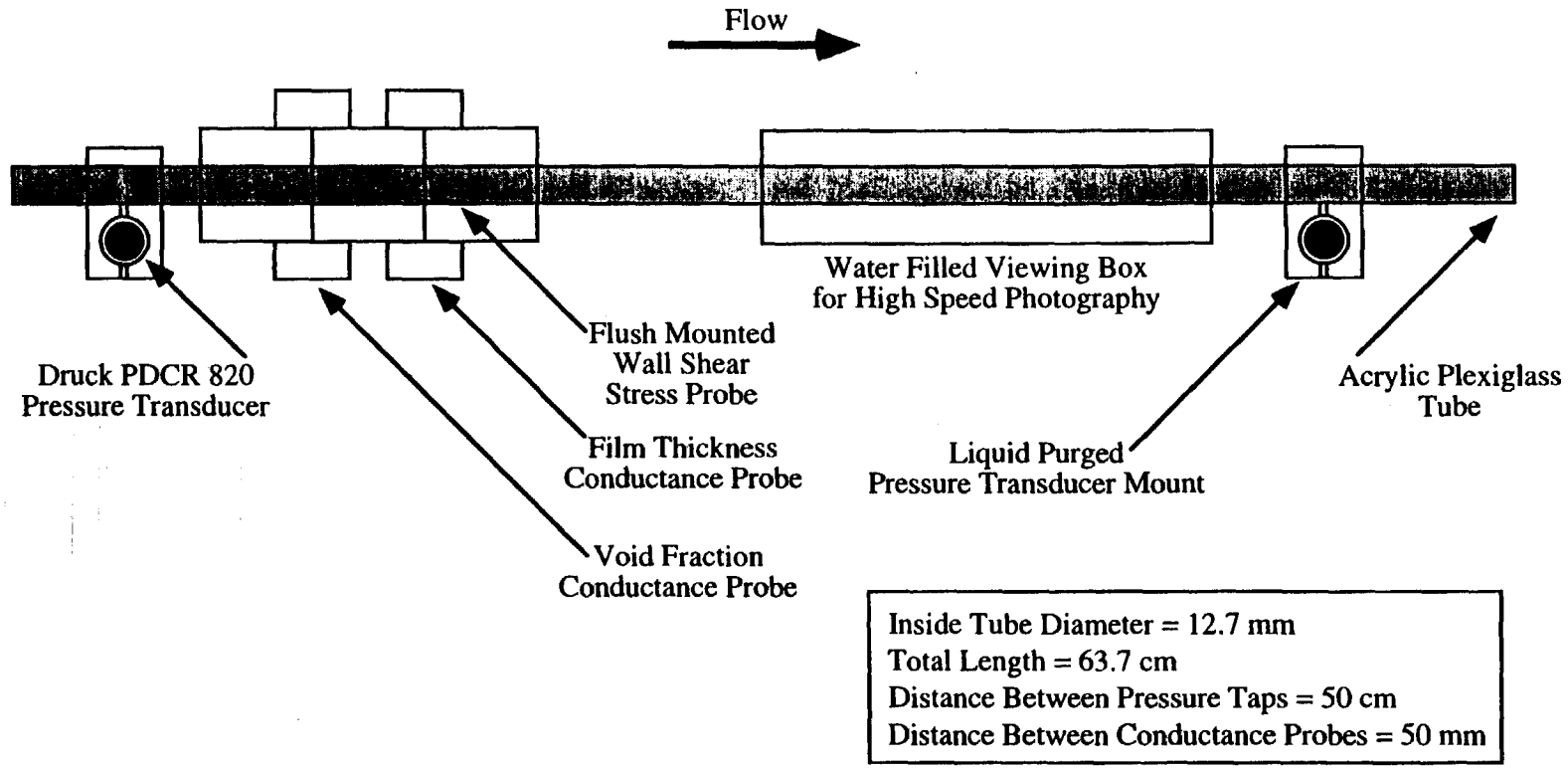

Figure 2.27 12.7 mm ID Annular Flow Test Section

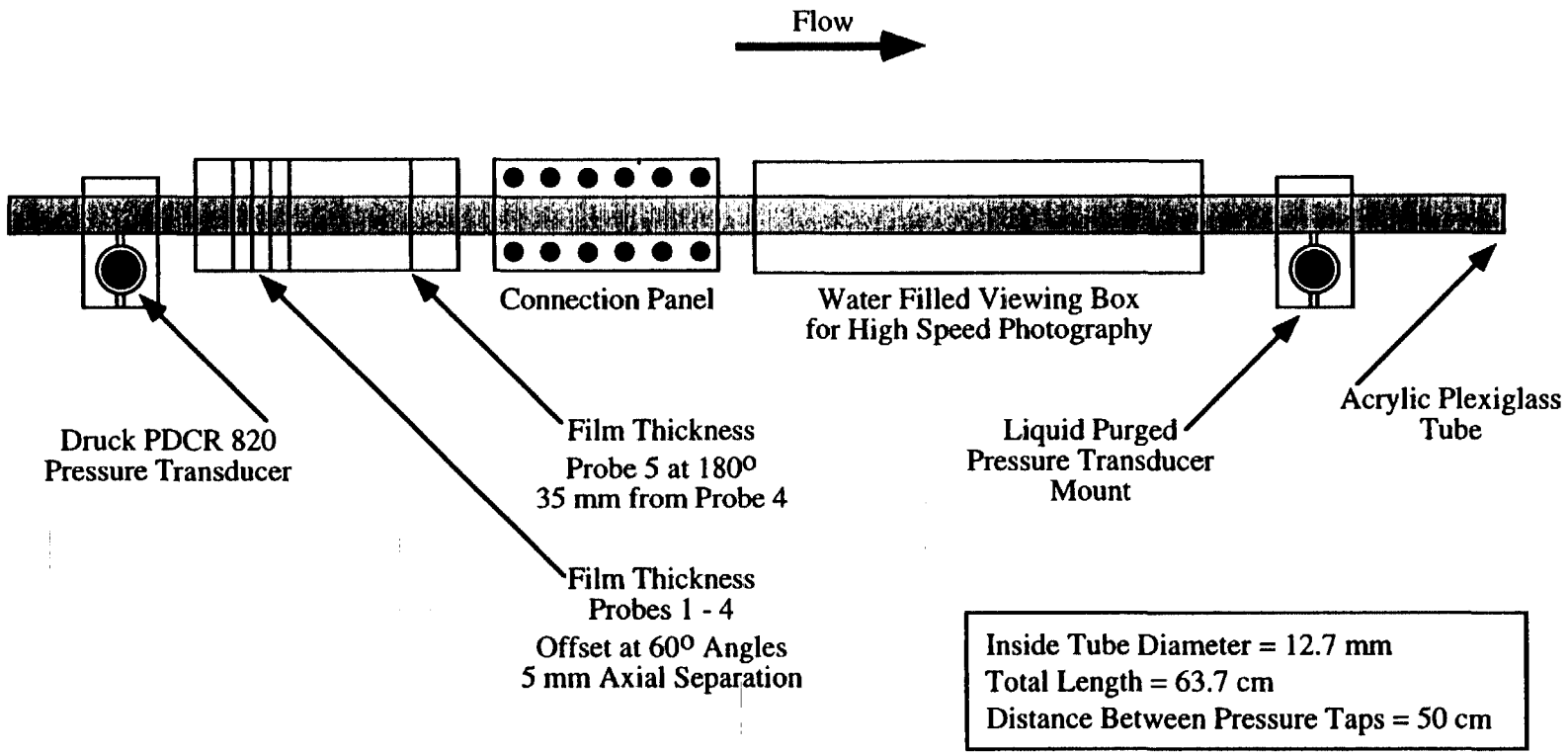

Figure 2.28 12.7 mm ID Axisymmetry Annular Flow Test Section

the 12.7 mm ID test sections were used in conjunction with the Learjet flow loop shown in Figure 2.3.

After many sets of experiments were conducted with the 12.7 mm ID test sections, it was desired to determine the effect of pipe diameter on the flow pattern maps and other measurements. This was the motivation behind the construction of the KC-135 flow loop shown in Figure 2.4 and the 25.4 mm ID general purpose test section shown in Figure 2.29. This test section was designed in a modular fashion to allow many different types of studies to be conducted. The system contains two identical instrument blocks each containing a void fraction, film thickness and wall shear stress probe as well as a pressure transducer mount. Movable pressure transducer mounts and viewing boxes allow for many configurations of the instruments. The configuration shown in Figure 2.29 was used to conduct the 25.4 mm ID flow pattern mapping study presented in this work. While this configuration located one instrument block at the outlet of the mixer, only the data taken at the downstream end of the test section were used for flow pattern mapping since fully developed flows were desired. Since the flow development length required for the 25.4 mm test section is twice that required for the 12.7 mm ID test section, this test section was only operated in the much larger KC-135 aircraft.

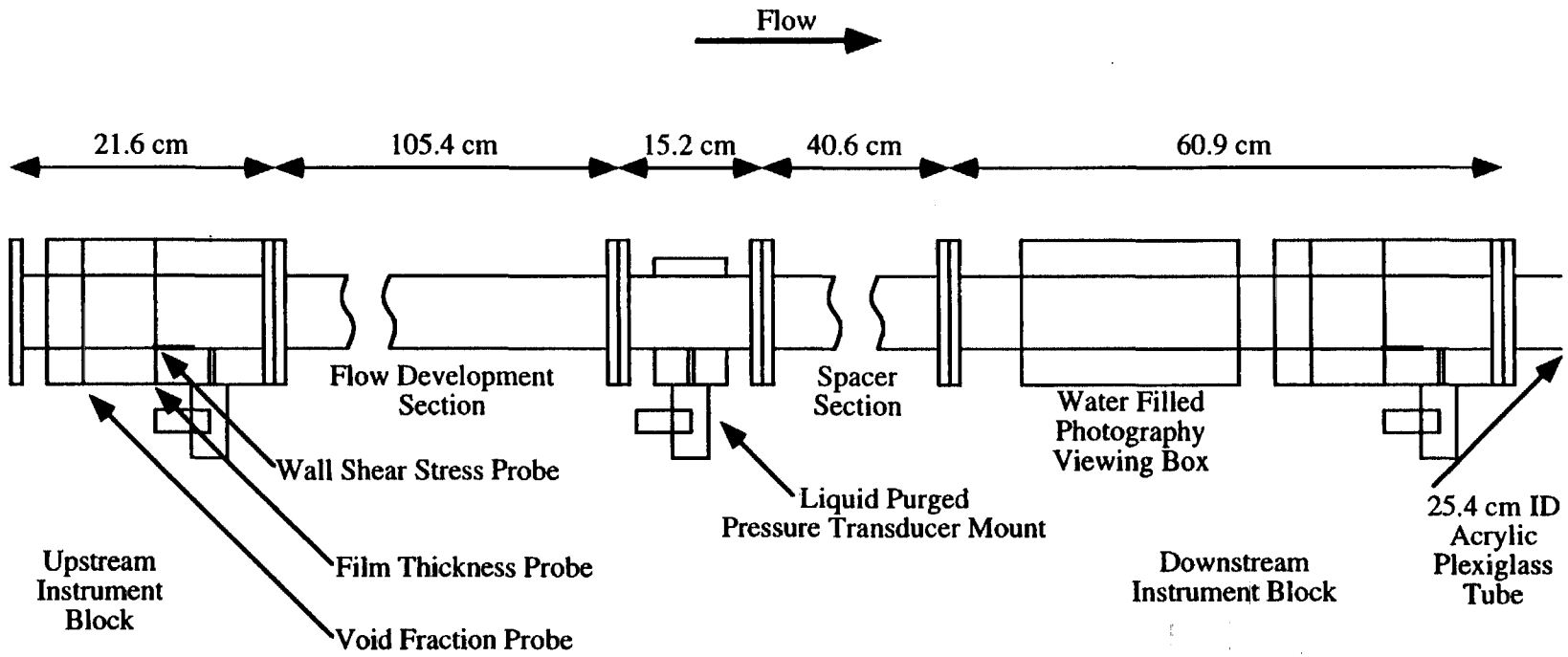

Figure 2.29 25.4 mm ID Test Section

Chapter 3 Experimental Flow Pattern Mapping Results

3.1 Introduction

Two-phase gas-liquid flows distribute themselves into several distinct flow patterns depending primarily on the flow rates of gas and liquid as well as on the physical properties of the fluids, the configuration of the flow system and the magnitude and orientation of gravity. The flow patterns observed in microgravity in this study are shown in Figure 1.1. As will be demonstrated in the course of this study, changes in the flow pattern produce large changes in key operating and design parameters such as the void fraction, pressure drop and heat and mass transfer rates. Because of this strong dependence on the flow pattern, it is unlikely that mechanistic models can be derived which would be valid for all flow patterns. A more realistic approach would be to develop mechanistic models which are specific to a single flow pattern. This requires that the flow pattern be known as a function of gas and liquid flow rates as well as the magnitude and orientation of gravity, fluid physical properties and the configuration of the flow system.

Flow pattern data are traditionally displayed in the form of flow pattern maps which indicate the flow pattern for a given combination of gas and liquid flow rates. Often, the flow rates of liquid and gas are represented on flow pattern maps as superficial velocities, U_{LS} and U_{GS}, respectively, which are the velocities which would be measured if each phase were flowing alone in the pipe. Flow pattern maps for two-phase flows in normal earth gravity have been well established in the literature for pipes oriented horizontally, vertically and at intermediate inclinations (Baker, 1954, 1958, Taitel and Dukler, 1976, Barnea, 1986). However, due to the difficulties associated with conducting microgravity experiments, only a few reduced gravity flow pattern mapping studies are currently available in the literature.

3.2 Previous Work

The first reported attempts at flow pattern mapping in microgravity were from Koestal and Gutstein, 1964 and Albers and Macosko, 1965. These studies used condensing mercury vapor to produce two-phase flow. However, since mercury is a nonwetting liquid, the results are difficult to compare to the present work.

The first air-water study was reported by Heppner et al., 1975, but the flow pattern was determined at a position just 24 L/D downstream of the mixer. Observations of the flow pattern near the mixer outlet in the present study have shown that the flow may not have been fully developed in such a short distance. The flow pattern at the mixer outlet is controlled by the geometry of the mixer and is often different than the flow pattern observed at 50 L/D or greater, where the flow pattern becomes invariant with distance. Thus the Heppner et al. data are considered unsuitable for comparison to the present work, although their study did lead to a careful consideration of flow development length in the design of the present experiment.

Chen et al., 1988 conducted a limited microgravity flow pattern mapping study using R114 in a 15.8 mm ID tube. The flow pattern map is shown in Figure 3.1. As shown, only nine data points were taken in microgravity. While the map in Figure 3.1 shows changes in the flow pattern across the parameter space, it lacks sufficient resolution to provide much insight into the effects of the key input variables on the resulting flow pattern. The data of Chen et al., 1988 as well as the other microgravity flow pattern data sets available in the literature are included in Appendix B.

The microgravity flow pattern map presented by Dukler et al., 1988 for air-water in a 12.7 mm ID tube was the first to span a significant portion of the gas and liquid flow rate parameter space. The map is shown in Figure 3.2. This study was conducted during the early development phase of the Learjet flow loop and test sections used in the present

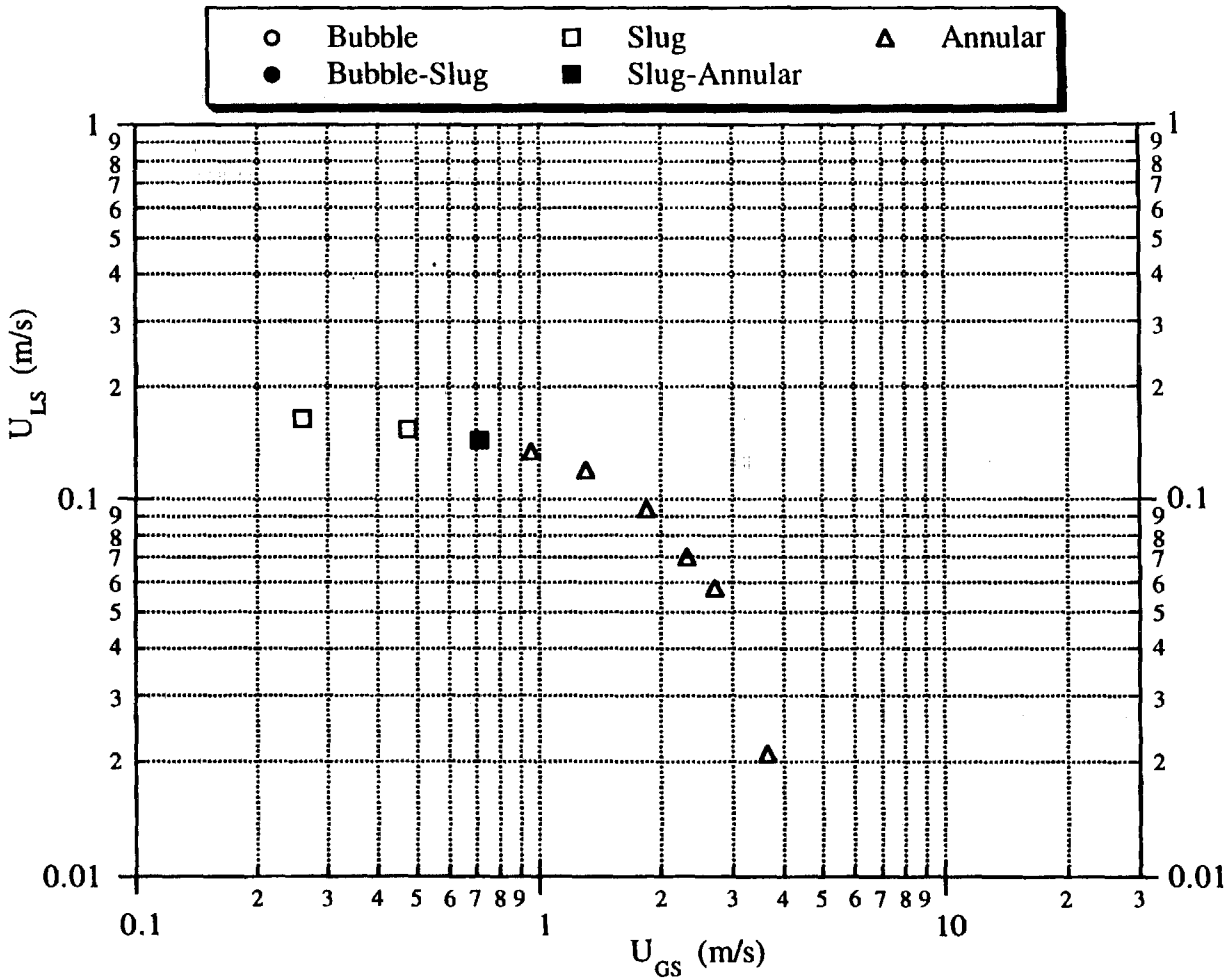

Figure 3.1 Microgravity Flow Pattern Map for R114 in a 15.8 mm ID Tube from Chen et al., 1988

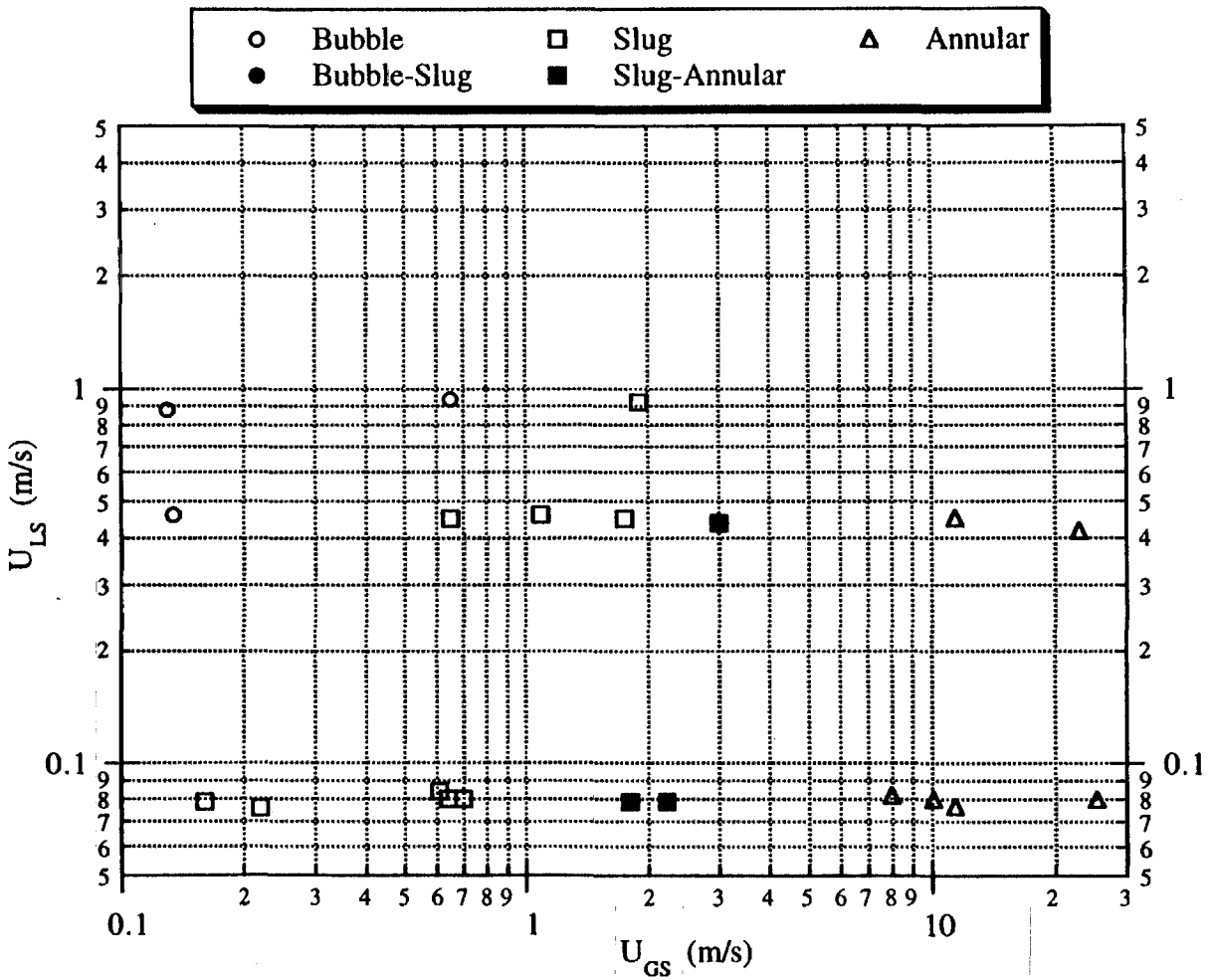

Figure 3.2 Microgravity Flow Pattern Map for Air-Water in a 12.7 mm ID Tube from Dukler et al., 1988

study. The flow pattern map in Figure 3.2 contains only 21 data points but begins to resolve the occurrence of the flow patterns across the parameter space.

An expanded version of the Dukler et al. flow pattern map containing an additional 14 data points was presented by Janicot, 1988 and is shown in Figure 3.3. The original publication also contained 18 experiments taken in the NASA Lewis Research Center 2.2 s Drop Tower Facility. It was discovered that the liquid flow rate was not constant throughout the drop tower experiments and the data were omitted from Figure 3.3. As shown, the resolution of the flow pattern map is slightly improved with the additional data. The flow maps of Dukler et al., 1988 and Janicot, 1988 provided guidance in the determination of the test matrix used for the present flow pattern mapping study.

An extensive study of the bubble and slug flow regimes in microgravity for air-water in a 40 mm ID tube was presented by Colin, 1990 and Colin et al., 1991. Their studies contain flow pattern data for these regions. The flow pattern was determined both at the mixer outlet and 3.2 m downstream of the mixer in these studies. The results showed that the flow pattern at the mixer was often different from that ultimately attained after the flow had developed. The fully developed flow pattern data reported in Colin, 1990 are shown in Figure 3.4 and clearly resolve the bubble and slug flow regions of the parameter space.

Crowley and Sam, 1991 conducted a microgravity two-phase flow study with R11 in a 6.34 mm ID tube. Unfortunately, problems with noncondensable gases in the Freon casts considerable doubt on the reliability of this study for purposes of flow pattern mapping. Hill and Best, 1991 conducted a study using R12 in 8.7 mm and 11.1 mm ID tubes but serious problems were reported with the accuracy of the vapor flow rate measurements (Reinarts, 1993), casting doubt on these results as well.

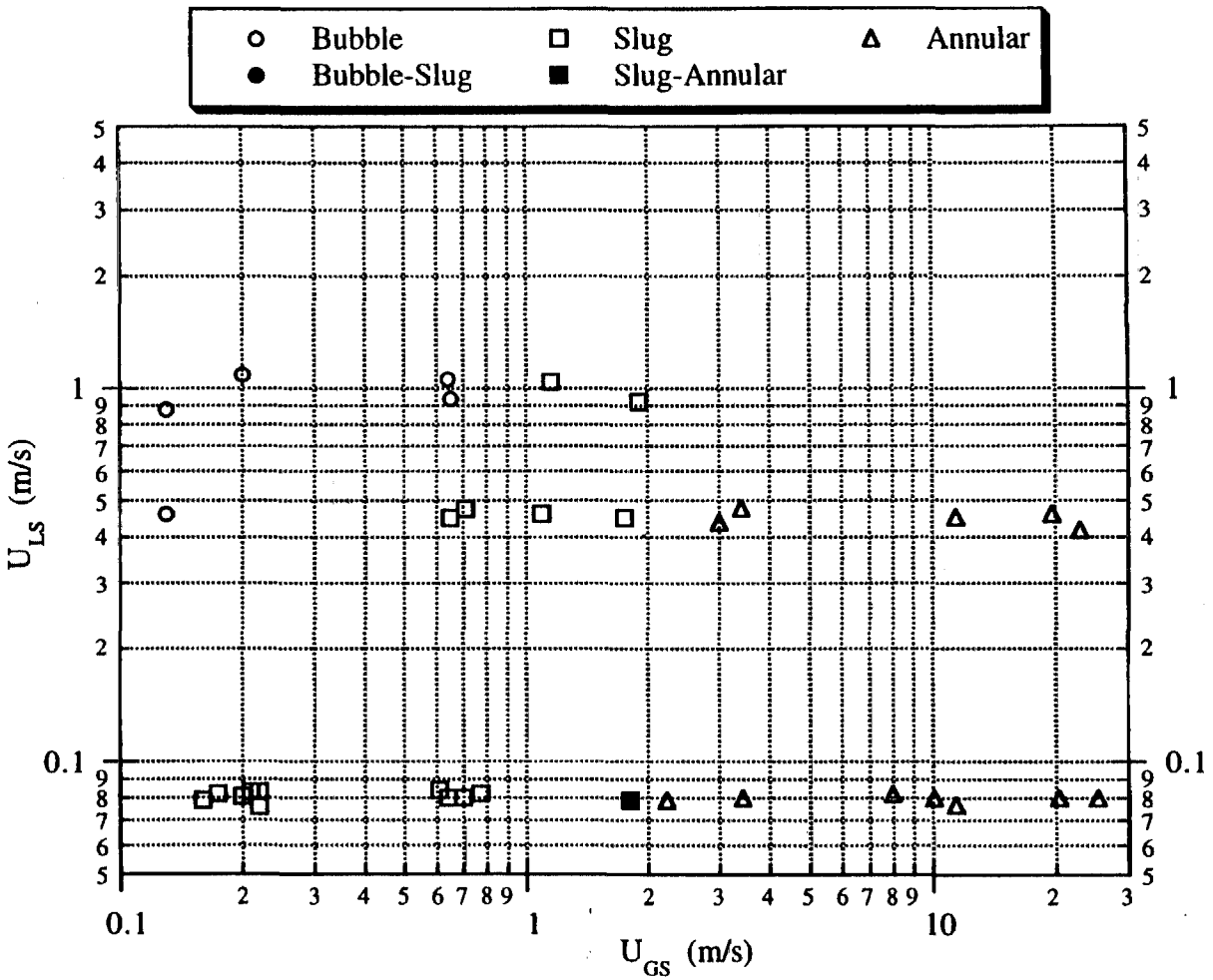

Figure 3.3 Microgravity Flow Pattern Map for Air-Water in a 12.7 mm ID Tube from Janicot, 1988

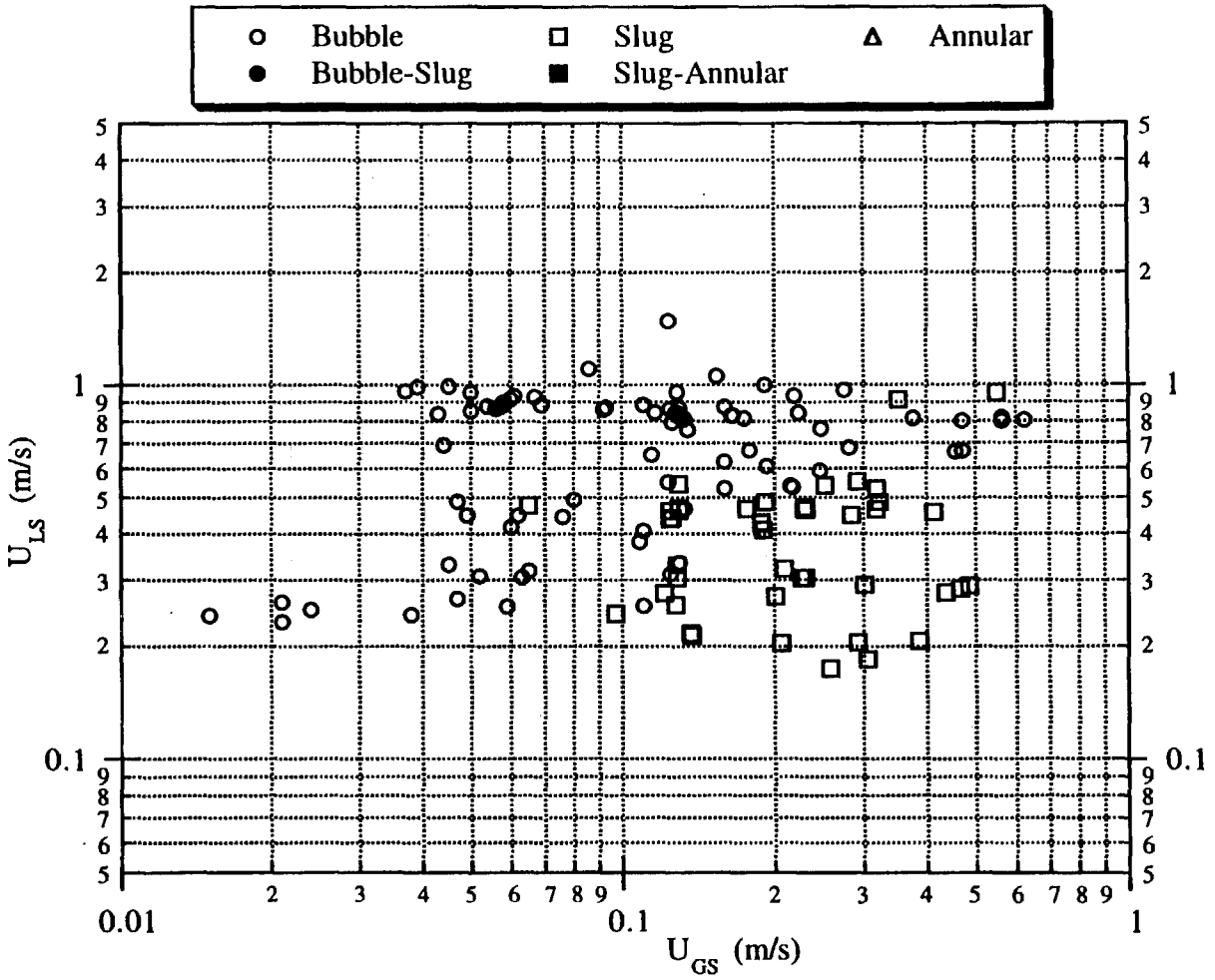

Figure 3.4 Microgravity Flow Pattern Map for Air-Water in a 40 mm ID Tube from Colin, 1990

Huckerby and Rezkallah, 1992 presented a microgravity air-water flow pattern mapping study in a 9.525 mm ID tube. As shown in Figure 3.5, this study spans much of the same parameter space as that of Janicot, 1988 with the exception of the annular flow region. With minor exceptions, the results are in fair agreement with the 12.7 mm ID tube results of Janicot, 1988. This study was followed by a more complete air-water microgravity flow pattern map for a 9.525 mm ID tube presented in Zhao and Rezkallah, 1993. As shown in Figure 3.6, the map spans a large part of the parameter space and shows clearly defined regions of bubble, slug, slug-annular and annular flow. The agreement between these results and those of Janicot, 1988 is good for the slug-annular transition but poor for the bubble-slug transition.

Another recent microgravity flow pattern mapping study was that of Reinarts, 1993 for R12 in 4.7 mm and 10.5 mm ID tubes. Only the annular flow region of the parameter space was mapped in the 4.7 mm ID tube experiments which is shown in Figure 3.7. The map for the 10.5 mm ID tube, shown in Figure 3.8, is much more complete and spans a large parameter space.. Only one experiment was identified as bubble flow, however as shown in Figure 3.8, a very low gas superficial velocity (< 0.05 m/s) was required to achieve this condition, making bubble flow a difficult regime to map for R12. The results are clearly different from those of the air-water studies, suggesting that the fluid physical properties are important factors in flow pattern mapping.

The small but growing body of literature on the subject of microgravity two-phase flow patterns indicates a steady improvement in the quality of the flow pattern mapping experiments as experimental techniques in the microgravity environment are refined. The flow maps presented in these studies indicate that fluid physical properties have a strong effect on the resulting flow pattern maps but this was not investigated systematically in any of the previous works. The literature also suggests a less important but significant effect of tube diameter on the resulting flow pattern maps. The effects of the physical properties as

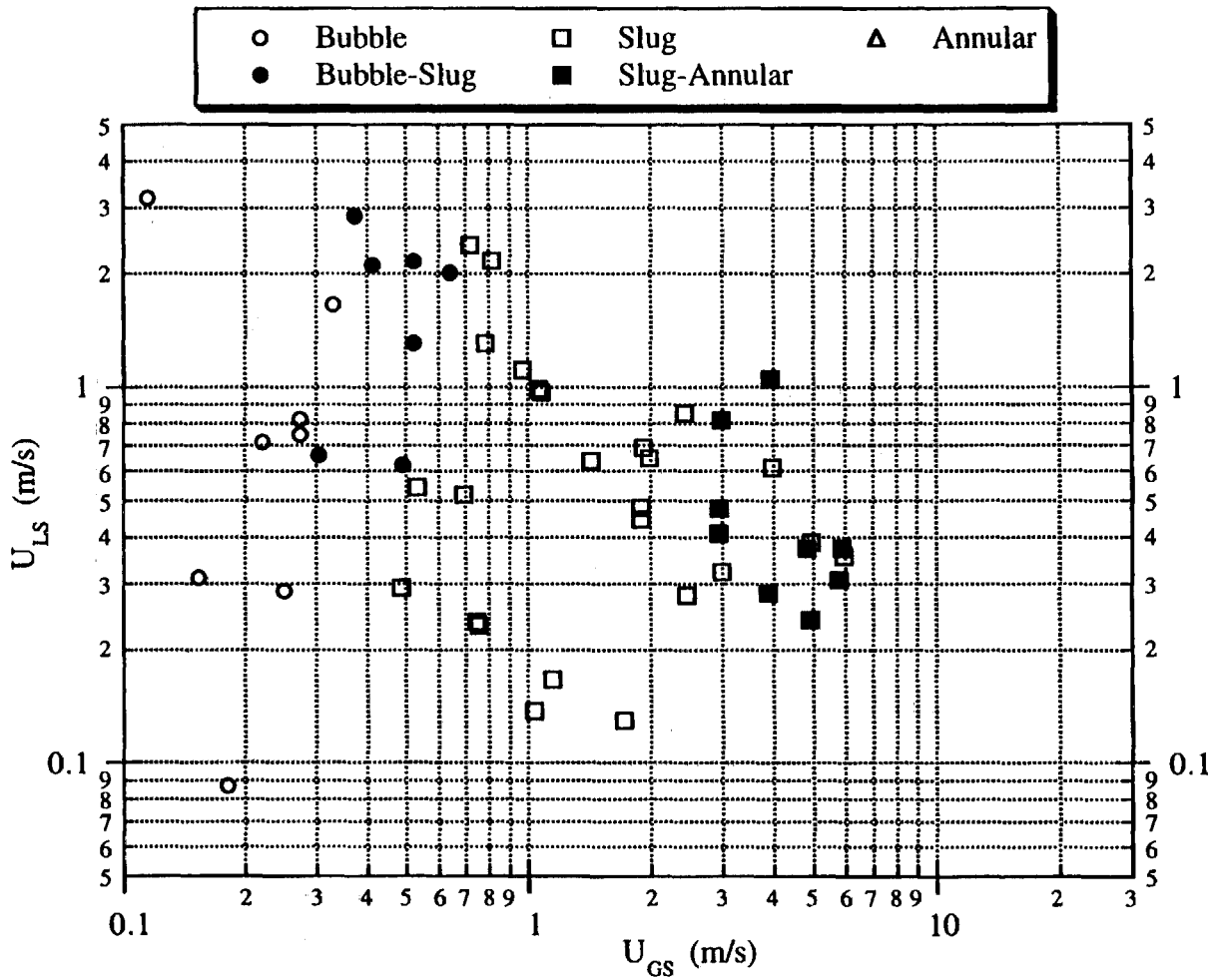

Figure 3.5 Microgravity Flow Pattern Map for Air-Water in a 9.525 mm ID Tube from Huckerby and Rezkallah, 1992

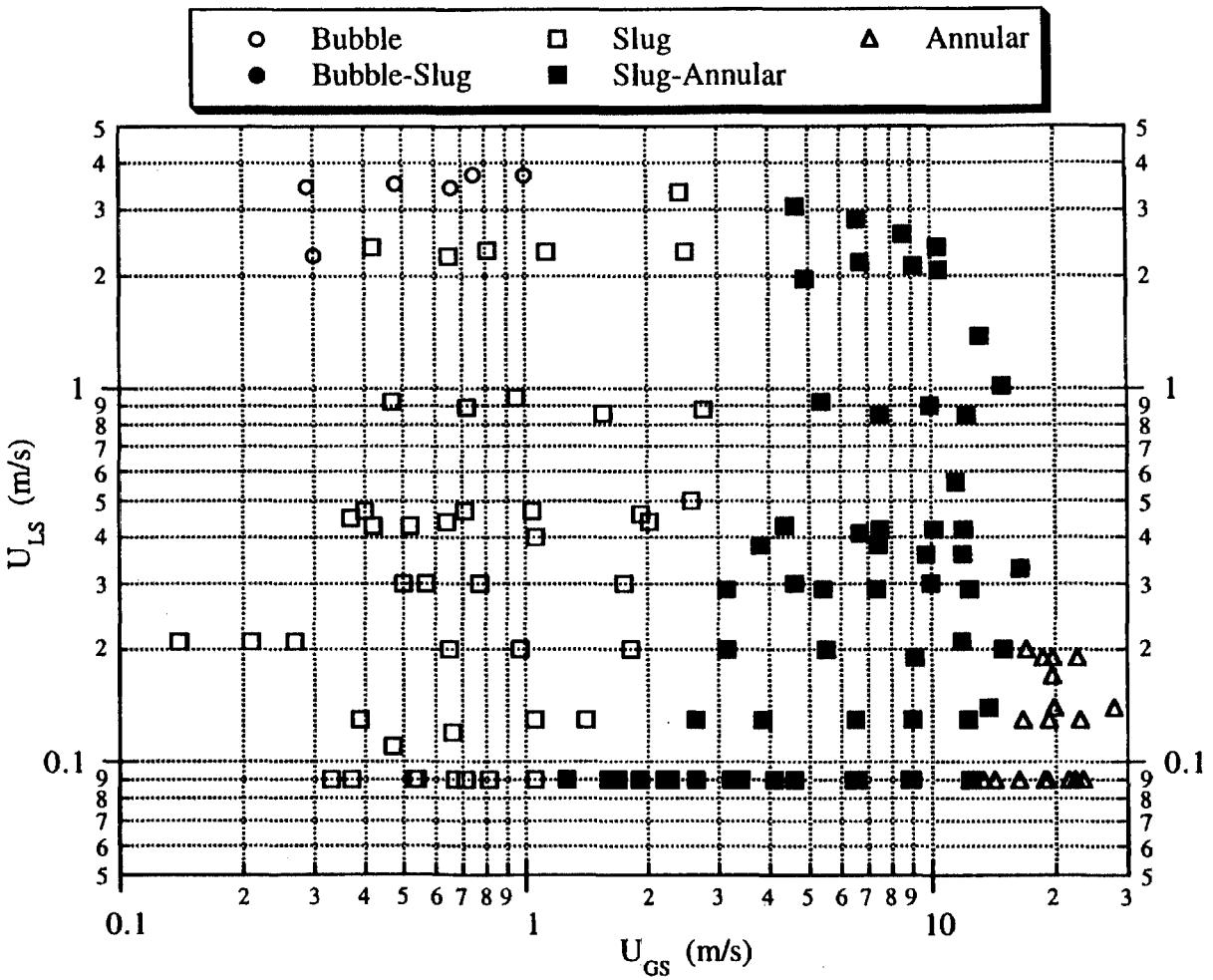

Figure 3.6 Microgravity Flow Pattern Map for Air-Water in a 9.525 mm ID Tube from Zhao and Rezkallah, 1993

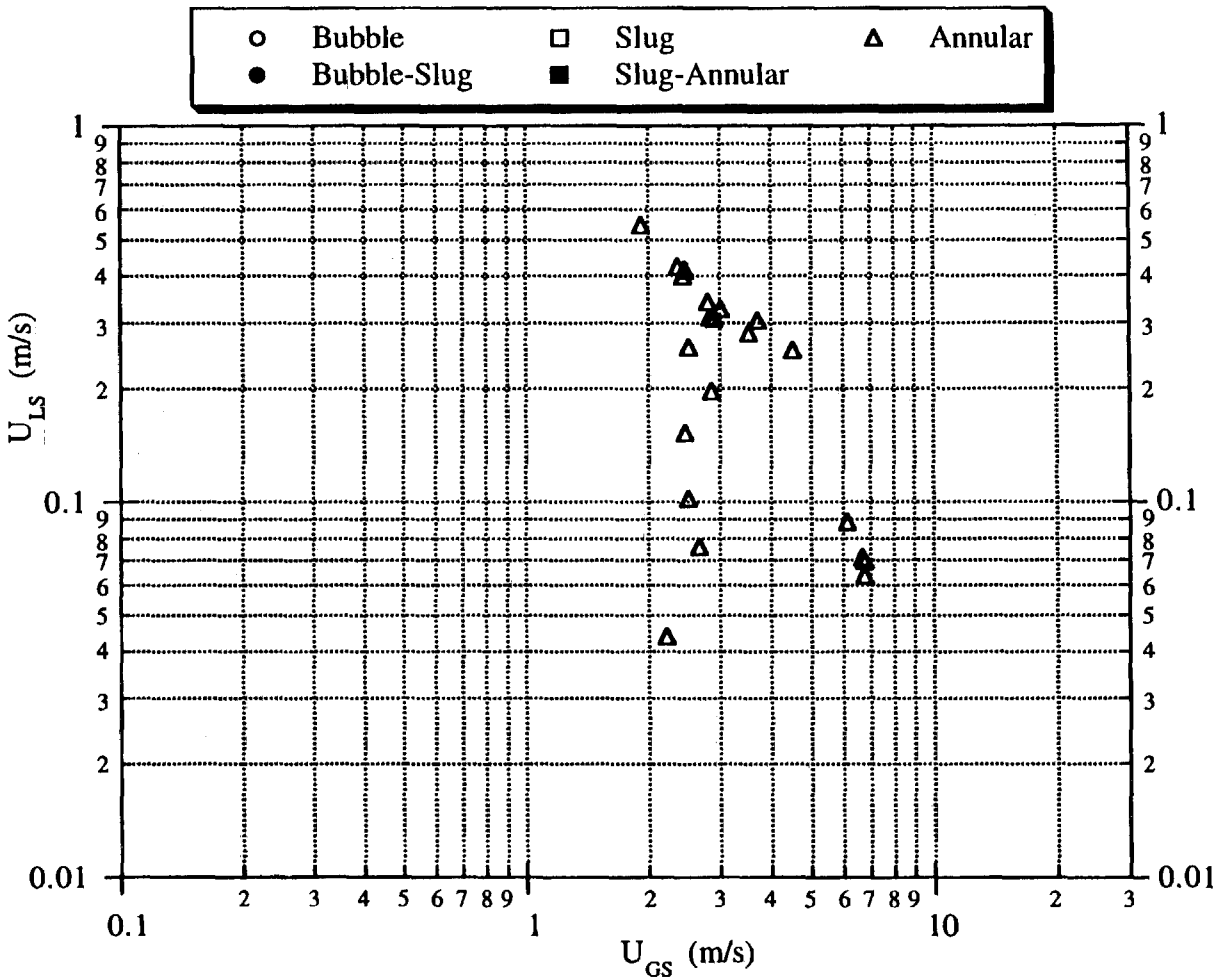

Figure 3.7 Microgravity Flow Pattern Map for R12 in a 4.7 mm ID Tube from Reinarts, 1993

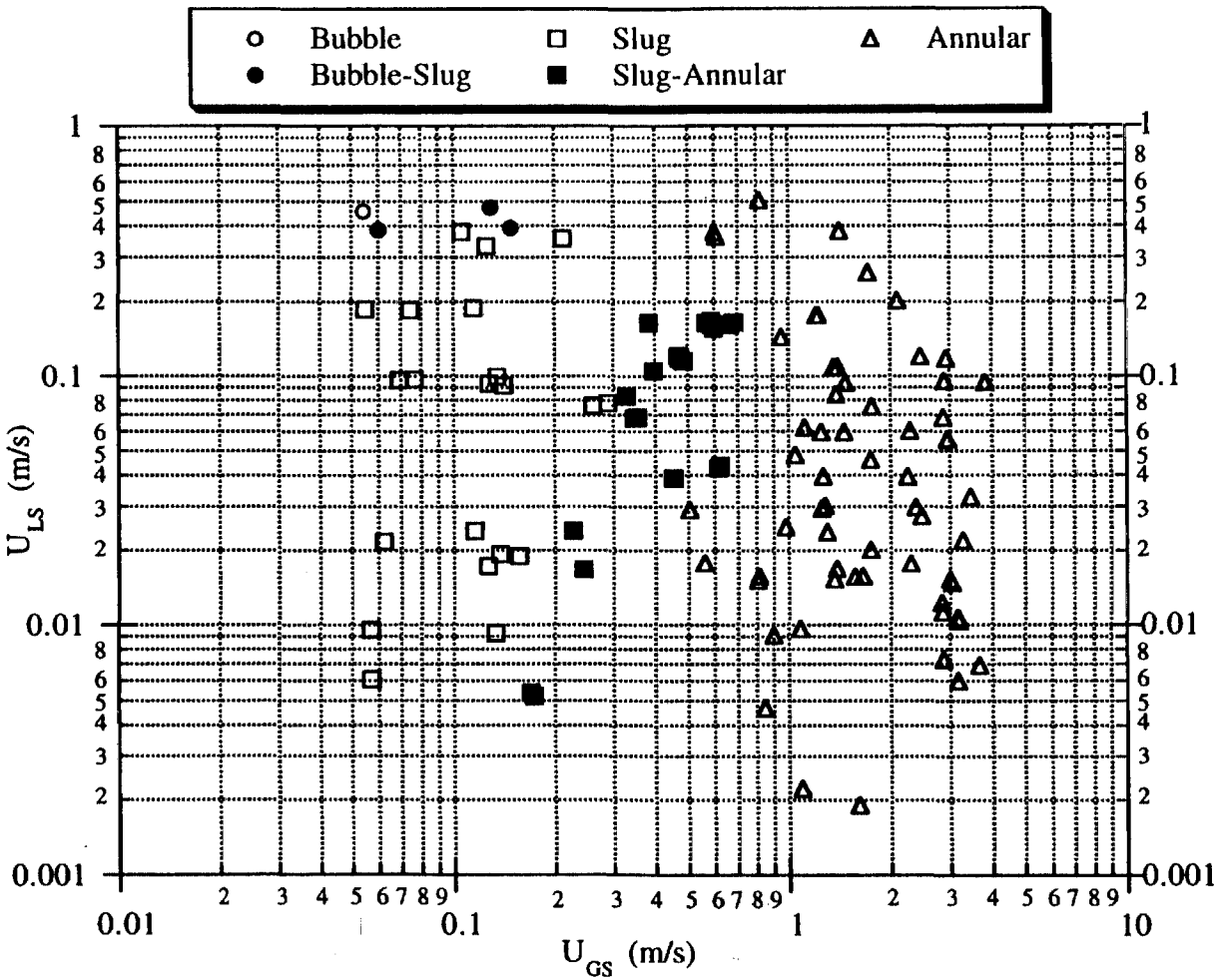

Figure 3.8 Microgravity Flow Pattern Map for R12 in a 10.5 mm ID Tube from Reinarts, 1993

well as the tube diameter on the flow pattern must be known if gas-liquid flow systems are to be designed and operated efficiently in the microgravity environment. The initial part of this study was therefore devoted to establishing the flow pattern maps in microgravity as a function of liquid physical properties (viscosity and surface tension) and tube diameter, which were thought to be the key parameters affecting the flow pattern maps. The previously cited studies also suggest that the density of both phases is a significant factor. Freon refrigerants could not be used in the flow loops used in the present study and thus the effect of a large change in fluid density on the flow pattern maps could not be investigated.

To test the effects of liquid viscosity and surface tension on the occurrence of the flow patterns, three liquids were tested (all at 21± 2 °C): water (μ = 1 cP, σ = 72 dynes/cm), 50-50 wt% water/glycerin (μ = 6 cP, σ = 63 dynes/cm), and water/Zonyl FSP (μ = 1 cP, σ = 21 dynes/cm). Zonyl FSP (manufactured by DuPont) is a powerful surfactant which, when used in low concentrations (0.5 wt% in these studies), lowers the surface tension to 21 dynes/cm (nearly independent of concentration for greater than 0.1 wt% concentration) without significantly affecting the other physical properties of the liquid. To determine the effect of tube diameter, flow pattern maps for all three liquids tested were established for 12.7 mm and 25.4 mm ID tubes.

3.3 Flow Pattern Identification Techniques

While the idealized microgravity flow patterns shown in Figure 1.1 are easily distinguished from one another, identifying the flow patterns in real two-phase flows can be difficult, especially when the gas superficial velocity is high. As a result, flow pattern identification remains partially subjective and this is responsible for some of the discrepancy in the flow pattern transitions reported in the literature.

All of the studies reported in the previous section relied entirely on photography to identify the flow patterns in the experiments. While photography was also used extensively in the present study, it was found that this alone was not always sufficient to reliably identify the flow patterns. Photographic identification of the slug-annular transition region for liquid superficial velocities in excess of 0.5 m/s was considered to be especially difficult. In order to more consistently identify the flow patterns, time-series data from the film thickness probes were used in conjunction with high-speed photography.

A large number of photographs of microgravity two-phase flows taken in the course of this study are shown in Appendix A, representing the different flow patterns observed. The flow pattern was judged to be bubble flow when the gas phase was distributed as discrete gas bubbles which were no longer than the diameter of the tube (roughly spherical) as shown in Figures A.1, A.2, A.3 and A.4. Slug flow was differentiated from bubble flow by the presence of Taylor bubbles which were longer than the tube diameter as shown in Figures A.8, A.9 and A.10. A transitional state labeled as bubble-slug flow was observed when short Taylor bubbles occasionally appeared in a flow which was otherwise bubble flow, as shown in Figures A.5, A.6 and A.7. The flow pattern was labeled as annular when the gas core remained continuous, as shown in Figures A.14, A.15 and A.16. Slug flow was differentiated from annular flow by the presence of liquid slugs which spanned the entire pipe diameter. A transitional state labeled as slug-annular flow was observed when large amplitude waves momentarily bridged the tube diameter and then ruptured. These bridging events, as shown in the sequences in Figures A.11 (a,b,c), A.12 (a,b,c) and A.13 (a,b,c), were often very short in duration, lasting only one or two frames (2.5 - 5 ms) and were often difficult to distinguish photographically from thin liquid slugs which did not rupture or from large amplitude waves which did not bridge the pipe. The distinction between slug, slug-annular and annular flows is subjective and can lead to discrepancies between different observers.

Because flow patterns, especially those near transition, were difficult to identify photographically, the time-series film thickness measurements were used to assist in the flow pattern determination. Bubble flows, though generally easy to identify photographically, have the characteristic film thickness signature shown in Figure 3.9. As shown, the normalized film thickness value spans a large portion of the entire range from zero to one with no discernible features. Slug flows were identified from the film thickness time-series which clearly shows the presence of liquid slugs (film thickness at or near that of the tube diameter) and Taylor bubbles (long duration regions of low film thickness) as shown in Figure 3.10. Bubble-slug transition flows have a film thickness signature closely resembling that of bubble flow as shown in Figure 3.11 since the Taylor bubbles in these flows are very short. Because the bubble-slug flow film thickness traces did not contain features which distinguished them from bubble flow, the film thickness trace was not considered to be a reliable tool for identifying this transitional state. Bubble-slug flows were therefore identified entirely by photography. Annular flows were identified from the film thickness measurements by the presence of numerous waves on a thin liquid substrate as shown in Figure 3.12. Slug-annular transition flows were sometimes difficult to identify from film thickness measurements because the short duration tube-bridging events usually did not occur at the same location as the film thickness wires. It was observed however that when the amplitude of the waves exceeded 70% of the tube diameter, tube bridging events could usually be found in the photographs. Film thickness measurements and high-speed photography were therefore used together to identify slug-annular transition flows. A normalized film thickness time-series for a slug-annular flow, including suspected tube bridging events, is shown in Figure 3.13.

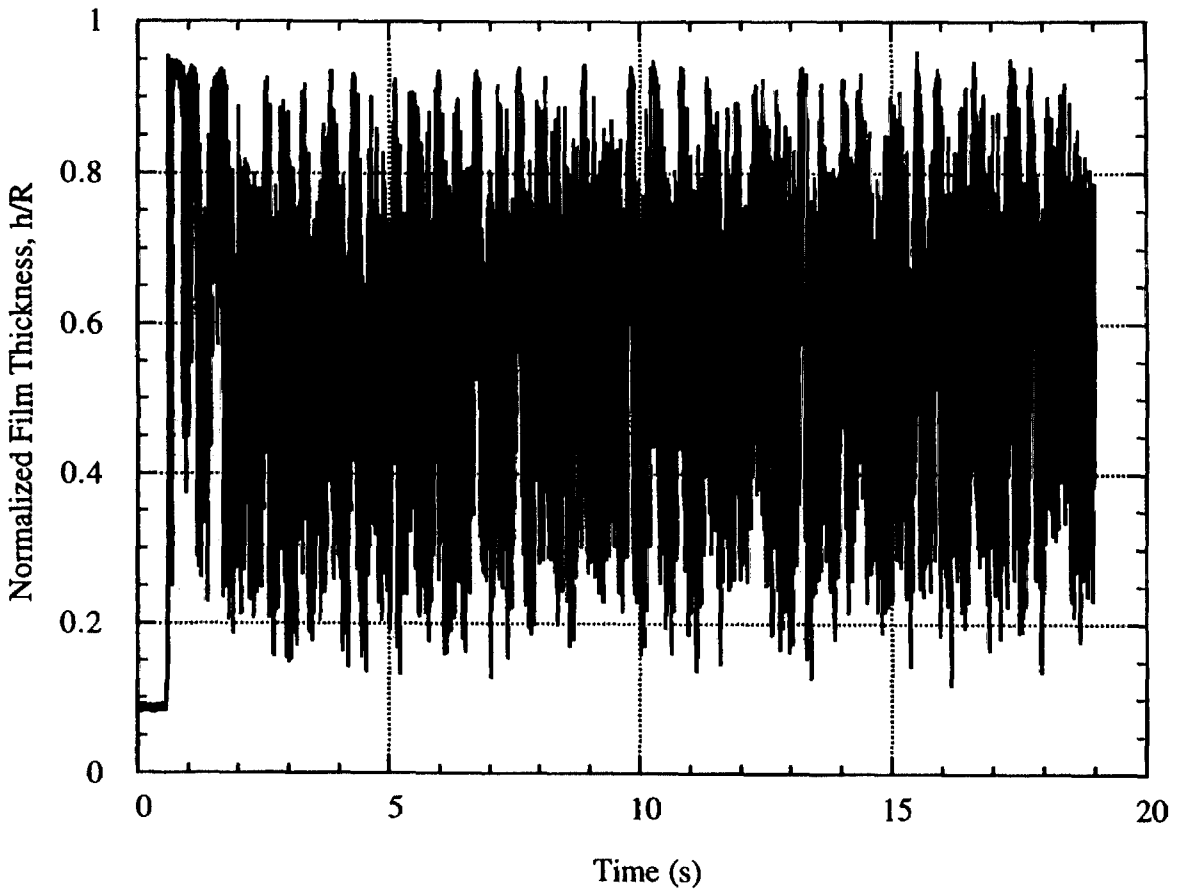

Figure 3.9 Characteristic Film Thickness Signature for Bubble Flow in Microgravity

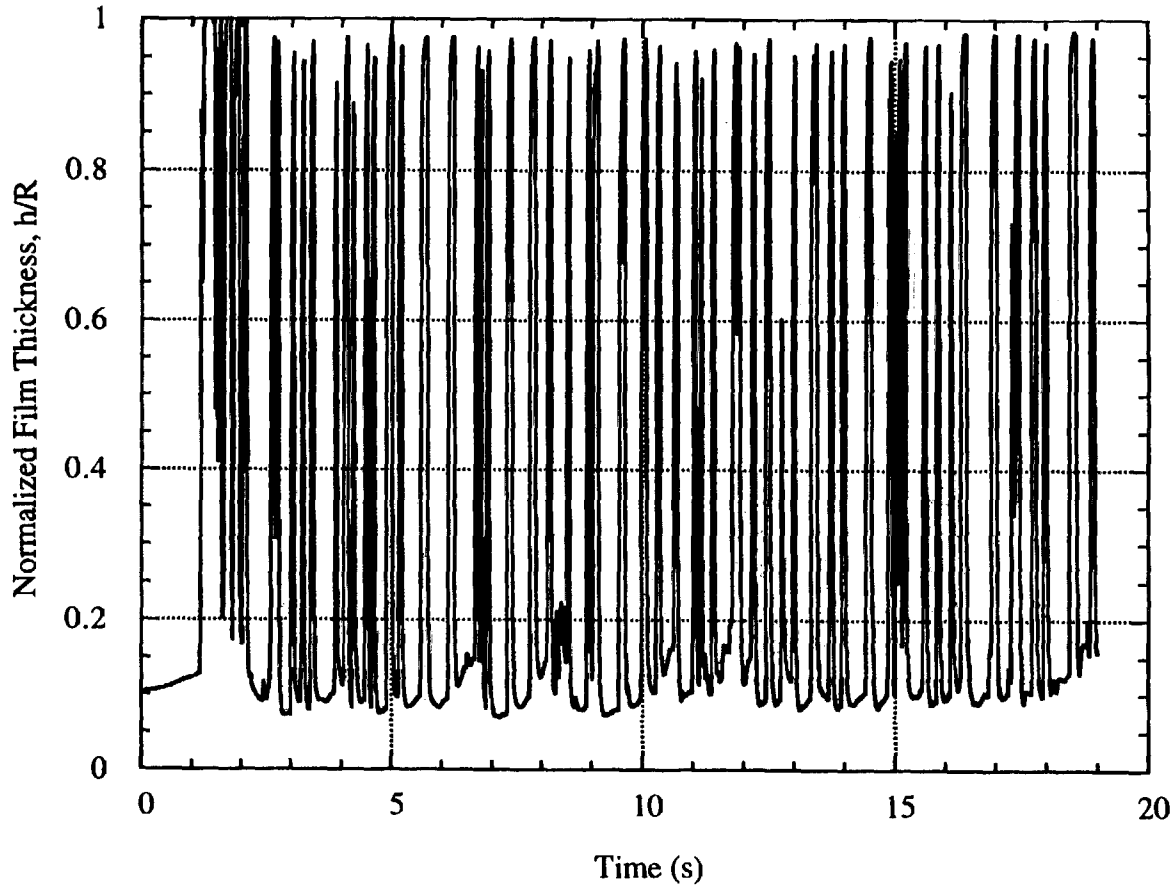

Figure 3.10 Characteristic Film Thickness Signature for Slug Flow in Microgravity

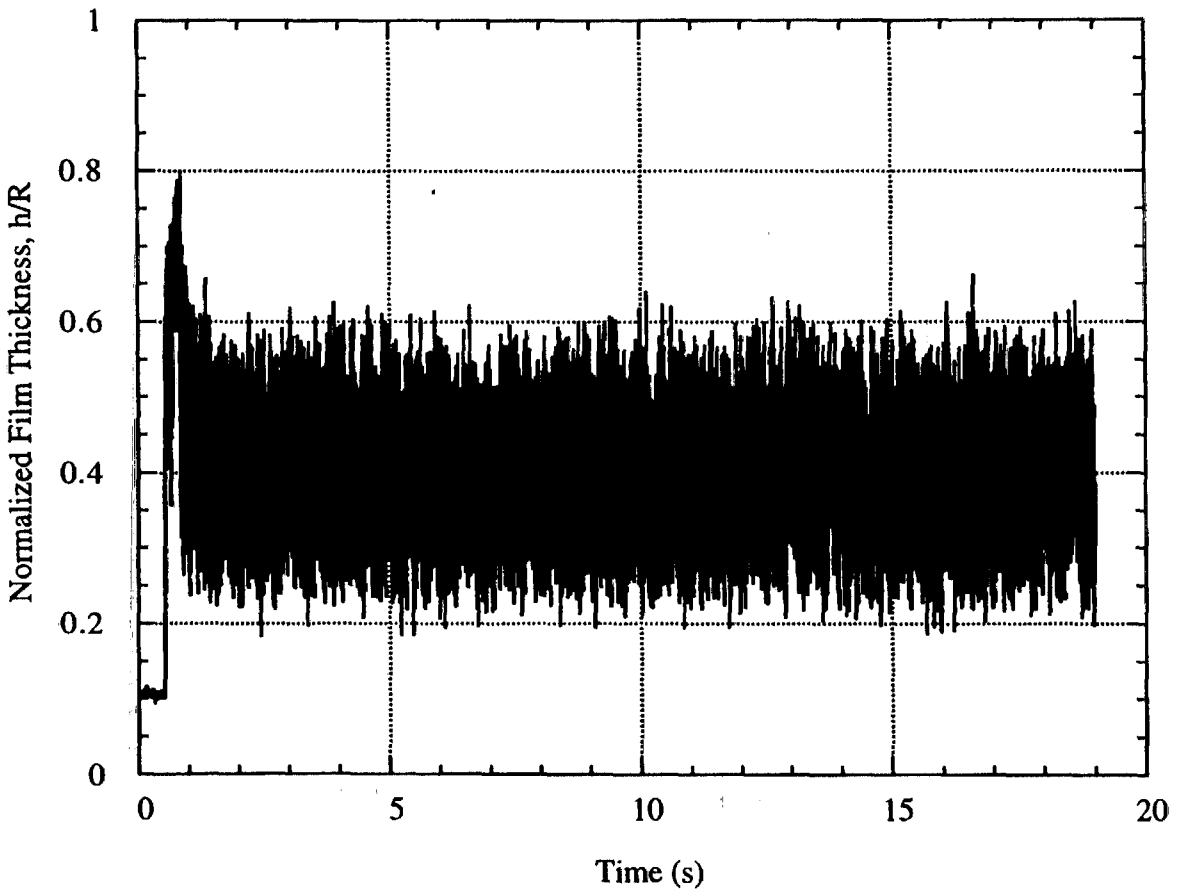

Figure 3.11 Characteristic Film Thickness Signature for Bubble-Slug Transition Flow in Microgravity

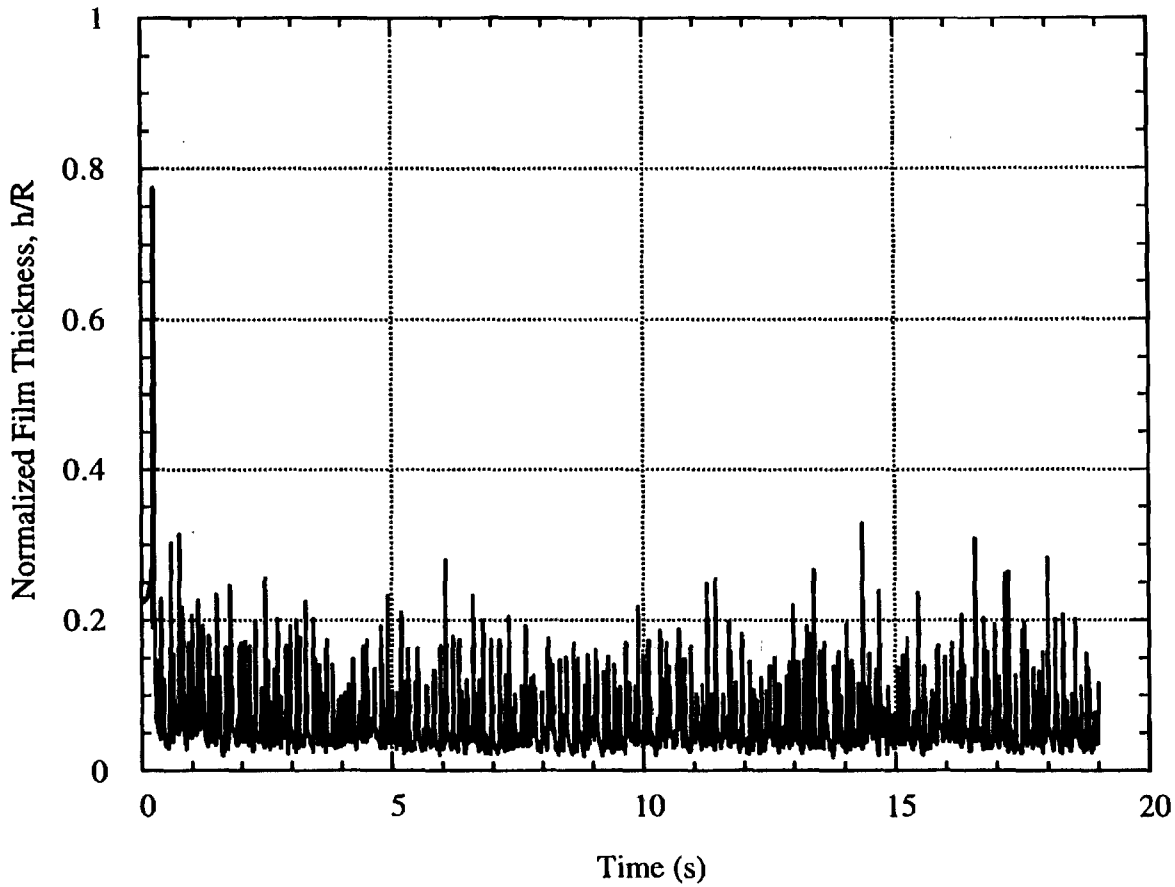

Figure 3.12 Characteristic Film Thickness Signature for Annular Flow in Microgravity

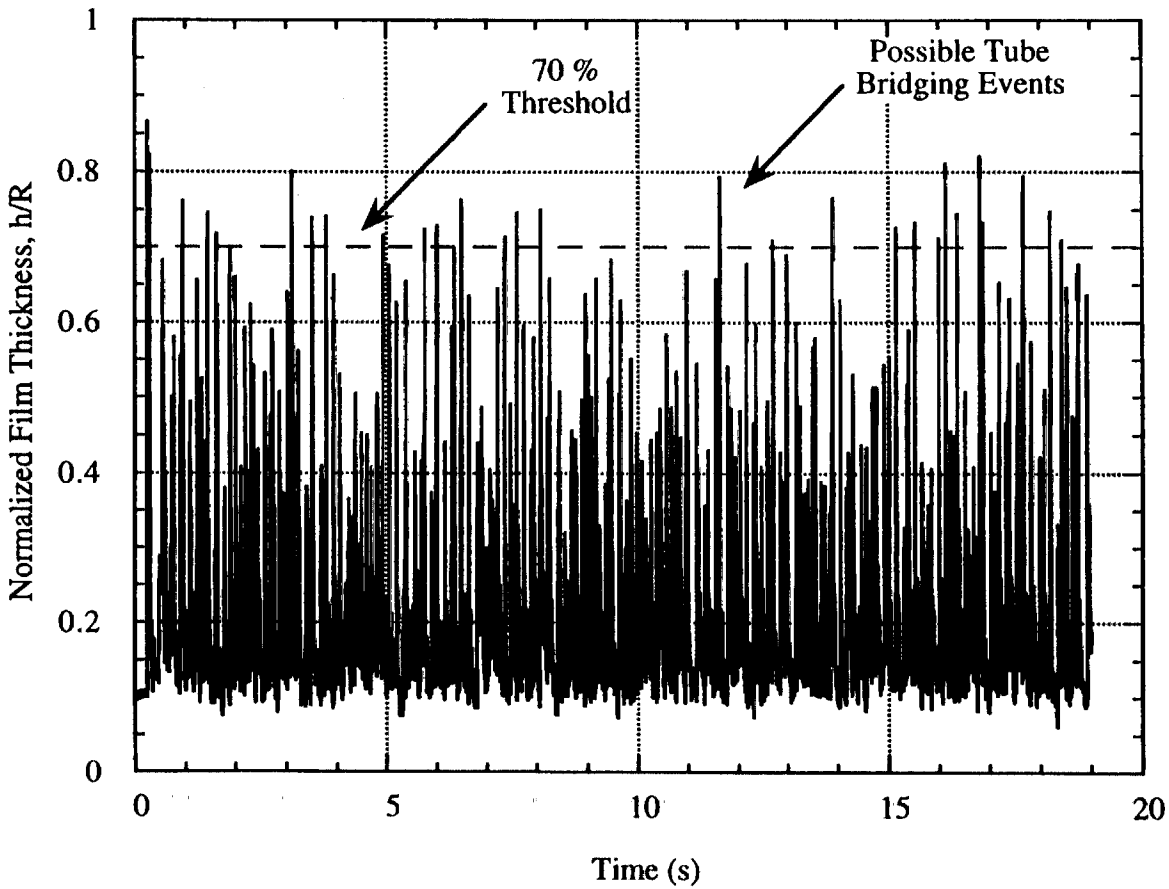

Figure 3.13 Characteristic Film Thickness Signature for Slug-Annular Transition Flow in Microgravity

3.4 Flow Pattern Maps

One of the primary objectives of this study was to establish microgravity flow pattern maps for 12.7 mm and 25.4 mm ID tubes using air-water, air-water/glycerin and air-water/Zonyl FSP. The flow pattern mapping data for the 12.7 mm ID tube were collected in a series of flight experiments spanning several years. These maps are shown in Figures 3.14, 3.15 and 3.16 for air-water, air-water/glycerin and air-water/Zonyl FSP, respectively. The initially strategy was to broadly cover the parameter space of 0.1 m/s < U_{GS} < 25 m/s and 0.05 m/s < U_{LS} < 1 m/s because the Janicot, 1988, results indicated that all flow patterns and transitions would be observed in this space. The flow pattern data displayed in the flow pattern maps from this study are included in Appendix C.

Once the approximate locations of the bubble-slug and slug-annular transitions were located, later experiment sets were taken at conditions near the transitions so that these regions could be better resolved. The 12.7 mm ID flow pattern maps also contain results from a later study focused on characterizing annular and slug flows. Since many improvements were made to the test sections, the Learjet flow loop and the operating procedure after the Janicot data were obtained, those data were not incorporated into the present flow maps. Experiments in which there were problems with flow rate control or gravity level were also omitted. The 12.7 mm ID flow maps therefore represent a composite of the reliable flow pattern data from many sets of experiments.

The approach to establishing the flow pattern maps for the 25.4 mm ID tube was entirely different because the KC-135 aircraft performs many more experiments per flight but is available much less frequently than the Learjet. The availability of the KC-135 allowed for a single, but extensive, experiment set consisting of eight flights, from which the flow pattern maps were established. No previous work suggested where the transitions would be located so a grid search strategy combined with knowledge gained from the 12.7 mm ID flow maps was used to cover the parameter space. Because the KC-135 flow loop

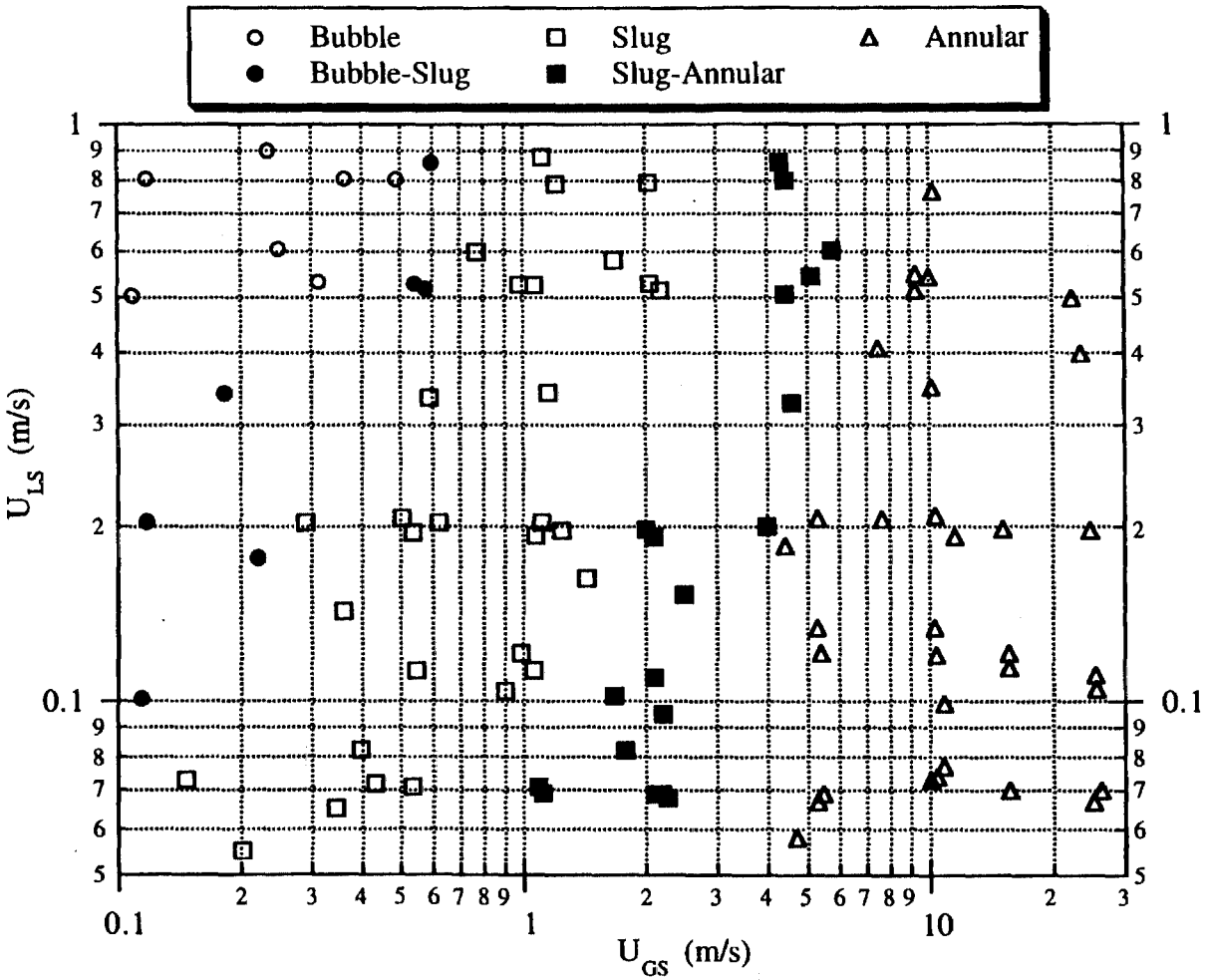

Figure 3.14 Microgravity Flow Pattern Map for Air-Water in a 12.7 mm ID Tube

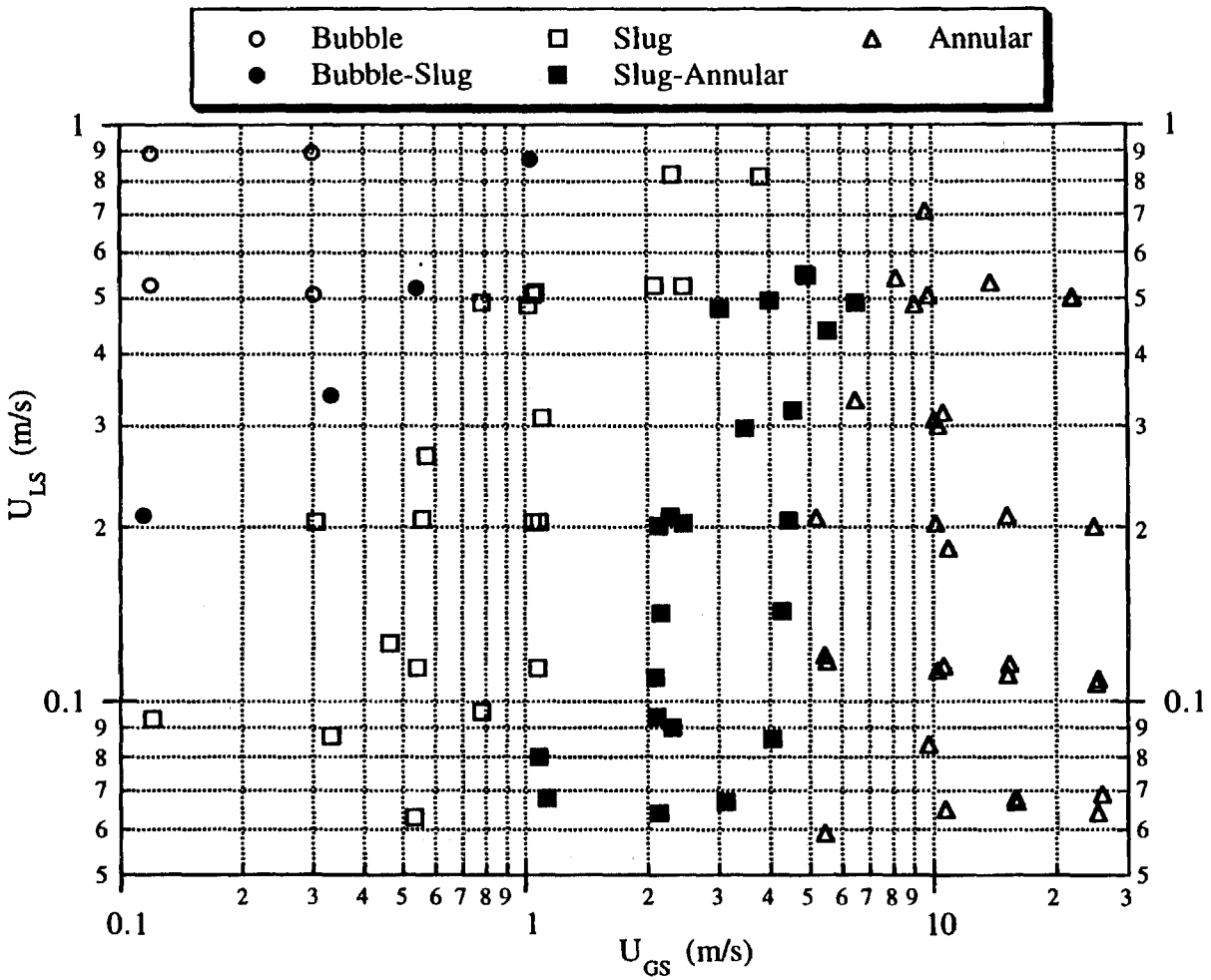

Figure 3.15 Microgravity Flow Pattern Map for Air-Water/Glycerin in a 12.7 mm ID Tube

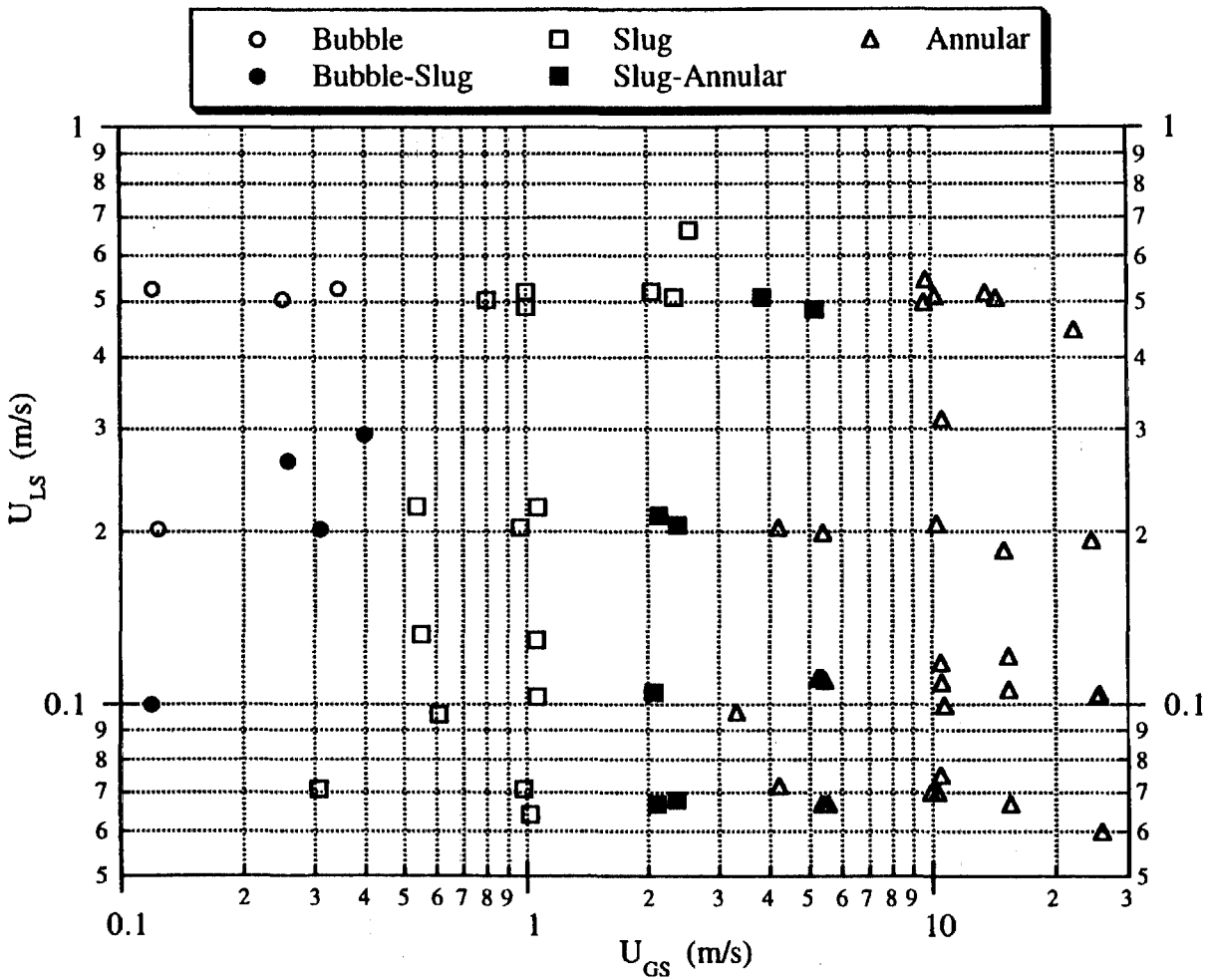

Figure 3.16 Microgravity Flow Pattern Map for Air-Water/Zonyl FSP in a 12.7 mm ID Tube

was previously untested in microgravity and the operation of the KC-135 was different from that of the Learjet, much of the electronic data from these experiments was lost. Sufficient film thickness data were collected to assist in flow pattern identification however. The resulting flow pattern maps are shown in Figures 3.17, 3.18 and 3.19 for air-water, air-water/glycerin and air-water/Zonyl FSP, respectively. Fortunately, all flow patterns and transitional states were located within the bounds of the parameter space tested.

3.5 Comparison of Results

The effect of tube diameter on the microgravity air-water flow pattern maps is shown by comparing Figure 3.14 to Figure 3.17. As shown, increasing the tube diameter from 12.7 to 25.4 mm leads to a shift in the bubble-slug transition to lower values of U_{GS} at a given value of U_{LS} (lower void fraction). The slug-annular transition region appears to be unchanging with tube diameter for the air-water system.

A similar result was obtained for the air-water/glycerin system which is shown by comparing Figures 3.15 and 3.18. These flow pattern maps also show that an increase in the tube diameter leads to a shift in the bubble-slug transition towards lower void fraction. The slug-annular transition runs occupy the same area on both flow maps which again suggests that there is little effect of tube diameter on this transition.

The effects of tube diameter on the air-water/Zonyl FSP system can be shown by comparing Figure 3.16 to Figure 3.19. Unlike the other two fluid systems, there is no shift in the bubble-slug transition with tube diameter on these maps. As was observed in the other fluid systems, the tube diameter had no effect on the slug-annular transition for the air-water/Zonyl FSP system.

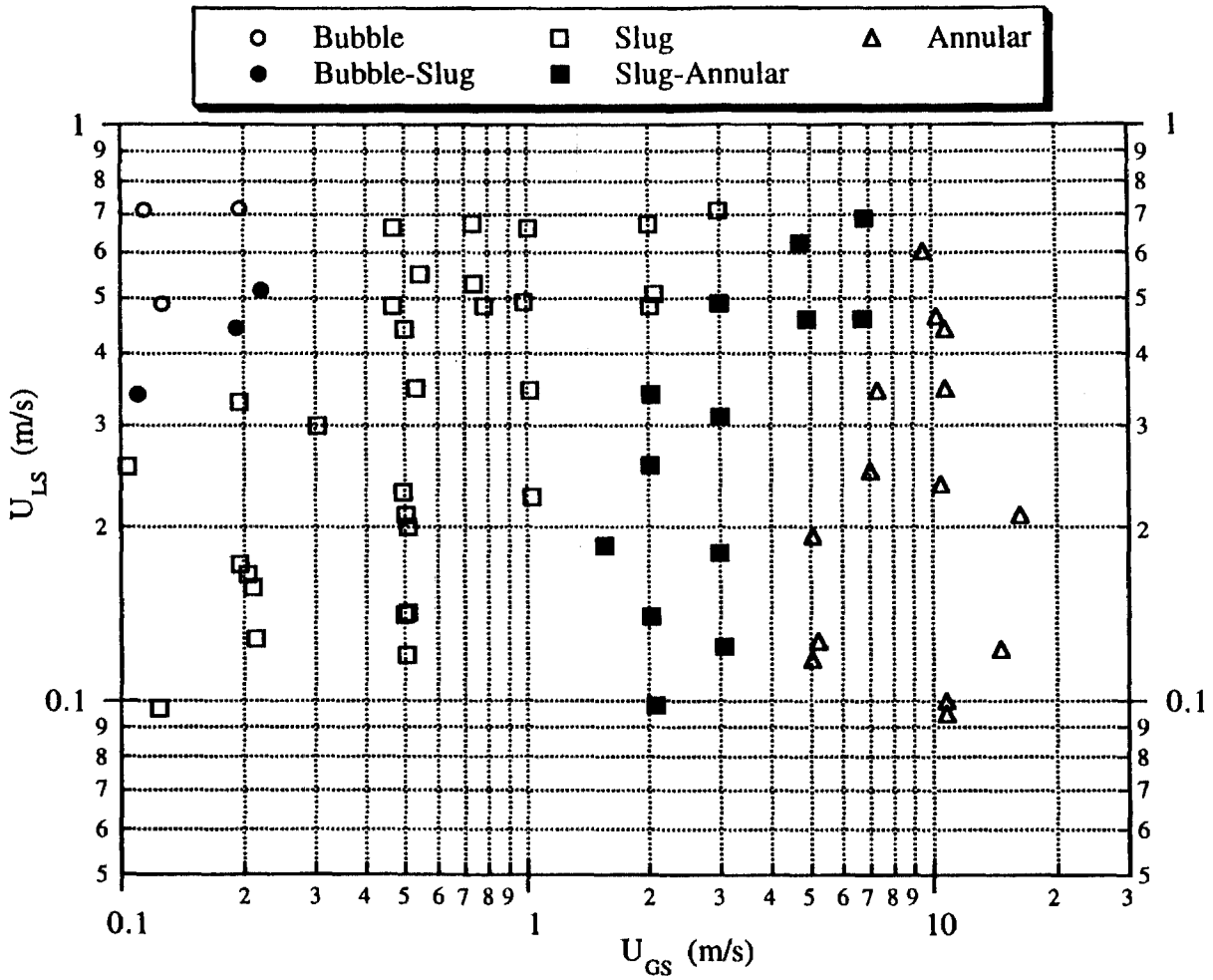

Figure 3.17 Microgravity Flow Pattern Map for Air-Water in a 25.4 mm ID Tube

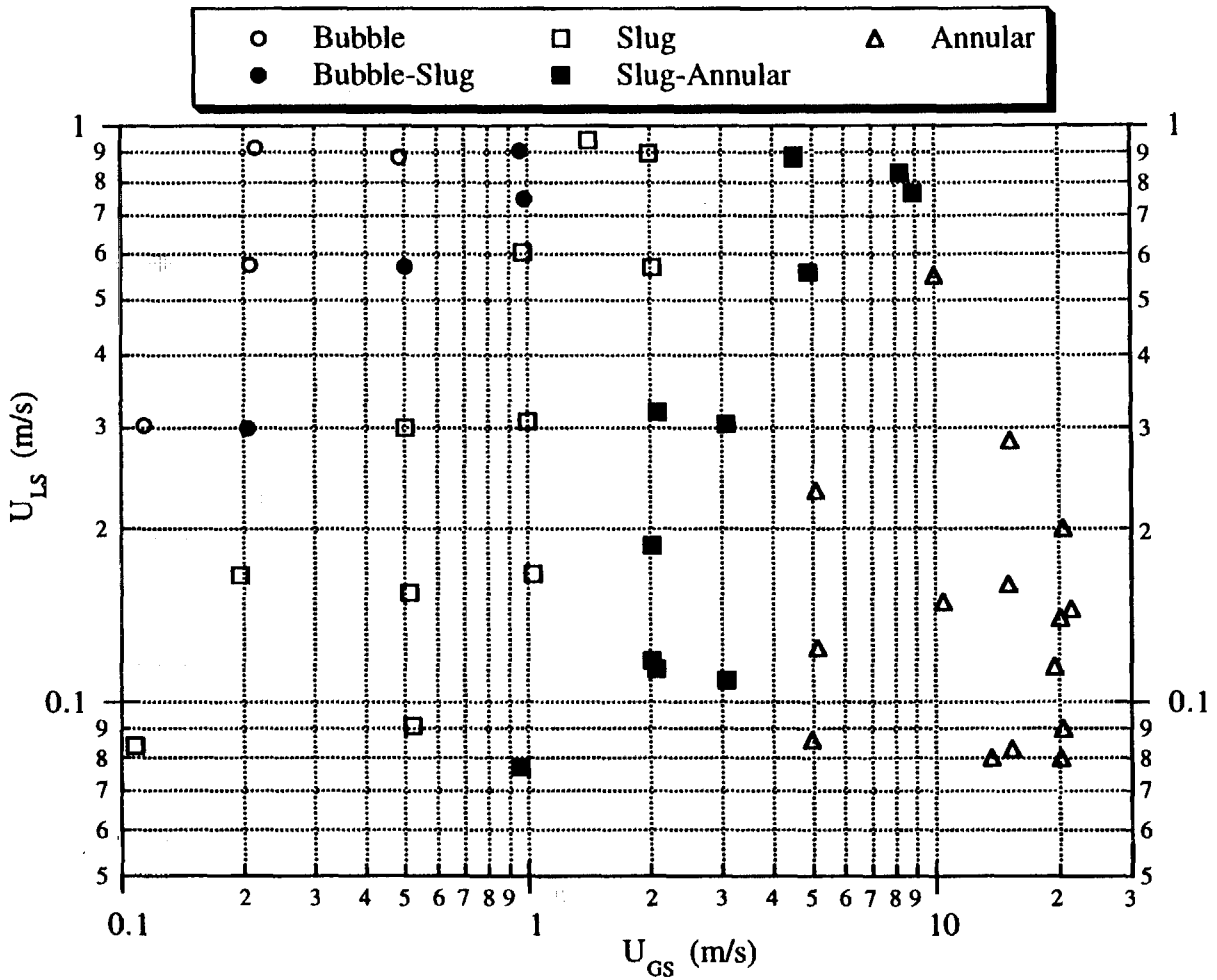

Figure 3.18 Microgravity Flow Pattern Map for Air-Water/Glycerin in a 25.4 mm ID Tube

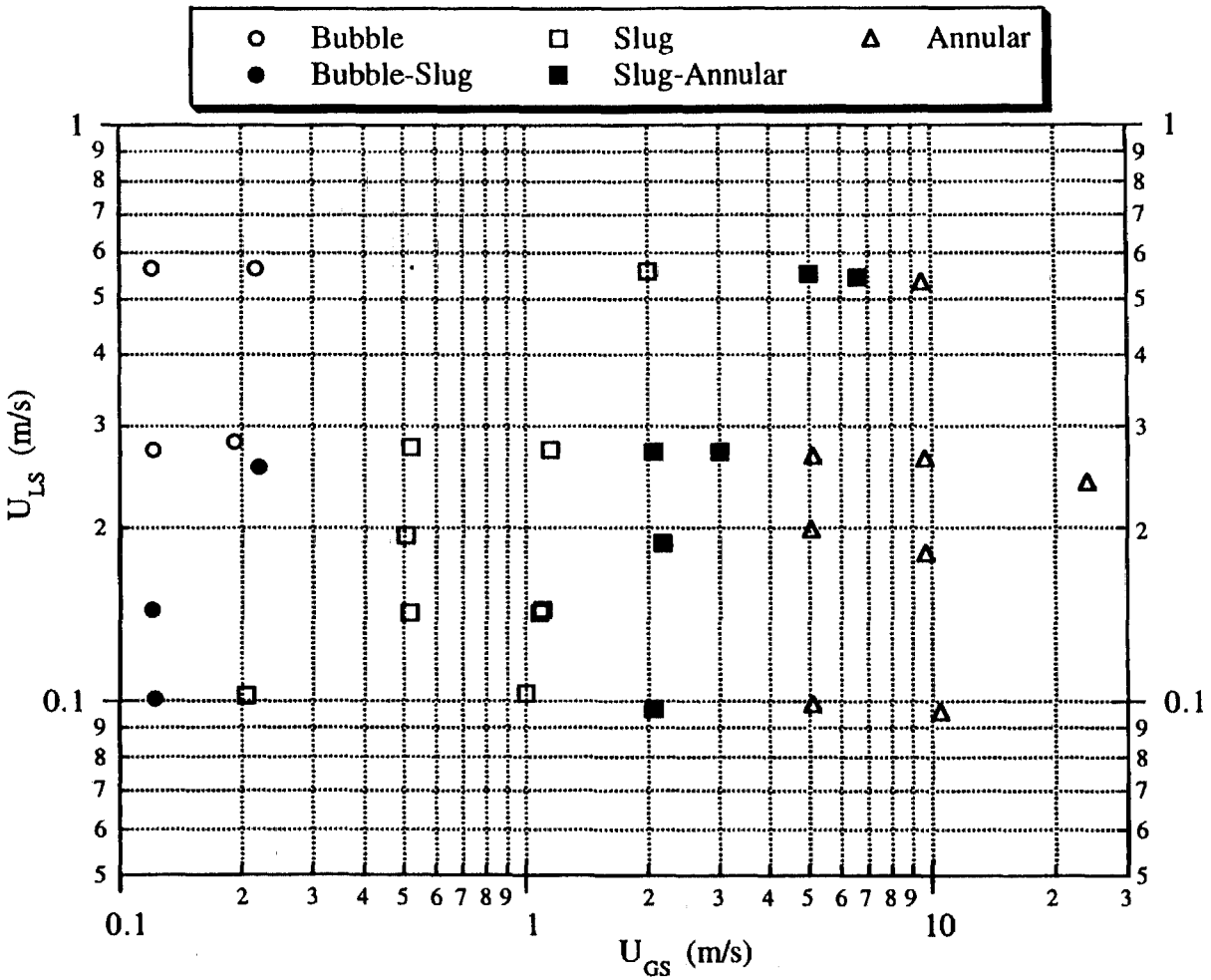

Figure 3.19 Microgravity Flow Pattern Map for Air-Water/Zonyl FSP in a 25.4 mm ID Tube

With the effect of tube diameter on the flow pattern maps established, the effect of the liquid physical properties can be assessed. The effect of liquid viscosity is shown by comparing Figure 3.14 to Figure 3.15 and Figure 3.17 to Figure 3.18. These maps show that a six-fold increase in the liquid viscosity produced no significant change in the location of either flow pattern transition on the flow maps indicating that liquid viscosity is not a major factor affecting flow pattern transitions. The effect of surface tension is shown by comparing Figure 3.14 to Figure 3.16 and Figure 3.17 to Figure 3.19. This comparison indicates that lowering the surface tension from 70 to 21 dyne/cm results in a shift in the bubble-slug transition to higher values of void fraction (higher values of U_{GS} at a given U_{LS}). This suggests that the surface tension plays a significant role in the bubble to slug flow transition mechanism.

With the microgravity flow pattern mapping results of this study established, it is useful to compare these to the maps available in previous works. The microgravity flow pattern map shown in Figure 3.14 is in good agreement with the limited data shown in the Dukler, 1988 and Janicot, 1988 maps, all for air-water in a 12.7 mm ID tube. Only a few data points were located near the transitions in the previous works but the maps show clearly defined regions of bubble, slug and annular flow which coincide with Figure 3.14. This result is to be expected since similar experimental apparatus and techniques were used to generate all three maps.

The transition between bubble and slug flow on the air-water microgravity flow pattern map of Colin, 1990, shown in Figure 3.4, compares well to the 25.4 mm ID flow pattern map, Figure 3.17, in the present study. As shown, the bubble-slug transition region is nearly the same for both maps for $U_{LS} < 0.8$ m/s. For $U_{LS} > 0.8$ m/s, the Colin, 1990 map shows a region containing both slug and bubble flows together. This phenomena was not observed in the 12.7 mm experiments for the same region of the flow pattern map and this region was not studied in the 25.7 mm experiments. While a shift in

the bubble-slug transition was noted when the tube diameter was increased from 12.7 mm to 25.4 mm in the present study, an additional shift is not seen when the tube diameter is increased to 40 mm in the Colin, 1990 results. This may indicate a nonlinear effect of tube diameter on the transition or a difference between experimenters and apparatus.

The results of Huckerby and Rezkallah, 1992 for air-water in a 9.525 mm ID tube, shown in Figure 3.5, show fair agreement with the results for the 12.7 mm ID tube in Figure 3.14. As shown, for $U_{LS} < 1.0$ m/s the bubble-slug transition region is similar in both studies, however the Huckerby and Rezkallah map shows the bubble-slug transition region to be nearly independent of U_{GS} while the present study does not confirm this. The slug-annular transition region occupies essentially the same region on both flow maps although the Huckerby and Rezkallah map contains some data points listed as slug flow in the transition region. This overlapping of flow pattern regions has never been observed in the present study and might be due to difficulties in flow pattern identification in the Huckerby and Rezkallah study.

The Zhao and Rezkallah, 1993 study for air-water in a 9.525 mm ID tube, shown in Figure 3.6, shows the bubble-slug transition region to be significantly different from both the Huckerby and Rezkallah, 1992 study using the same apparatus and the present study in the 12.7 mm ID tube. The map in Figure 3.6 shows bubble flow only for $U_{LS} > 2$ m/s. As shown in Figure 3.14, bubble flows were observed at much lower superficial liquid velocities in the present study. The photos of bubble flow in Zhao and Rezkallah, 1993 show irregularly shaped bubbles (perhaps due to the high liquid velocity) while most of the bubbles in the present study were essentially spherical. The large discrepancy in the location of the bubble-slug transition region between the Zhao and Rezkallah map and the map in the present study as well as that in Huckerby and Rezkallah, 1992 is unexplained. The slug-annular transition region reported in Zhao and Rezkallah, 1993 is in good agreement with results in Figure 3.14 for the present study. The transition region in the

Zhao and Rezkallah map extends to larger values of U_{GS} but this is likely due to the subjective nature of flow pattern identification in this region of the flow map.

Comparing the microgravity flow pattern maps for Chen et al. (R114 in a 15.8 mm ID tube) in Figure 3.1 and Reinarts (R12 in a 10.5 mm ID tube) in Figures 3.8 with the map in Figure 3.14 (air-water in a 12.7 mm ID tube) shows a large difference in the location of the slug-annular transition between the two fluid systems. While the Chen et al. map contains only a few points, the slug-annular transition shown in Figure 3.1 is in reasonable agreement with the 10.5 mm results of Reinarts (the physical properties of R12 and R114 are very similar). Both show a slug-annular transition region which is shifted to much lower values of U_{GS} as compared to the air-water results. This is most likely due to the large difference in vapor density between air and the R12 and R114 refrigerants. The density of the R12 vapor at the conditions used in the Reinarts study is about 30 times that of air while the R12 liquid is only about 1.3 times as dense as water. The gas phase therefore possesses considerably more momentum relative to the liquid phase in the R12 system than in the air-water system. This may lead to rupture of the liquid slugs to form annular flow at much lower values of U_{GS}. The bubble-slug transition on the Reinarts 10.5 mm flow map for R12 is also shifted to much lower values of U_{GS} with bubble flow being observed only at very low void fraction.

While the variation in fluid physical properties (liquid viscosity and surface tension) tested in the present study had a relatively small effect on the flow pattern maps, the differences in physical properties (primarily vapor density) between R12 and air-water produced much greater changes. The tube diameter was also shown to have a relatively small effect on the flow pattern transitions. These observations may lead to the development and refinement of transition mechanisms. This will be explored in greater detail when the flow pattern transition models are developed in Chapter 6.

Chapter 4 Properties of Microgravity Bubble and Slug Flows

4.1 Introduction

While many multiphase heat transfer systems are designed to operate in the annular flow regime, bubble and slug flows are still expected to occur in space operations. Partial vaporization of liquids such as in cryogenic transfer lines or in heat transfer equipment will generate bubble and slug flows in at least part of the system. Heat removal from annular flows in radiators and condensers will lead to a transition to slug and then bubble flow as the two-phase system is condensed to a single-phase liquid.

Several of the bubble and slug flow measurements made during the course of this study could be of interest to the designers and operators of microgravity two-phase flow systems. Knowledge of the void fraction in the system as a function of measurable parameters is necessary for good heat transfer design. An understanding of the pressure drop is required for hydrodynamic design. Vibration aboard spacecraft is also a concern, so measurements of the propagation velocities of bubbles and slugs are also useful. In addition to providing design data, bubble and slug flow measurements may be useful in gaining a better mechanistic understanding of these flows and for verification of flow simulations. All microgravity bubble and slug flow measurements taken in this study are included in Appendix D.

4.2 Void Fraction Modeling and Experimental Results

Over several decades of two-phase flow research in normal gravity, the simple but highly accurate Drift-Flux model has been developed to predict both the void fraction and bubble propagation velocity in bubble and slug flows. The model is more effective for

vertical flows than horizontal or inclined flows in normal gravity because vertical flows are axisymmetric. It is therefore logical to test the validity of this model for microgravity bubble and slug flows, which are also axisymmetric.

Void fraction prediction from the Drift-Flux model is described by Zuber and Findlay, 1965. Measurements of void fraction, including those from the parallel wire conductance probes used in this study, usually represent an average over the tube cross-section rather than a radially local value. Thus in order to develop a model with inputs which can be readily measured, it is important to derive the model in terms of cross-sectional average quantities defined as

$$\langle F \rangle = \frac{1}{A} \int_A F dA \ , \tag{4.1}$$

where F is any local quantity varying with radial position and A is the cross sectional area of the test section.

The average superficial velocities of the gas and liquid can be related to the cross-sectional average gas and liquid velocities, $\langle U_G \rangle$ and $\langle U_L \rangle$, and the cross-sectional average void fraction, $\langle \alpha \rangle$, by

$$U_{GS} = \langle \alpha \rangle \langle U_G \rangle \tag{4.2}$$

and

$$U_{LS} = (1-\langle \alpha \rangle) \langle U_L \rangle \ , \tag{4.3}$$

while the total is defined as

$$U_{MS} = U_{GS} + U_{LS} \ . \tag{4.4}$$

The quantity U_M is defined as the local volumetric flux of liquid plus gas at any radial position while U_{MS} is the cross sectional average.

From a mass balance, the average gas velocity can be expressed as the sum of a flux term and a drift term,

$$<U_G> = \frac{<\alpha\, U_M>}{<\alpha>} + \frac{<\alpha\, U_o>}{<\alpha>}\,, \tag{4.5}$$

where $<U_o>$ is the average net drift velocity of the gas with respect to $<U_M>$. This drift should not be significant in microgravity due to the lack of buoyancy between the liquid and gas. Observations of the movie films of bubble and slug flows confirm that the drift velocity between the phases is negligible in the microgravity experiments and the drift term in (4.5) can be neglected.

To account for the non-uniform distribution of the void fraction over the cross section, Zuber and Findlay, 1965 defined the distribution coefficient C_o as

$$C_o = \frac{<\alpha\, U_M>}{<\alpha>\, U_{MS}}\,. \tag{4.6}$$

By combining (4.2), (4.5) and (4.6), the relationship between the void fraction and the superficial velocities is obtained,

$$\frac{U_{GS}}{U_{MS}} = C_o <\alpha>\,. \tag{4.7}$$

Once C_o is known, this relationship provides a model for predicting the cross sectional average void fraction from the gas and liquid superficial velocities.

Zuber and Findlay, 1965 derived a model to predict C_o from the distribution of void fraction and velocity across the tube cross-section. Although this model does not yield a definitive value of C_o, it does offer theoretical guidance.

The distributions of velocity and void fraction over the cross-section are assumed to be of the form,

$$\frac{U}{U_c} = 1 - \left[\frac{r}{R}\right]^m \tag{4.8}$$

and

$$\frac{\alpha - \alpha_w}{\alpha_c - \alpha_w} = 1 - \left[\frac{r}{R}\right]^n , \tag{4.9}$$

where c and w refer to the centerline and wall, respectively. This is reasonable only for axisymmetric flows. If these expressions are substituted into (4.6) and integrated over the cross-section as indicated by (4.6), the following expression for C_o is obtained,

$$C_o = \frac{m+2}{m+n+2}\left[1 + \left[\frac{n}{m+2}\right]\left[\frac{n+2}{n+2\left[\frac{\alpha_w}{\alpha_c}\right]}\right]\right] . \tag{4.10}$$

Values of C_o computed from (4.10) for (α_w/α_c) ranging from zero to one assuming several values of m and n are shown in Figure 4.1. Steep gradients of velocity or void fraction occur when m and n are equal to one while nearly flat profiles are obtained by setting m or n to seven. The proper value of (α_w/α_c) for slug flows should be zero because the movie films and film thickness measurements indicate that there is a continuous gas-free film on the tube wall in slug flow. The value of (α_w/α_c) for bubble flow is nearly zero as well. The movie films show that the bubble density is nearly zero along the tube surface although occasional bubbles rolling along the surface have been observed. Assuming that (α_w/α_c) is zero, Figure 4.1 shows that the range of C_o values should be $1.13 < C_o < 1.5$ with the steeper gradients producing the larger values of C_o. Predictions of C_o made from propagation velocity arguments will be presented in the next section.

To test the Drift-Flux void fraction model (4.7), the mean void fraction of the microgravity bubble and slug flow experiments was plotted against U_{GS}/U_M in Figures 4.2, 4.3 and 4.4 for air-water, air-water/glycerin and air-water/Zonyl FSP, respectively. Good void fraction measurements were not obtained for all of the bubble and slug flow runs shown in the 12.7 mm ID test section flow maps so only those runs in which a

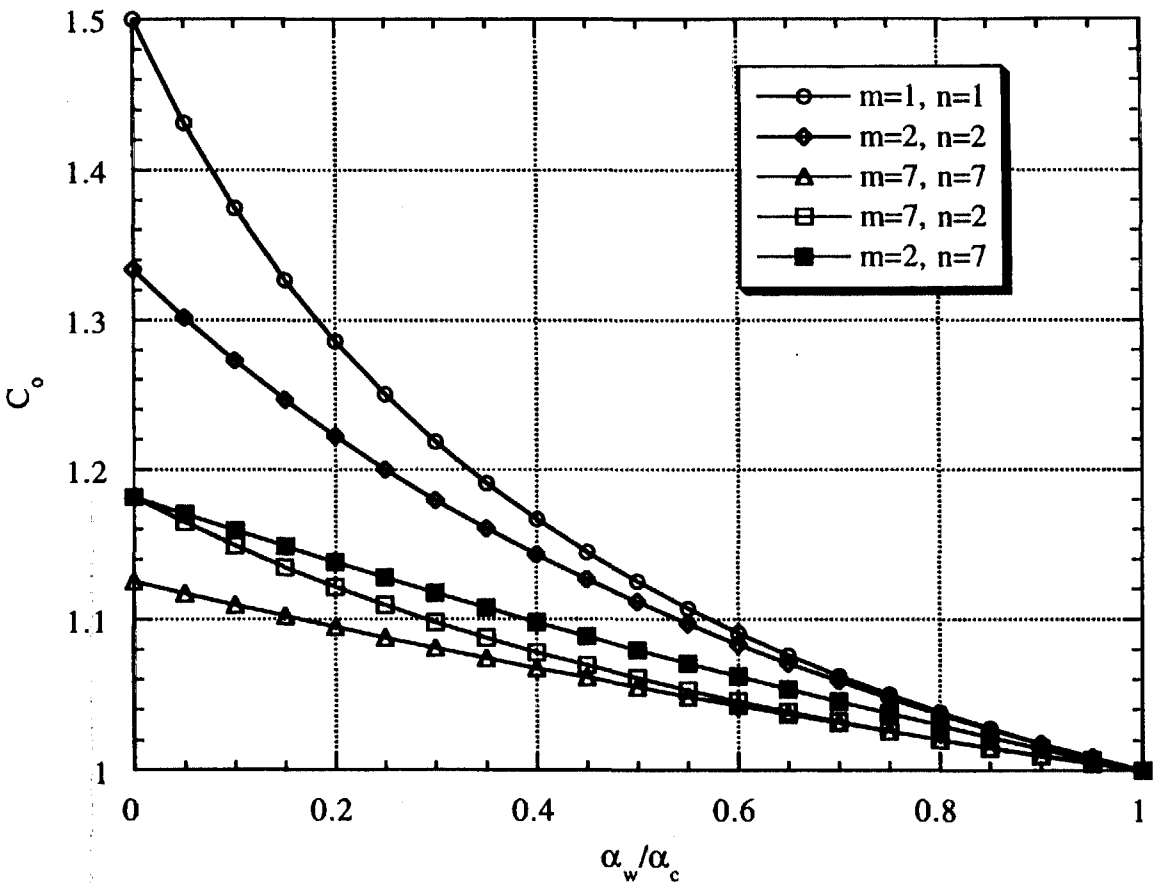

Figure 4.1 Prediction of C_o from the Drift-Flux Model of Zuber and Findlay, 1965

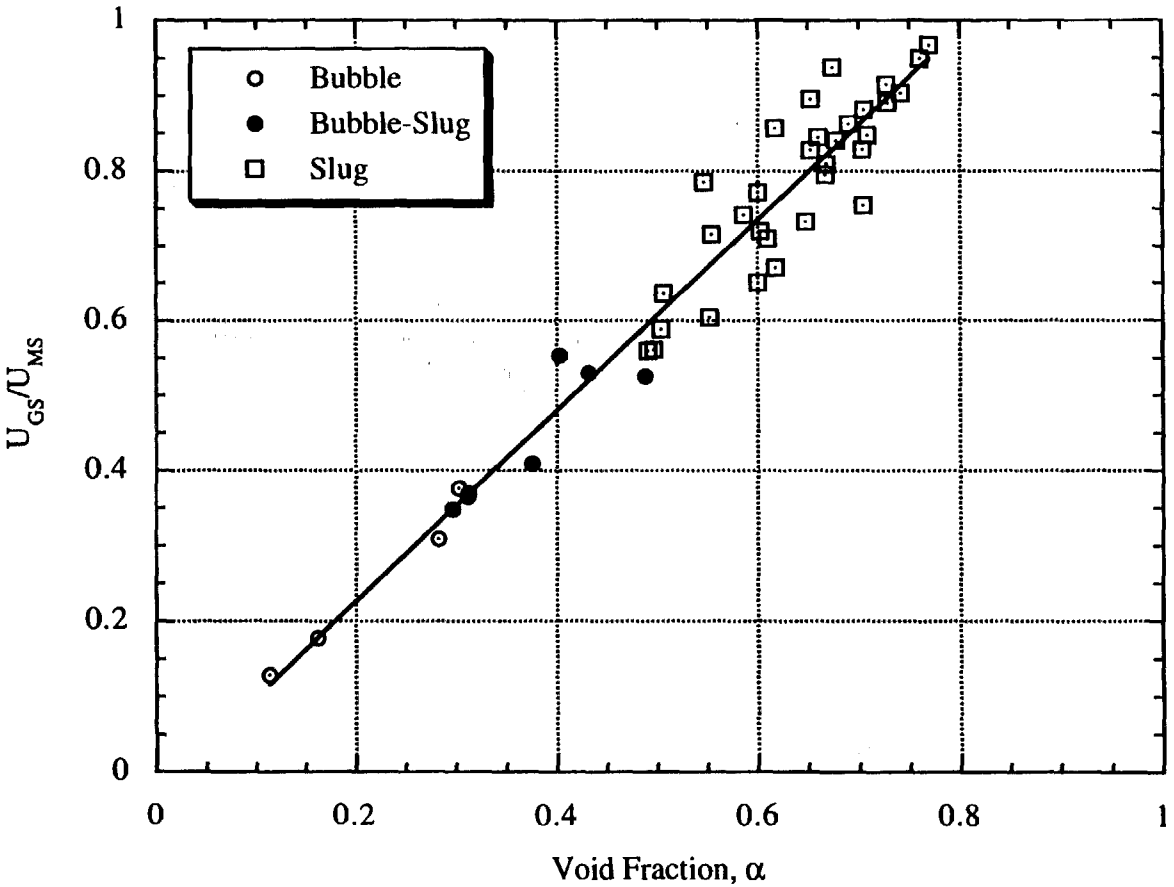

Figure 4.2 Relationship Between U_{GS}/U_{MS} and Void Fraction for Air-Water in a 12.7 mm ID Tube in Microgravity

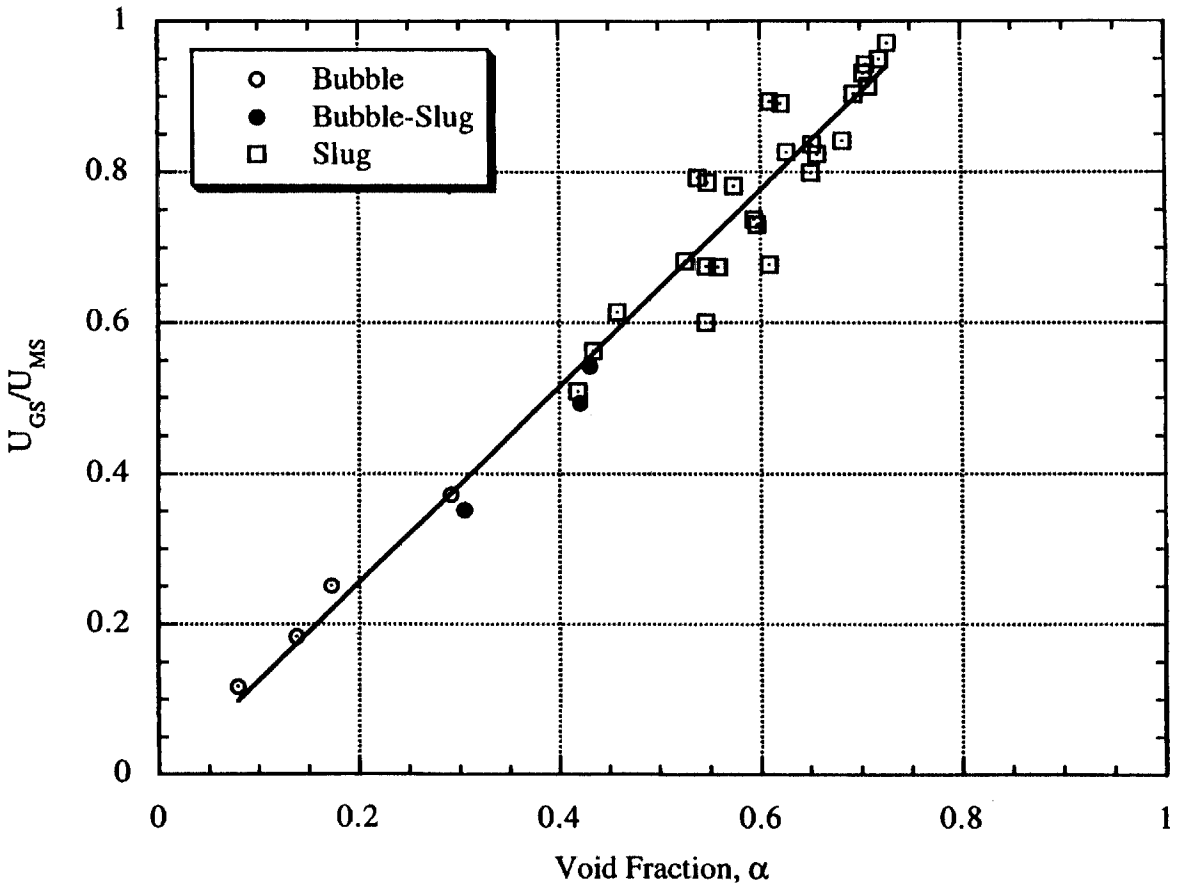

Figure 4.3 Relationship Between U_{GS}/U_{MS} and Void Fraction for Air-Water/Glycerin in a 12.7 mm ID Tube in Microgravity

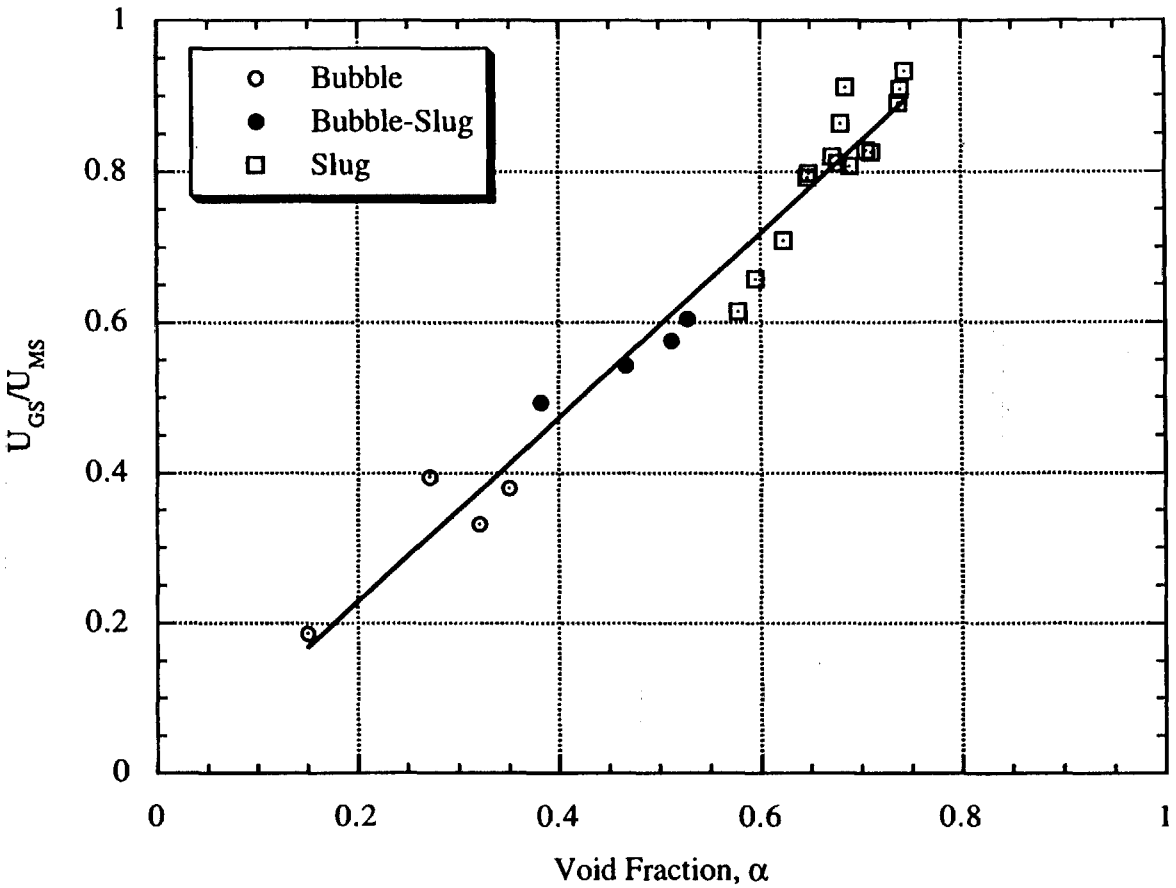

Figure 4.4 Relationship Between U_{GS}/U_{MS} and Void Fraction for Air-Water/Zonyl in a 12.7 mm ID Tube in Microgravity

stationary average void fraction could be obtained were included in Figures 4.2, 4.3 and 4.4. As shown, in all cases the results indicate a linear trend as predicted by (4.7) although there is considerable scatter in the slug flow results. The value of C_o is obtained by determining the best fit slope of this trend using linear regression. The slopes yielded C_o values of 1.27, 1.30 and 1.22 for air-water, air-water/glycerin and air-water/Zonyl FSP, respectively. The fact that $C_o > 1$ in the figures indicates that both the velocity and void fraction are greater towards the center of the tube, as expected. Using the profiles in Figure 4.1, the values of C_o suggest that the velocity and void fraction distributions lie between the nearly flat and steeply linear cases.

The error in determining C_o from Figures 4.2, 4.3 and 4.4 could be considerable since the slopes of these trends can be substantially influenced by the scatter in the slug flow data. The scatter in the slug flow data could be due to a propagation of measurement uncertainties or to an insufficient sample period in which to obtain a stationary average. However, on average, the Drift-Flux void fraction model (4.7) using the reported values of C_o does predict the measured void fraction to within ±5%. This will be discussed further in relation to the values of C_o determined from the propagation velocity.

4.3 Bubble Propagation Velocity Modeling and Experimental Results

Much of the Drift-Flux model development was related to predicting the propagation velocity of a bubble rising in a vertical or inclined tube of stagnant or flowing liquid. The relationship between bubble propagation velocity and superficial velocities is obtained from the void fraction model derived in the previous section by combining (4.2), (4.5) and (4.6) to yield

$$\langle U_G \rangle = C_o U_{MS} + U_o \, . \qquad (4.11)$$

Nicklin et al., 1962 determined (4.11) empirically and found that for vertical flow in the range of $8000 < Re < 50000$, $C_o = 1.2$. These authors further noted that the value of C_o closely resembled the ratio of centerline to average velocity for a turbulent profile modeled with the one seventh law profile ($U_c/\overline{U} = 1.22$).

The distribution coefficient was investigated analytically by Collins et al., 1978. The flow field in the liquid around a rising Taylor bubble was obtained with a perturbation solution. When the liquid ahead of the bubble was turbulent, the results confirmed the speculation of Nicklin et al., 1962 that $C_o = U_c/\overline{U} = 1.22$. The analysis also predicted that $C_o = 2.27$ when the liquid ahead of the bubble was laminar.

In an experimental study of bubbles rising in a flowing liquid, Bendiksen, 1984 reported that the value of C_o was independent of Re for $Re > 3000$ but did vary with the Froude number, $Fr = U_{LS}/\sqrt{gD}$. For $Fr < 3.5$, C_o increased monotonically from 1.0 to 1.2 as the angle of inclination varied from 0° (horizontal) to 90° (vertical). For $Fr > 3.5$, $C_o = 1.2 \pm 0.1$ for all angles of inclination. For microgravity two-phase flows, $Fr >> 3.5$, and thus the results of Bendiksen, 1984 would suggest that $C_o = 1.2$ for turbulent bubble and slug flows in microgravity.

Dukler et al., 1988 reported that $C_o = 1.0 - 1.5$ for microgravity bubble and slug flows. This range of values came from a void matching bubble-slug transition model (to be discussed in Chapter 6). A value of $C_o = 1.22$ was then speculated to be correct because this provided a good fit for the bubble-slug transition model proposed in the study. Colin, 1990 reported a value of $C_o = 1.2$, derived from velocity measurements as suggested by (4.11), for microgravity bubble and slug flow in a 40 mm ID tube. A plot of $\langle U_G \rangle$ vs U_{MS} in Colin, 1990 shows that the data cluster closely about a line of slope 1.2 for $U_{MS} \leq 1.6$ m/s but deviate from this line for $U_{MS} > 1.6$ m/s.

Velocity data from the 12.7 mm ID test section experiments were used to test (4.11) by plotting the bubble propagation velocity, as determined by cross correlation of the film thickness and void fraction signals, against U_{MS}. These plots are shown for air-water, air-water/glycerin and air-water/Zonyl in Figures 4.5, 4.6 and 4.7, respectively. As shown, in all three cases the data show a highly linear trend. The distribution coefficients computed from linear regression of the data, are 1.21, 1.48 and 1.27 for air-water, air-water/glycerin and air-water/Zonyl, respectively. The slope of the line in Figure 4.7 for air-water/Zonyl is heavily influenced by three points which lie at values far beyond the main data cluster. The slope of the line computed without these three points (for $U_{MS} < 2$ m/s) is 1.21, which is thought to be a more reliable value of the distribution coefficient for air-water/Zonyl.

The results for the microgravity air-water and air-water/Zonyl systems are in excellent agreement with the turbulent vertical flow results reviewed previously. If the liquid Reynolds number is computed as

$$Re_L = \frac{D\, U_{MS}}{\nu_L}, \tag{4.12}$$

which is the same definition used to establish the turbulent flow value of C_o in the previously mentioned studies, then all of the air-water and air-water/Zonyl data are in the fully turbulent region ($Re_L > 4000$). Therefore the Drift-Flux model with a value of $C_o = 1.2$ is confirmed for turbulent microgravity bubble and slug flows.

The value of the distribution coefficient computed from the air-water/glycerin experiments was considerably higher than the accepted value for turbulent flow. Based on the Reynolds number criteria of (4.12), most of the data points shown in Figure 4.6 lie in the laminar ($Re_L < 2000$) or laminar-turbulent transition region ($Re_L < 4000$). These regions are shown in Figure 4.6. The analytical results of Collins et al., 1978 indicated

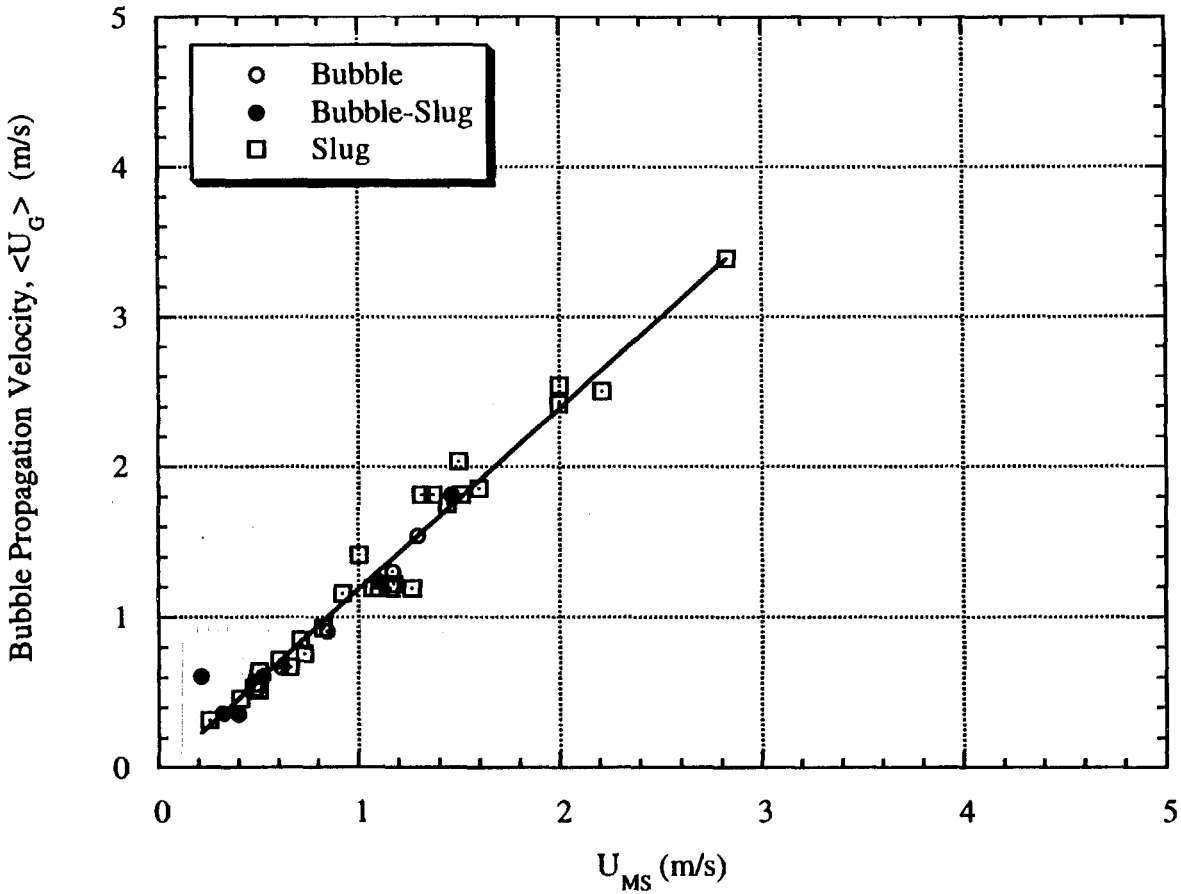

Figure 4.5 Relationship Between $\langle U_G \rangle$ and U_{MS} for Air-Water in a 12.7 mm ID Tube in Microgravity

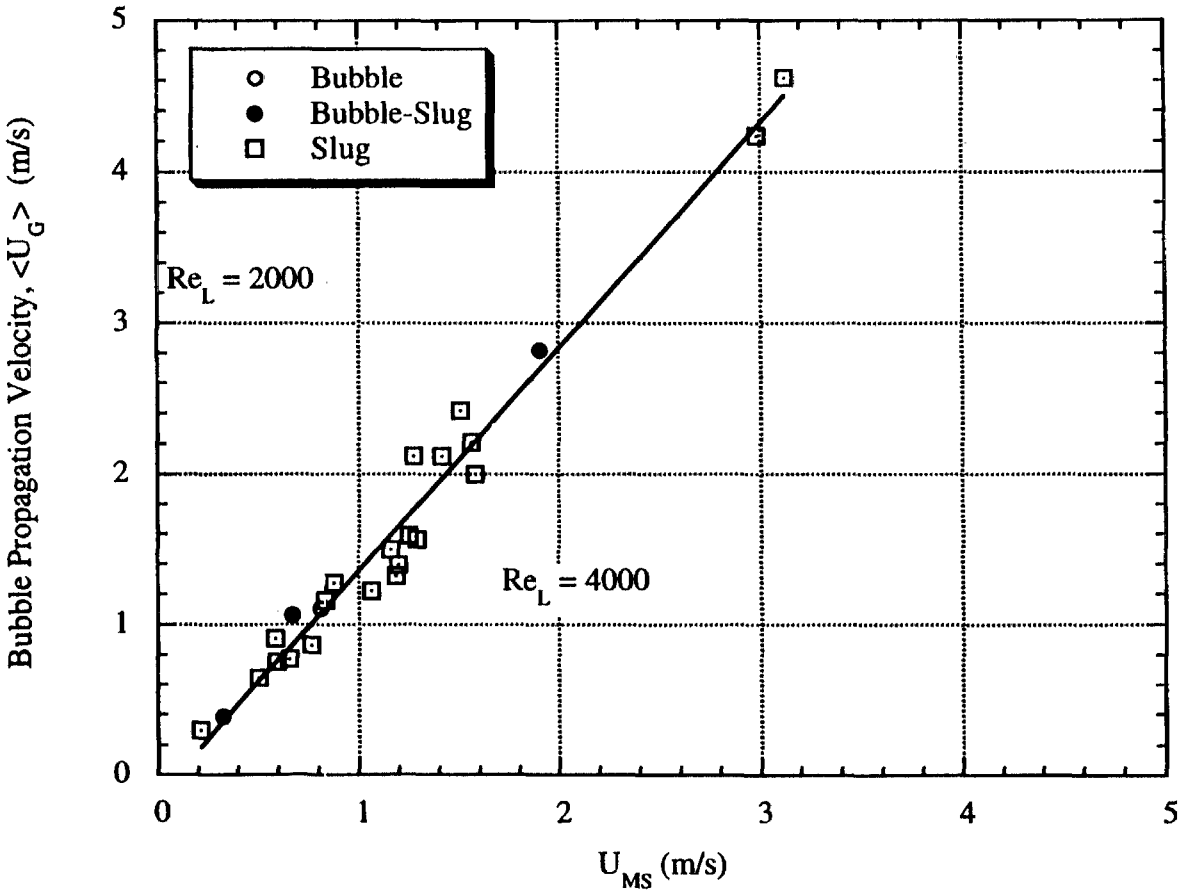

Figure 4.6 Relationship Between $\langle U_G \rangle$ and U_{MS} for Air-Water/Glycerin in a 12.7 mm ID Tube in Microgravity

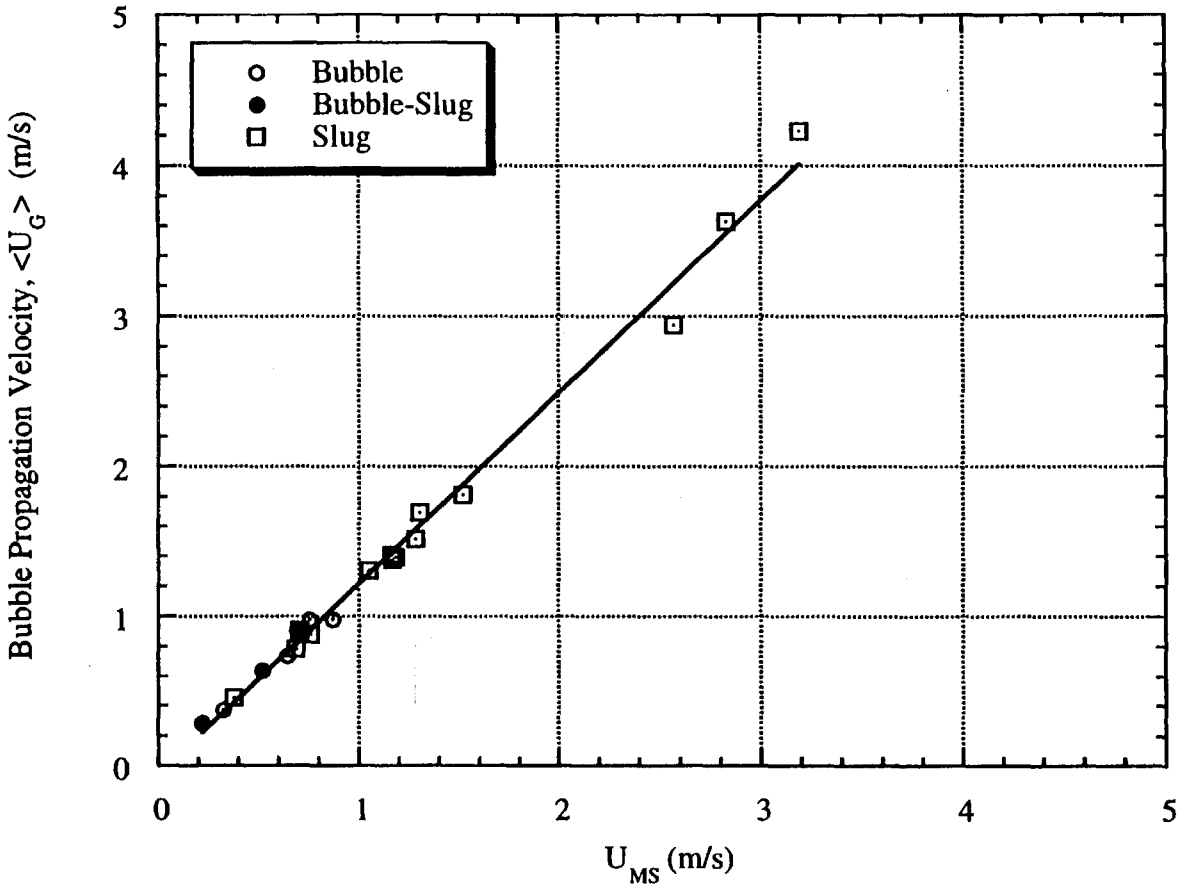

Figure 4.7 Relationship Between $<U_G>$ and U_{MS} for Air-Water/Zonyl FSP in a 12.7 mm ID Tube in Microgravity

that the value of C_o should be much higher for laminar flow (C_o = 2.23) and this may partially explain the higher value of C_o for the air-water/glycerin system.

As shown in Figures 4.5, 4.6 and 4.7, there is considerably less scatter in the velocity results as compared to the void fraction results of Figures 4.2, 4.3 and 4.4. This is attributed to greater experimental error in the results used to construct the void fraction plots. This would suggest that velocity measurements are the preferred method for the determination of the distribution coefficient (at least for the apparatus used for this study) and that the values of C_o obtained from the velocity measurements are more reliable.

Establishing the validity of the Drift-Flux model for microgravity bubble and slug flows provides simple yet accurate models to predict the void fraction and bubble propagation velocity from the flow rates of the gas and liquid phases. These results also generalize the model to include all axisymmetric flows, in both normal gravity and microgravity. It should be noted however that the results of the Drift-Flux model for microgravity will be different from those in normal gravity because of the negligible drift velocity in microgravity flows.

4.4 Pressure Drop Modeling and Experimental Results

Traditionally, physically-based pressure drop modeling of two-phase flows has incorporated two approaches: homogeneous models and separated flow models (Wallis, 1969, Hewitt and Hall-Taylor, 1970). Homogeneous models treat the two-phase mixture as a single fluid having physical properties related to the proportions of liquid and gas in the system. Separated flow models assume that each phase flows through a channel proportional to the area of the pipe occupied by that phase and then combines the effects of each to determine the total pressure drop. The success of these approaches is highly dependent upon the flow regime. Homogeneous models are more successful when one

phase is continuous while the other is dispersed, such as in bubble flow. Separated flow models tend to be more successful when both phases are continuous and separated such as in annular flow. Slug flow approaches the homogeneous case at low void fraction when the Taylor bubbles are small, but more closely approximates a separated flow at higher void fraction when the Taylor bubbles are very long. Despite the promise of these models, large errors are not uncommon when modeling two-phase flow pressure drops (Wallis, 1969).

The homogeneous pressure drop model is developed by considering the two-phase mixture to be a single, homogeneous fluid. The Fanning equation for single phase pressure drop, using physical properties of the mixture, becomes

$$\frac{dP}{dx} = \frac{2\, f_{TP}\, \rho_M\, U_{MS}^2}{D}\,, \tag{4.13}$$

where f_{TP} is the two-phase friction factor, to be determined, and ρ_M is the mixture density given by

$$\rho_M = <\alpha> \rho_G + (1-<\alpha>)\, \rho_L\,. \tag{4.14}$$

The Reynolds number for the mixture is defined as

$$Re_{TP} = \frac{D\, \rho_M\, U_{MS}}{\mu_L}\,. \tag{4.15}$$

The viscosity of the liquid, μ_L, is used rather than that of the mixture because the wall region of bubble and slug flows is mostly gas free. The two-phase friction factor is then computed using the Blasius relation,

$$f_{TP} = \frac{C}{Re_{TP}^n}\,, \tag{4.16}$$

where C = 16 and n = 1 for laminar flow and C = 0.046 and n = 0.2 for turbulent flow.

While this approach has been shown to provide reasonable results for 1g bubble flows (Wallis, 1969), only two studies other than the present one have evaluated this model for microgravity two-phase flows. Lambert, 1990 evaluated this model and variants of it, as well as separated flow models, for microgravity flows of Freon R-12 in an 8.7 mm ID tube. The model shows fair agreement with measured pressure drop for bubble-slug and slug flow when the measurements are corrected for nonzero axial accelerations of the aircraft. Some error was introduced when the void fraction was calculated from the superficial velocities of vapor and liquid (implicitly assuming that $C_0 = 1$). Unfortunately, the mixture Reynolds number (or the data needed to compute it) was not reported in Lambert's study. Lambert's study also concluded that the bubble and slug flow pressure drops were essentially identical for microgravity and normal gravity.

Colin, 1990, compared the homogeneous model to microgravity bubble flow measurements made in a 40 mm ID tube for $Re_{TP} > 10000$. Measured void fractions were used in the model. The model showed excellent agreement with the measured pressure drop in nearly all cases, confirming the validity of the homogeneous model for fully turbulent microgravity bubble flows.

Because tube roughness, misaligned flanges and other imperfections can cause deviations in pressure drop from the Blasius model, the test section pressure drop was verified for single phase water and water-glycerin flows in normal gravity using the same apparatus as in the microgravity experiments. As shown in Figure 4.8, the agreement between the model and the measured pressure drop is excellent for the water-glycerin solution for $400 < Re < 6000$. Even the laminar-turbulent transition, traditionally a troublesome region, behaves in accordance with the Blasius model for water-glycerin. The results in Figure 4.8 for water demonstrate the behavior usually observed in single phase pipe flow. As shown, in the laminar-turbulent transition region there is considerable discrepancy between the measurements and the Blasius model predictions, while the

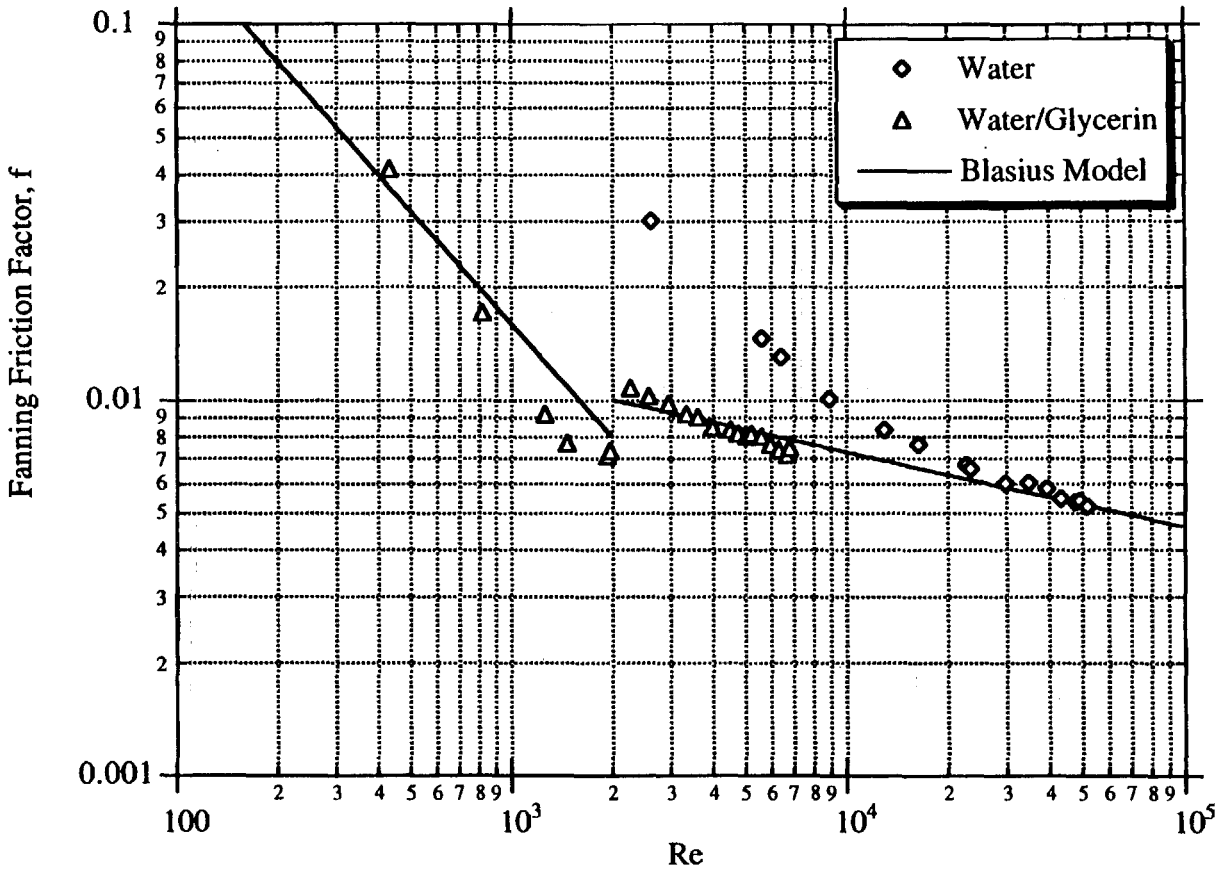

Figure 4.8 Single-Phase Friction Factor Verification of the 12.7 mm ID Test Section

discrepancy disappears for Re >30000. This is likely due to perturbations in the flow which were not completely damped for the water experiments in Figure 4.8. This indicates that the Blasius model can be expected to accurately predict the pressure drop for fully laminar and fully turbulent flows while large errors may be incurred in the transition region.

The two-phase friction factors calculated for the valid microgravity bubble and bubble-slug flow experiments are shown in Figure 4.9. Many of the bubble and slug flow experiments shown in the previous flow pattern maps were taken prior to correcting problems with the pressure measurement system and are not included in the pressure drop analysis. As shown, in all cases, the homogeneous model significantly underpredicted the measured pressure drops with the greatest deviation occurring in the laminar-turbulent transition region. The data do appear to have the same trends as the model however. The same analysis was made for the valid slug flow experiments as shown in Figure 4.10. This figure shows a large amount of scatter in the results for all three liquids tested and a significant discrepancy between the homogeneous models and the experiments.

The discrepancies between the homogeneous model and the experimental measurements shown in Figure 4.9 and 4.10 may be attributed to several factors. Unfortunately, for the tube diameter tested and the flow rates available in the test rig, many of the values of Re_{TP} lie in the laminar-turbulent transition region. This is a difficult region in which to take measurements due to the instability in the flow. In Figures 4.9 and 4.10, the discrepancy between the model and the experiments is considerably reduced for the few runs in which $Re_{TP} > 10000$ and in this higher Reynolds number region, results comparable to those of Colin, 1990 were obtained. Hydraulic limitations in the liquid flow system prevented a more complete investigation of the fully turbulent region within the time constraints of this study.

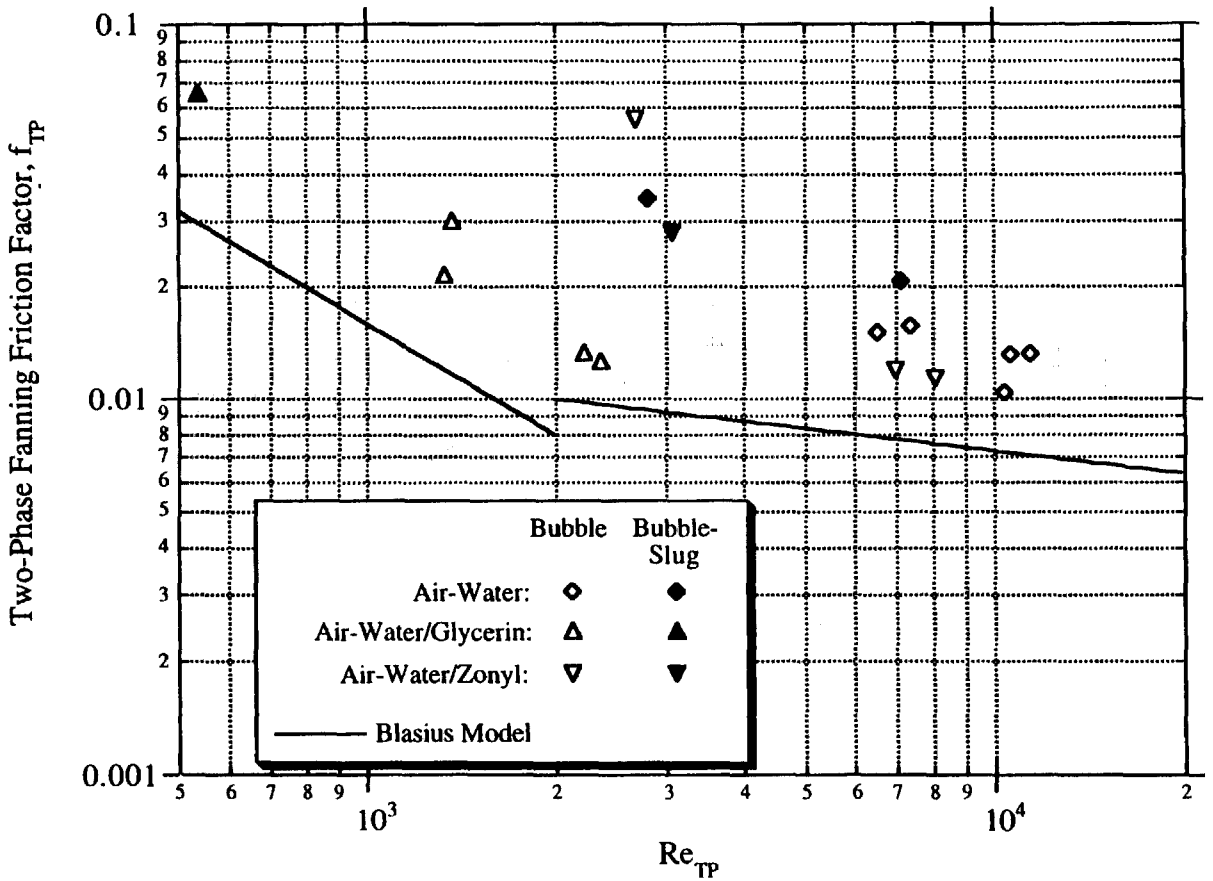

Figure 4.9 Two-Phase Homogeneous Friction Factor for Microgravity Bubble Flow in a 12.7 mm ID Tube

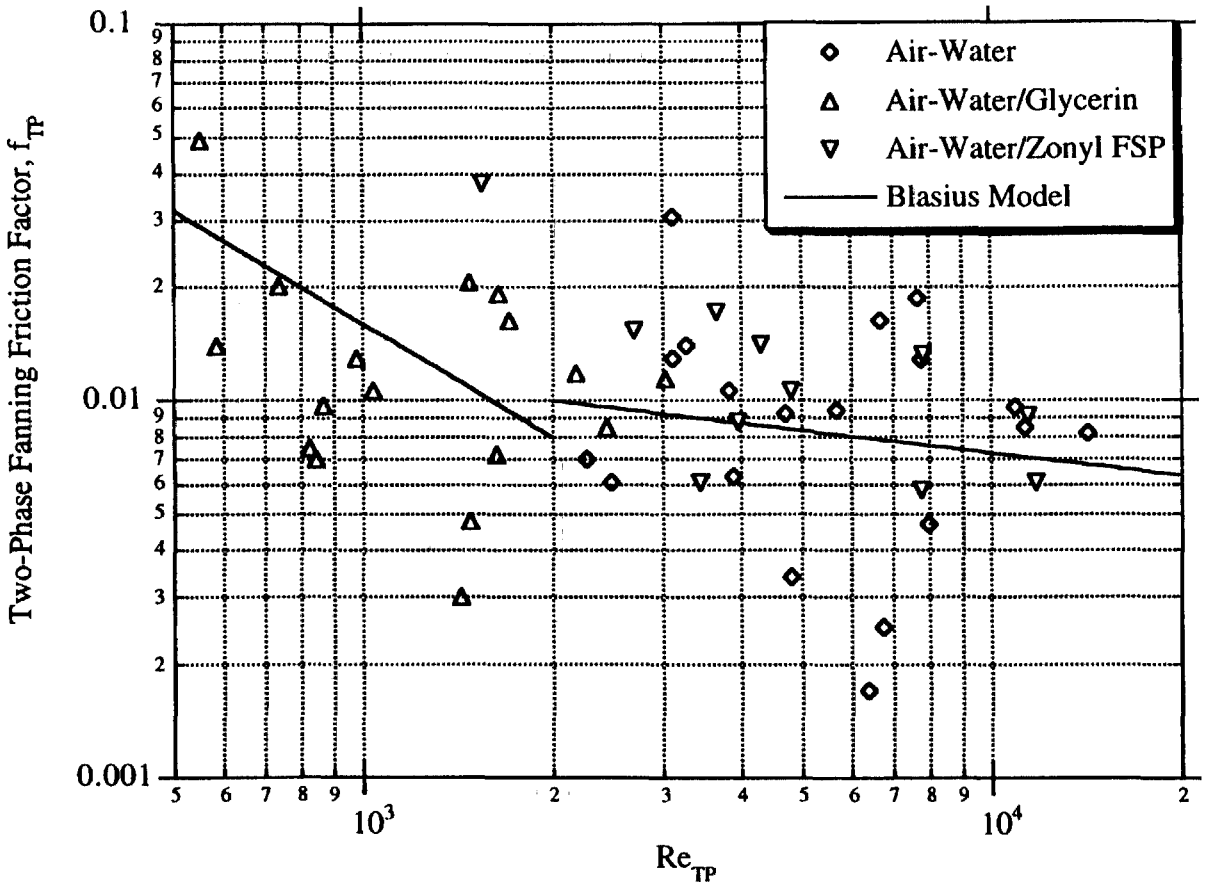

Figure 4.10 Two-Phase Homogeneous Friction Factor for Microgravity Slug Flow in a 12.7 mm ID Tube

The short length of the test section used for these experiments, which was limited by the space constraints of the Learjet aircraft, may also have led to errors in the pressure drop measurements. The pressure drop in the bubble and slug flow experiments was sufficiently small for the experimental error to become significant. The estimated error of 0.03 psi in each transducer leads to errors as large as 40% for the lowest velocity experiments. The experimental error could be reduced by using a much longer test section, leading to a much greater pressure difference between transducers. The short test section length and short duration of the experiment also leads to concerns about the stationarity of the resulting signals. In the high void fraction slug flow runs, a single long Taylor bubble may occupy the majority of the test section for a significant portion of the run. Even though the pressure drop is averaged over the length of the run, the total number of measurements may be insufficient to obtain a stationary mean value. Unfortunately, longer duration runs require the use of the space shuttle, which was not available during this study.

Finally, the validity of the assumptions implicit in the homogeneous model must be considered. In bubble and slug flows, the gas phase is dispersed heterogeneously in the liquid and the assumption of a single-phase, homogeneous mixture is imperfect. The value of Re_{TP} represents an average condition while local regions of laminar, turbulent and transitional behavior may exist within the flow. As a result this model may be incapable of predicting the complex behavior associated with the transition region. The results of Colin, 1990 and the few higher Reynolds number experiments in the present study indicate however that the model is valid for the region in which $Re_{TP} > 10000$.

A separated flow model (Lockhart-Martinelli, 1949) was also applied to the slug flow data but this resulted in very poor agreement with the measured pressure drop and was therefore not included. Newer approaches including detailed simulation around

bubbles and slugs (Mao, 1988) may eventually yield better mechanistic models for pressure drop but these techniques are currently very difficult to use for design purposes.

The objective of these studies, and those that follow, is to determine when bubble and slug flow models developed in earth-gravity are suitable for use in microgravity and when new models must be developed. The results of this study indicate that the Drift-Flux model for void fraction and velocity developed for earth gravity is also suitable for microgravity when a zero drift velocity is used. The results of the pressure drop analysis in this study are inconclusive although Colin, 1990 indicates that the homogeneous two-phase friction factor model is suitable for turbulent microgravity bubble and slug flows. Further study is required to fully develop the understanding of microgravity bubble and slug flow pressure drop needed for design and operation.

Chapter 5 Properties of Microgravity Annular Flows

5.1 Introduction

The microgravity flow pattern maps shown in Figures 3.14 - 3.19 clearly show that the majority of the gas and liquid superficial velocity parameter space lies within the annular flow region of the maps. Many near term space applications such as two-phase spacecraft thermal management systems and two-phase power cycles will operate primarily in the annular flow regime. Annular flow is also the most prevalent flow pattern encountered in earth-based industrial applications such as natural gas wells and pipelines, boilers and evaporators.

Annular flow is characterized by the presence of an irregular, wavy gas-liquid interface. Across this interface, momentum, heat and mass transfer are greatly enhanced, in a complex way, due to the presence of the waves. Despite many years of research, the understanding of annular flows remains largely empirical (Dukler, 1977) and a more fundamental insight into the nature of the wavy interface is just beginning to emerge (Wasden, 1989). Due to the difficulties inherent in microgravity experimentation, the understanding of annular flow in microgravity is far worse yet, with the few studies available being limited to flow pattern identification and perhaps pressure drop. A basic qualitative understanding of the nature of microgravity annular flow as well as key measurements such as liquid film thickness, wave amplitude, velocity and frequency, pressure drop and wall shear stress are largely absent from the literature. Because of the lack of research on this important flow regime, much of the current study was focused on the annular flow pattern in microgravity. The microgravity annular flow measurements recorded in this study are included in Appendix E.

5.2 Qualitative Observations of Microgravity Annular Flows

While many high speed movie films of microgravity annular flows were recorded during the flow pattern mapping studies, these movie films did not provide sufficient clarity to permit an understanding of the physical nature of the flow. While the gas-liquid interface appeared to be axisymmetric in the mean sense, it appeared to be locally rough and irregular. The shape of the waves appeared to be in a continuous state of change but this was difficult to confirm photographically. The nature of the interface also appeared to vary with the changes in physical properties examined during these studies. Because these effects were difficult to resolve photographically, special test sections, described in detail in Chapter 2, were constructed in order to provide the measurements needed to better understand microgravity annular flow. These measurements allowed for a level of detail in the description of microgravity annular flows which does not currently exist in the literature.

The test section shown in Figure 2.28 allowed for measurement of the liquid film thickness simultaneously at four locations around the perimeter of the tube. A fifth probe was located 5 cm downstream with the same angular orientation as the first probe (on the bottom of the tube). A typical time series output from these probes is shown in Figure 5.1. The time lag between the first and fifth probes is approximately 0.02 s in this particular experiment. As shown by examining the traces from the first four probes in Figure 5.1, the gas-liquid interface is not axisymmetric in a local sense. The waves are not of uniform amplitude or shape around the perimeter. The mean film thicknesses of these traces are essentially equal though, confirming that microgravity annular flows are axisymmetric in the mean as would be expected. The traces in Figure 5.1 also show that the large waves are essentially ring-like in nature. Nearly all of the large waves shown at the bottom of the tube have counterparts at the other measurement points.

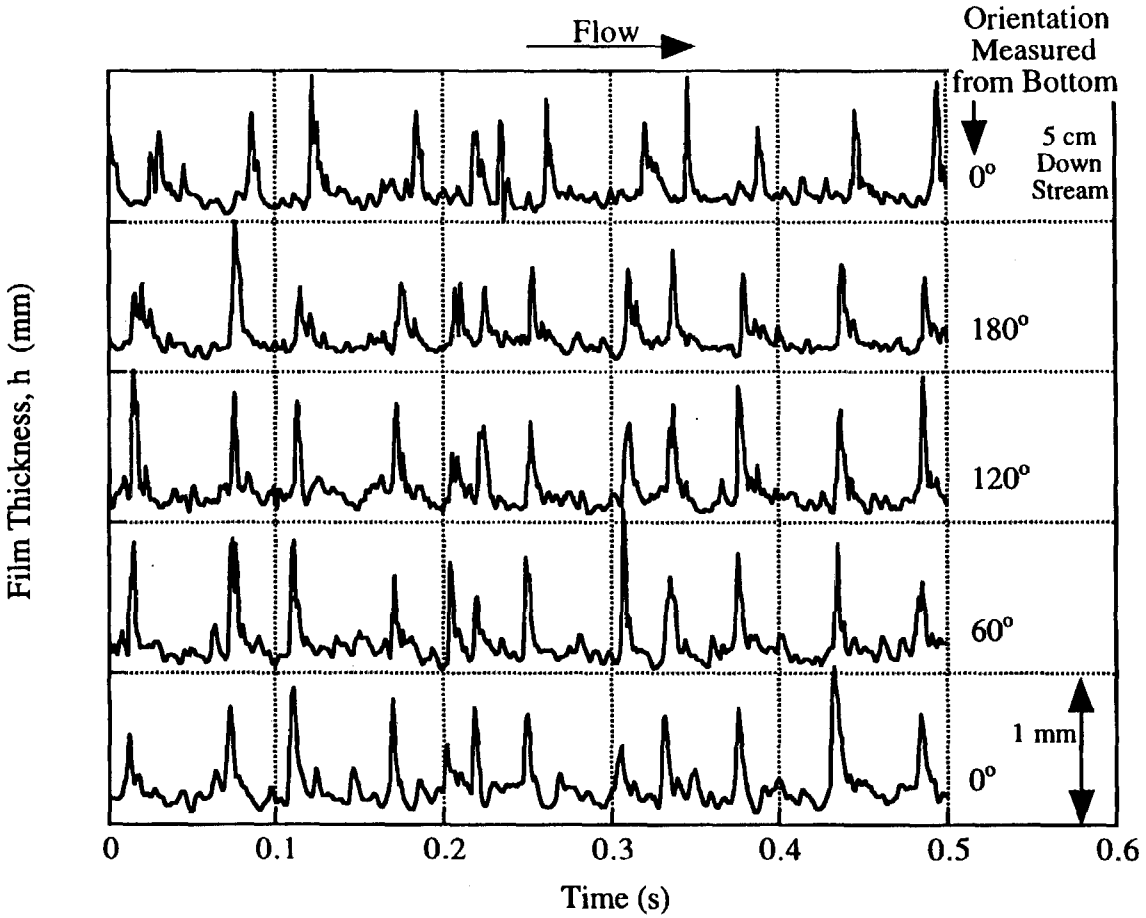

Figure 5.1 Circumferential Distribution of a Microgravity Annular Film in a 12.7 mm ID Tube

A comparison of the film thickness measurements shown in Figure 5.1 at the bottom of the tube shows that the shapes of the waves are changing as they move down the tube. This is expected since the gas-liquid interface is a deformable boundary which is being subjected to strong pressure and shearing forces. In several cases, wave splitting is observed in which a single wave measured at the upstream probe is observed to be breaking into two smaller waves at the downstream probe. An example of this can be seen in Figure 5.1 by comparing the first wave in the lower most time series with the first wave in the upper most time series. Wave splitting and joining is only possible if the two daughter waves have different celerities (axial propagation velocities). This behavior is also observed in soliton waves where the wave celerity is a function of the wave amplitude. In such systems, large amplitude waves overtake the smaller amplitude waves leading to joining and splitting phenomena.

Only a few experiments were performed with the five-probe test section shown in Figure 2.28 before the test section was damaged. Because the results obtained from the few experiments that were performed were sufficient to provide insight into the nature of microgravity annular flows, the decision was made to abandon this test section and proceed with other annular flow measurements rather than rebuild it. The test section shown in Figure 2.27 was then constructed specifically for annular flow measurements.

Another qualitative observation made during the course of the annular flow studies was the effect of the liquid physical properties on the nature of the gas-liquid interface. Figure 5.2 shows film thickness time series of microgravity annular flows made with air-water, air-water/glycerin and air-water/Zonyl FSP, all at the same superficial gas and liquid velocities. The effect of liquid viscosity is shown by comparing the air-water and air-water/glycerin results. These show that a higher viscosity liquid results in a thicker liquid film with larger amplitude waves. Enlargements of a few of the air-water and air-water/glycerin waves in Figure 5.2 are shown in Figure 5.3. While the space between the

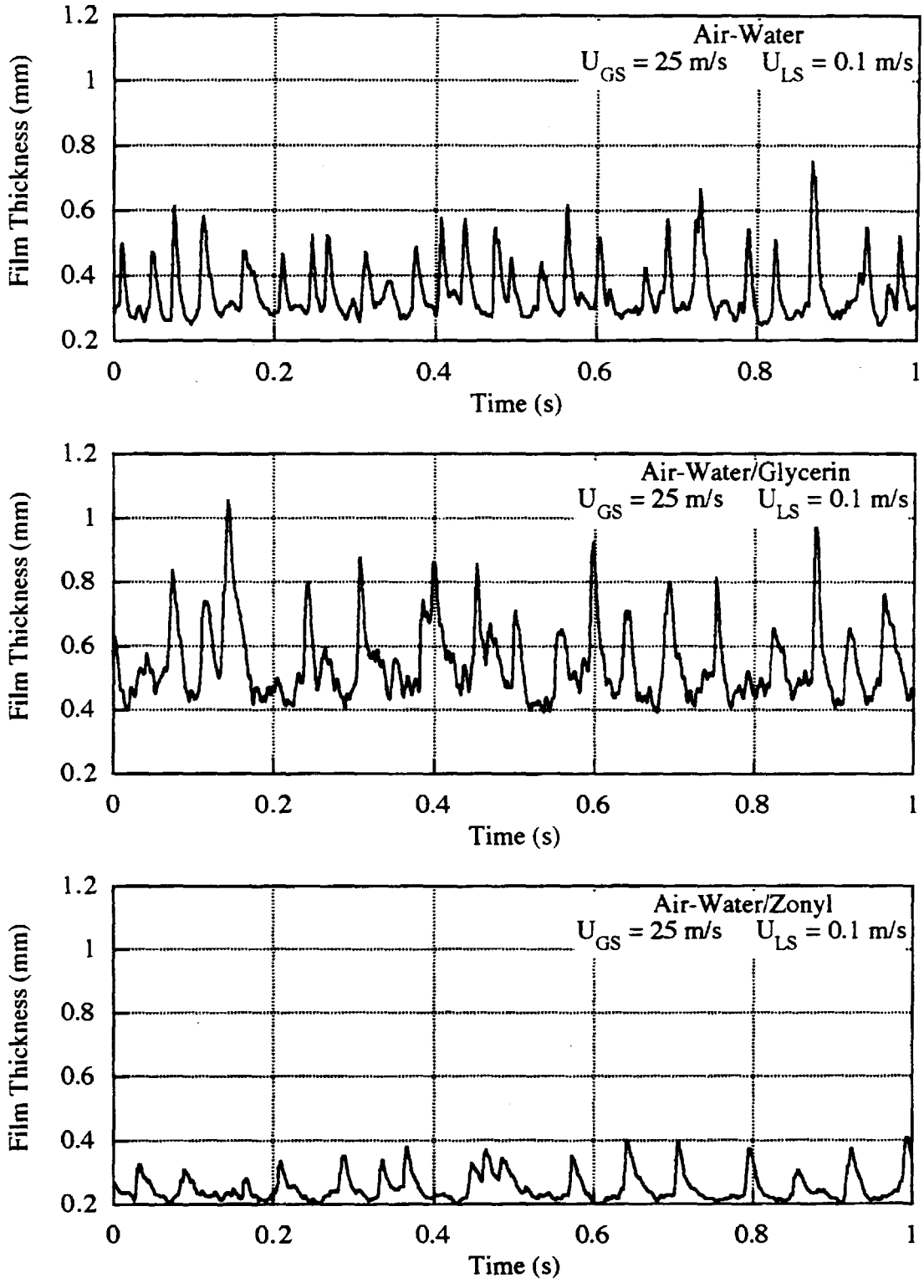

Figure 5.2 Effect of Liquid Properties on the Structure of Microgravity Annular Films

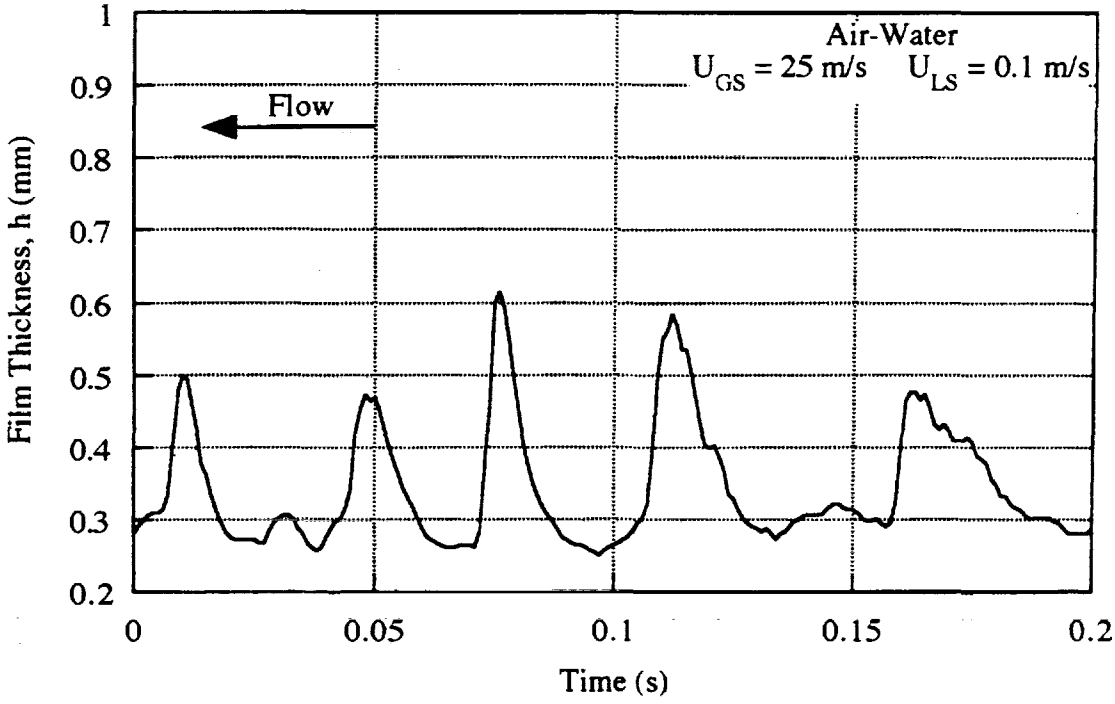

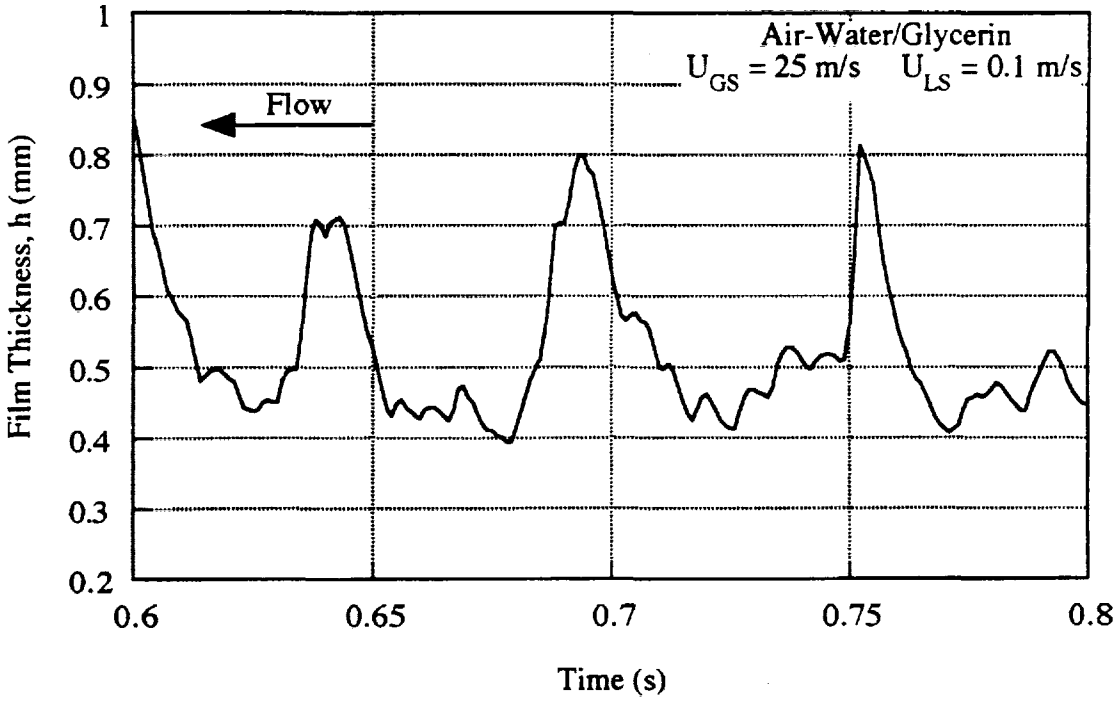

Figure 5.3 Comparison of Annular Waves for Air-Water and Air-Water/Glycerin

large waves is smooth in the air-water trace, the space between large waves in the air-water/glycerin trace contains small ripple waves and no smooth regions of the film are present.

Comparing the air-water and air-water/Zonyl FSP traces in Figure 5.2 shows the effect of surface tension on the nature of the gas-liquid interface. As shown, both the substrate thickness and wave amplitude are significantly smaller for the reduced surface tension case. There are also fewer large waves present on the air-water/Zonyl FSP interface. Enlargements of the air-water and air-water/Zonyl FSP waves are shown in Figure 5.4. As shown, the waves on the air-water/Zonyl FSP interface appear to be broader and the back sides of the waves have a smaller slope. The regions between the waves appear to be equally smooth for both liquid systems. It should also be noted that in some of the low velocity air-water/Zonyl FSP annular flow runs, tube dry-out events were observed in the movie films in which the liquid film dissipated and became discontinuous in a small region of the tube.

These initial qualitative observations of microgravity annular flows were constructive in setting the direction for more detailed quantitative measurements and analysis. These are presented in the sections that follow.

5.3 Film Thickness Measurements

In addition to the qualitative film thickness results presented previously, the accuracy of the film thickness probes used in this study (±5%) allows for quantitative measurements as well. These are of use in formulating overall heat and mass balances for design as well as for gaining deeper insight into the nature of the gas-liquid interface.

The mean film thickness for microgravity annular flow in a 12.7 mm ID tube is plotted as a function of gas and liquid superficial velocities in Figures 5.5, 5.6 and 5.7 for

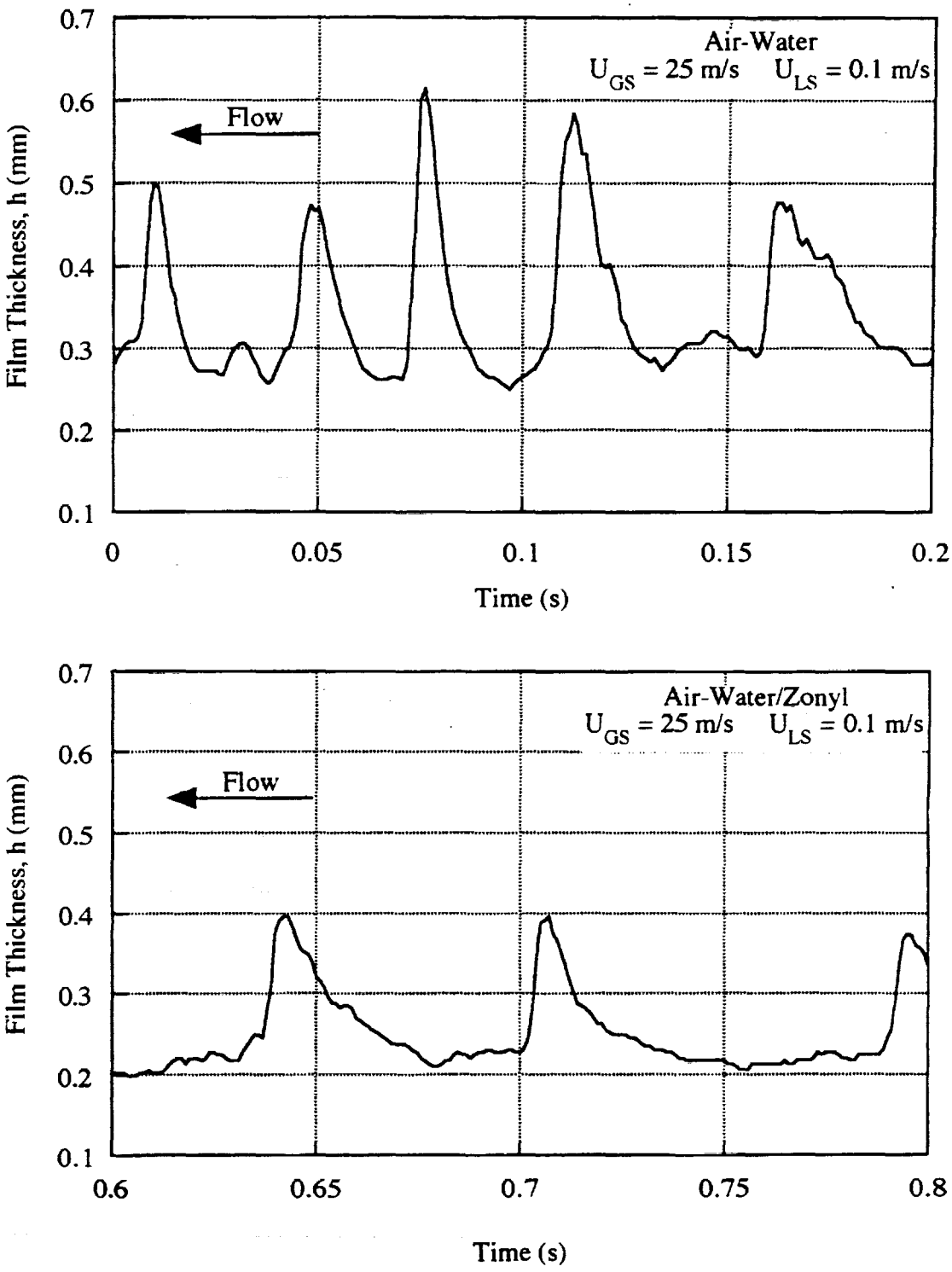

Figure 5.4 Comparison of Annular Waves for Air-Water and Air-Water/Zonyl FSP

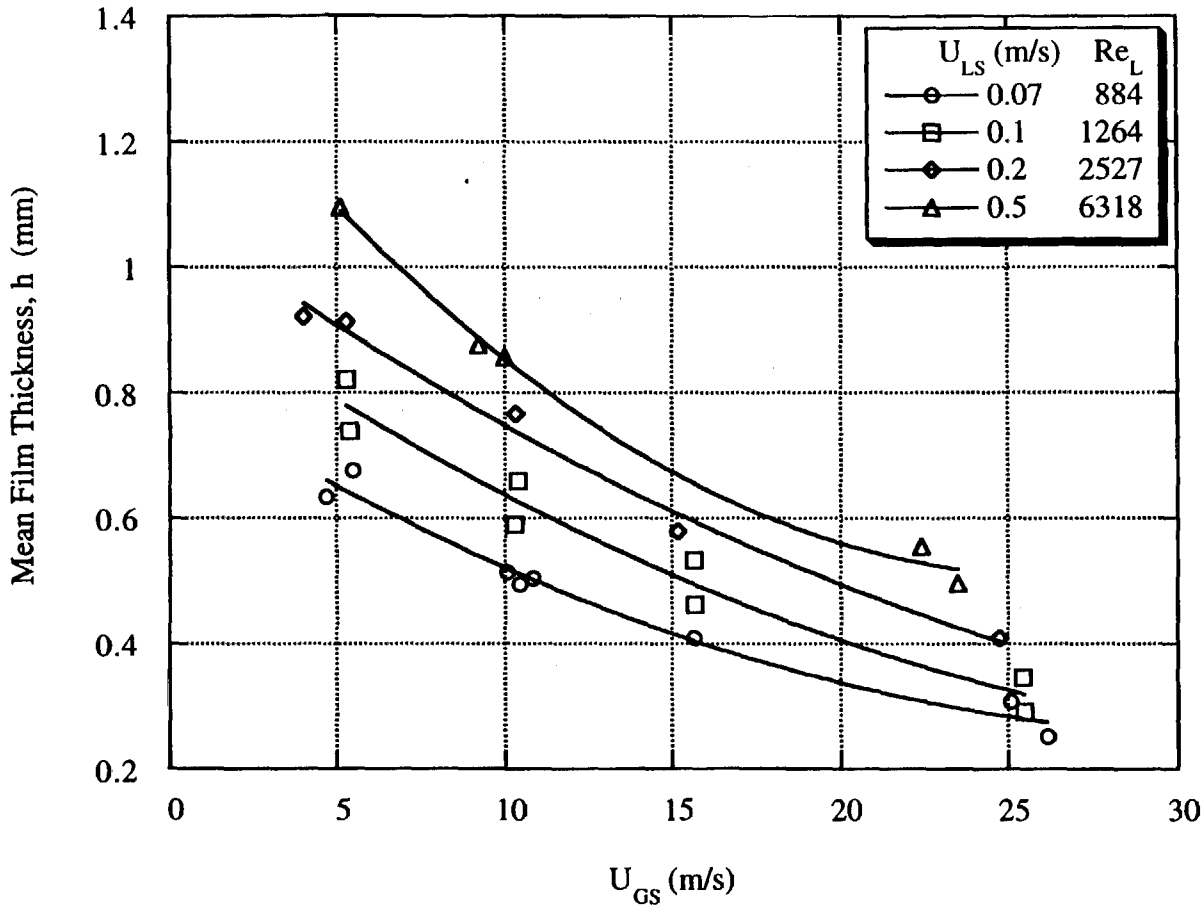

Figure 5.5 Mean Film Thickness for Microgravity Air-Water Annular Flow in a 12.7 mm ID Tube

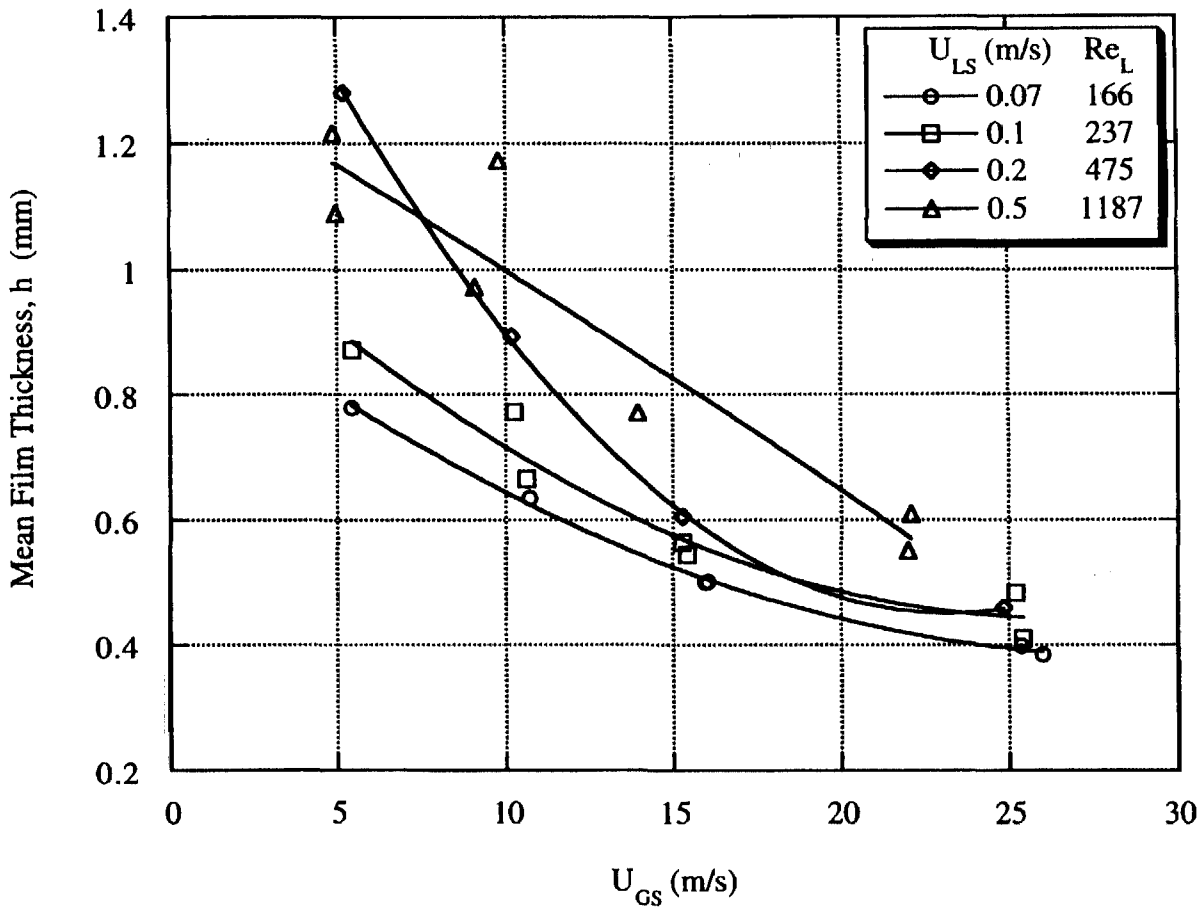

Figure 5.6 Mean Film Thickness for Microgravity Air-Water/Glycerin Annular Flow in a 12.7 mm ID Tube

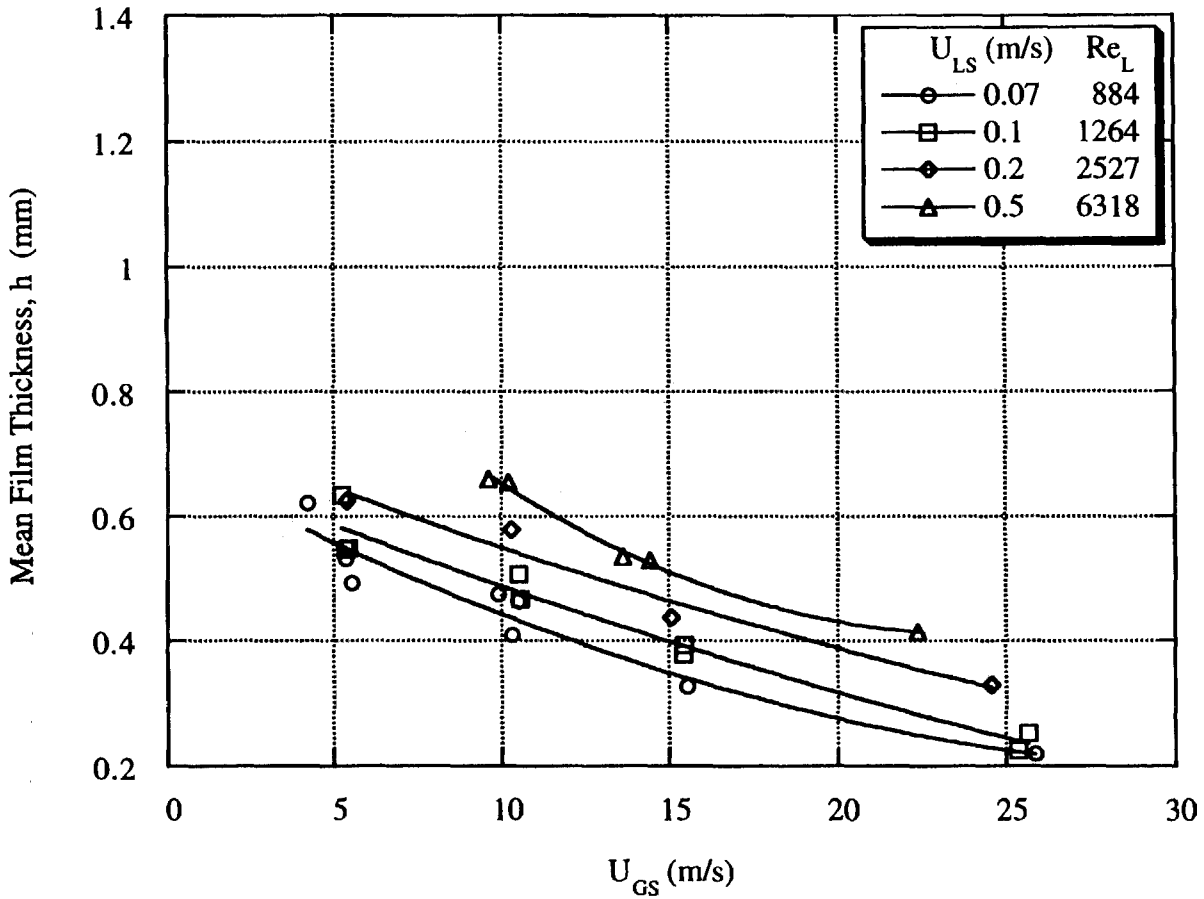

Figure 5.7 Mean Film Thickness for Microgravity Air-Water/Zonyl FSP Annular Flow in a 12.7 mm ID Tube

air-water, air-water/glycerin and air-water/Zonyl FSP, respectively. The data are fitted with second order polynomials to indicate trends. As expected, the mean liquid film thickness increases with increasing liquid superficial velocity, but, as shown, the film thickness decreases with increasing superficial gas velocity. In all cases, the liquid films are very thin, with even the thickest films occupying less than 20% of the tube radius.

The effect of liquid viscosity on the mean film thickness is demonstrated by comparing Figures 5.5 and 5.6. The air-water/glycerin annular films are significantly thicker than the air-water annular films at the same gas and liquid superficial velocities. This was shown qualitatively in Figure 5.2 where it can be seen that this increase in mean film thickness can be attributed both to a thicker liquid substrate film and a greater average wave amplitude. While the curves in Figure 5.5 remain equally spaced across the range of gas superficial velocities, the curves in Figure 5.6 appear to converge towards a single value at high gas superficial velocity, becoming independent of liquid superficial velocity. At low gas superficial velocity, the curves for the two highest levels of superficial liquid velocity cross in Figure 5.6 and the values in that region show more scatter. This may be due to flow pattern transition effects because these conditions are close to the slug-annular transition region on the flow pattern maps. Near the transition, the wave amplitude approaches the tube radius and the standard deviation of these experiments is nearly equal to the mean value. Since the sampling time is relatively short in the microgravity aircraft, these large waves can lead to a large amount of scatter in the results. Annular film thickness measurements taken in 1g for large sampling times (> 2 minutes) are much more reproducible (Fore, 1993).

The effect of surface tension on the mean film thickness is shown by comparing Figures 5.5 and 5.7. As shown, the air-water/Zonyl FSP annular films are much thinner than air-water annular films at the same conditions. This was also shown in Figure 5.2 to be due to both a thinner liquid substrate film and a smaller average wave amplitude for the

air-water/Zonyl FSP films. The potential causes of these physical property effects on the mean film thickness will be discussed in later sections of this chapter.

5.4 Wave Characteristics

The conductance probe data allows for additional analysis of the characteristics of annular waves beyond the qualitative results presented previously. These include the wave amplitude, celerity (axial velocity) and frequency. This may lead to a better understanding of the processes occurring in and around the annular waves in microgravity.

The film thickness time series shown in Figure 5.1 show that the liquid film consists of a substrate film and large amplitude waves. Since the major deviation in film thickness from the mean value is the large waves and not the small ripples, the standard deviation in the film thickness time series provides a measure of the height of these waves relative to the mean. Because the mean value lies near the substrate thickness, the standard deviation is also a measure of the wave amplitude relative to the substrate thickness.

The standard deviation of the film thickness, σ_h is shown as a function of superficial gas and liquid velocities in Figures 5.8, 5.9 and 5.10 for air-water, air-water/glycerin and air-water/Zonyl FSP, respectively. As shown in all three plots, σ_h decreases with increasing U_{GS}, but the rate of decrease is less at the highest values of U_{GS}. For low U_{GS}, σ_h increases with increasing U_{LS}, but σ_h becomes essentially independent of U_{LS} for the highest values of U_{GS}. As was shown previously in the qualitative examination of the film thickness traces, a comparison of Figure 5.8 to Figure 5.9 indicates that an increase in liquid viscosity leads to an increase in wave amplitude. Similarly, a comparison of Figures 5.8 and 5.10 shows that a decrease in the surface tension leads to a decrease in wave amplitude.

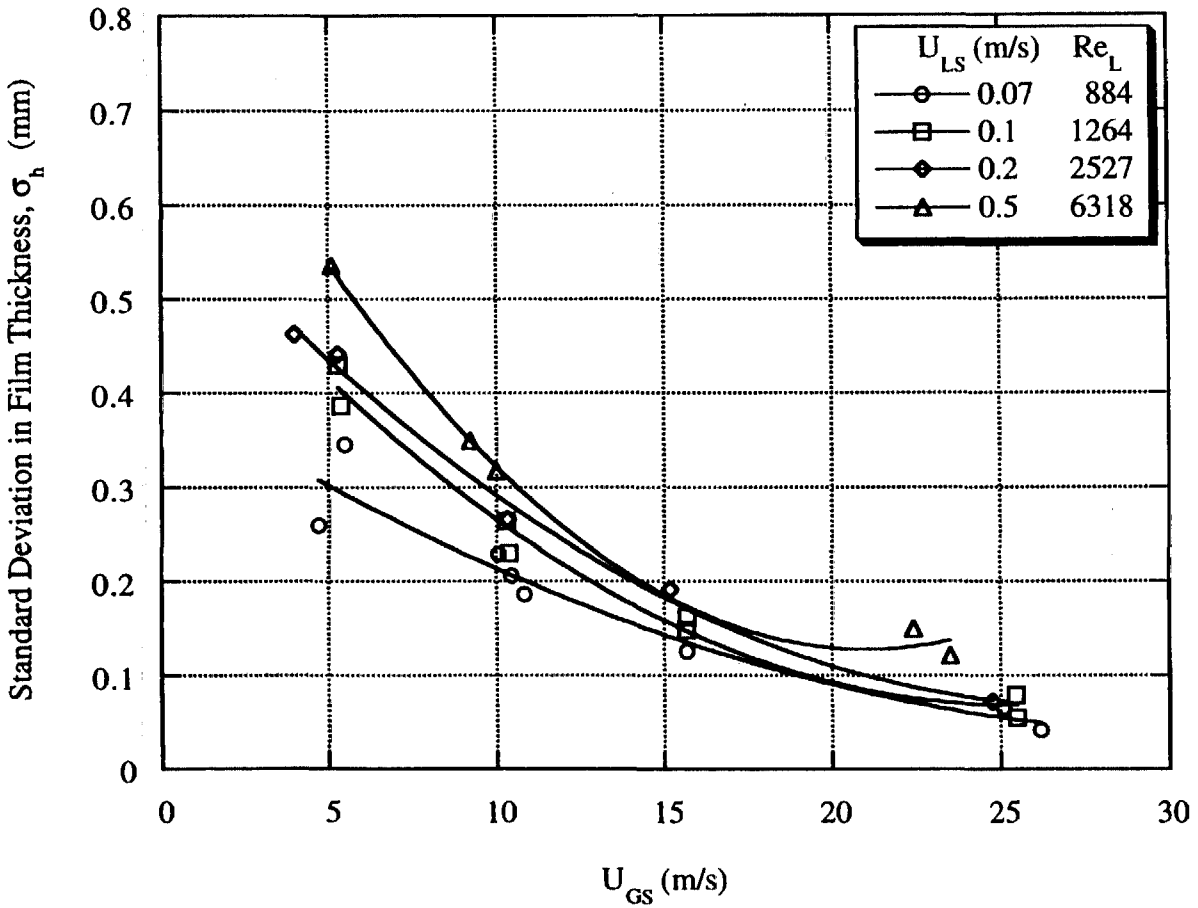

Figure 5.8 Film Thickness Standard Deviation for Microgravity Air-Water Annular Flow in a 12.7 mm ID Tube

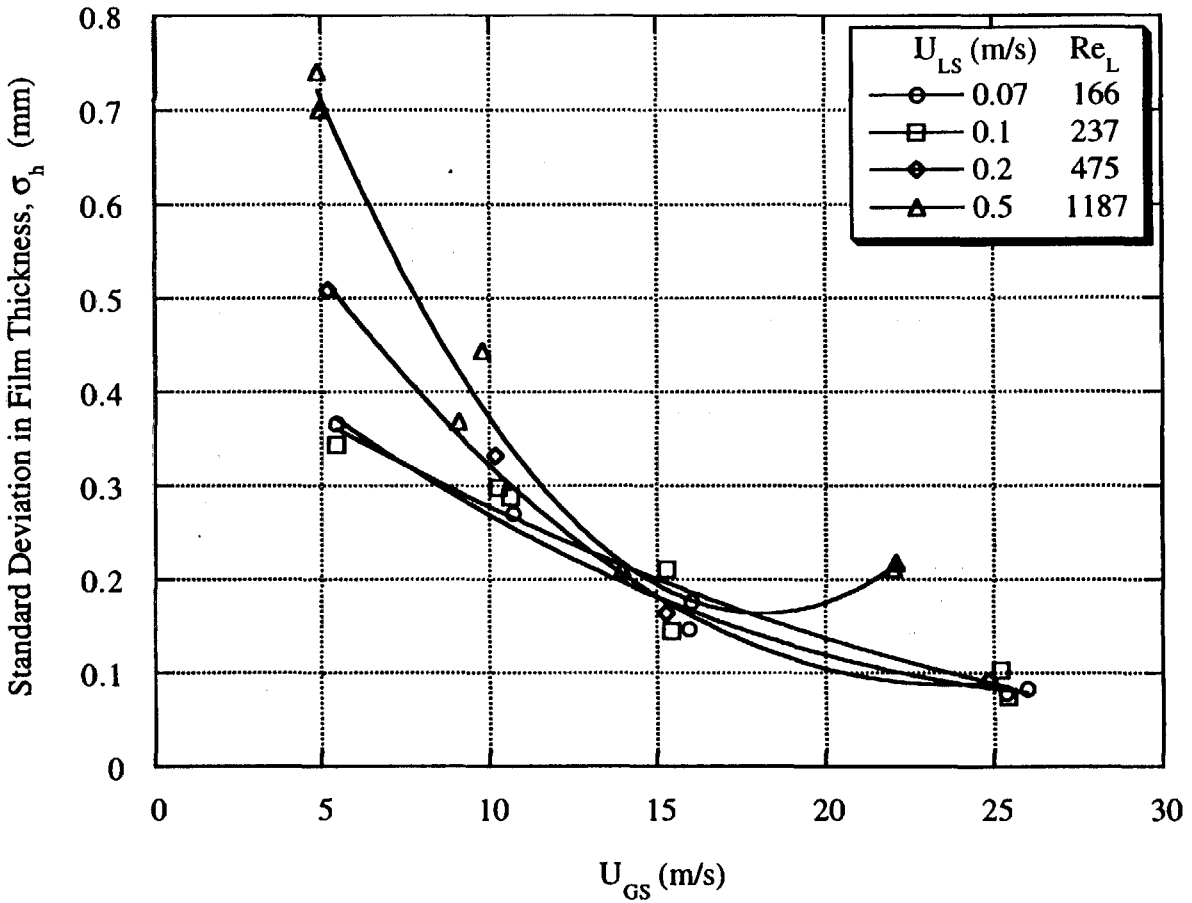

Figure 5.9 Film Thickness Standard Deviation for Microgravity Air-Water/Glycerin Annular Flow in a 12.7 mm ID Tube

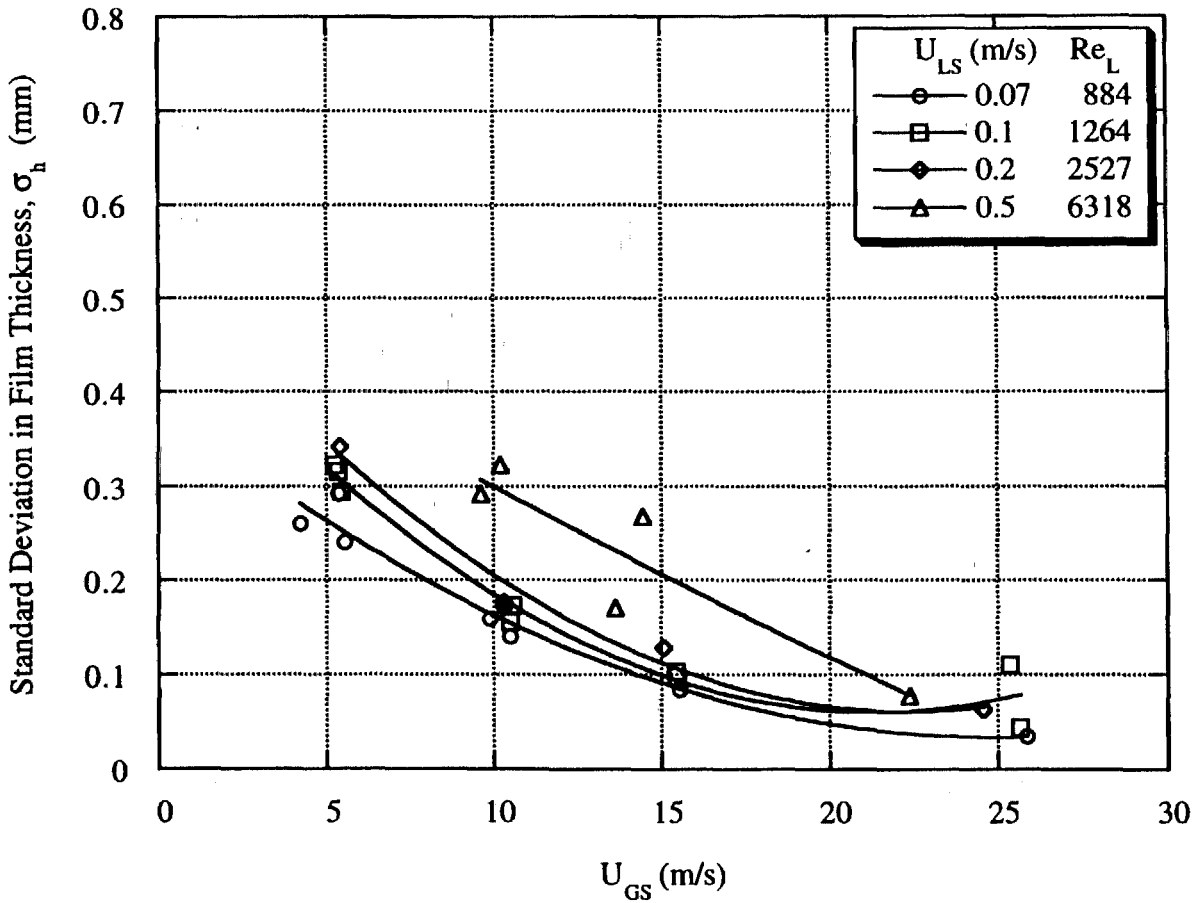

Figure 5.10 Film Thickness Standard Deviation for Microgravity Air-Water/Zonyl FSP Annular Flow in 12.7 mm ID Tube

As was shown previously, the mean film thickness also decreased with increasing U_{GS}. The ratio of mean to standard deviation in film thickness was computed so that the height of the waves relative to the substrate could be more readily quantified. This ratio is shown in Figures 5.11, 5.12 and 5.13 for air-water, air-water/glycerin and air-water/Zonyl FSP, respectively. These figures indicate that the wave amplitude decreases faster than the mean film thickness as U_{GS} increases. Similar results were also reported by Fore, 1993 for vertical upward annular flows at 1g. It was found in the laboratory in vertical downward flow that for $U_{GS} > 50$ m/s, the waves virtually disappear. Figures 5.11, 5.12 and 5.13 also indicate that the ratio of mean to standard deviation in film thickness is nearly independent of both U_{LS} and the liquid viscosity and surface tension.

The celerity (axial velocity) of the waves is also of interest for better understanding the nature of microgravity annular flows. Because there is significant slip between the two phases and the interaction between the two phases is complex, no simple relation between superficial velocities and wave celerities exists analogous to the Drift-Flux model for bubble and slug flows. The wave celerity is expected to not only depend on the superficial gas velocity but also on the wave shape, wall and interfacial friction and droplet entrainment from the wave crests.

The wave splitting and joining phenomena noted in Figure 5.1 suggest that a distribution of wave celerities exists within an annular flow. The typical cross-correlation result shown in Figure 2.16 also shows that the wave celerities are distributed in a nearly Gaussian fashion around a mean value. Analysis of individual waves has not shown the celerity to be a simple function of measurable quantities such as wave amplitude or slopes of the wave fronts or tails but instead the celerity is probably a complex function of the wave shape. Since the shape of the wave appears to be in a state of continuous change, this would suggest that the celerity of a given wave is also changing continuously.

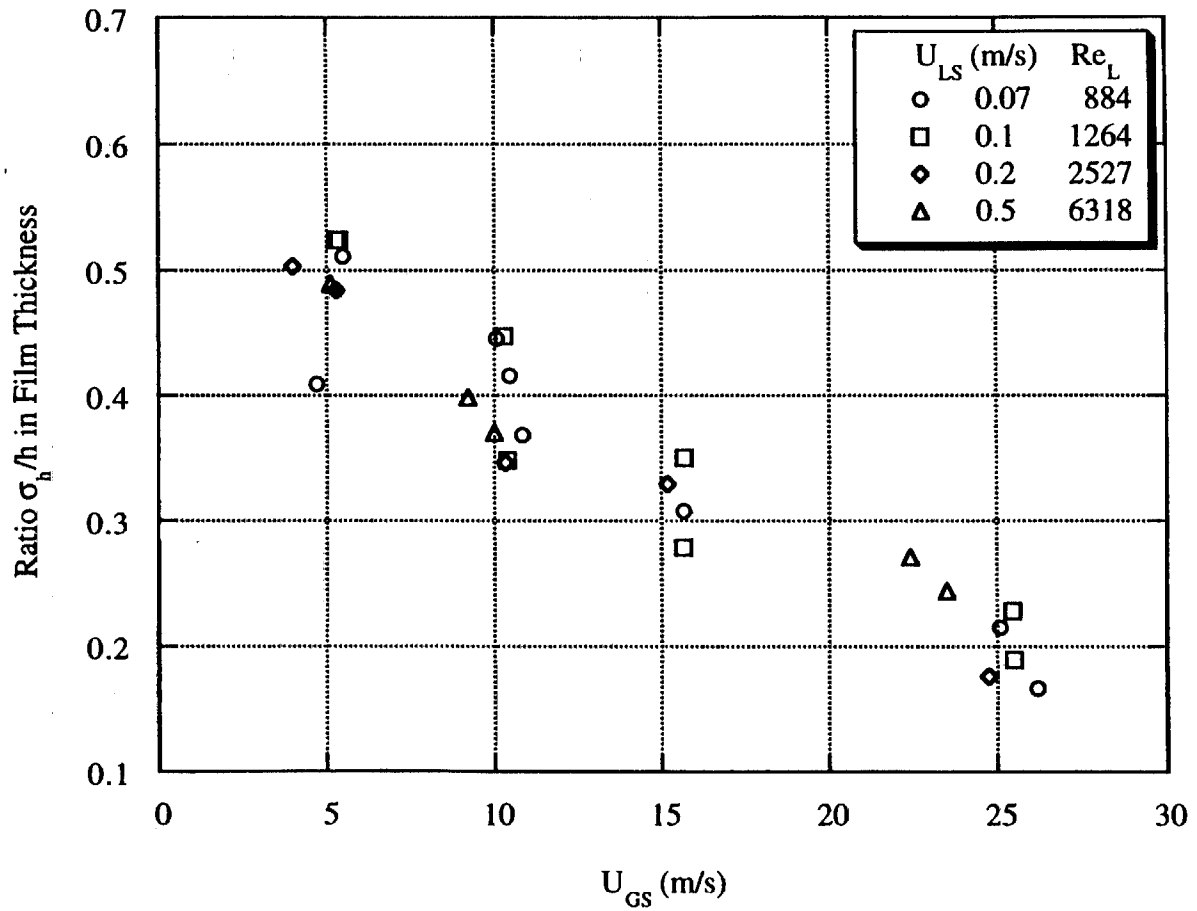

Figure 5.11 Ratio of Standard Deviation to Mean Film Thickness for Air-Water Annular Flow in a 12.7 mm ID Tube

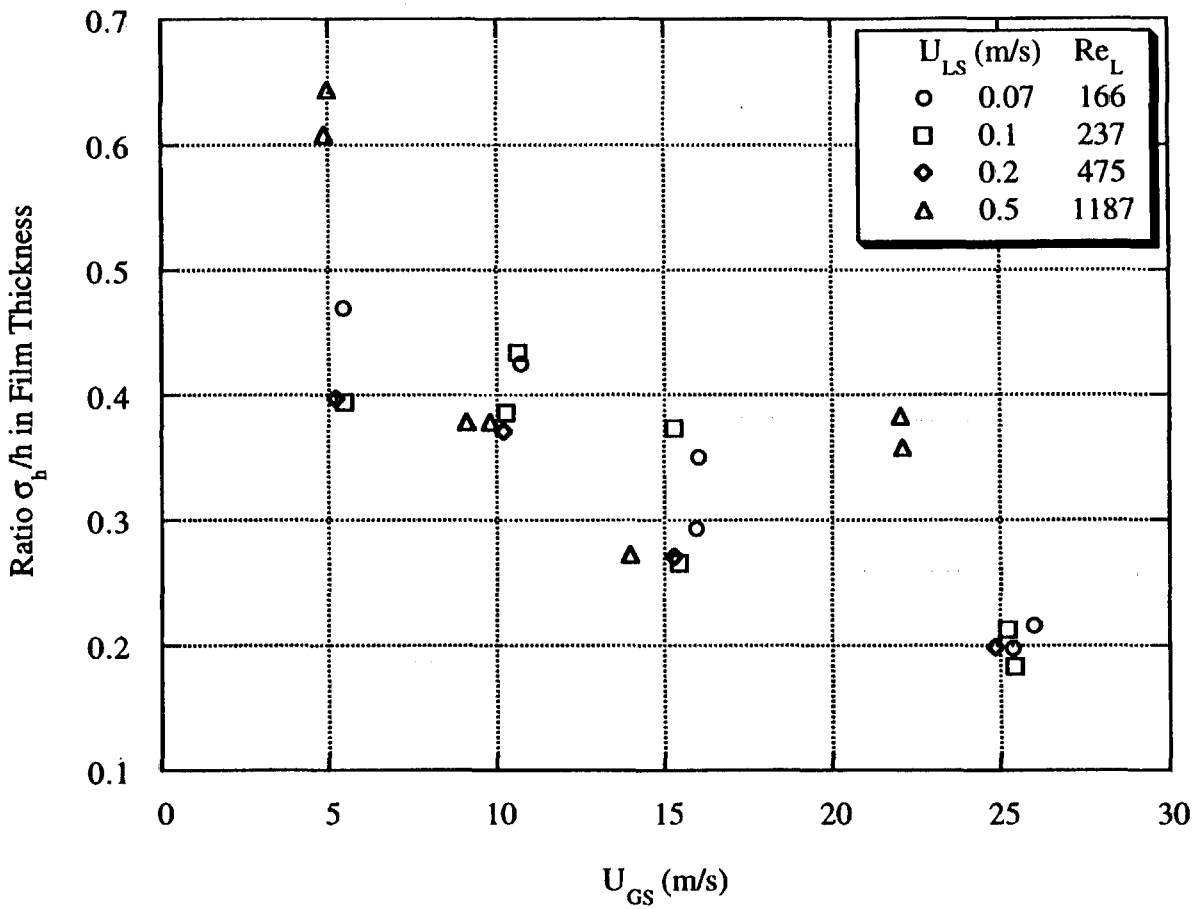

Figure 5.12 Ratio of Standard Deviation to Mean Film Thickness for Air-Water/Glycerin Annular Flow in a 12.7 mm ID Tube

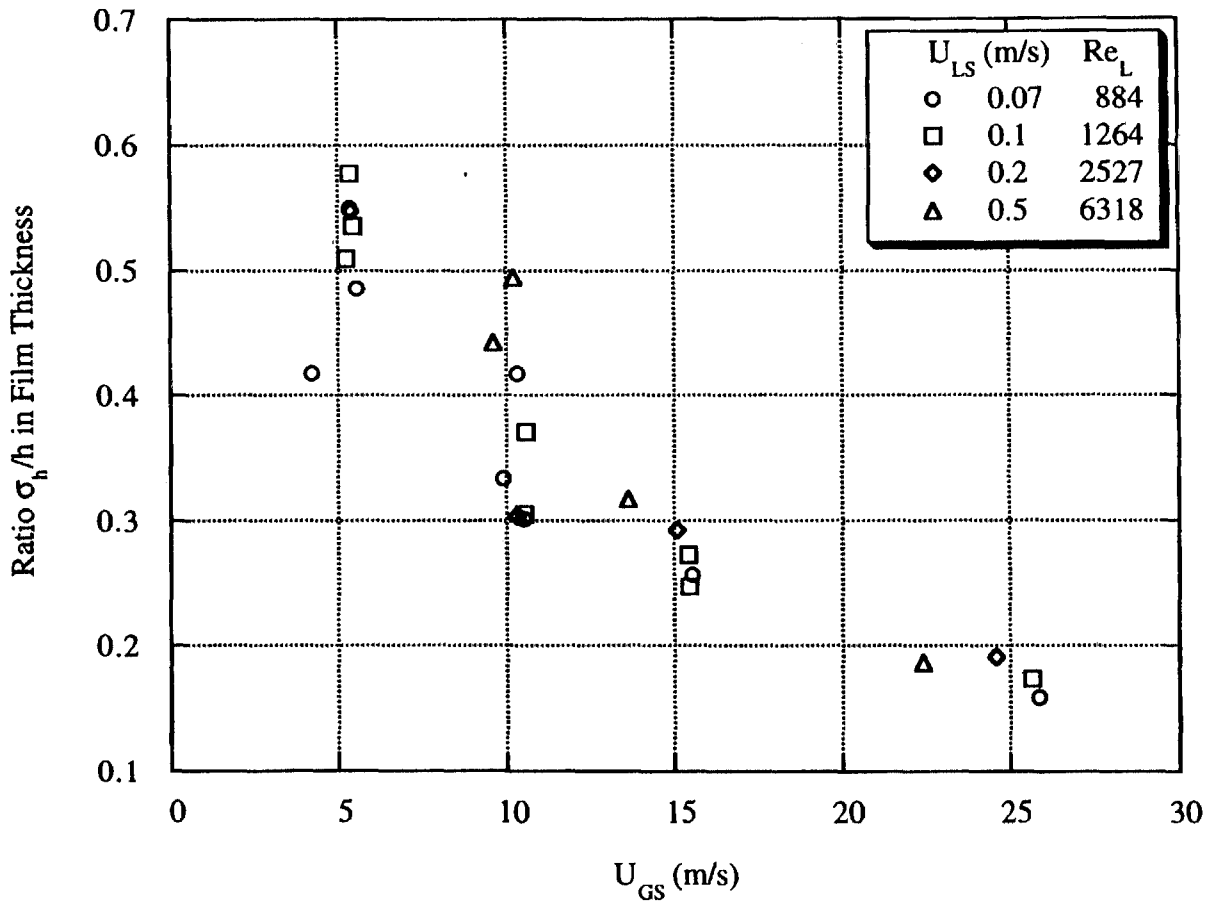

Figure 5.13 Ratio of Standard Deviation to Mean Film Thickness for Air-Water/Zonyl Annular Flow in a 12.7 mm ID Tube

A detailed study of the factors affecting the celerity of individual waves is beyond the scope of the present study, however the mean celerity of each of the annular experiments can be computed from the cross-correlations of the conductance probe signals as discussed in Chapter 2. The mean wave celerity values are shown as a function of superficial velocities in Figures 5.14, 5.15 and 5.16 for air-water, air-water/glycerin and air-water/Zonyl FSP, respectively. In all cases, the mean celerity increases as U_{LS} increases. The celerity also increases with increasing U_{GS} except for the highest liquid rate experiments in Figures 5.15 and 5.16. The increase in U with decreasing U_{GS} ($U_{GS} < 15$ m/s) at $U_{LS} = 0.5$ m/s for the air-water/glycerin system may be due to flow pattern transition effects since these runs lie very close to the transition region on the flow pattern map. The large amount of scatter in the air-water/Zonyl FSP results for $U_{LS} = 0.5$ m/s is difficult to explain since other quantities measured in these experiments, such as mean film thickness, do not show such variation. It should also be noted that with the exception of the experiments taken at $U_{LS} = 0.5$ m/s, there is little effect of liquid physical properties on the mean wave celerity.

Another wave property which can be deduced from the film thickness data recorded in this study is the frequency distribution. Current annular flow simulations reported in the literature focus primarily on modeling a single wave (McLean, 1983, Chauve and Schiestel, 1985, Wasden, 1989). In order to scale up results such as pressure drop and heat and mass transfer rates to the entire flow system, knowledge of the frequency of occurrence of these waves is necessary.

The cross-correlation function (2.4) is modified to form the autocorrelation function,

$$R_{11}(\tau) = R_{11}(s-t) = E\{X_1(t)\, X_1(s)\}, \qquad (5.1)$$

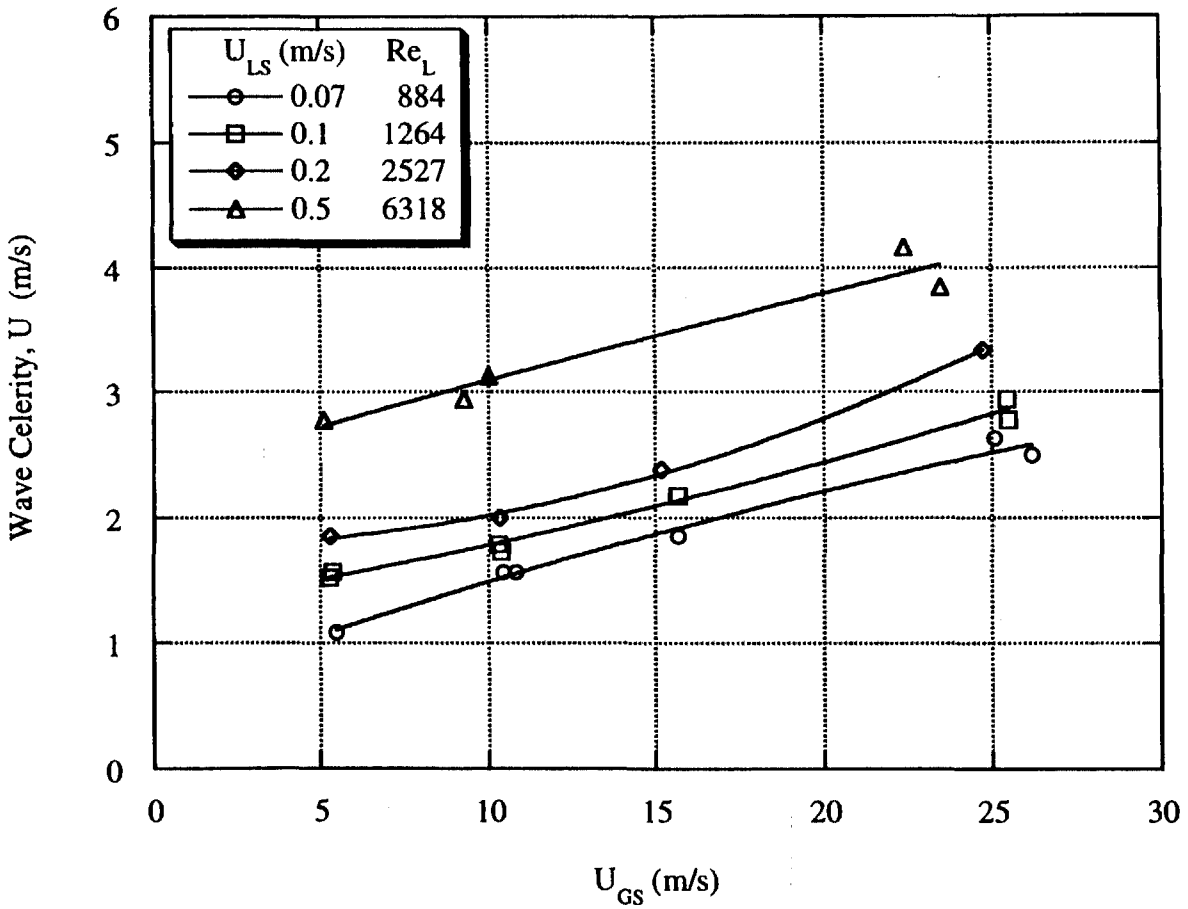

Figure 5.14 Wave Celerity for Microgravity Air-Water Annular Flow in a 12.7 mm ID Tube

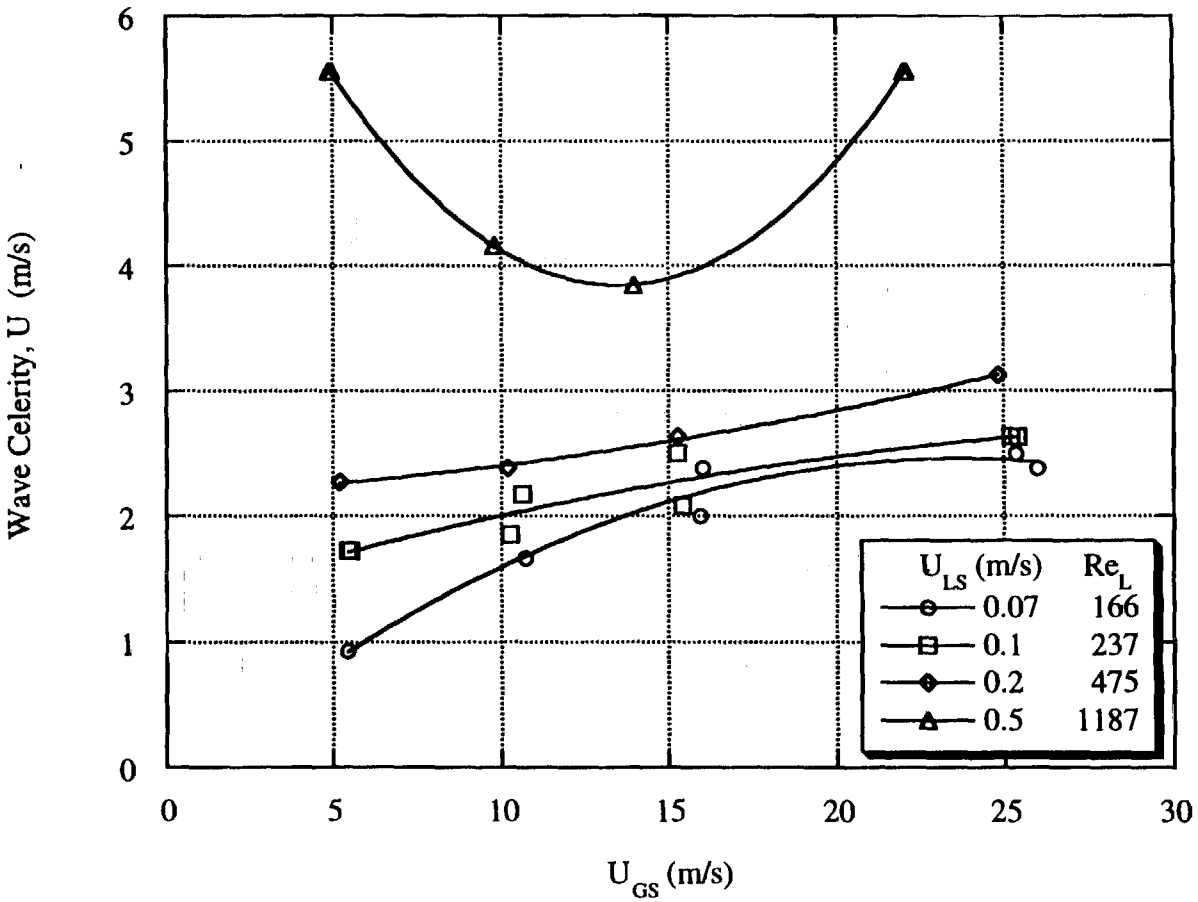

Figure 5.15 Wave Celerity for Microgravity Air-Water/Glycerin Annular Flow in a 12.7 mm ID Tube

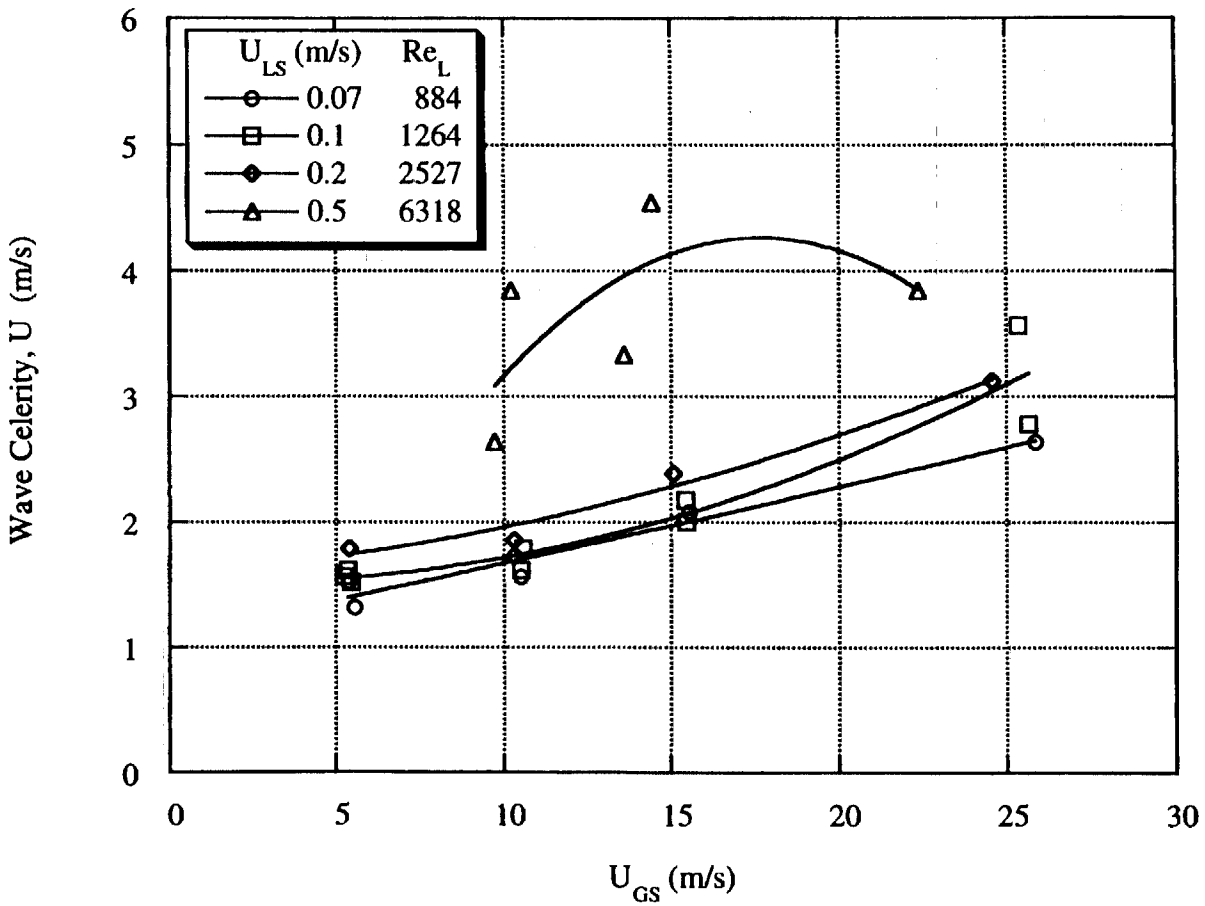

Figure 5.16 Wave Celerity for Microgravity Air-Water/Zonyl FSP Annular Flow in a 12.7 mm ID Tube

where E represents the expectation value (Bendat and Piersol, 1986). This function quantifies the degree of correlation between a given measurement in a process and other measurements in the same process. The film thickness time series can be assumed to be stationary processes since segments of these series have nearly the same mean values and standard deviations. If the process is assumed to be stationary, the autocorrelation is a function only of the time lag τ between two measurements in the same process as indicated in (5.1). The autocorrelation is transformed to the frequency domain by computing the power spectral density function as the Fourier transform of the autocorrelation,

$$\phi(\omega) = \int_{-\infty}^{\infty} R_{11}(u)\, e^{-i\omega u}\, du \,. \tag{5.2}$$

The power spectral density function is usually normalized by the total power,

$$\Phi(\omega) = \frac{\int_{-\infty}^{\infty} R_{11}(u)\, e^{-i\omega u}\, du}{\int_{-\infty}^{\infty} \phi(\omega)\, d\omega} \,. \tag{5.3}$$

Since the film thickness time series represents a discrete rather than continuous process, the power spectral density function is most efficiently computed using the Fast Fourier Transform (FFT) algorithm. In using this algorithm, a problem known as side lobe leakage arises which causes power at one frequency to "leak" into adjacent frequencies. This problem is significantly reduced by the use of one of many available windowing functions (Press et al., 1992). Several common windowing functions were tested and no discernible difference was detected. The often-used Hanning window was therefore used for all power spectral analysis in this study.

A typical normalized power spectral density function for microgravity annular flow is plotted versus frequency in Figure 5.17. This function was computed using a 2048

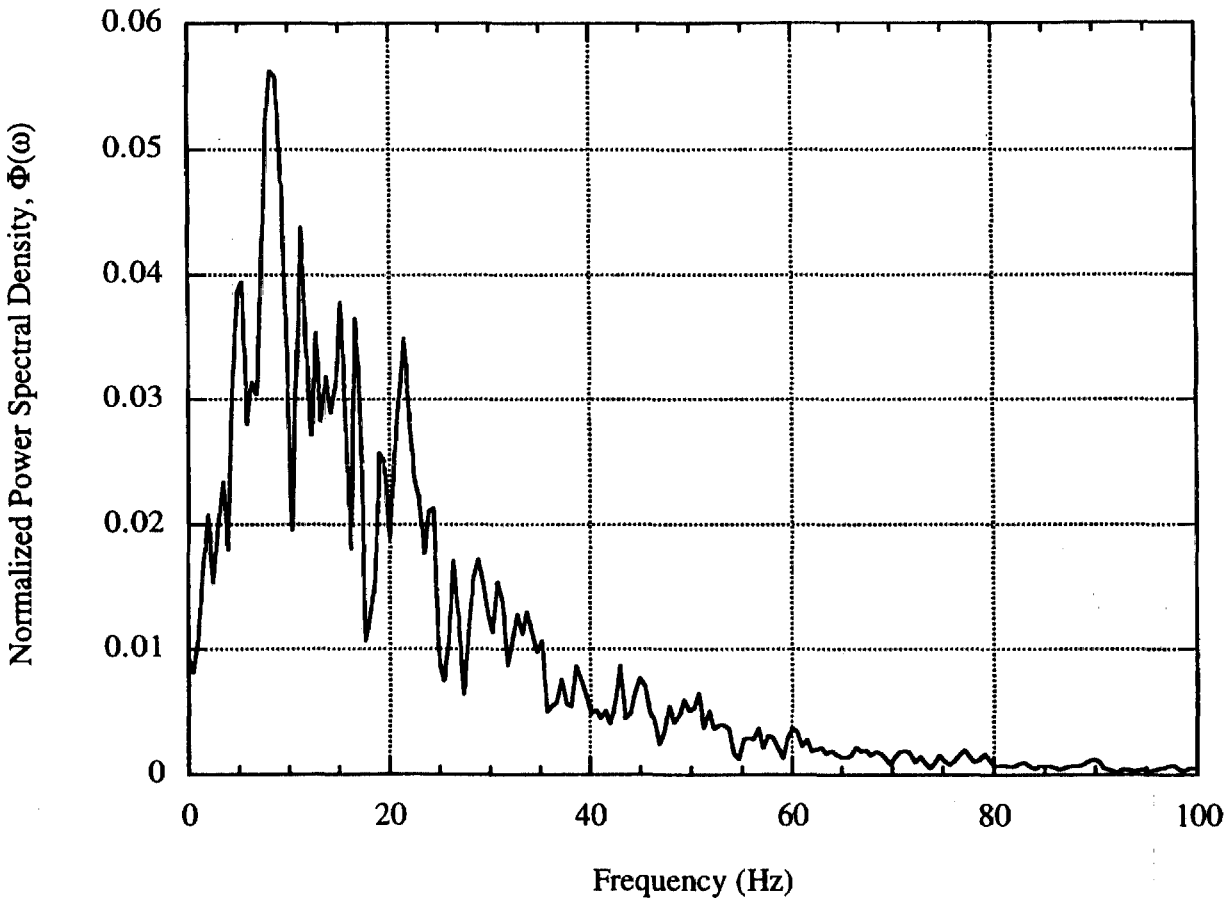

Figure 5.17 Typical Normalized Power Spectral Density Function of Film Thickness for Microgravity Annular Flow

point Hanning window with segments overlapping 50% (Press et al., 1992). The frequency resolution with this method is 0.5 Hz. As shown, the wave frequency is concentrated at low frequency with 90% of the spectral power below 49 Hz. The power is essentially zero at frequencies above 100 Hz. The power spectrum also exhibits a sharp maximum with a modal value of 8.3 Hz. Analysis of all of the annular flow experiments showed that this modal value was a function of the superficial gas and liquid velocities. Since this modal value was also easily and unambiguously identified in each power spectrum, it was chosen as the characteristic frequency measurement for wave frequency analysis.

The power spectrum modal frequency for microgravity annular flow, computed as described above, is shown as a function of gas and liquid superficial velocities in Figures 5.18, 5.19 and 5.20 for air-water, air-water/glycerin and air-water/Zonyl FSP in a 12.7 mm ID tube. While the results exhibit considerable scatter, the plots show the characteristic frequency to be a strong function of U_{GS} and a weaker function of U_{LS}. The frequencies are generally largest for the air-water system. The air-water/glycerin system shows little effect of U_{LS}. For U_{LS} = 0.5 m/s, the air-water/Zonyl FSP results are similar to those of the air-water system but for the lower superficial liquid velocities, the modal frequencies are approximately one half of the air-water modal frequencies under the same conditions.

While no frequency results are reported in the literature for microgravity annular flow, both Chu and Dukler, 1975 and Jayawardena, 1993 report annular wave modal frequencies of less than 10 Hz for 1g air-water concurrent upward annular flow for flow conditions similar to those in the present study. This suggests that gravity acts as a strong damping force on wave formation and growth processes.

Annular wave formation is thought to be due to instabilities occurring at the gas-liquid interface (Andreussi et al., 1985, Jurman et al., 1989). Factors influencing the gas-

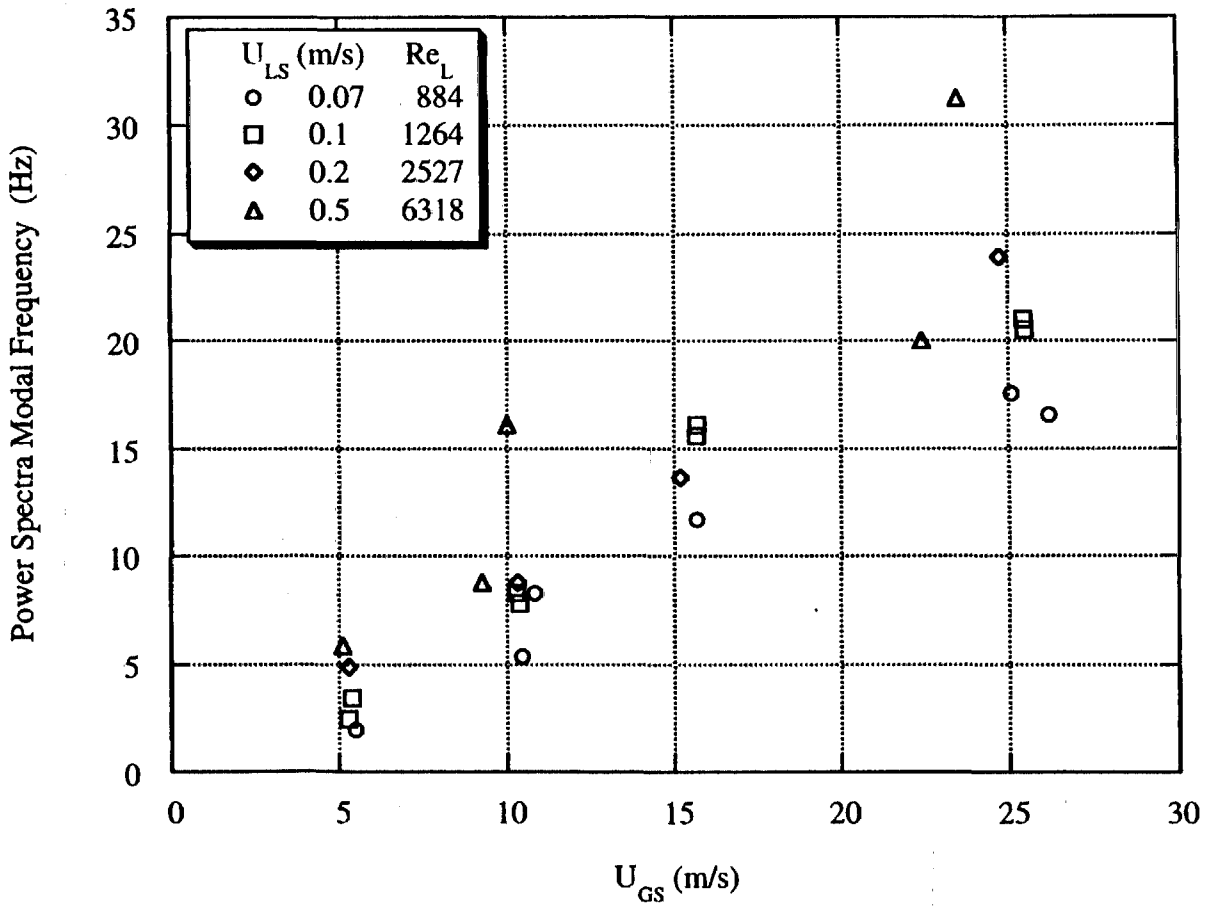

Figure 5.18 Power Spectral Modal Frequency for Microgravity Air-Water Annular Flow in a 12.7 mm ID Tube

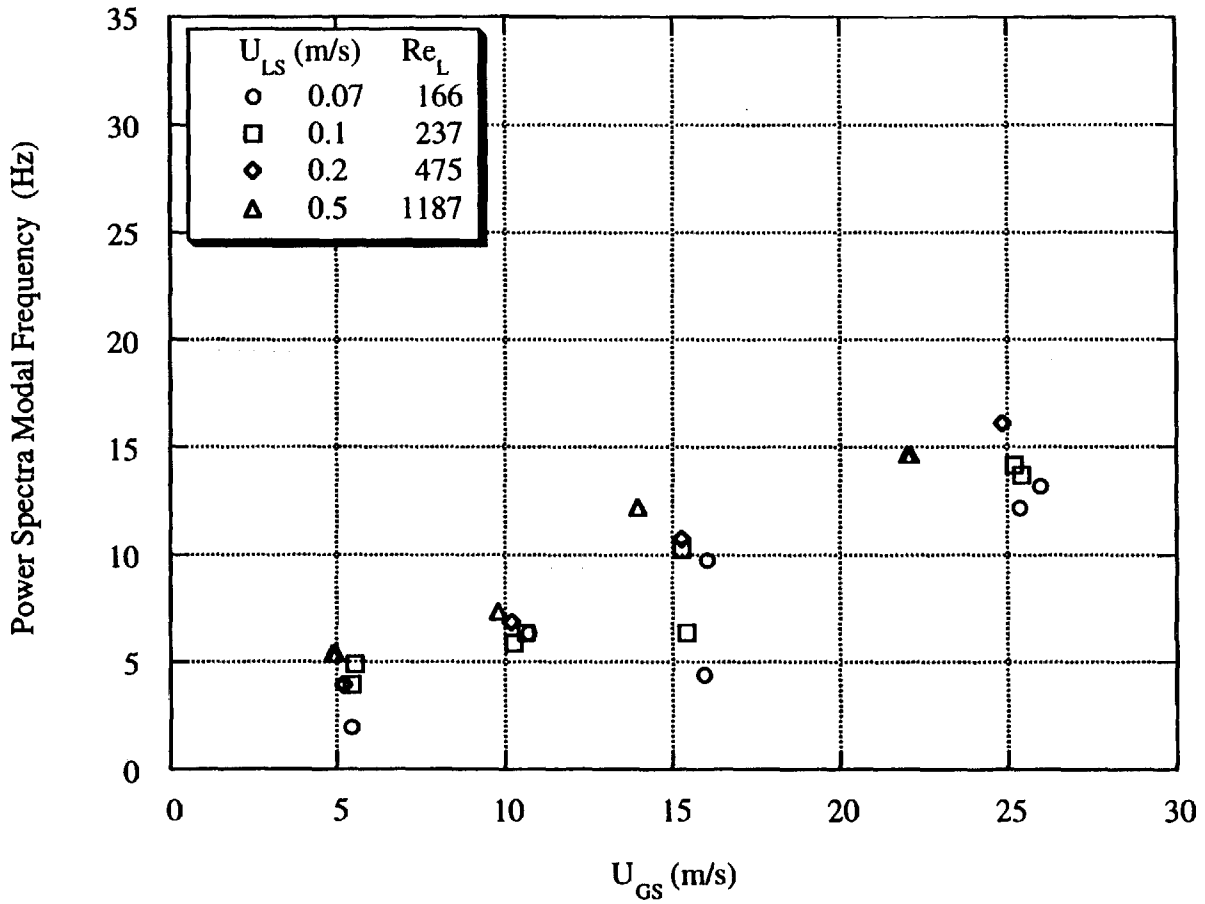

Figure 5.19 Power Spectral Modal Frequency for Microgravity Air-Water/Glycerin Annular Flow in a 12.7 mm ID Tube

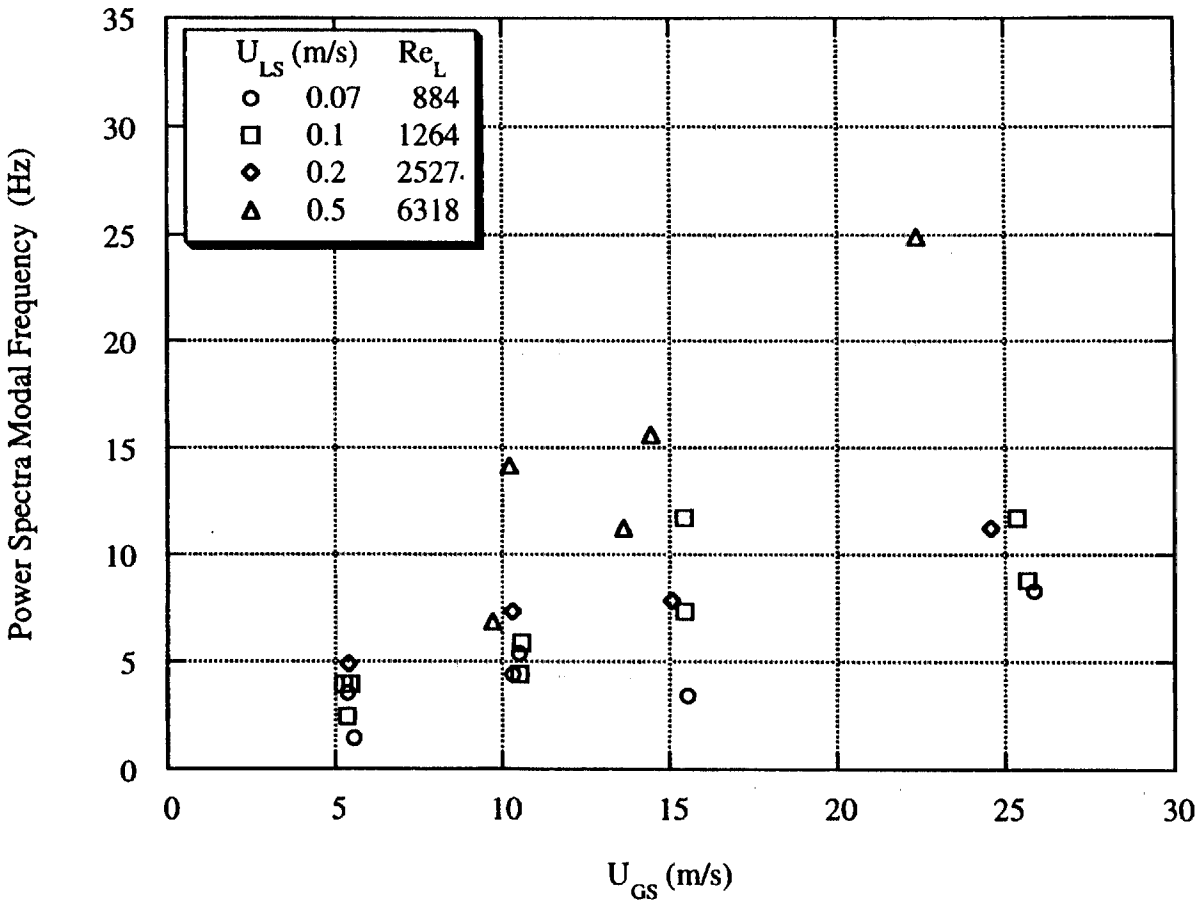

Figure 5.20 Power Spectral Modal Frequency for Microgravity Air-Water/Zonyl FSP Annular Flow in a 12.7 mm ID Tube

liquid interface such as the shear rate at the surface and gravity as well as the surface tension and liquid viscosity may influence this instability in complex ways, and detailed simulation studies are needed to better quantify these effects. The present results do however establish bounds on the annular wave frequencies and indicate the relative importance of the variables on the results.

5.5 Annular Flow Pressure Drop

The pressure drop encountered in an annular flow system is one of the most important quantities to the designers of these systems. It is well established on earth that the introduction of a thin film of liquid onto the perimeter of a gas pipeline can increase the pressure drop by an order of magnitude. This increase is much more than would be expected due to the reduction in flow area in the pipe. This suggests that a strong interaction exists between the two phases.

As two-phase systems become a part of large space-based research and manufacturing facilities, the ability to predict the pressure drop in annular systems will be crucial to proper design and operation. For this reason, much of the effort in this study was devoted towards obtaining accurate pressure drop measurements in microgravity annular flow. As described in Chapter 2, pressure drop measurement in the reduced gravity aircraft is difficult due to vibrations and small acceleration components. However, the pressure measurement system used in this study as well as the operating procedure were refined until reproducible measurements could be obtained.

The pressure drop obtained in microgravity annular flow in a 12.7 mm ID tube is shown as a function of U_{GS} and U_{LS} in Figures 5.21, 5.22 and 5.23 for air-water, air-water/glycerin and air-water/Zonyl FSP, respectively. As shown, the pressure drop measurements are smoothly increasing functions of both superficial velocities and are well

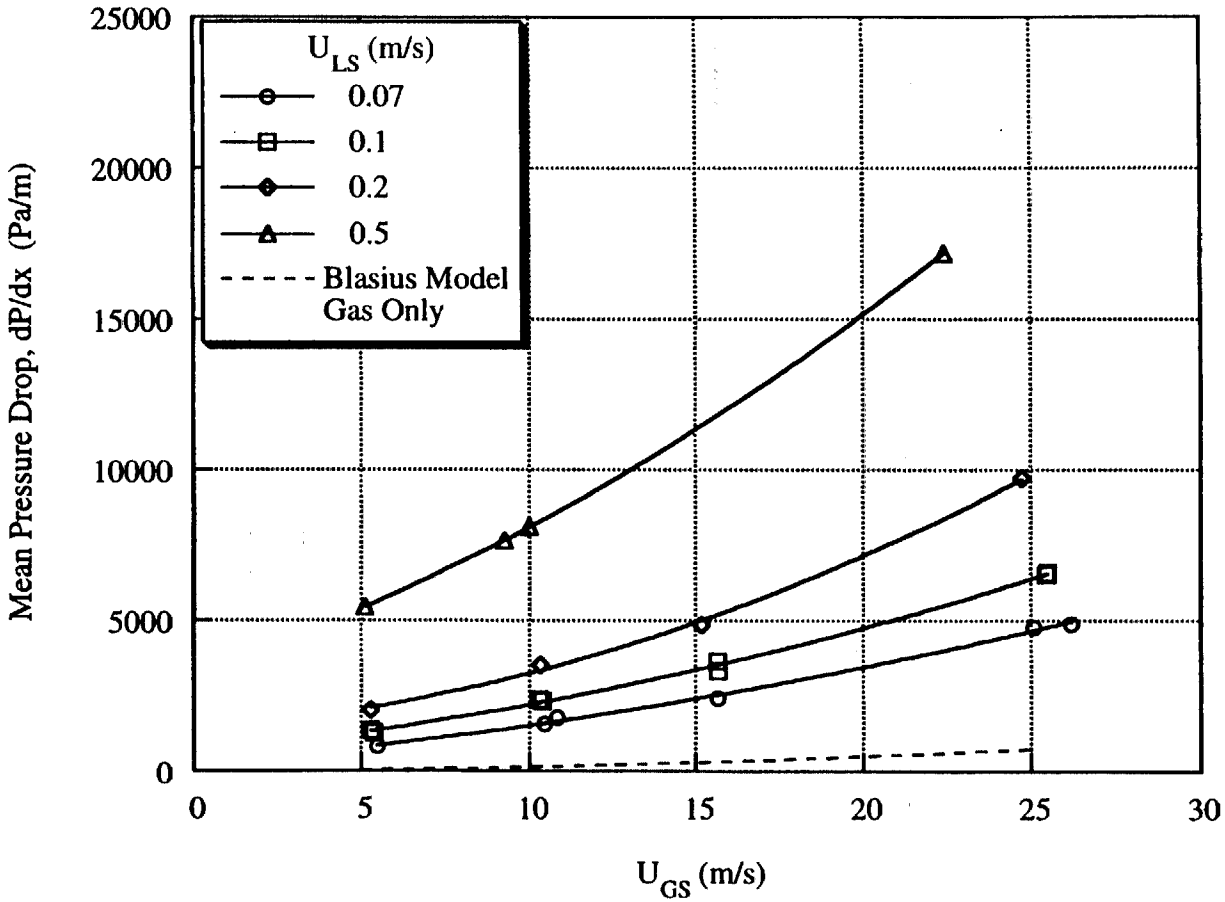

Figure 5.21 Mean Pressure Drop for Microgravity Air-Water Annular Flow in a 12.7 mm ID Tube

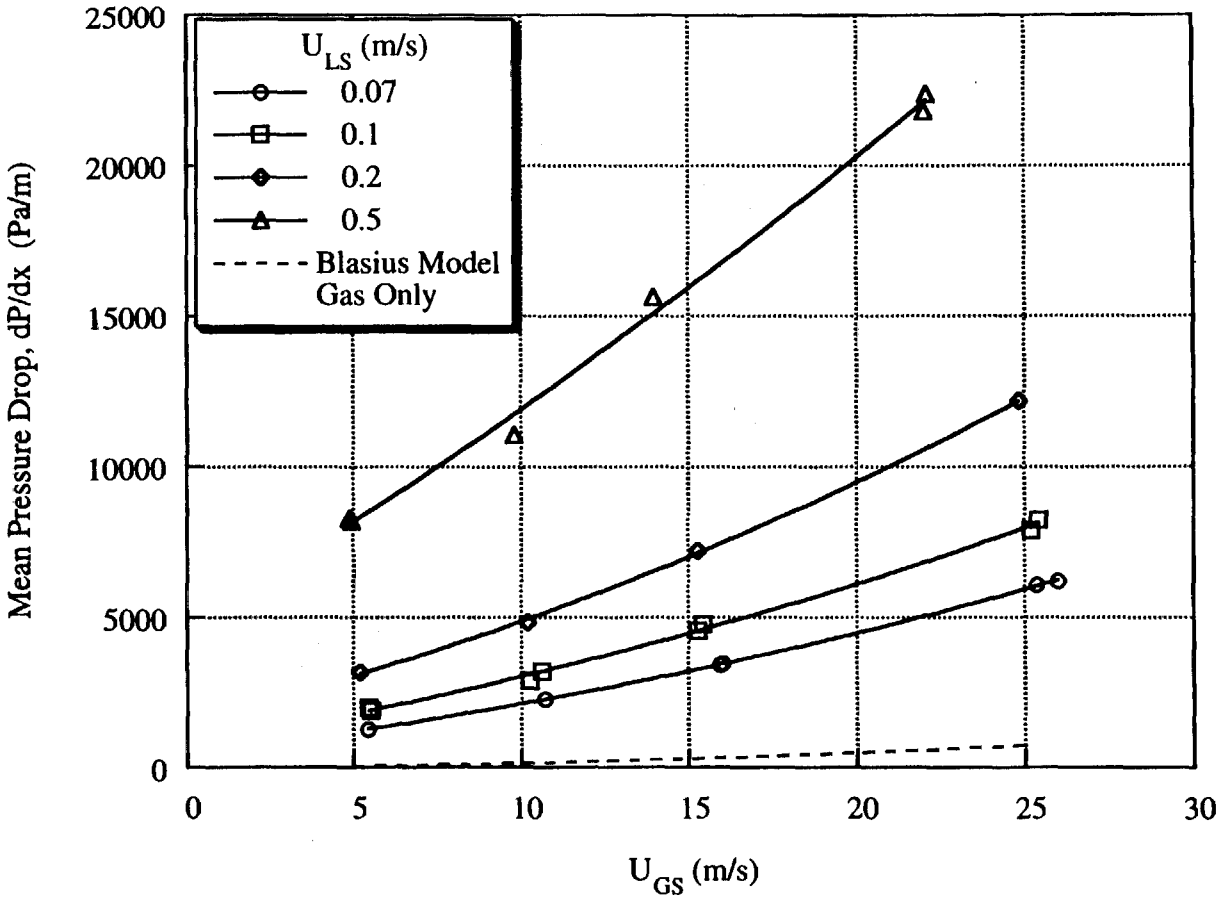

Figure 5.22 Mean Pressure Drop for Microgravity Air-Water/Glycerin Annular Flow in a 12.7 mm ID Tube

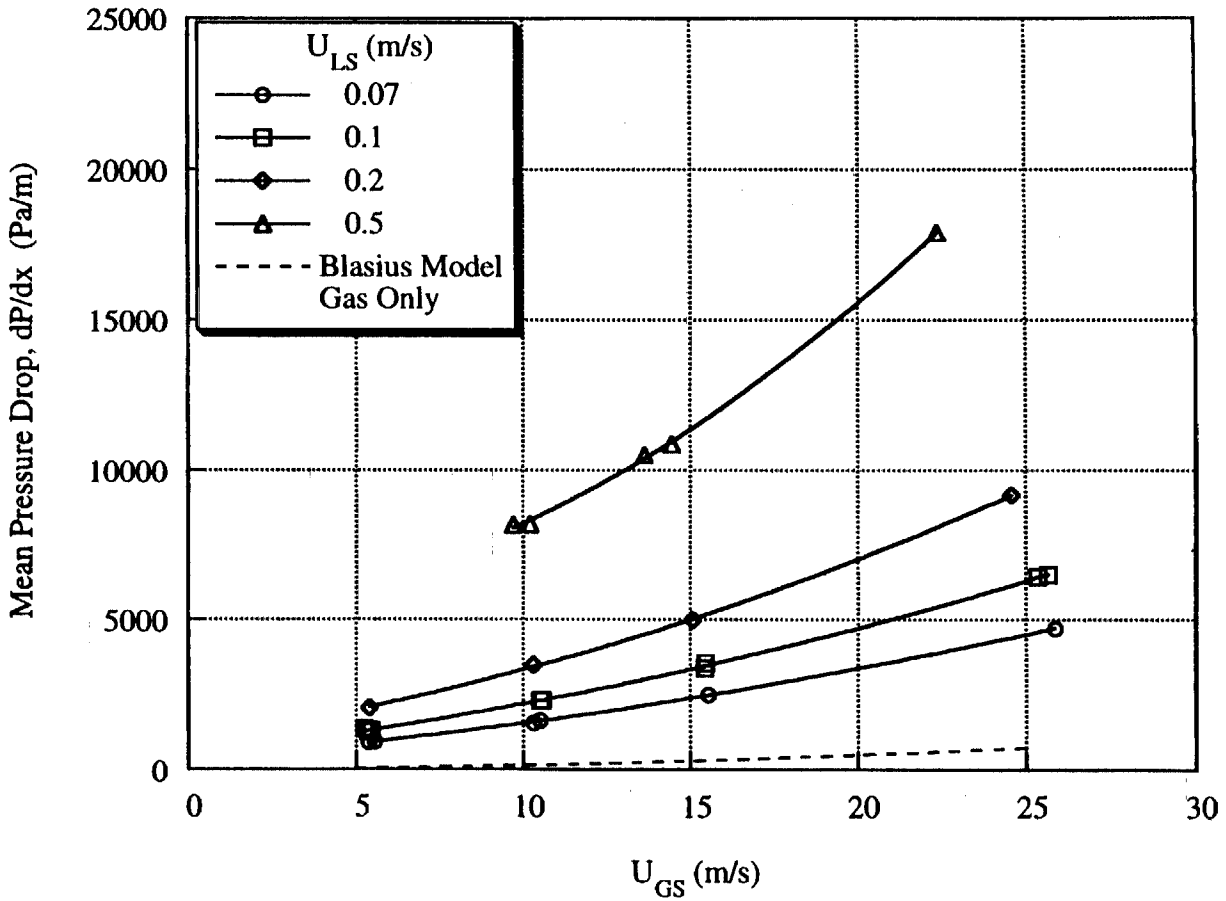

Figure 5.23 Mean Pressure Drop for Microgravity Air-Water/Zonyl FSP Annular Flow in a 12.7 mm ID Tube

fit with second order polynomials. The replicated experimental points indicate that the reproducibility of the measurements was excellent with an average deviation between replicates of 3%. In all cases, the two-phase pressure drop greatly exceeds the single-phase gas pressure drop predicted from the Blasius model.

Comparing Figures 5.21 and 5.22 shows that increasing the viscosity of the liquid results in a significant increase in the pressure drop in all cases. This difference in pressure drop becomes larger as U_{GS} and U_{LS} increase. This increase is likely due in large part to the increased roughness of the higher viscosity liquid films as seen when comparing the film thickness traces in Figure 5.3. Chu and Dukler, 1975 showed that for 1g vertical upward annular flow, the large increase in pressure drop in annular flow over that in single-phase gas flow was due primarily to the small ripple waves on the liquid film and not the form drag over the large waves.

A comparison of Figures 5.21 and 5.23 shows that there is no significant effect of surface tension on the pressure drop with all measurements in the two plots being nearly identical. The comparison of film thickness traces for high and low surface tension in Figure 5.4 shows that there is a large difference in shape and amplitude of the large waves but that both liquid films are relatively smooth. These measurements and observations further support the conclusion of Chu and Dukler, 1975 that the surface roughness, and not the large waves, controls the pressure drop in annular flow.

As discussed in Chapter 4, for purposes of modeling pressure drop in microgravity annular flow, the separated flow models are more appropriate than homogeneous models since there is considerable slip between the phases. One of the earliest but most time-tested annular pressure drop models is the Lockhart-Martinelli model (Lockhart and Martinelli, 1949). This scheme relates the pressure drop of the annular flow to the pressure drops of each phase flowing alone in the pipe. This has the advantage of being easy to use since

correlations for single-phase pressure drop are well established. Miller et al., 1993, showed that the Lockhart-Martinelli model was in fairly good agreement with pressure drop measurements for microgravity annular flow of R-12 in 4.6 mm and 10.5 mm tubes. Based on these results, the Lockhart-Martinelli model was evaluated for the present measurements as well.

In the Lockhart-Martinelli model, the gas two-phase flow multiplier, defined by

$$\phi_G^2 = \frac{\Delta P_{TP}}{\Delta P_G}, \tag{5.4}$$

is used to relate ΔP_{TP}, the two-phase pressure drop, to ΔP_G, the pressure drop of the gas flowing alone in the tube. The Lockhart-Martinelli model provides correlations for ϕ_G based on the Martinelli parameter defined as

$$X^2 = \frac{\Delta P_L}{\Delta P_G}, \tag{5.5}$$

where ΔP_L is the pressure drop of the liquid flowing alone in the tube. The original correlations consisted of a set of graphs to predict ϕ_G based on whether the liquid or gas phases were laminar or turbulent. A more convenient correlation is that provided by Chisholm, 1967,

$$\phi_G^2 = 1 + CX + X^2 . \tag{5.6}$$

The value of C depends on whether the liquid and gas streams would be laminar or turbulent if they were flowing alone in the tube. The appropriate values of C are given in Table 5.1.

Table 5.1

Values of the C constant for the Lockhart-Martinelli-Chisholm Model

Gas Phase	Liquid Phase	C
Turbulent	Turbulent	20
Turbulent	Laminar	12
Laminar	Turbulent	10
Laminar	Laminar	5

The Martinelli parameter can be calculated from the single-phase pressure drops using the standard friction factor approach. The single-phase pressure drops are calculated for either phase with the Fanning equation,

$$\left[\frac{dP}{dx}\right] = \frac{2 f \rho U^2}{D} . \tag{5.7}$$

The Martinelli parameter then becomes

$$X^2 = \frac{f_L \rho_L U_{LS}^2}{f_G \rho_G U_{GS}^2} . \tag{5.8}$$

The single phase friction factors are calculated using the Blasius relation,

$$f = \frac{C_B}{Re^n} , \tag{5.9}$$

where $C_B = 16$, $n = 1$ for laminar flow ($Re < 2000$) and $C_B = 0.046$, $n = 0.2$ for turbulent flow ($Re > 2000$). Once the values of X and ϕ_G have been determined, the two-phase pressure drop is calculated from (5.4).

The pressure drop predicted from the Lockhart-Martinelli-Chisholm model for the superficial velocity conditions in each microgravity annular flow experiment is plotted

against the measured pressure drop in Figure 5.24. As shown, the agreement is fairly good for all three gas-liquid systems studied with an average error of ±20%. A similar level of agreement is reported for 1g vertical annular flows by Wallis, 1969. Miller et al., 1993 reports an average error of 22% for the 10.5 mm ID tube but 56% for the 4.6 mm tube for microgravity annular flow of R-12. Thus based on the present study and the 10.5 mm ID tube results of Miller et al., 1993, it appears that the Lockhart-Martinelli model provides about the same quality of prediction for annular flow pressure drop in microgravity as it does in normal gravity.

Another approach to two-phase pressure drop prediction, presented in Wallis, 1969, is to determine the interfacial friction factor by modifying the Fanning equation (5.7). This approach assumes the gas is flowing through a tube of diameter D - $2\bar{h}$, which is the tube diameter corrected for the average liquid film thickness. The velocity of the gas must also be corrected for the reduced tube diameter by

$$U_G = \frac{U_{GS}}{\left[1-2\frac{\bar{h}}{D}\right]^2} . \tag{5.10}$$

Substituting these modifications into (5.7) leads to the interfacial friction factor,

$$f_i = \frac{(1-2\frac{\bar{h}}{D})^5 D}{2\rho_G U_{GS}^2}\frac{dP}{dx} . \tag{5.11}$$

Predicting the interfacial friction factor from the Blasius correlation would be equivalent to assuming that the liquid film was smooth, and this would lead to a large underprediction of the pressure drop. To account for the roughness of the liquid film, Wallis, 1969, developed an empirical correlation from a large collection of 1g annular flow data. For $0 < \bar{h}/D < 0.04$ (very thin liquid films), the data are well fitted by

$$f_i = 0.005\left[1 + 300\frac{\bar{h}}{D}\right] . \tag{5.12}$$

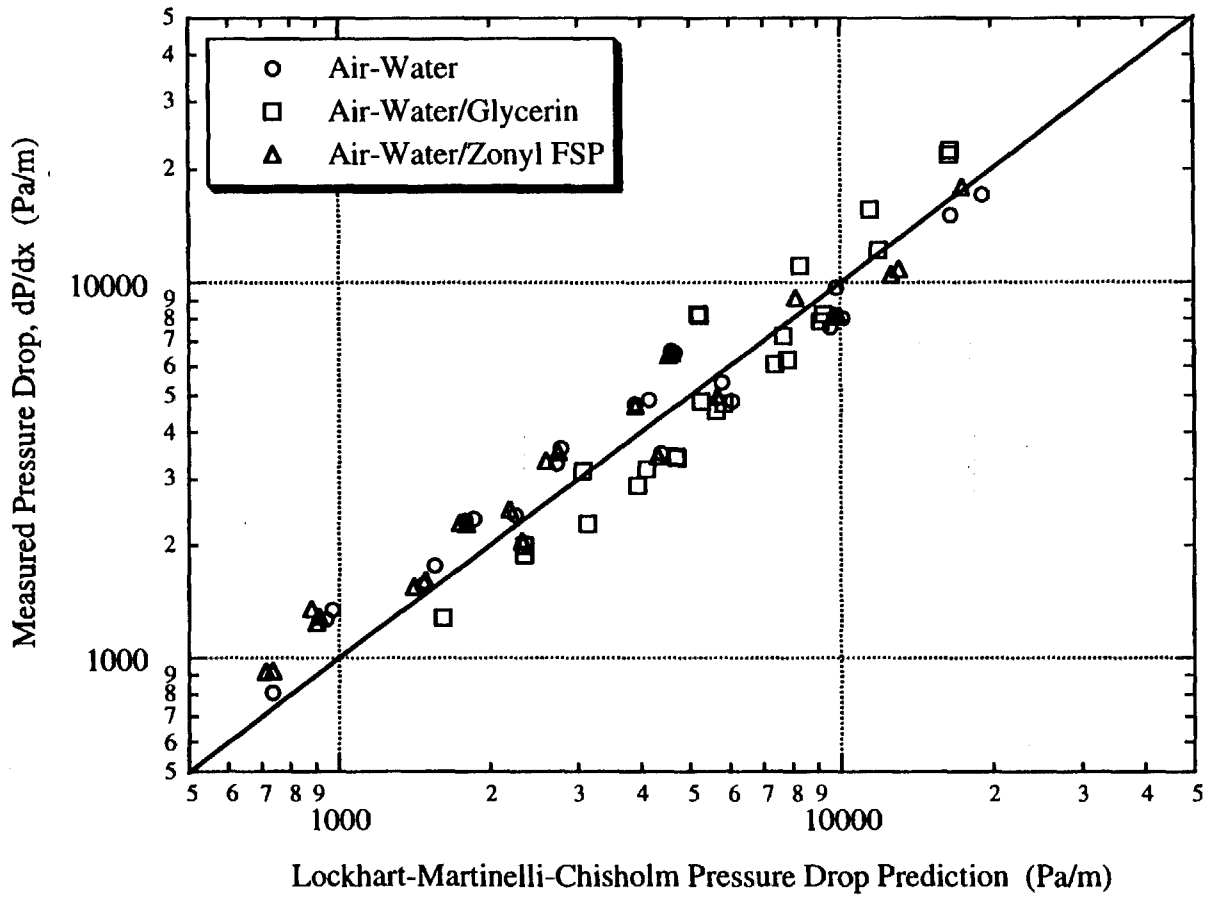

Figure 5.24 Comparison of the Lockhart-Martinelli Model to Measured Microgravity Annular Flow Pressure Drop

The interfacial friction factor was computed from (5.11) for the microgravity annular flow experiments. These are plotted as a function of the dimensionless film thickness, $\bar{h}/D$, in Figures 5.25, 5.26 and 5.27 for air-water, air-water/glycerin and air-water/Zonyl FSP, respectively. As shown, the Wallis model gives good agreement with the data for very thin liquid films but the discrepancy increases sharply with increasing $\bar{h}/D$. This behavior suggests that the assumptions implicit in the derivation of (5.11) and in the data used to develop (5.12) are violated as $\bar{h}/D$ increases. The fact that the discrepancy begins at lower values of $\bar{h}/D$ for higher values of U_{GS} suggests that entrainment of liquid droplets from the film, which also increases with increasing U_{GS}, may be the major cause for this discrepancy. This will be discussed further in later sections. Based on the results in Figures 5.25, 5.26 and 5.27, it is reasonable to conclude that the Wallis model provides a poor prediction of the interfacial friction factor for microgravity annular flow except for very thin liquid films.

5.6 Wall Shear Stress Measurements

Another quantity of interest in developing an understanding of the processes occurring in annular flows is the wall shear stress. The wall shear stress is a measure of the interaction of the liquid film with the tube wall and is an essential component of a force balance on the annular flow. Measurements of wall shear stress may also provide input for simulations of the waves (Wasden, 1989).

The wall shear stress time series trace shown in Figure 2.25 shows a wavy pattern which is qualitatively similar to the film thickness time series. Since the sensing element of the wall shear stress probe was carefully positioned at the same axial location as the film thickness probe (but offset 21° angularly), it is possible to examine the connection between features in the wall shear stress and film thickness time series. As shown in Figure 5.28, the waves in the film thickness trace coincide with the peaks in the wall shear stress

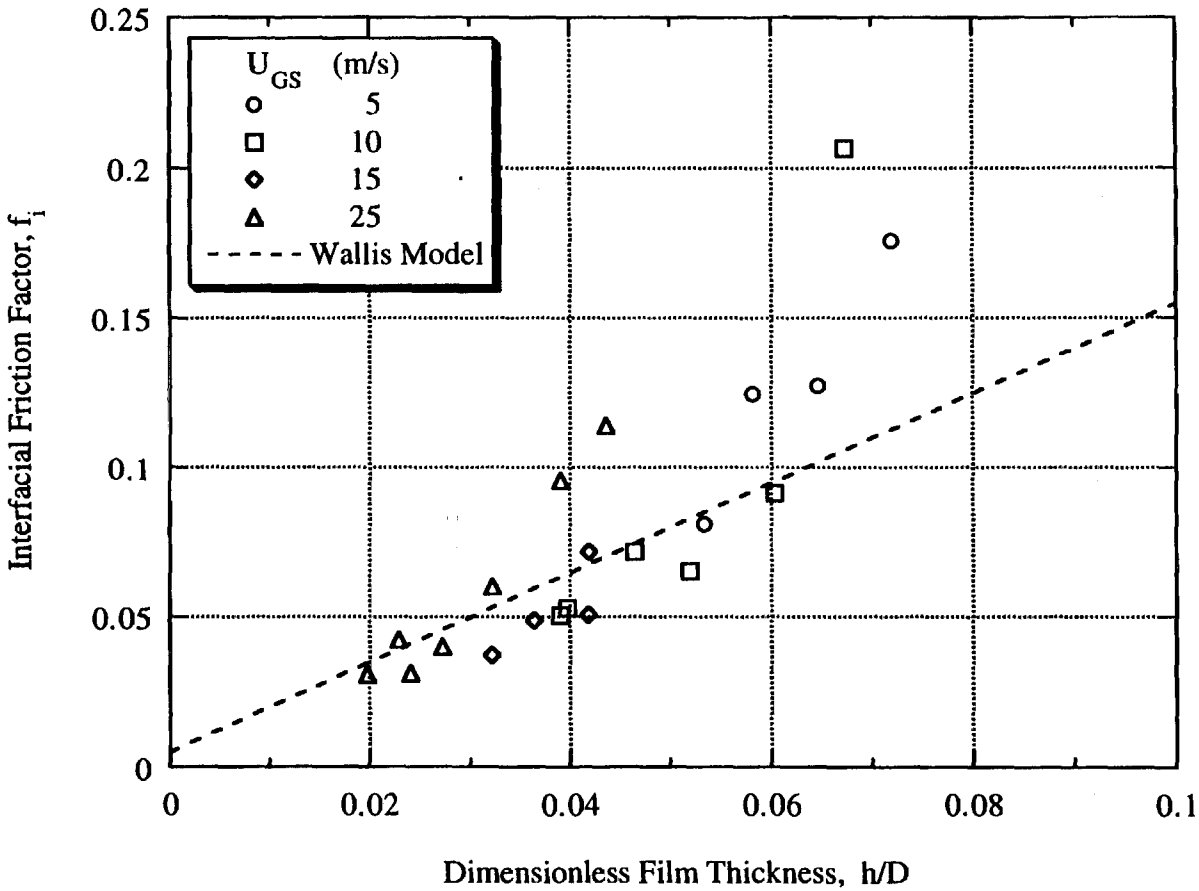

Figure 5.25 Interfacial Friction Factor for Microgravity Air-Water Annular Flow in a 12.7 mm ID Tube

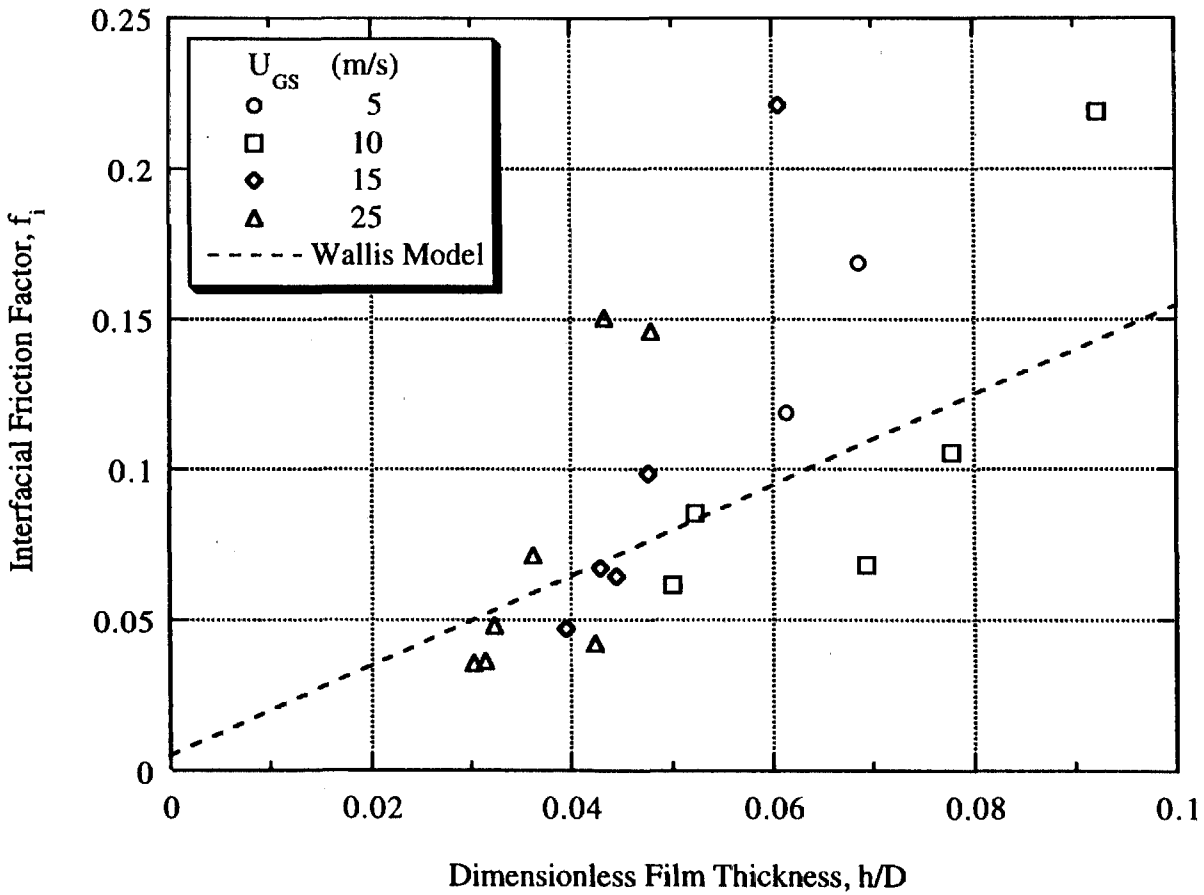

Figure 5.26 Interfacial Friction Factor for Microgravity Air-Water/Glycerin Annular Flow in a 12.7 mm ID Tube

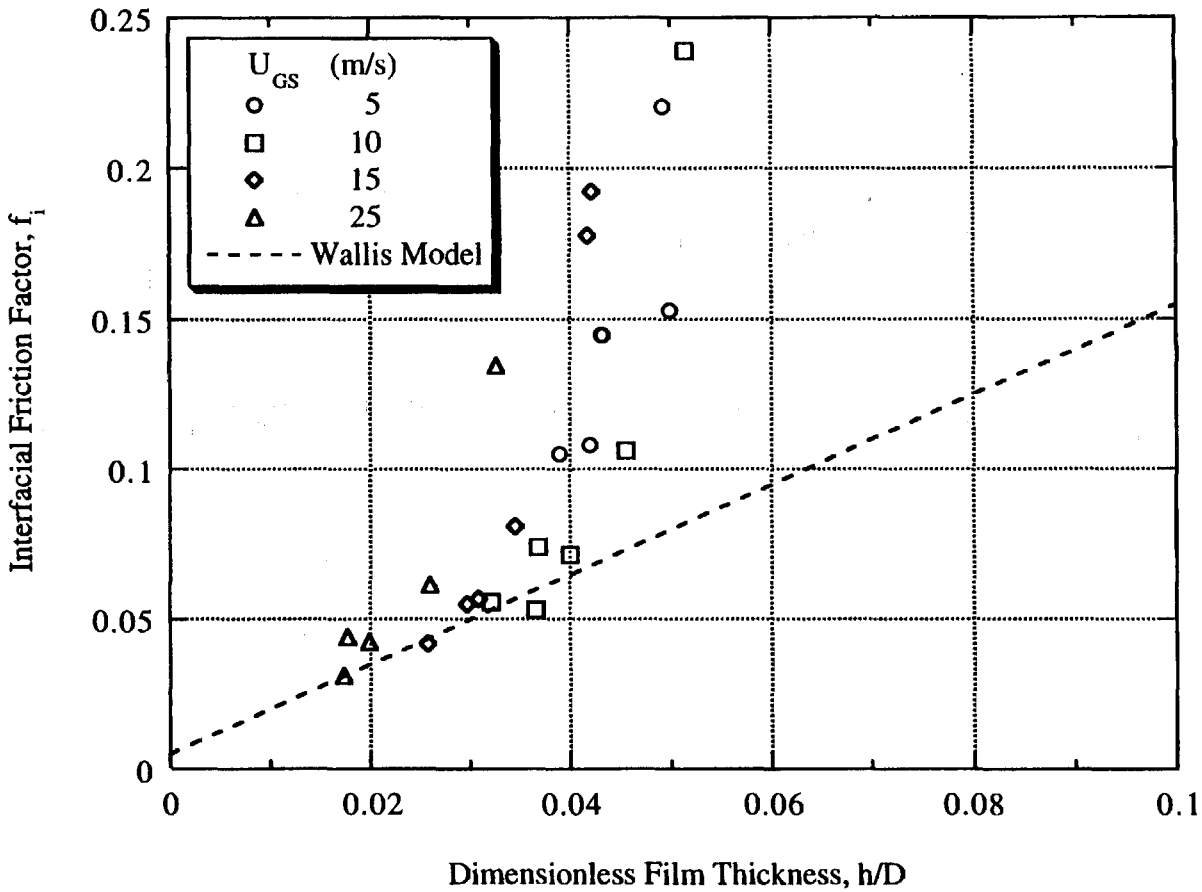

Figure 5.27 Interfacial Friction Factor for Microgravity Air-Water/Zonyl FSP Annular Flow in a 12.7 mm ID Tube

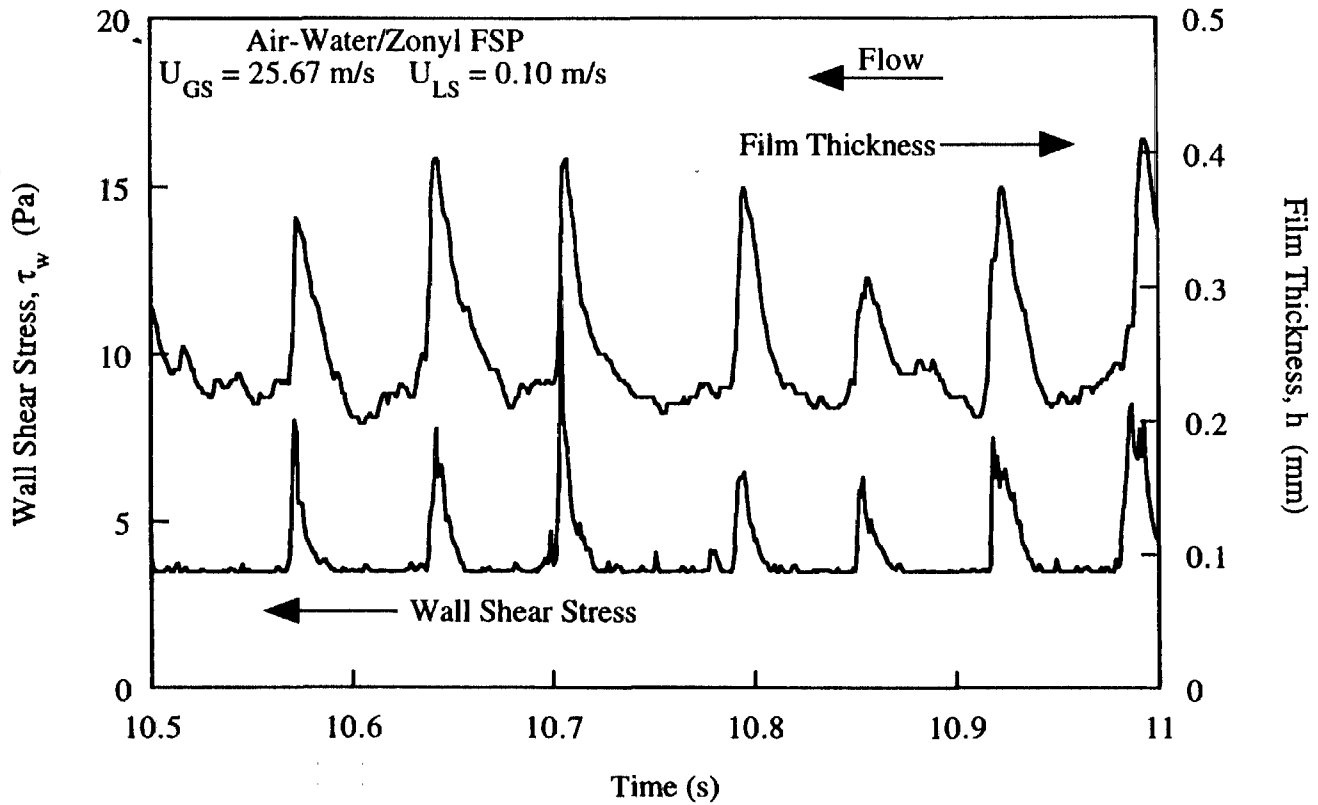

Figure 5.28 Comparison of Wall Shear Stress and Film Thickness Time Series for Microgravity Annular Flow

indicating that the region of the film under the waves experiences the greatest wall shear stress. An expanded view of a single wave, shown in Figure 5.29, indicates that, within the resolution of the measurements, the maximum value in both film thickness and wall shear stress occurs at the same time. This suggests that some of the form drag across the wave is transmitted to the wall of the tube. This was also demonstrated in the wave simulations of Wasden, 1989 for waves on falling films, which show a recirculating region under the wave penetrating into the substrate film near the wall.

The mean values of wall shear stress are shown as a function of U_{LS} and U_{GS} in Figures 5.30, 5.31 and 5.32 for air-water, air-water/glycerin and air-water/Zonyl FSP, respectively. The wall shear stress for air-water/glycerin in Figure 5.31 shows a monotonic increase with both U_{LS} and U_{GS}, but Figures 5.30 and 5.32 exhibit more complex behavior. As shown, for the air-water and air-water/Zonyl FSP plots, the wall shear stress for the lower values of U_{LS} exhibit a minimum while those for the higher values of U_{LS} increase monotonically. The increase in wall shear stress with U_{GS} can be attributed to higher interfacial shear as U_{GS} increases. The presence of a minimum suggests that a second mechanism is also present which becomes important when both U_{LS} and U_{GS} are small.

To gain insight into a possible second mechanism affecting the wall shear stress at low values of both superficial velocities, the high-speed movie films were reexamined. In the air-water and air-water/Zonyl FSP runs for which $U_{LS} \leq 0.1$ m/s and $U_{GS} < 10$ m/s, the waves exhibit a wider range of celerities than at other conditions, as indicated by both movie films and film thickness cross correlations. These waves can be observed growing from a slow moving perturbation in an otherwise smooth film. As the amplitude of these waves increases, they experience a rapid acceleration because the force imposed on the wave by the gas core increases with wave amplitude in a nonlinear fashion. Following this acceleration, the wave amplitude declines again and the celerity decreases. This decline

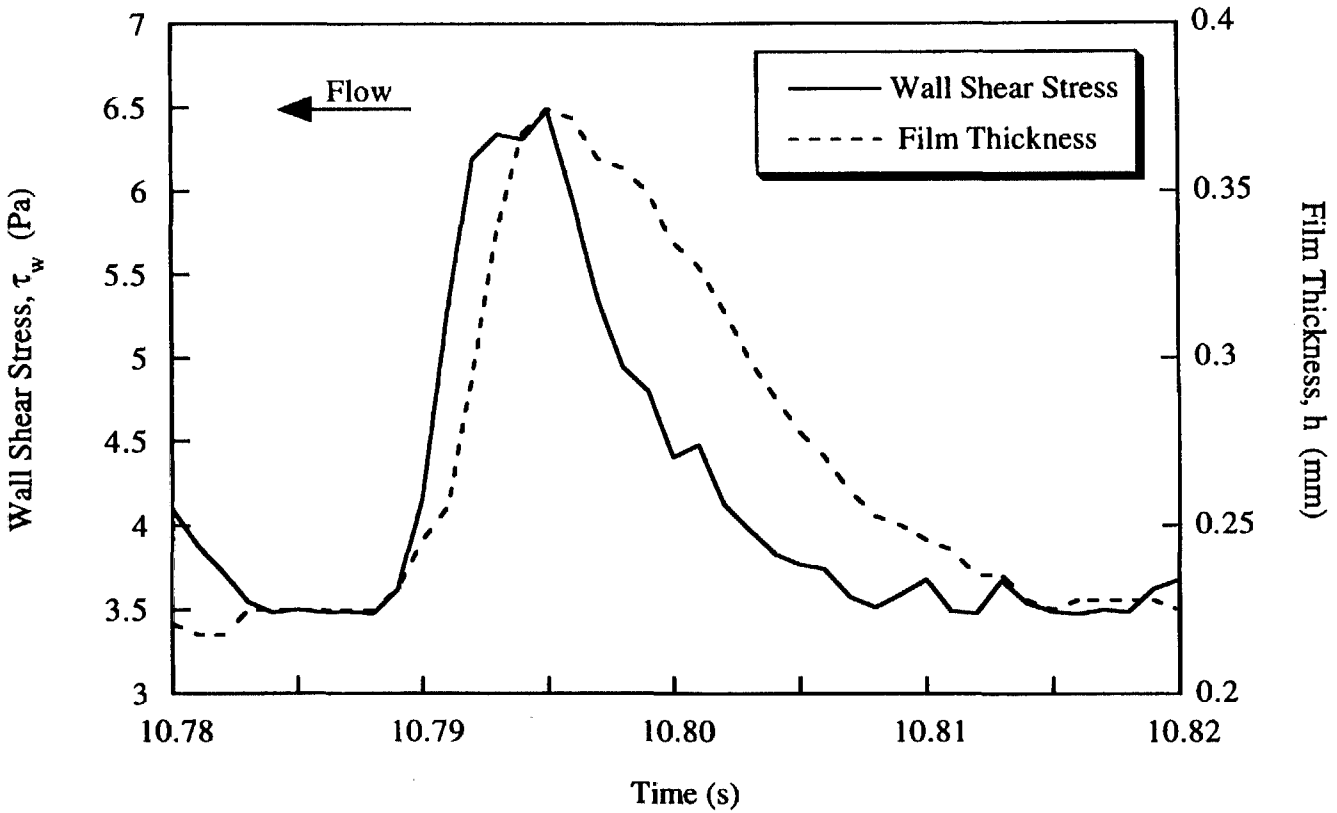

Figure 5.29 Simultaneous Wall Shear Stress and Film Thickness for a Single Microgravity Annular Wave

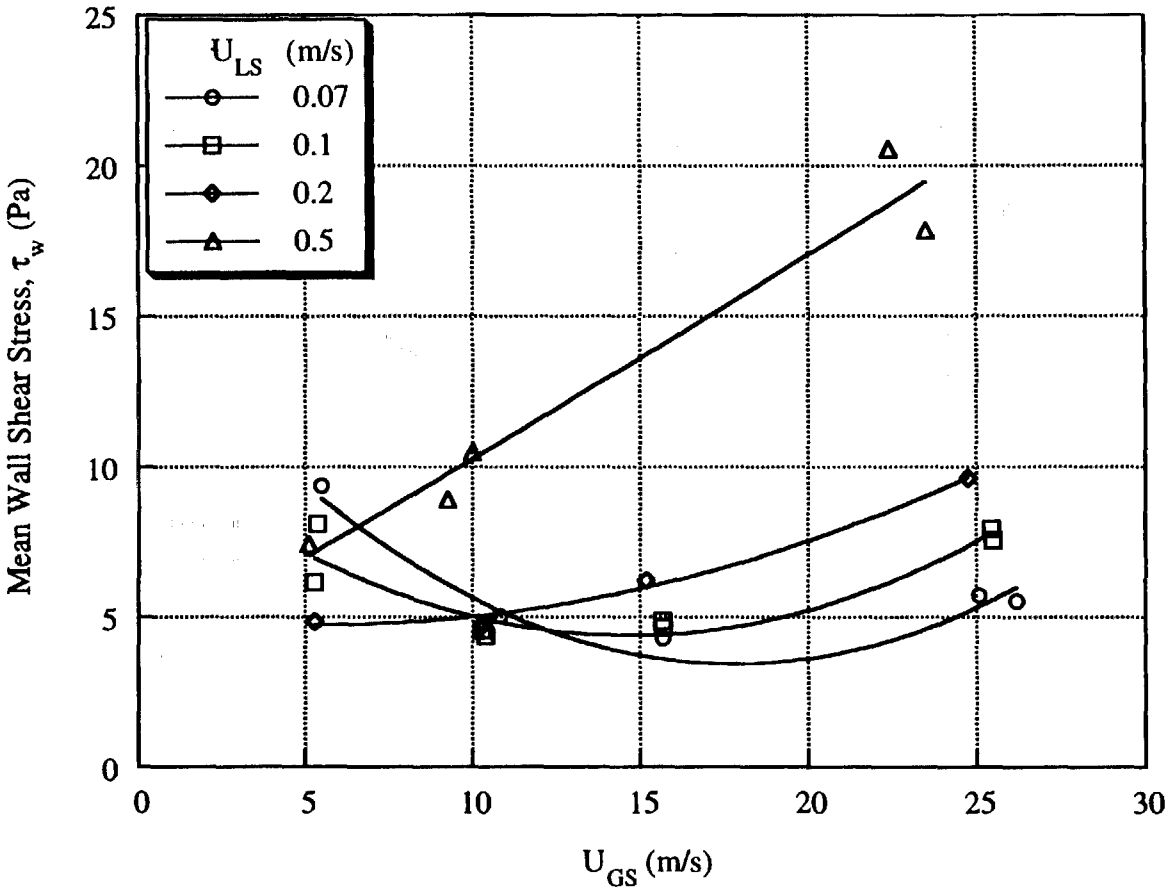

Figure 5.30 Mean Wall Shear Stress for Microgravity Air-Water Annular Flow in a 12.7 mm ID Tube

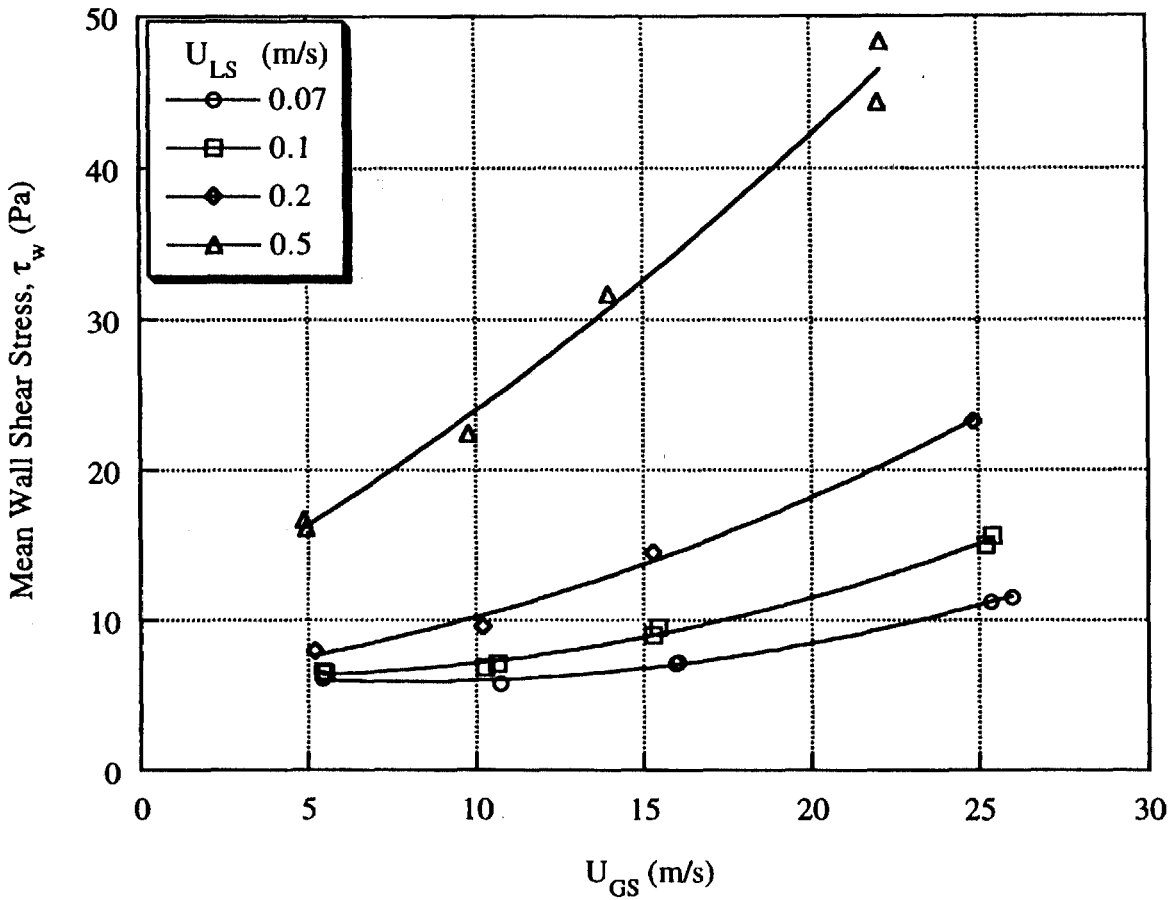

Figure 5.31 Mean Wall Shear Stress for Microgravity Air-Water/Glycerin Annular Flow in a 12.7 mm ID Tube

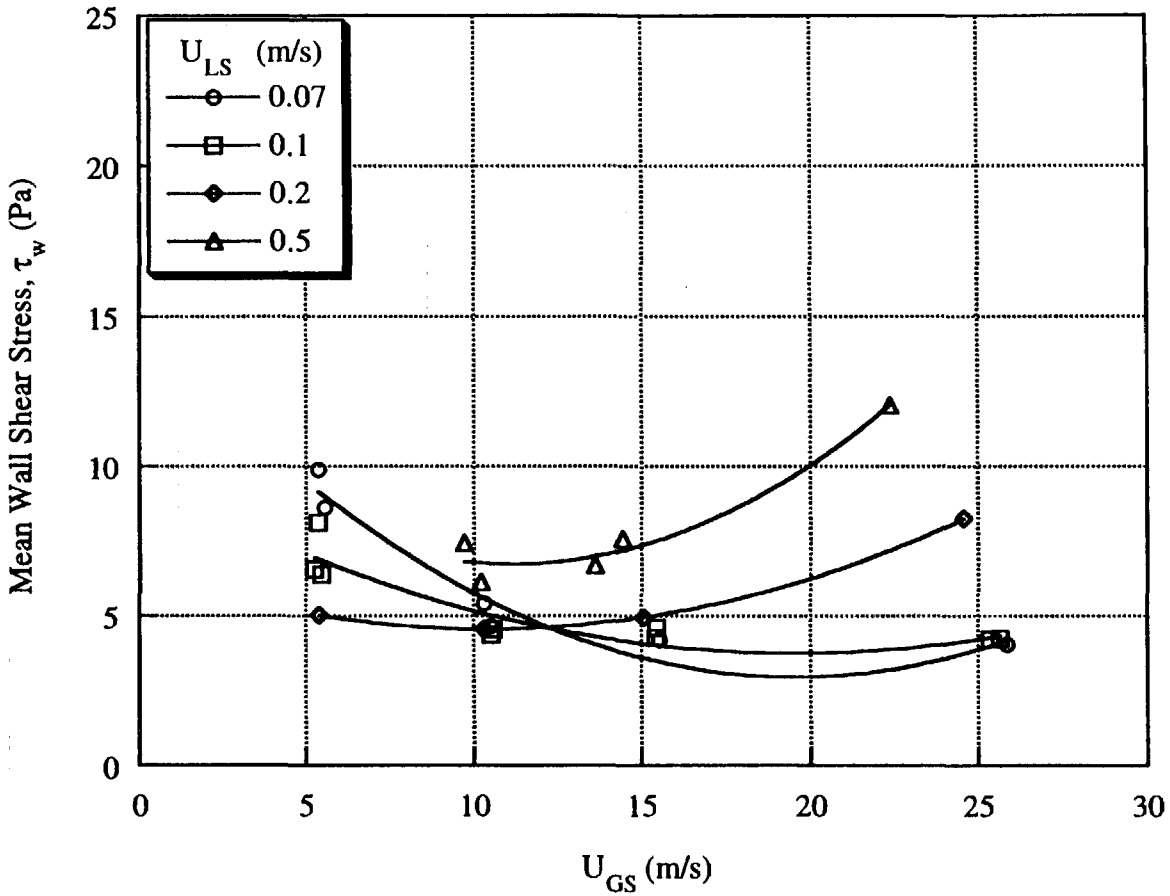

Figure 5.32 Mean Wall Shear Stress for Microgravity Air-Water/Zonyl FSP Annular Flow in a 12.7 mm ID Tube

may be caused by a local increase in the gas velocity over the wave due to a decreased area for flow. As shown previously, as the gas velocity increases, the wave amplitude is suppressed. The overall result is a wave which grows, surges forward and then partially dissipates. These surges create large increases in the wall shear stress leading to a larger mean value. This phenomenon was not observed at higher values of U_{GS} perhaps because the higher velocities may prevent sufficiently large waves from forming. The higher viscosity of the liquid film in the air-water/glycerin experiments may have prevented the rapid growth of large waves since the phenomenon described above is not observed in the air-water/glycerin experiments.

If the proposed mechanism is correct, there should be a larger variation in the wall shear stresses measured for the air-water and air-water/Zonyl FSP experiments conducted at low superficial velocities. The standard deviation of the wall shear stress time series measurements is shown in Figures 5.33, 5.34 and 5.35 for air-water, air-water/glycerin and air-water/Zonyl FSP, respectively. As shown, these measurements follow the same trend as the mean wall shear stress measurements with a large increase in the standard deviation at low values of both U_{GS} and U_{LS} for both the air-water and air-water/Zonyl FSP experiments. The air-water/glycerin experiments do not show this increase in standard deviation. While the data are consistent with the proposed mechanism, a more detailed study would be required to verify this.

5.7 Annular Flow Force Balances

A more detailed understanding of microgravity annular flow is possible if the total pressure drop is separated into its component parts, as was demonstrated by Lopes and Dukler, 1986 and Fore, 1993 for 1g annular flows. An overall force balance on the annular flow yields

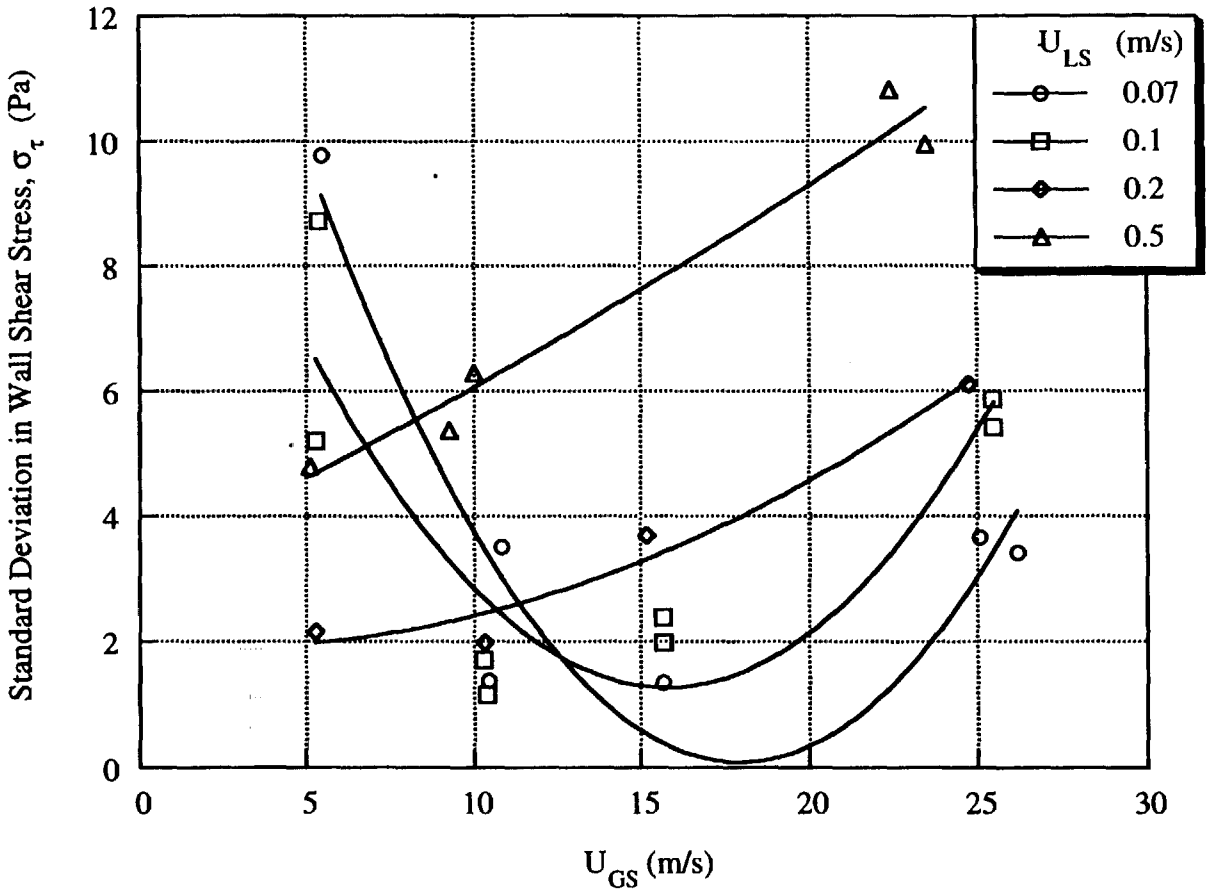

Figure 5.33 Standard Deviation in Wall Shear Stress for Microgravity Air-Water Annular Flow

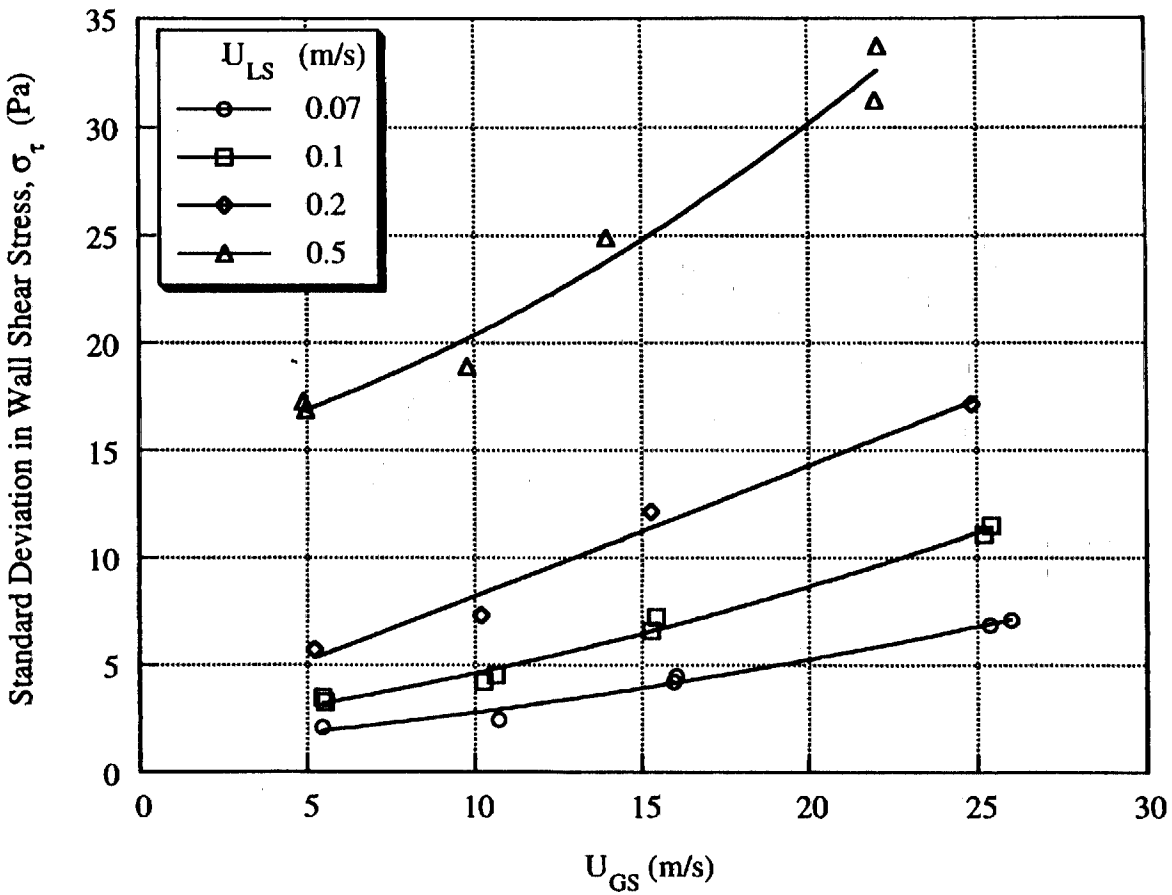

Figure 5.34 Standard Deviation in Wall Shear Stress for Microgravity Air-Water/Glycerin Annular Flow

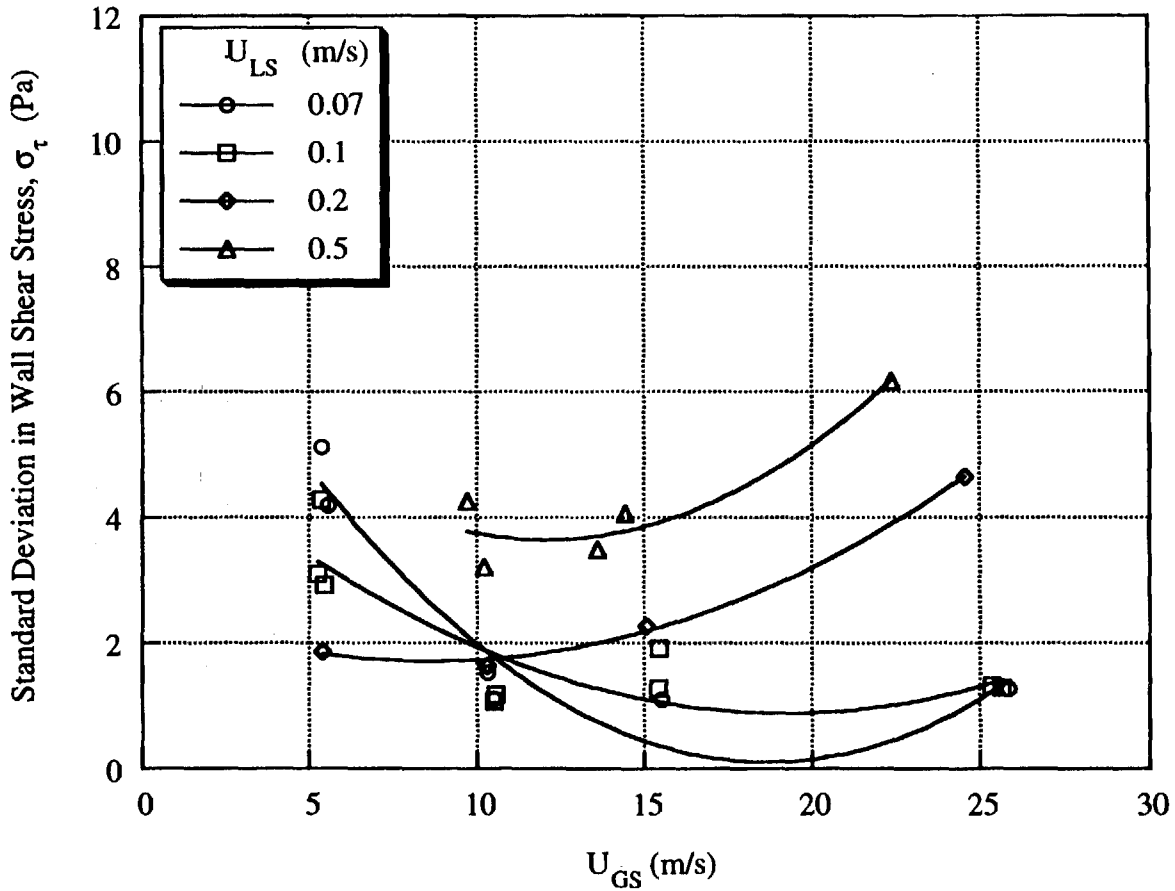

Figure 5.35 Standard Deviation in Wall Shear Stress for Microgravity Air-Water/Zonyl FSP Annular Flow

$$-\frac{\Delta P}{L} = \frac{4}{D}\tau_w + \frac{4}{D} g \rho_L \bar{h} + g \rho_{GC} \frac{(D-2\bar{h})^2}{D^2} + A_E \,, \tag{5.13}$$

where ρ_{GC} is the density of the gas core (including entrained droplets) and A_E is the net momentum loss due to droplet entrainment, acceleration and deposition. The second and third terms on the right side of (5.13) represent the hydrostatic pressures for the liquid film and the gas core, which are negligible in microgravity. The remaining terms on the right side of (5.13) can be thought of as contributions to the total pressure drop. Thus the total pressure drop can be represented as

$$-\frac{\Delta P_T}{L} = \frac{\Delta P_{WF}}{L} + \frac{\Delta P_E}{L} \,. \tag{5.14}$$

The first term on the right in (5.14) is the pressure drop due to wall friction while the second term is the pressure drop due to entrainment, acceleration and deposition of droplets.

The total pressure drop was measured directly and the pressure drop due to wall friction can be computed from the wall shear stress measurements and $(4/D)\tau_w$ on the right side of (5.13). Entrainment characteristics could not be measured directly in this study.

Entrainment measurements even in normal gravity are difficult to perform. The procedure requires either removing the liquid film through a porous section of the tube wall and collecting the liquid remaining in the gas core (Fore, 1993) or sampling the gas core with a pitot tube (Asali, 1984). Both techniques require careful experimental attention and are not, in present form, suitable for automated operation in the microgravity environment. The entrained liquid fraction is also sufficiently small so that several minutes of collection time are required to obtain an accurately measurable sample. These problems prevented entrainment measurements in the short microgravity periods available in the present study.

Since two of the three terms in (5.14) were measured directly, the difference between these yields information about droplet entrainment and deposition. The ratio of total pressure drop to pressure drop due to wall friction is shown in Figures 5.36, 5.37 and 5.38 for air-water, air-water/glycerin and air-water/Zonyl FSP, respectively. In the limit of $U_{GS} = 0$, the rate of entrainment would be negligible and the ratio shown in Figures 5.36, 5.37 and 5.38 should become unity. In Figures 5.37 and 5.38, the ratio slightly exceeds unity at the lowest values of U_{GS}, but this difference is within the 10-15% uncertainty estimated for the wall shear measurements. As U_{GS} increases, the rate of entrainment should also increase and the ratio of wall frictional to total pressure drop should decrease. As shown in all three cases, the ratio tends towards unity for the lowest values of U_{GS} and U_{LS} and decreases as U_{GS} increases. In all cases, the ratio converges to a single value, independent of U_{LS}, at the highest value of U_{GS}.

The results in Figures 5.36, 5.37 and 5.38 suggest that much of the total pressure drop can be attributed to entrainment effects. At the highest values of U_{GS}, only 37% of the total pressure drop can be accounted as wall friction in Figure 5.36 for air-water. The increased liquid viscosity results in about 60% of the total being attributable to wall friction at high U_{GS} in Figure 5.37, suggesting that entrainment is reduced for the high viscosity liquid case. The ratio of wall frictional to total pressure drop decreases to 20% at high U_{GS} in Figure 5.38 for the air-water/Zonyl FSP case suggesting that entrainment increases with a decrease in surface tension. This is reasonable since surface tension forces play a large role in maintaining the cohesiveness of the liquid film. As the surface tension is reduced, the rate of entrainment would be expected to increase. This effect may also be responsible for the decreased wave amplitude and film thickness for the air-water/Zonyl annular flows if the wave crests are more easily entrained into the gas core.

Similar analyses by Lopes and Dukler, 1986 and Fore, 1993 for air-water vertical upward annular flow in 1g showed similar qualitative behavior but the fraction of the total

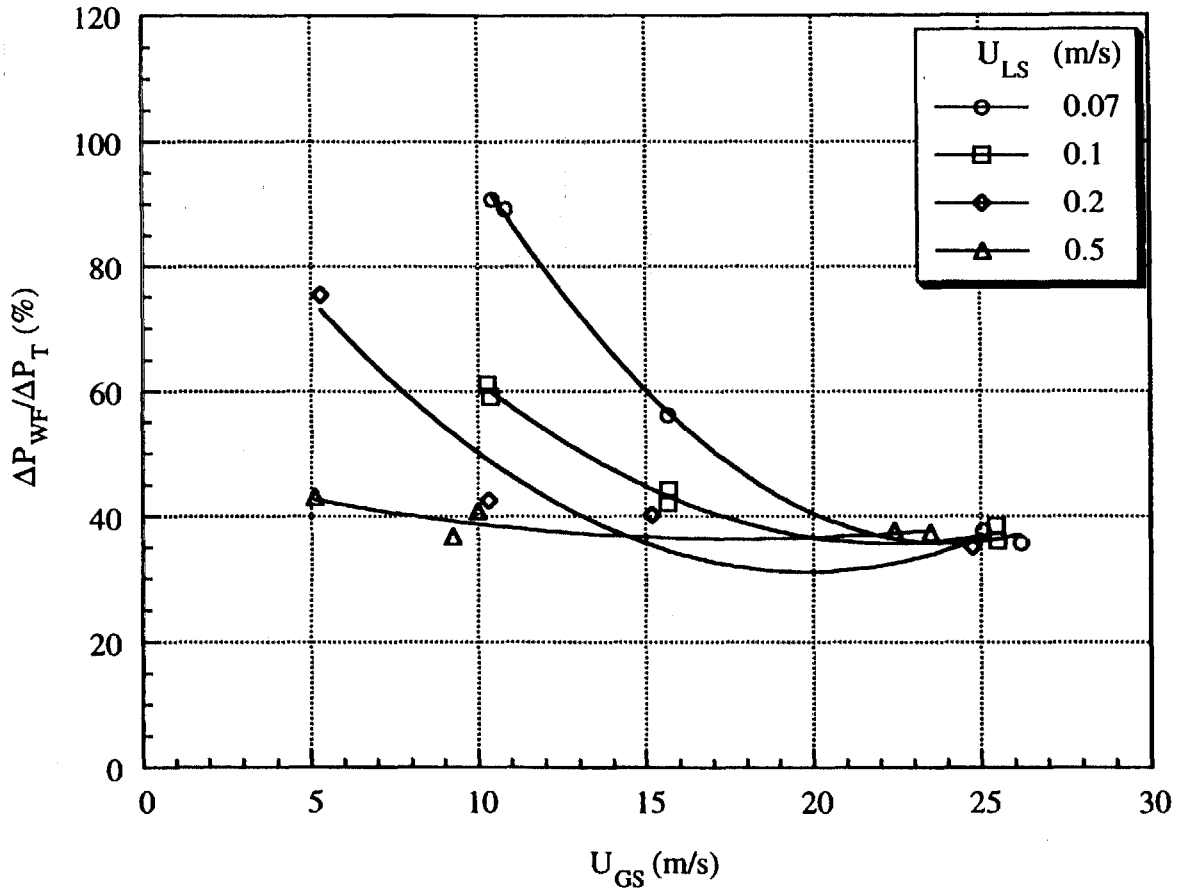

Figure 5.36 Fraction of Total Pressure Drop Due to Wall Friction for Microgravity Air-Water Annular Flow

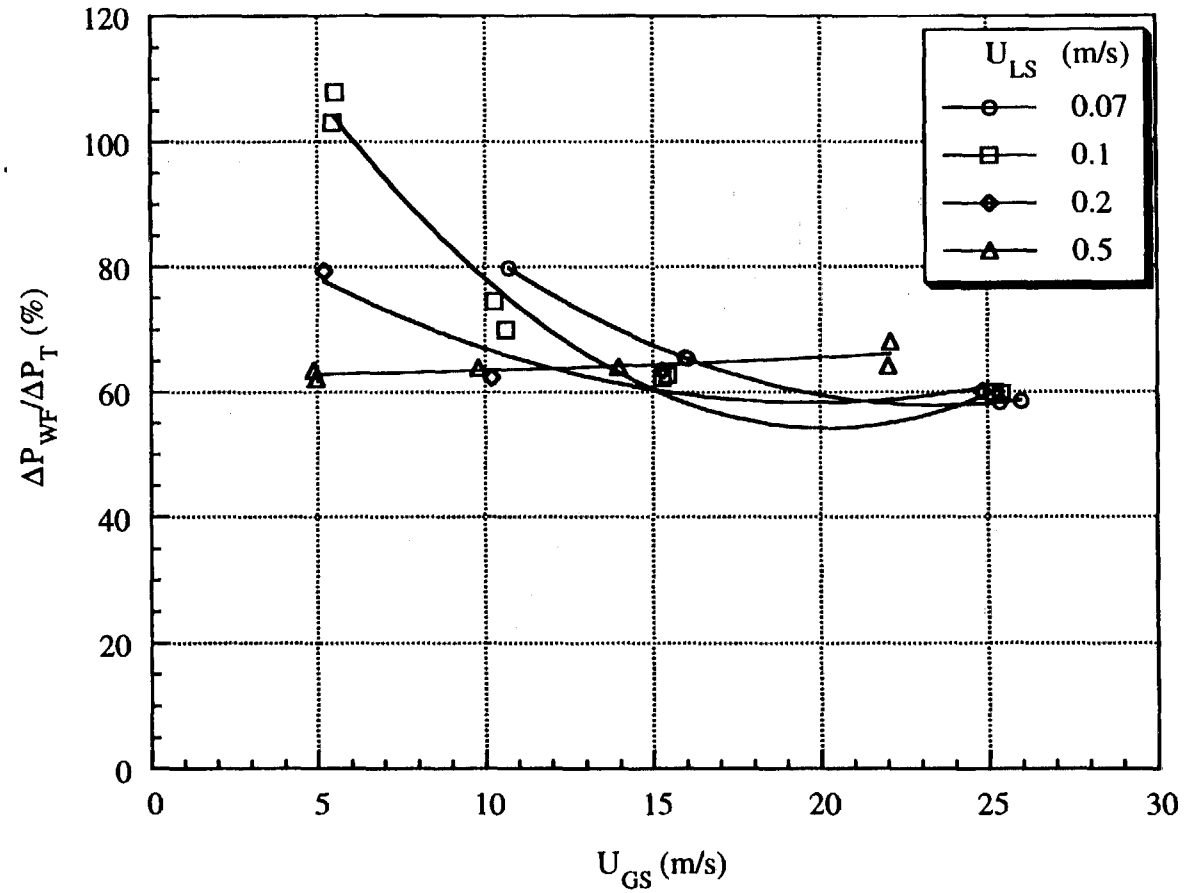

Figure 5.37 Fraction of Total Pressure Drop Due to Wall Friction for Microgravity Air-Water/Glycerin Annular Flow

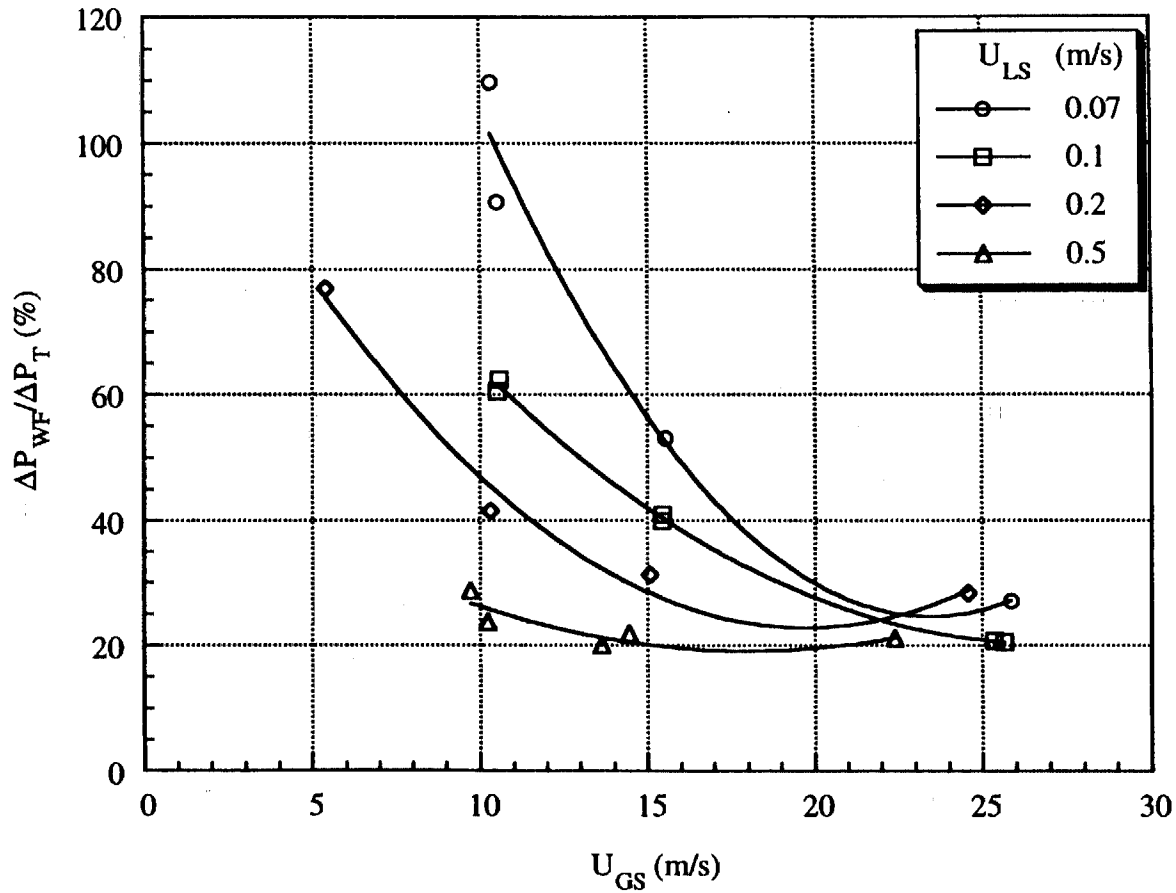

Figure 5.38 Fraction of Total Pressure Drop Due to Wall Friction for Microgravity Air-Water/Zonyl FSP Annular Flow

pressure drop attributed to entrainment was only about 20% at high U_{GS}. In those studies however, the pressure drop due to gravitational terms was more than 50% of the total pressure drop. When the dominant gravitational force is removed, weaker forces have a greater impact on the overall result. In the absence of direct entrainment measurements, the results cannot be checked by comparing the left and right hand sides of (5.14). In the present analysis, measurement errors or other pressure drop effects are included in the entrainment term. This makes the accuracy of the quantitative results in Figures 5.36, 5.37 and 5.38 suspect. However the qualitative effects of U_{GS} and the liquid physical properties on entrainment seem reasonable.

If the entrainment results presented in this study are correct, entrainment processes are the dominant component in microgravity annular pressure drop and the proportion of liquid existing in the form of entrained droplets may be large. This would suggest the need for direct measurements of the entrainment rate in the microgravity environment. Long duration spacecraft experiments would likely be required to make such measurements accurately.

5.8 Film Thickness Modeling

The film thickness, wall shear stress and pressure drop measurements presented previously can also be used to assess the utility of film thickness models available in the literature for use in microgravity annular flow.

The general consensus in the 1g annular flow literature (Kosky, 1971, Henstock and Hanratty, 1976, Laurinat et al., 1984, Asali et al., 1985 and Ambrosini et al., 1991) is that the mean film thickness can be expressed in the form,

$$h_L^+ = X\, Re_{LF}^Y , \qquad (5.15)$$

where X and Y are constants. The dimensionless film thickness, h_L^+, is defined as

$$h_L^+ = \frac{h\, U_L^*}{\nu_L}, \tag{5.16}$$

with the liquid friction velocity, U_L^*, calculated as

$$U_L^* = \sqrt{\frac{\tau_c}{\rho_L}}. \tag{5.17}$$

The characteristic shear stress, τ_c, is usually taken to be either the wall or interfacial shear stress or a combination of the two. Ambrosini et al., 1991 claims that the difference between τ_w and τ_i is negligible and thus the value of U_L^* is fairly insensitive to the particular combination of these used to define τ_c. The film Reynolds number is defined as

$$Re_{LF} = \frac{4\,\Gamma_{LF}}{\mu_L}, \tag{5.18}$$

where Γ_{LF} is the mass flow rate of the liquid film (corrected for entrainment) per unit perimeter (Kosky, 1971).

The simplest model, proposed by Kosky, 1971, assumes that the film is a smooth parallel flow. The film Reynolds number is then calculated as

$$Re_{LF} = 4 \int_0^{\delta^+} u^+ \, dy^+, \tag{5.19}$$

where the dimensionless velocity is

$$u^+ = \frac{u}{U_L^*}, \tag{5.20}$$

and the dimensionless distance from the wall is

$$y^+ = \frac{y\, U_L^*}{\nu_L}. \tag{5.21}$$

Using the accepted turbulent velocity profile for pipe flow, for $y^+ < 5$, the velocity profile is

$$u^+ = y^+ , \tag{5.22}$$

which leads to

$$\delta^+ = \left[\frac{Re_L}{2}\right]^{1/2} . \tag{5.23}$$

For thicker films ($y^+ > 5$), Kosky, 1971 used the Prandtl power law profile

$$u^+ = 8.74\,[y^+]^{1/7} , \tag{5.24}$$

which leads to

$$\delta^+ = 0.0504\,Re_{LF}^{7/8} . \tag{5.25}$$

The two models match at $Re_{LF} = 1143$.

Kosky, 1971 was able to show that air-water vertical annular flow data available from several sources in the literature was in fair agreement with this model. An extension of this model was presented by Henstock and Hanratty, 1976. This model incorporates the van Driest eddy viscosity model into the velocity profile and uses a weighted average of the wall and interfacial shear stresses for the characteristic shear stress. The resulting film thickness model, valid over the entire range of Re_{LF}, is

$$h^+ = \left[(0.707\,Re_{LF}^{0.5})^{2.5} + (0.0379\,Re_{LF}^{0.9})^{2.5}\right]^{0.4} , \tag{5.26}$$

with the characteristic shear stress for use in (5.17) computed by

$$\tau_c = \frac{1}{3}\tau_i + \frac{2}{3}\tau_w . \tag{5.27}$$

Henstock and Hanratty, 1976 as well as Ambrosini et al., 1991, showed that this model was also in fairly good agreement with experimental measurements available in the literature.

The liquid film Reynolds number, Re_{LF}, used in these studies is based on the flow rate of liquid in the film, which is the difference between the input liquid flow rate and the volume of liquid entrained into the gas stream. Computing the Reynolds number in this way requires that the fraction of liquid entrained into the gas core be known. The difficulties associated with entrainment measurements or predictions severely limit the usefulness of models requiring this measurement. As mentioned previously, entrainment measurements could not be made in the present study and the Reynolds number based on the liquid film flow rate could not be computed.

The entrainment studies of Fore, 1993 showed the rate of entrainment to be a strong function of U_{GS} but a weak function of U_{LS} for $Re_L > 750$ and it is therefore reasonable to assume that the mean film thickness should vary with Re_L (based on U_{LS}) in approximately the same manner as with Re_{LF} (based on the film flow rate). The validity of this assumption may be limited at the lower values of U_{GS} where Figures 5.36, 5.37 and 5.38 suggest that the rate of entrainment is a strong function of U_{LS}. The film thickness was modeled with (5.15), (5.16) and (5.17) using the Reynolds number based on the superficial liquid velocity rather than that based on the film flow rate. The characteristic shear stress was taken to be the wall shear stress since this was measured directly in the present study.

The microgravity annular flow film thickness data, non-dimensionalized with the measured wall shear stress, are plotted against Re_L in Figure 5.39. The predictions from the Kosky model, (5.23) and (5.25), and the Henstock and Hanratty Model, (5.26) are also shown. As shown, the models coincide at both high and low Reynolds number but

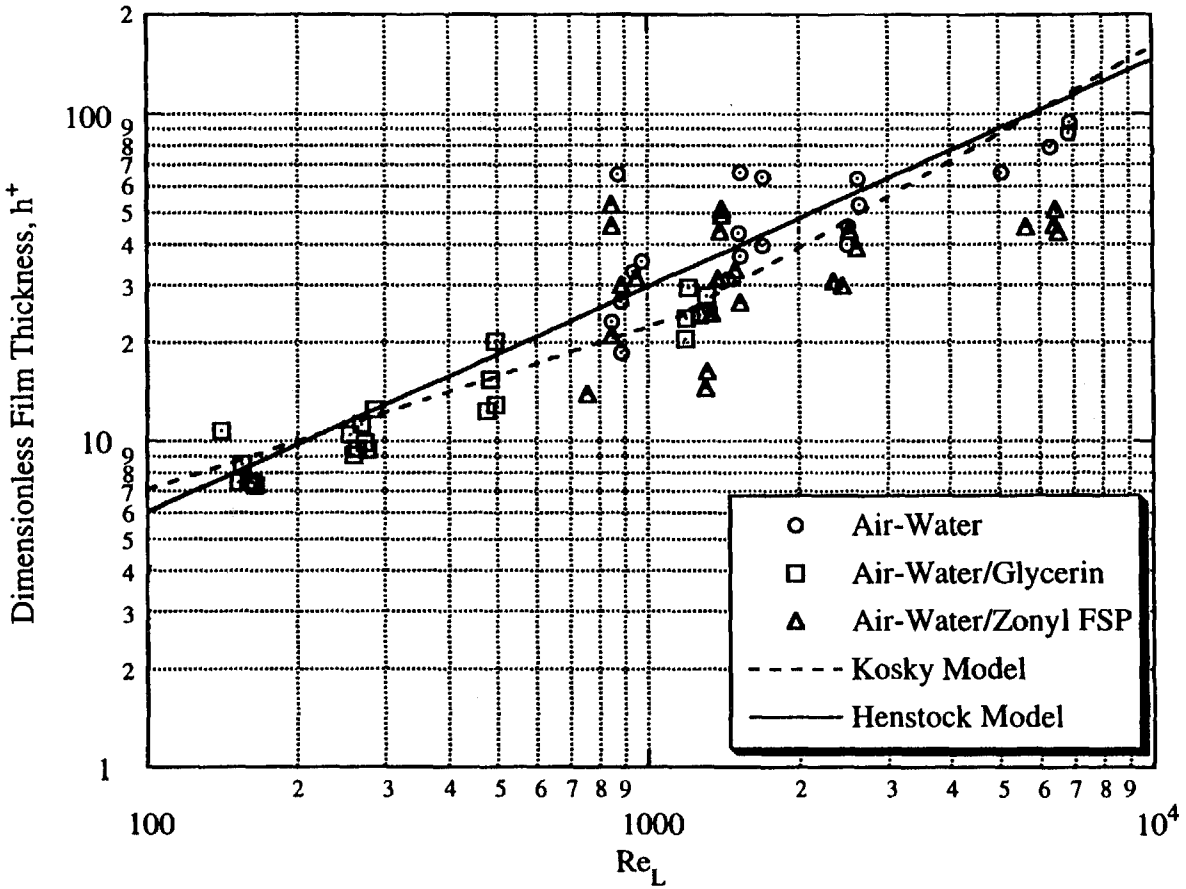

Figure 5.39 Comparison of Experimental Results and Film Thickness Models for Microgravity Annular Flow

deviate from each other in the laminar-turbulent transition region. The air-water/glycerin data are in good agreement with both models at low Re_L while the air-water data show fair agreement at high Re_L. The air-water/Zonyl FSP data show poor agreement with the models at all Re_L. The data show much scatter in the transition region.

The results shown in Figure 5.39 indicate that the film thickness models of Kosky, 1971 and Henstock and Hanratty, 1976 are only moderately successful. The large discrepancy between the models and the low surface tension results may again indicate that entrainment increases as the surface tension decreases. Similar agreement between the models and 1g annular data was reported in the original works. While these models have attempted a mechanistic approach to film thickness modeling, they still do not appear to capture all of the processes occurring in the flow.

Unfortunately, the strictly empirical approach to film thickness modeling provides a more satisfactory near-term result. The best agreement was found using the functionality of (5.15) with the film thickness nondimensionalized with the wall shear stress calculated from the total pressure drop. This result serves as a design equation because only quantities which are easily measured or predicted are required. The results are shown in Figure 5.40 for microgravity annular flow. As shown, when the film thickness is non-dimensionalized by the wall shear stress computed from the total pressure drop, the data from all three fluids nearly collapse into a single trend. As shown, the data are well fitted by

$$h^+ = 0.265\, Re_L^{0.695} \,. \qquad (5.28)$$

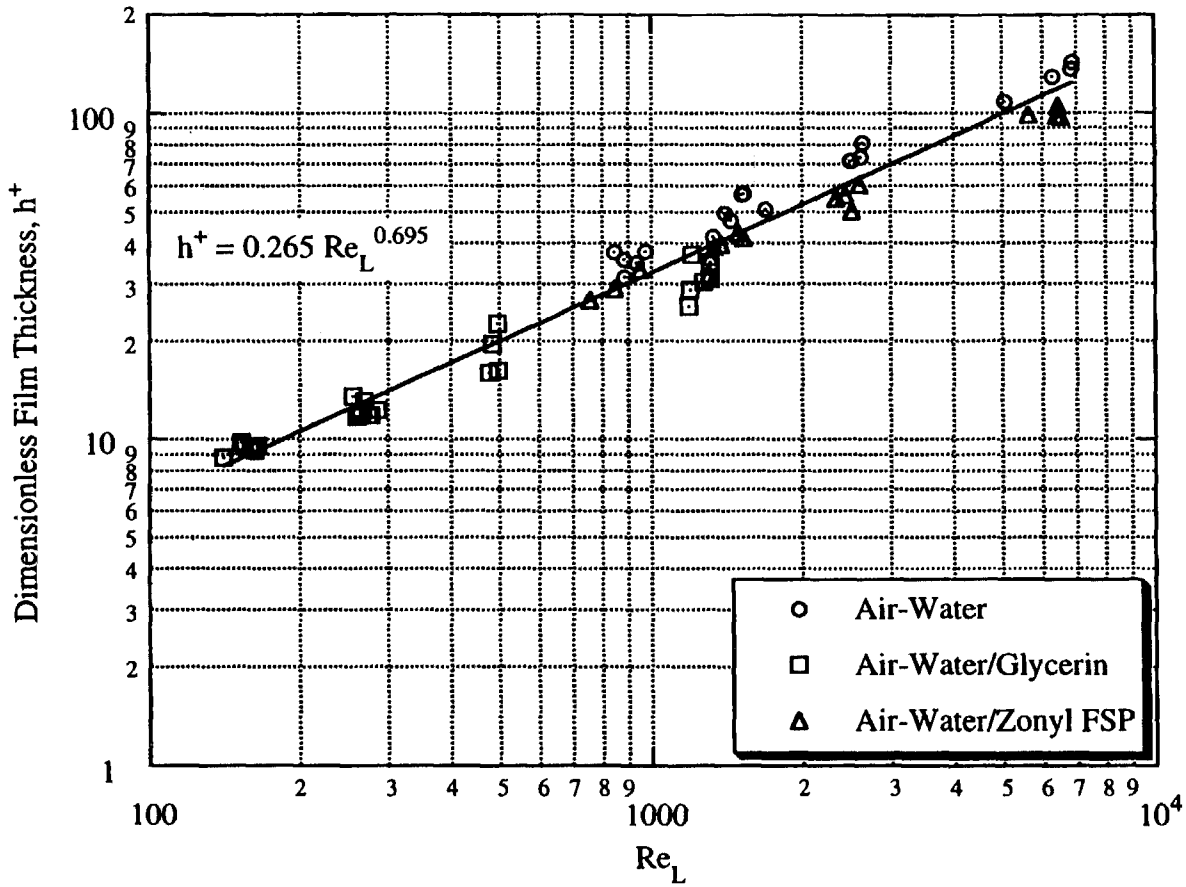

Figure 5.40 Empirical Model for Dimensionless Film Thickness for Microgravity Annular Flow

Chapter 6 Flow Pattern Transition Models

6.1 Introduction

Flow pattern maps were presented in Chapter 3 which showed the occurrence of the different patterns as a function of superficial velocities, liquid physical properties and tube diameter. Two transitional states, bubble-slug flow and slug-annular flow, were identified as having characteristics common to both adjacent patterns. These transitional states were studied in detail to determine possible mechanisms of transition from one pattern to the other. For both transitions, the void fraction was found to be a unique indicator of the flow pattern since experiments with different flow patterns were never found to have the same void fraction. Based on these findings, and the more detailed knowledge of the properties of these flow patterns developed in chapters 4 and 5, mechanistic flow pattern transition models can be developed. Such models would be useful in the design and operation of microgravity gas-liquid flow systems since the behavior of these systems is strongly dependent on the flow pattern.

Another indicator of flow pattern, suggested recently by Zhao and Rezkallah, 1993, is the Weber number. Since this model also shows promise, it will be evaluated with the current flow pattern data and compared to void fraction based models.

6.2 Void Fraction Based Bubble-Slug Transition Model

A simple mechanism for the transition from bubble to slug flow assumes that the transition occurs when the bubble density is sufficient for the bubbles to encounter each other and coalesce due to surface tension (Dukler, et al. 1988). This mechanism implies that the transition should occur at a distinct value of void fraction.

The void fraction measurements shown in Figures 4.2, 4.3 and 4.4 indicate that the experiments identified as bubble-slug transition lie in a range of void fractions separating the bubble and slug flow experiments. As shown, each flow pattern occupies a distinct range of void fractions with little overlap. The slight overlap between flow patterns is probably a result of the subjective nature of flow pattern identification. For the 12.7 mm ID test section experiments, the range of void fractions occupied by the bubble-slug experiments is shown in Table 6.1. As noted previously, reliable void fraction data were not obtained for the 25.4 mm ID test section experiments.

Table 6.1

Range of Void Fraction for the Microgravity Bubble-Slug Transition Experiments in a 12.7 mm ID Tube

Fluids	Range of Void Fraction	Center Point of Range
Air-Water	0.31 - 0.49	0.40
Air-Water/Glycerin	0.30 - 0.43	0.36
Air-Water/Zonyl FSP	0.38 - 0.53	0.46

The maximum packing density of the bubbles imposes a limitation on the maximum void fraction which can exist before the bubble must touch and coalesce. For spherical bubbles packed into a cylinder, a maximum void fraction of 0.52, independent of bubble diameter, can be achieved. The maximum value of 0.53 reported for air-water/Zonyl FSP in Table 6.1 is consistent with this limit within the error of the void fraction measurement. While a void fraction of 0.52 represents the upper limit for stationary spherical bubbles

packed into a tube, distortion of the bubble shape and radial bubble motion in the tube due to turbulence cause bubbles to contact each other at lower values of void fraction. This is demonstrated in Figures 4.2 and 4.3 for air-water and air-water/glycerin where slug flow clearly exists at void fraction values less than 0.52.

To develop a void fraction based bubble-slug transition model, the Drift-Flux model development presented in Chapter 4 will be utilized since this model was shown to be valid for microgravity bubble and slug flows. By substituting (4.3) into (4.7) and solving for U_{LS}, the following relation, valid for bubble and slug flow, is obtained,

$$U_{LS} = \frac{(1 - C_o\langle\alpha\rangle)}{C_o \langle\alpha\rangle} U_{GS} \, . \tag{6.1}$$

To utilize (6.1) as a transition model, a transition void fraction value is required. Since the transition experiments occupied a range of void fractions rather than a single value, the center point of this range was chosen as the transition void fraction, as shown in Table 6.1. The value of C_o was taken to be 1.21 for both air-water and air-water/Zonyl FSP as determined from the velocity measurements in Chapter 4. The value of C_o determined in this manner for air-water/glycerin (C_o = 1.48) yields poor agreement between the transition model and the flow pattern experimental results and was not used. Instead, a value of C_o = 1.21 was also used for this system because this yields a reasonable result. Substituting the transition void fraction into (6.1) leads to microgravity bubble-slug transition models (6.2), (6.3) and (6.4) for air-water, air-water/glycerin and air-water/Zonyl FSP, respectively, each in a 12.7 mm ID tube,

$$U_{LS} = 1.07 \, U_{GS} \, , \tag{6.2}$$

$$U_{LS} = 1.30 \, U_{GS} \, , \tag{6.3}$$

$$U_{LS} = 0.80 \, U_{GS} \, . \tag{6.4}$$

The locus of points satisfying each transition model is superimposed onto the appropriate flow pattern map in Figures 6.1, 6.2 and 6.3 for air-water, air-water/glycerin and air-water/Zonyl FSP, respectively. This locus is a line of constant void fraction on the flow pattern maps. In all three cases, the model separates the bubble and slug flow points across the entire parameter space. Both the models (6.2) and (6.3) as well as the experimental results, Figures 6.1 and 6.2, indicate that there is only a small effect of the liquid viscosity on the location of the bubble-slug transition. A similar comparison between (6.2) and (6.4) as well as Figures 6.1 and 6.3 shows that reduced surface tension leads to a small shift in the location of the bubble-slug transition to higher values of void fraction. The upper boundary on the void fraction range reported in Table 6.1 for air-water/Zonyl FSP experiments was even slightly larger than the limit imposed by the maximum packing density. This shift in transition void fraction may be the result of a less efficient coalescence mechanism since the distribution of voids, as indicated by the value of C_o, is identical for both fluid systems.

The air-water results in this study compare favorably with the results of Dukler, et al., 1988 using similar apparatus. In that work, a transition void fraction of 0.45 was determined to give a reasonable fit. The data available in the Dukler, et al., 1988 study were sparser and thus the results of the present study can be considered to be a refinement of the previous results.

The lack of reliable void fraction data from the 25.4 mm ID test section experiments makes incorporating the tube diameter effect into the transition model difficult. The flow pattern maps in Figures 3.17, 3.18 and 3.19 for the 25.4 mm ID tube show that an increase in tube diameter leads to a decrease in the transition void fraction in the case of air-water. The effect of tube diameter on the air-water/glycerin and air-water/Zonyl FSP results appears to be small.

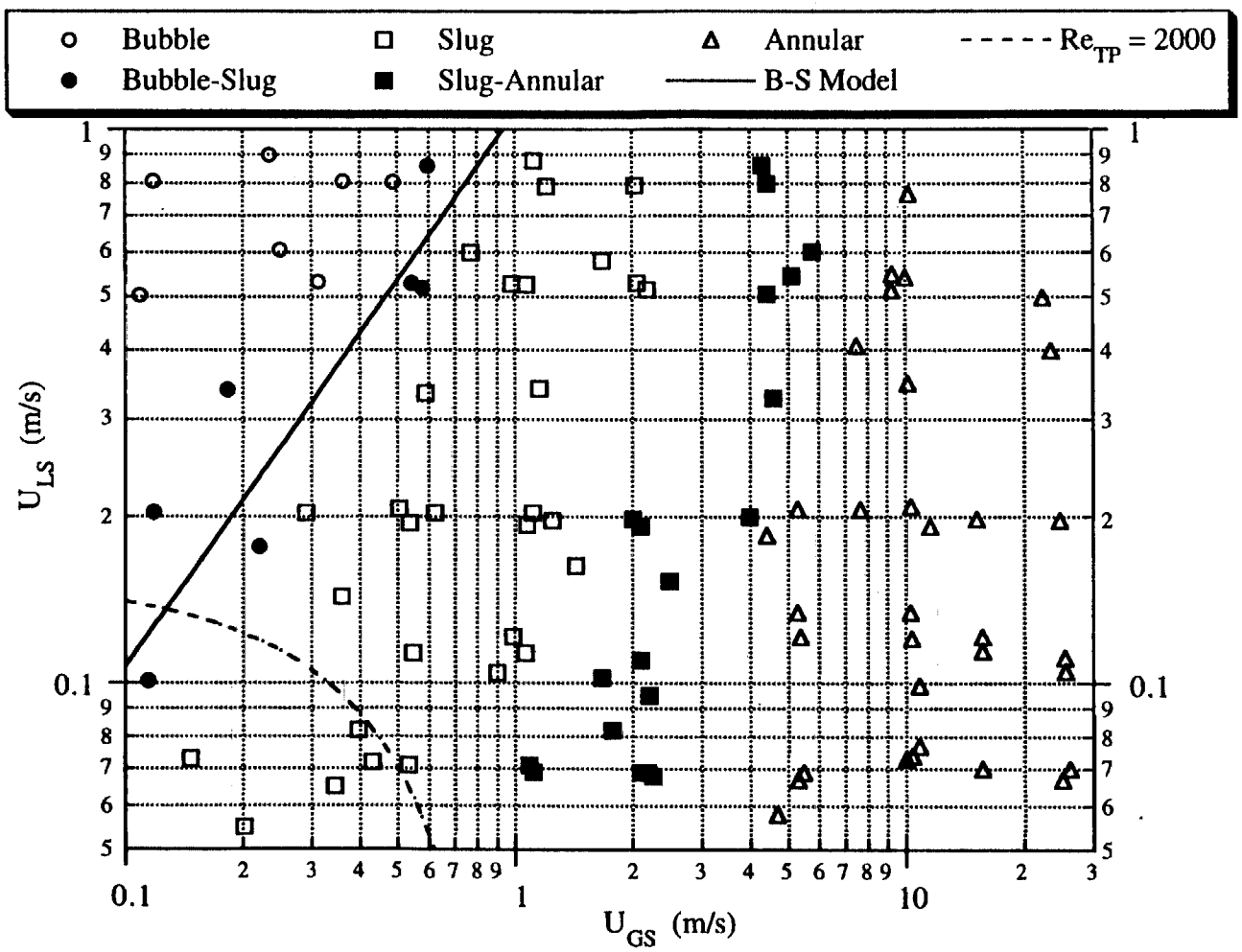

Figure 6.1 Flow Pattern Map for Air-Water in a 12.7 mm ID Tube with Bubble-Slug Transition Model

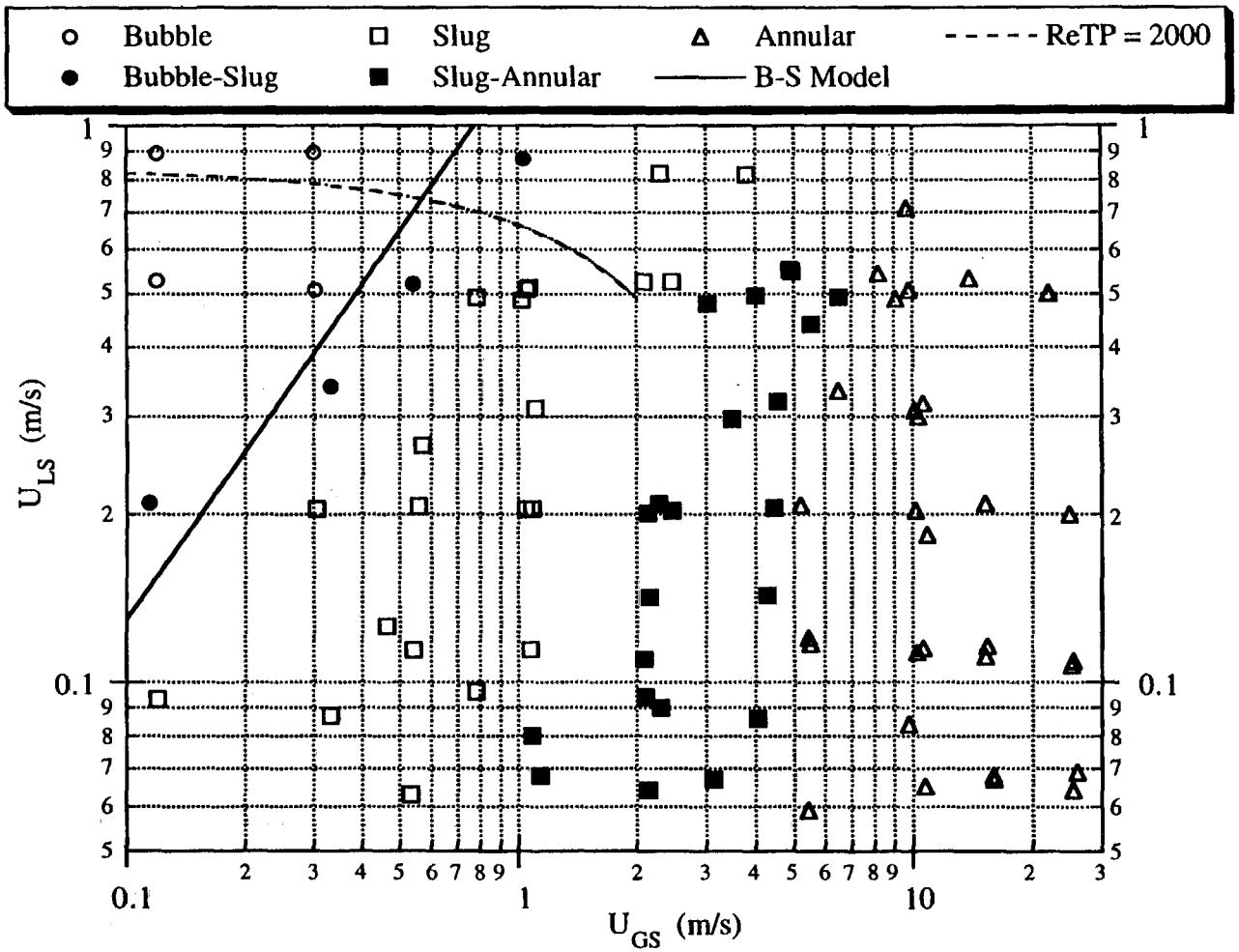

Figure 6.2 Flow Pattern Map for Air-Water/Glycerin in a 12.7 mm ID Tube with Bubble-Slug Transition Model

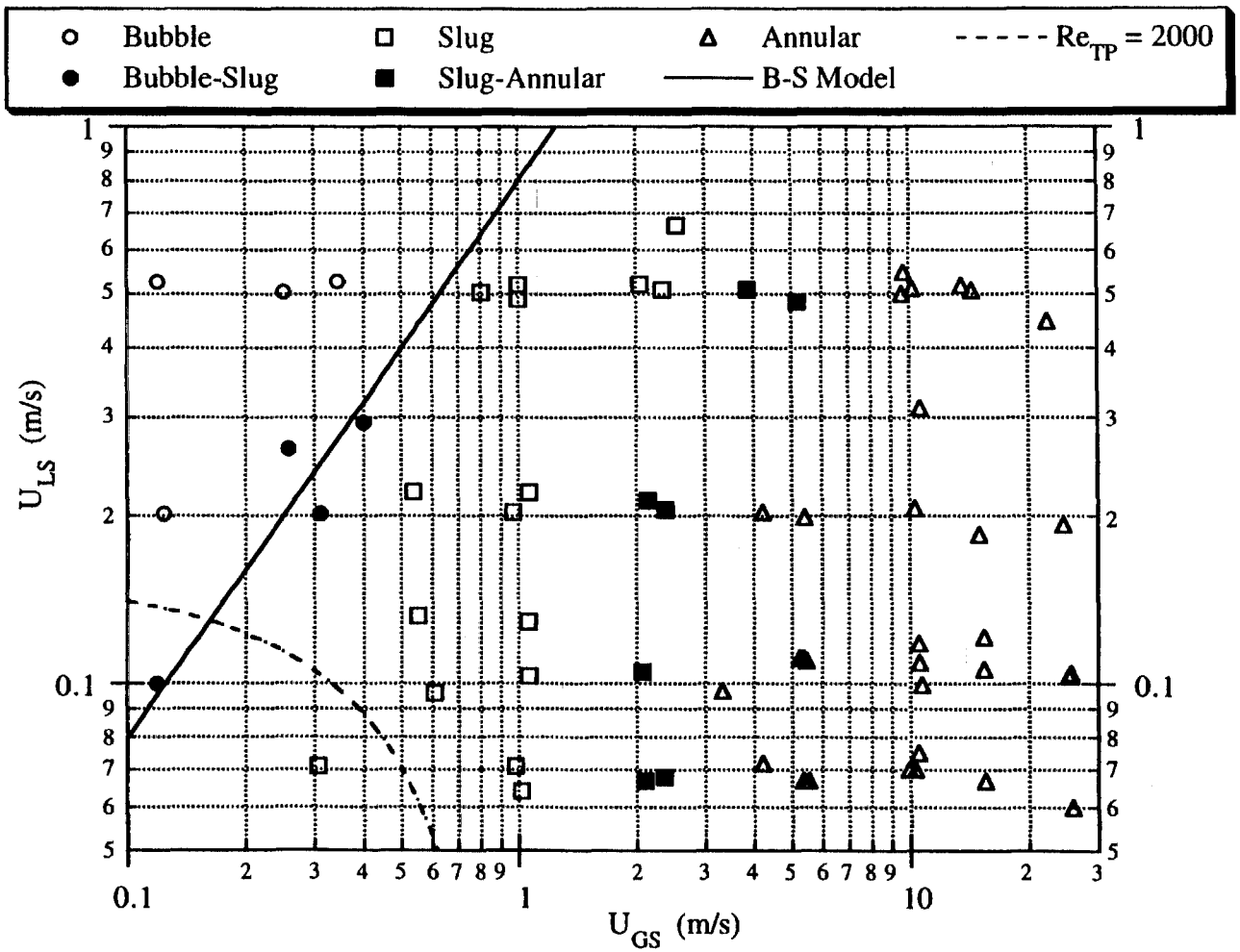

Figure 6.3 Flow Pattern Map for Air-Water/Zonyl FSP in a 12.7 mm ID Tube with Bubble-Slug Transition Model

The transition void fraction for the 25.4 mm ID tube results can be estimated for each transition experiment by solving (6.1) for $<\alpha>$. Since the distribution coefficient based on experimental measurements was also unavailable for the 25.4 mm ID test section experiments, a value of 1.21 was again used. This choice is supported by the work of Colin, 1990 in which a distribution coefficient of 1.2 was reported for microgravity air-water bubble and slug flows in a 40 mm ID tube, suggesting that the distribution coefficient is independent of diameter, at least for air-water. The transition void fraction was computed for each bubble-slug transition experiment and the results were averaged for each fluid system. This results in estimated transition void fractions of 0.23, 0.40 and 0.40 for air-water, air-water/glycerin and air-water/Zonyl FSP, respectively. If these transition void fraction values are substituted into (4.1), the following microgravity bubble-slug transition models result for air-water, air-water/glycerin and air-water/Zonyl FSP, respectively,

$$U_{LS} = 2.58\, U_{GS}\,, \tag{6.5}$$

$$U_{LS} = 1.08\, U_{GS}\,, \tag{6.6}$$

$$U_{LS} = 1.07\, U_{GS}\,. \tag{6.7}$$

The locus of points satisfying each transition model is superimposed onto the appropriate flow pattern map in Figures 6.4, 6.5 and 6.6 for air-water, air-water/glycerin and air-water/Zonyl FSP, respectively. As shown, the models separate the bubble and slug experiments across the entire parameter space. While these models appear to be reasonably successful, it should be remembered that these are empirical fits because the values of the distribution coefficient and transition void fraction could not be determined from experimental measurements.

As was noted previously, the largest diameter effect on the location of the transitions occurs with the air-water system. This shift is also present in the flow pattern map presented by Colin, 1990 for microgravity air-water bubble and slug flow in a 40 mm

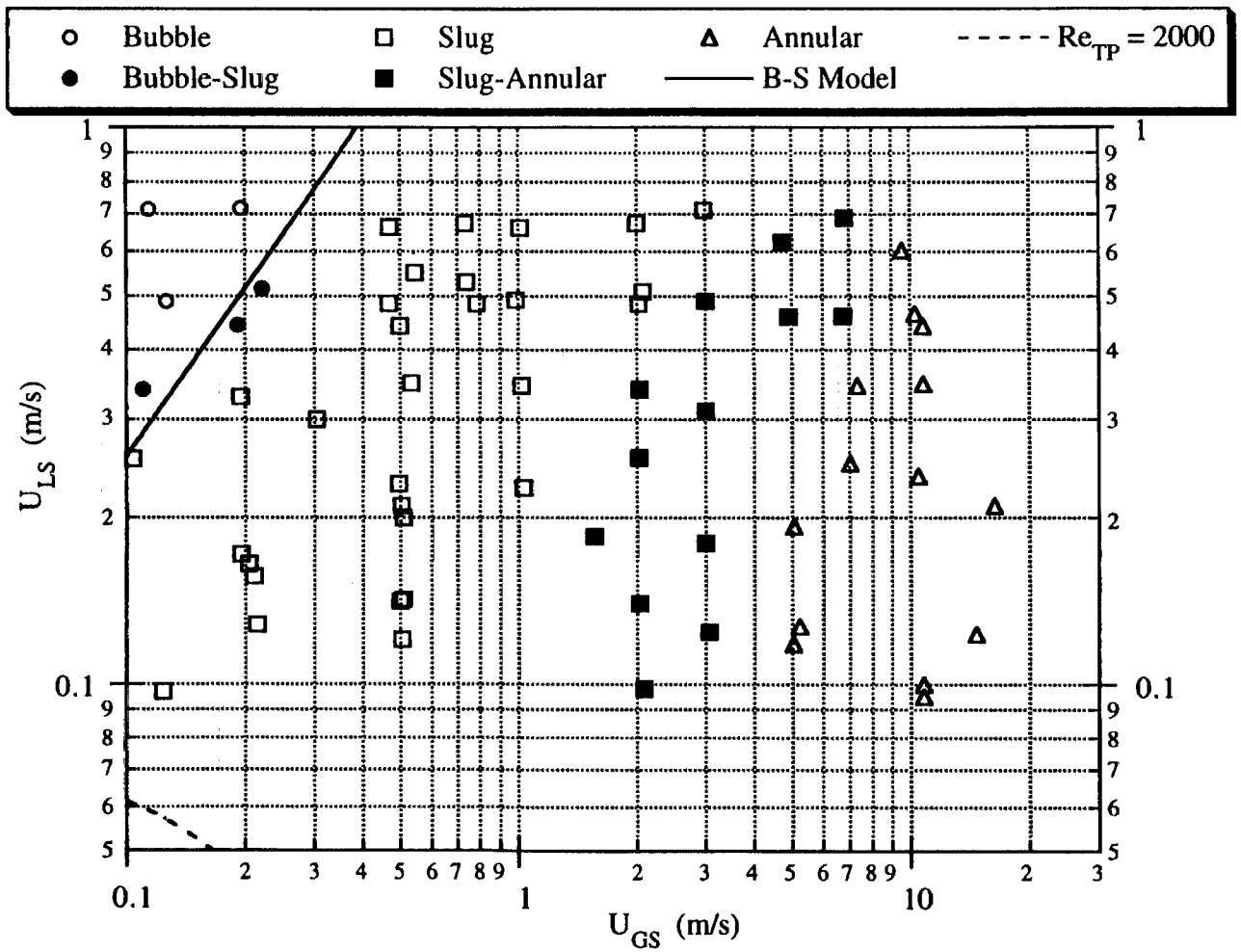

Figure 6.4 Flow Pattern Map for Air-Water in a 25.4 mm ID Tube with Bubble-Slug Transition Model

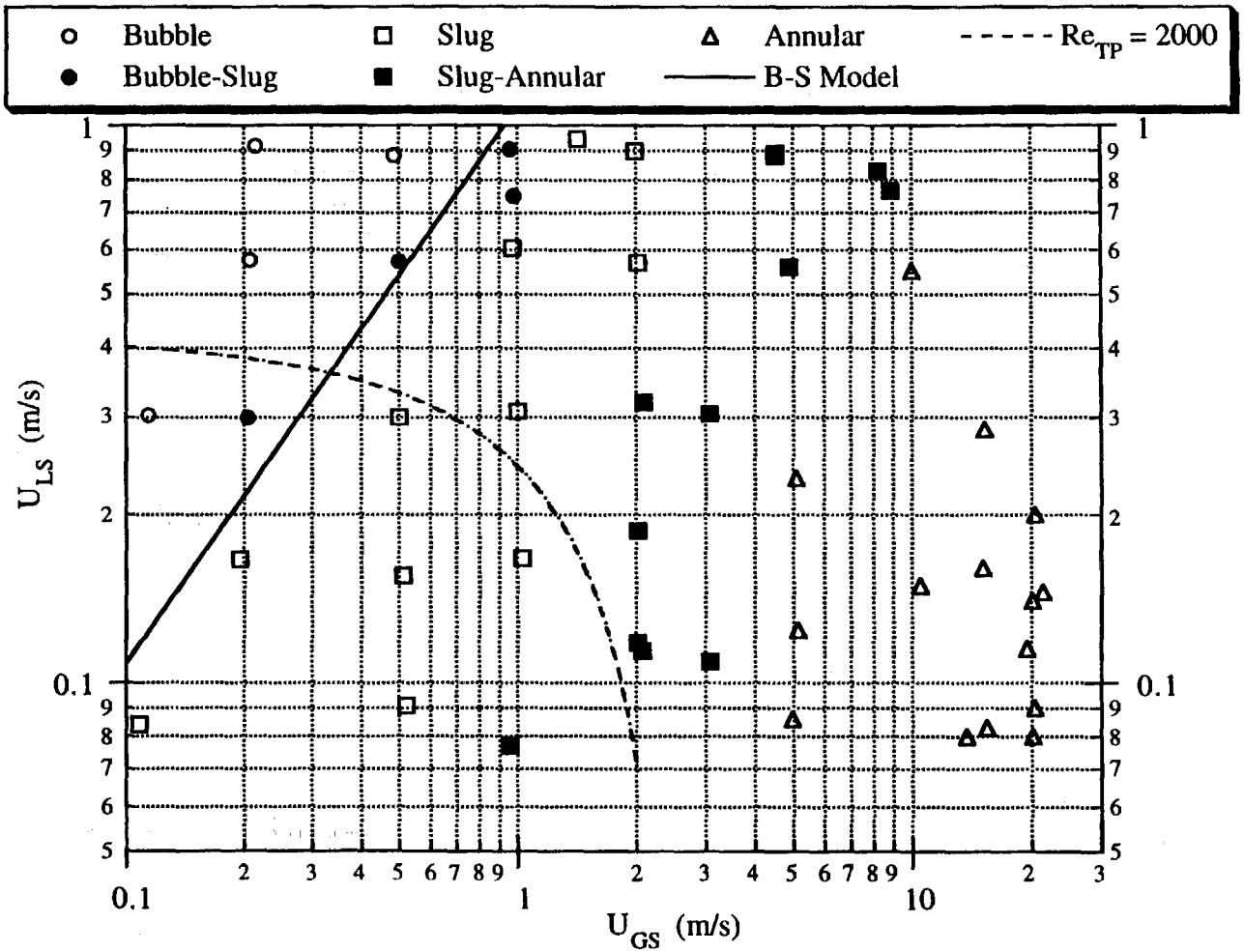

Figure 6.5 Flow Pattern Map for Air-Water/Glycerin in a 25.4 mm ID Tube with Bubble-Slug Transition Model

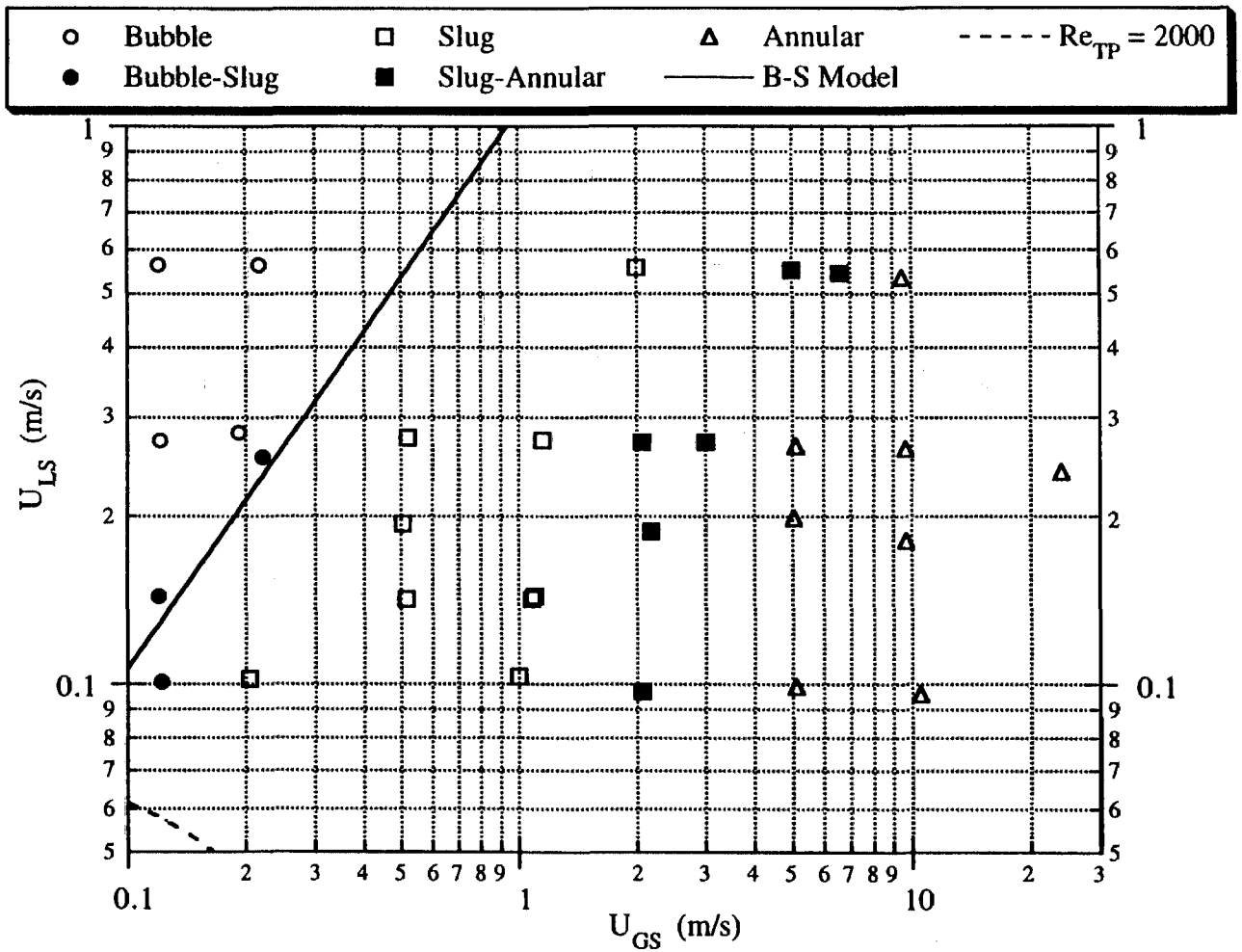

Figure 6.6 Flow Pattern Map for Air-Water/Zonyl FSP in a 25.4 mm ID Tube with Bubble-Slug Transition Model

ID tube. The air-water bubble-slug transition model (4.5) for the 25.4 mm ID tube is in good agreement with the Colin, 1990 results shown in Figure 3.4.

The air-water/Zonyl FSP results show a smaller shift with the change in tube diameter in the same direction as the shift in the air-water results while the air-water/glycerin transition is slightly shifted towards higher void fraction. The significance of these smaller shifts is questionable considering the method by which the transition models were developed for the 25.4 mm ID tube. It should be noted that the transition models developed for air-water/glycerin and air-water/Zonyl FSP in a 12.7 mm ID tube would also provide a reasonable result for the 25.4 mm ID tube experiments with these two fluid systems.

To explain the observed effects of tube diameter on the bubble-slug transition results, the movie films were examined to look for differences in the bubble-slug transition experiments in both tube diameters. The most apparent qualitative difference occurred in the air-water system where the bubbles in the larger tube were clearly affected by turbulence. The interfaces of both the spherical and Taylor bubbles in the transition experiments in the 25.4 mm ID tube were in a continuous state of fluctuation while those in the 12.7 mm ID tube appeared to be more stable. The air-water/Zonyl FSP transitional experiments in the 25.4 mm ID tube also appeared to have significant turbulent effects while the air-water/glycerin experiments showed less fluctuation. The observed bubble oscillations in the larger tube give the bubbles a larger effective diameter and this increases the probability of contacting other nearby bubbles. The result would be a transition to slug flow at a lower void fraction as is observed in the air-water results. This effect would be partially offset by decreased surface tension which should reduce the probability of coalescence once the bubbles contact each other. As noted previously, the shift to lower void fraction was much less for the low surface tension fluid system.

To examine the possible effect of turbulence on the transition, the locus of points corresponding to Re_{TP} = 2000, where Re_{TP} is defined by (4.15), was also superimposed on the bubble and slug flow regions of Figures 6.1-6.6. As shown, nearly the entire parameter space in the air-water and air-water/Zonyl FSP maps for both tube diameters lies in the turbulent region. The 12.7 mm ID tube map for air-water/glycerin, Figure 6.2, shows that nearly the entire parameter space lies in the laminar region, while Figure 6.5 shows that most of the parameter space lies in the laminar or laminar-turbulent transition region for air-water/glycerin in the 25.4 mm ID tube. These results would suggest that turbulence is at least partially responsible for the shift in transition void fraction for the air-water system. This analysis also shows that turbulence should have a much smaller effect on the air-water/glycerin system, which is in agreement with the flow pattern mapping results shown.

In evaluating the usefulness of the void matching bubble-slug transition model, it should be remembered that the experimental results show the transition between the two flow patterns to be a fairly wide zone rather than a distinct line. The proposed model lies within this zone but does not demarcate either edge. Thus this model is useful for general design and operations purposes if it is realized that the transitional flow pattern will exist on both sides of the model prediction.

6.3 Void Fraction Based Slug-Annular Transition Model

As mentioned in chapter 3, photographic evidence suggests that the transition from slug and annular flow occurs when the length of the liquid slugs decreases to the point where the slugs rupture, resulting in a continuous gas core. Alternatively, the transition from annular to slug flow appears to occur when the amplitude of the waves increases to the point where the waves bridge the tube, forming a liquid slug. Photographic sequences

demonstrating these phenomena are shown in Appendix A, Figures A.11, A.12 and A.13. The decrease in the thickness of the liquid slugs near transition can be associated with an increase in the void fraction. Similarly, as the void fraction of annular flow decreases, the wave amplitude increases, leading to the transition to slug flow. The void fraction therefore appears to be a potential indicator which could be used to model the transition from slug to annular flow.

Modeling the transition from bubble to slug flow was relatively simple because both flow patterns have a continuous liquid phase and a discrete gas phase and both could be described by the same Drift-Flux model. The modeling of the slug to annular transition is more complex because a transition from a continuous liquid phase (slug flow) to a continuous gas phase (annular flow) is required. No mechanistic model similar to the Drift-Flux model is currently in existence which adequately describes both slug and annular flow. Thus the region where the Drift-Flux model for slug flow and a force balance for annular flow predict the same void fraction will be determined and checked against the experimental flow pattern maps to determine if this approach provides a reasonable transition model. This approach was first suggested for microgravity two-phase flows by Dukler et al., 1988 but has been subsequently refined in this study.

To determine a mechanistic model of the void fraction of microgravity annular flows, two force balances can be written on an idealized system consisting of a smooth liquid film of mean thickness $\bar{h}$ surrounding a continuous gas core. This system is shown schematically in Figure 6.7. The greatly enhanced pressure drop due to the presence of waves and entrained droplets which would not be present in the idealized system of Figure 6.7 will be reincorporated in the model by using the results of the experimental measurements.

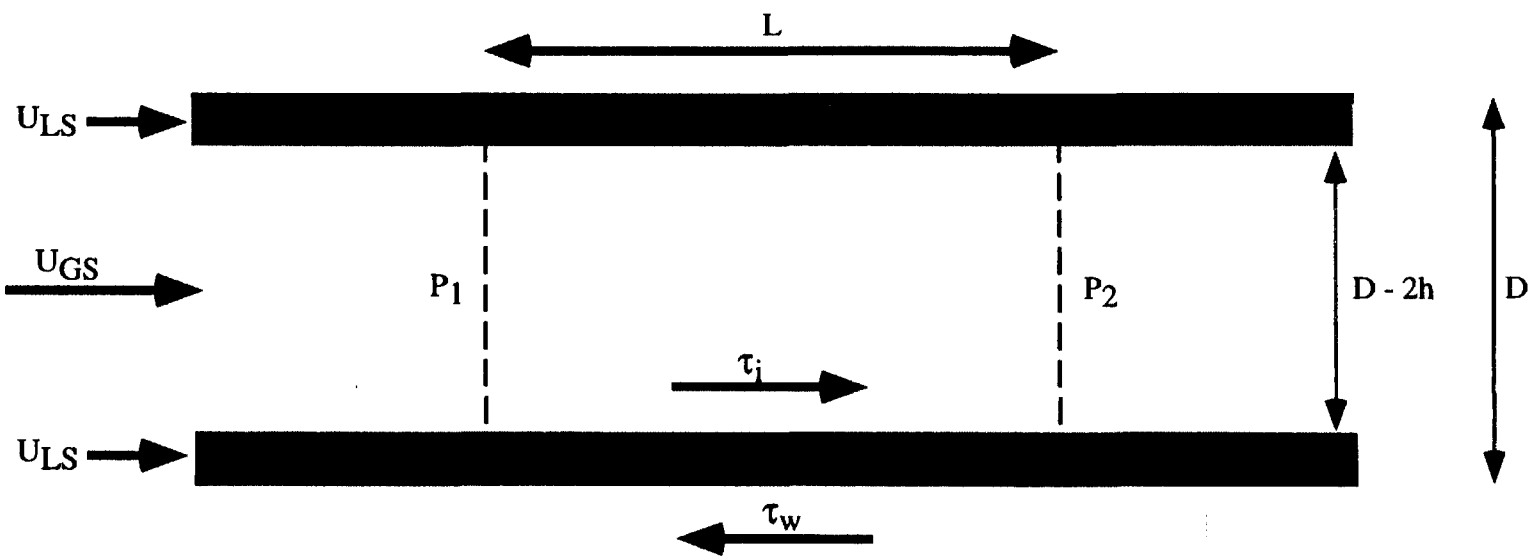

Figure 6.7 Idealized Annular Flow Setup for Force Balances

A force balance on the control volume bounded by the tube walls and planes perpendicular to the flow leads to

$$-\frac{dP}{dz} = \frac{2\,\tau_w}{R} . \tag{6.8}$$

A similar force balance on the liquid film leads to

$$(1 - \alpha)\left[-\frac{dP}{dz}\right] = \frac{2\,\tau_w}{R} - \frac{2\,\tau_i}{R}\,\alpha^{1/2} . \tag{6.9}$$

This requires the conversion between film thickness and void fraction, which is given by

$$\langle\alpha\rangle = \left[1 - \frac{\bar{h}}{R}\right]^2 . \tag{6.10}$$

Since these two conditions must be satisfied simultaneously, (6.8) can be substituted into (6.9) to yield

$$\tau_i = \tau_w\,\alpha^{1/2} . \tag{6.11}$$

The shear stresses in (6.11) can be expressed in terms of friction factors defined by

$$\tau_i = \frac{f_i\,\rho_G\,\langle U_G\rangle^2}{2} = \frac{f_i\,\rho_G\,\langle U_{GS}\rangle^2}{2\,\langle\alpha\rangle^2} \tag{6.12}$$

and

$$\tau_w = \frac{f_w\,\rho_L\,\langle U_L\rangle^2}{2} = \frac{f_w\,\rho_L\,\langle U_{LS}\rangle^2}{2\,(1-\langle\alpha\rangle)^2} . \tag{6.13}$$

Substituting these definitions into (6.11) yields

$$\frac{\langle\alpha\rangle^{5/2}}{(1 - \langle\alpha\rangle)^2} = \frac{f_i}{f_w}\,\frac{\rho_G}{\rho_L}\left[\frac{U_{GS}}{U_{LS}}\right]^2 . \tag{6.14}$$

The pressure drop measurements shown in Figures 5.25, 5.26 and 5.27 for microgravity annular flow in a 12.7 mm ID tube suggest that for thin liquid films, it is reasonable to assume that the interfacial friction factor can be expressed in terms of an

enhancement of the single phase friction factor. The interfacial friction factor results also suggest that this enhancement factor should be a function only of the void fraction when the liquid films are thin. This leads to the assumed relation for the interfacial friction factor,

$$f_i = \phi(<\alpha>)\, f_G \,, \tag{6.15}$$

where f_G is the friction factor of the gas flowing alone in a tube of diameter D-2$\bar{h}$. The validity and limits of this expression will be explored in more detail when the transition model is implemented. Substituting (6.15) into (6.14) yields

$$\frac{<\alpha>^{5/2}}{(1 - <\alpha>)^2} = \phi(<\alpha>)\, \frac{f_G}{f_w}\, \frac{\rho_G}{\rho_L} \left[\frac{U_{GS}}{U_{LS}}\right]^2 . \tag{6.16}$$

Suitable expressions for the gas and liquid single-phase friction factors can be obtained from the Blasius relation,

$$f = \frac{C}{Re^n} \,, \tag{6.17}$$

where C = 0.046, n = 0.2 for turbulent flow and C = 16, n = 1 for laminar flow. The appropriate Reynolds numbers for use in (6.17) are

$$Re_G = \frac{D\, U_{GS}\, \rho_G}{\mu_G\, <\alpha>^{1/2}} \tag{6.18}$$

and

$$Re_L = \frac{D\, U_{LS}\, \rho_L}{\mu_L} \,. \tag{6.19}$$

It can be seen that the model will be different depending on whether the liquid is laminar or turbulent. For turbulent gas and liquid flow, substituting (6.18) and (6.19) with the appropriate Blasius constants into (6.16) leads to the turbulent annular flow relation,

$$U_{LS} = U_{GS} \left[\frac{(1-<\alpha>)^2\, \phi(<\alpha>)}{<\alpha>^{2.4}\, B}\right]^{1/1.8} , \tag{6.20}$$

where

$$B = \left[\frac{\nu_L}{\nu_G}\right]^{0.2}\left[\frac{\rho_L}{\rho_G}\right]. \tag{6.21}$$

The value of B is 481.5 for the air-water and air-water/Zonyl FSP systems and 759.8 for the air-water/glycerin system.

For turbulent gas flow and laminar liquid flow, substitution of (6.18) and (6.19) with the appropriate Blasius constants into (6.16) results in the laminar annular flow relation,

$$U_{LS} = \frac{0.00288\, D^{0.8}\, \nu_G^{0.2}\, \rho_G\, U_{GS}^{1.8}\, \phi(<\alpha>)\, (1 - <\alpha>)^2}{\mu_L\, <\alpha>^{2.4}}. \tag{6.22}$$

Void fraction models for microgravity annular flow have now been developed. These can be equated to the Drift-Flux relation for slug flow,

$$\frac{U_{GS}}{U_{GS} + U_{LS}} = C_o\, <\alpha>\,, \tag{6.23}$$

to determine the conditions under which the void fraction predicted for each flow pattern is equal.

Equating the slug flow void fraction model (6.23) with the turbulent annular void fraction model (6.20) leads to the turbulent void matching slug-annular transition model,

$$<\alpha> = \frac{1}{C_o} - <\alpha>\left[\frac{(1 - <\alpha>)^2\, \phi(<\alpha>)}{<\alpha>^{2.4}\, B}\right]^{5/9}. \tag{6.24}$$

The model was displayed in this form because the equation is implicit in $<\alpha>$ and can be solved numerically by successive substitution. An important result of (6.24) is that if C_o is a constant and ϕ is only a function of $<\alpha>$, then this model predicts that the transition will lie along a line of constant void fraction. Furthermore, the experimental flow pattern results show that the void fraction of the transition runs is approximately 0.75

which is near the value of $1/C_o$. Combining this knowledge with the form of (6.24) shows that the transition void fraction is equal to the sum of a constant ($1/C_o$) and a presumably small correction factor. Since all components of the second term on the right side of (6.24) are uniformly positive, the transition void fraction predicted by this model cannot exceed the value of $1/C_o$.

Equating the slug flow void fraction model (6.23) with the laminar annular void fraction model (6.22) leads to the laminar void matching slug-annular transition model,

$$U_{GS}\left[\frac{1 - C_o \langle\alpha\rangle}{C_o \langle\alpha\rangle}\right] = \frac{0.00288\, D^{0.8}\, \nu_G^{0.2}\, \rho_G\, U_{GS}^{1.8}\, \phi(\langle\alpha\rangle)\, (1 - \langle\alpha\rangle)^2}{\mu_L \langle\alpha\rangle^{2.4}} . \qquad (6.25)$$

The functionality of this relation shows that the laminar void fraction matching transition does not fall along a line of constant void fraction but is instead also a function of the superficial gas velocity, liquid and gas physical properties and the tube diameter. For a given value of $\langle\alpha\rangle$, (6.25) is solved explicitly for U_{GS}. The corresponding value of U_{LS} for the transition is then computed from (6.23). The result is a locus of points on the flow pattern maps in which the void fraction predictions from (6.22) and (6.23) are equal. The values of U_{GS} and U_{LS} predicted by the laminar and turbulent models are equal at a void fraction equal to that predicted by (6.24). The relation (6.25) is undefined when $\langle\alpha\rangle = 1/C_o$ and thus the laminar relation (6.25) will be valid only in the narrow range between the turbulent transitional void fraction and $1/C_o$.

The remaining step prior to implementing the transition models is to determine a suitable expression for the friction factor enhancement function ϕ. An examination of Figures 5.25, 5.26 and 5.27 shows that the interfacial friction factor is in fairly good agreement with the Wallis model up to a dimensionless film thickness of about 0.05, corresponding to a void fraction of 0.81. The agreement is worse for higher values of U_{LS} and for the air-water/Zonyl system. For void fractions less than 0.81, the experimental

measurements deviate significantly from the Wallis model predictions. For $C_o = 1.21$, the maximum transition void fraction which could be predicted by either the laminar or turbulent transition models would be 0.826 which is at the limit of validity for the Wallis model. The fact that the Wallis model, determined from annular flow measurements, begins to fail near the region associated with a transition to slug flow is probably not coincidental and may in fact be another indicator of the transition region.

For lack of a better relation, the Wallis model will be used to determine $\phi(<\alpha>)$,

$$\phi(<\alpha>) = 1 + 150\,(1 - \alpha^{1/2})\,. \tag{6.26}$$

As indicated by Figures 5.25, 5.26 and 5.27, as the value of $<\alpha>$ approaches 0.8, the Wallis model will tend to underpredict the interfacial friction factor. As shown by the turbulent transition model, underprediction of $\phi(<\alpha>)$ will lead to overprediction of the transition void fraction, causing the model prediction to lie to the right of the actual transition on the flow pattern maps. This error will increase with increasing U_{LS} as mentioned previously. For the laminar transition model, void fraction values up to $1/C_o$ are valid but the highest values of $<\alpha>$ correspond with the lowest values of U_{LS} along this transition and a partial cancellation of errors is possible.

The turbulent transition model (6.24) was solved numerically with $C_o = 1.21$. Convergence to a single value of void fraction was achieved in less than 20 iterations for any initial value in the range $0.5 < \alpha < 1/C_o$. The solution appears to be unique within the realistic range of void fraction values because no other solutions could be found. The turbulent transition void fraction predicted by the model was 0.798 for air-water and air-water/Zonyl FSP and 0.806 for air-water/glycerin. Within the accuracy of the model inputs, the model predicts a transition void fraction of 0.8 for all systems tested in this study. As mentioned in the previous section, the value of Co = 1.48 determined

experimentally for the air-water/glycerin system, yielded results which are in poor agreement with the experimental results and this value was not used.

Once the turbulent transition void fraction was determined, the locus of points satisfying the laminar model was also determined for each fluid system and both tube diameters. The laminar and turbulent model results are superimposed on the microgravity flow pattern maps in Figures 6.8 - 6.13. The lower curve is the laminar model result while the upper curve is the line of constant void fraction predicted by the turbulent model. As shown, the two models coincide at only one point, representing the laminar-turbulent transition. At this point, the Reynolds numbers for the liquid as computed from (6.19) are 1204 and 1381 for air-water and air-water/Zonyl FSP in the 12.7 mm and 25.4 mm ID tubes, respectively, which are close to the accepted transition value of 1200 for liquid films (Wasden, 1989). For the air-water/glycerin system at the transition point, the liquid Reynolds numbers are 890 and 1024 in the 12.7 mm and 25.4 mm ID tubes, respectively. The gas Reynolds numbers at the transition point as computed from (6.18) are 1673 and 1921 for air-water and air-water/Zonyl FSP in the 12.7 mm and 25.4 mm ID tubes, respectively, which are close to the expected value of 2000. For the air-water/glycerin system at the transition point, the gas Reynolds numbers are 1376 and 1597 in the 12.7 mm and 25.4 mm ID tubes, respectively, which are lower than expected. As anticipated, the majority of the parameter space for the air-water and air-water/Zonyl FSP flow pattern maps lies in the turbulent regime while the parameter space in the air-water/glycerin map lies in both the laminar and turbulent regimes.

As shown, in all cases, the turbulent transition model predictions for $\langle\alpha\rangle = 0.8$ lie to the right of the boundary between the slug-annular and annular flow experiments as anticipated. The laminar model prediction for the air-water and air-water/Zonyl FSP systems separates the slug-annular and annular experiments while the laminar prediction for the air-water/glycerin system lies in the annular flow parameter space on the maps. The

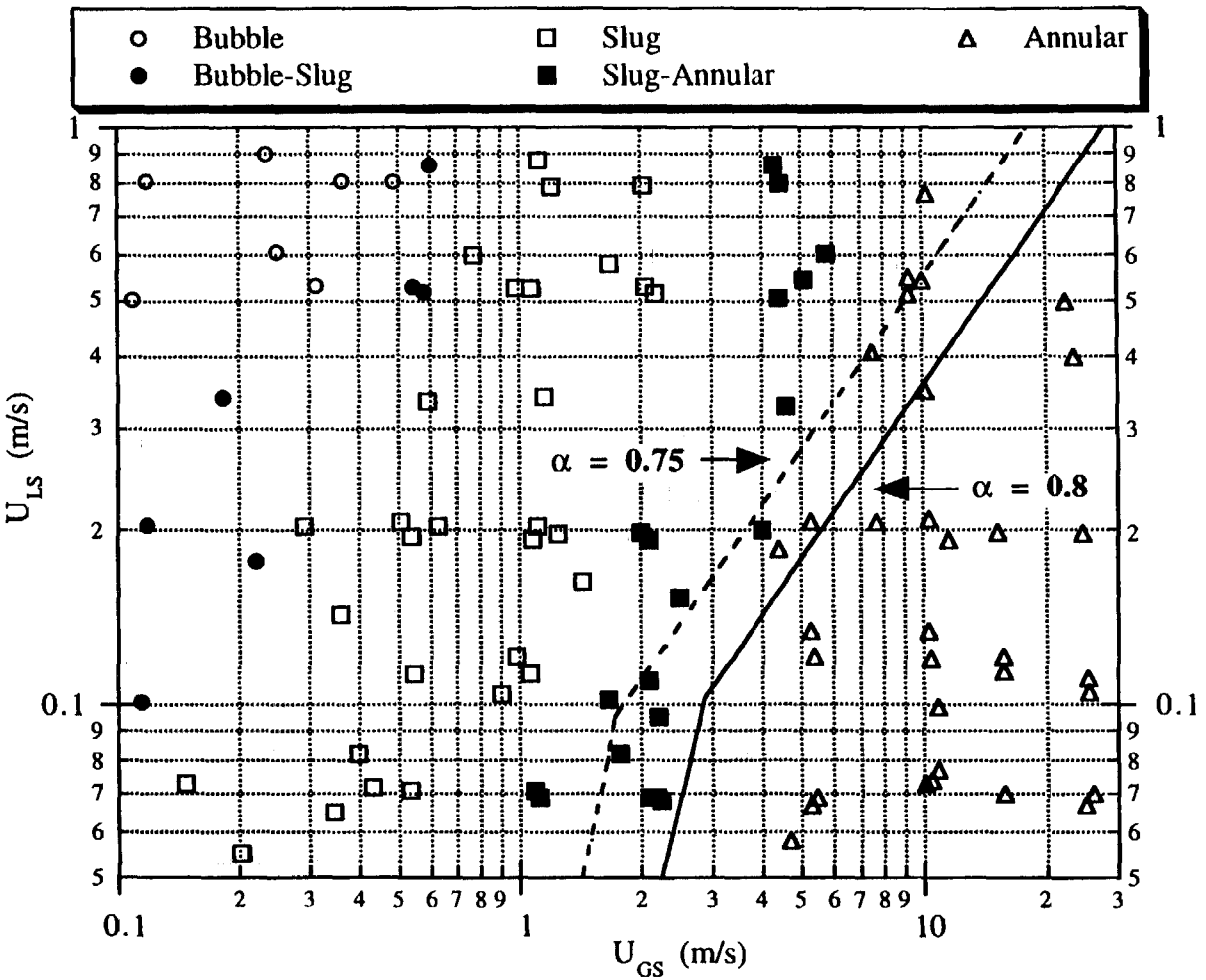

Figure 6.8 Flow Pattern Map for Air-Water in a 12.7 mm ID Tube with Slug-Annular Transition Model

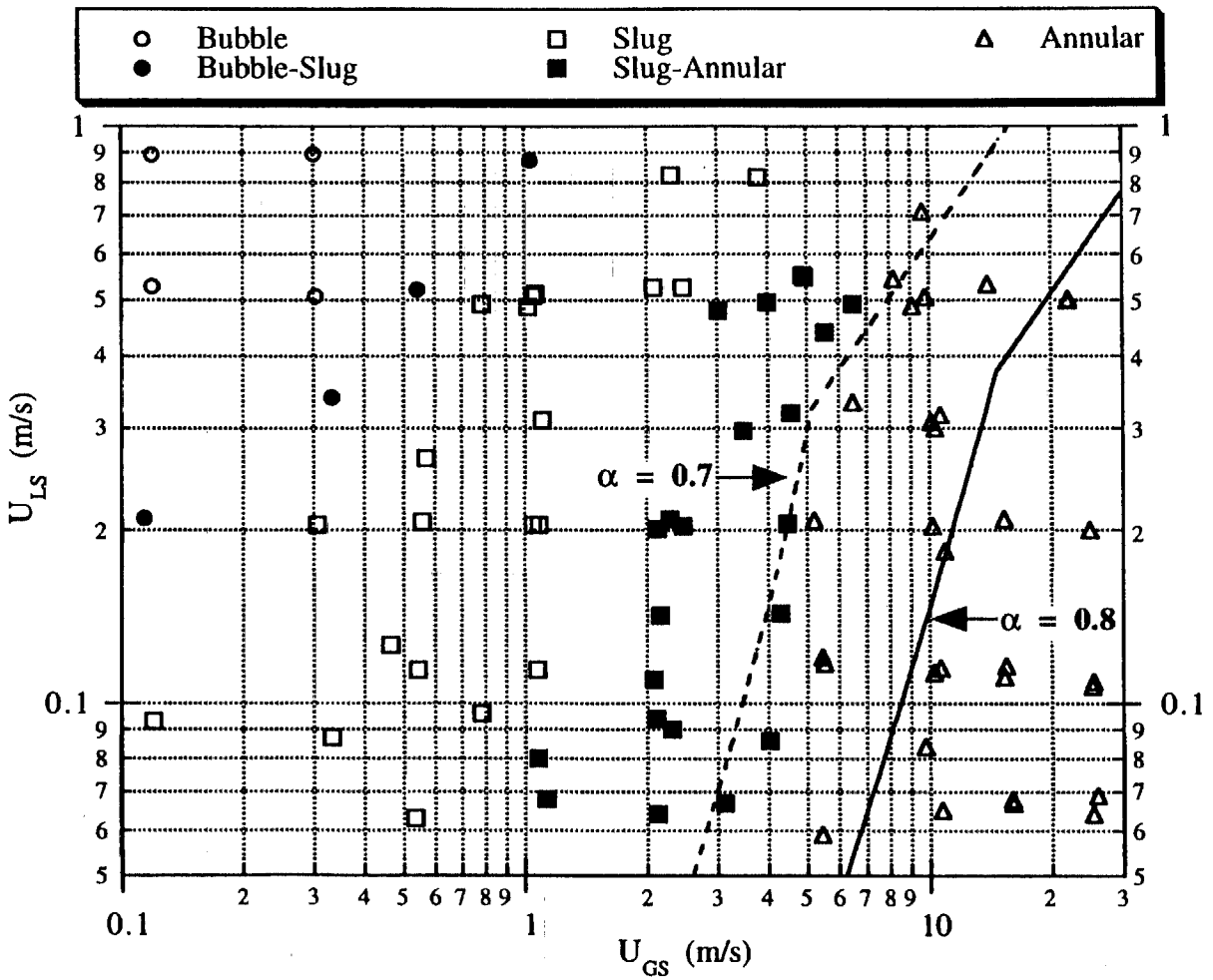

Figure 6.9 Flow Pattern Map for Air-Water/Glycerin in a 12.7 mm ID Tube with Slug-Annular Transition Model

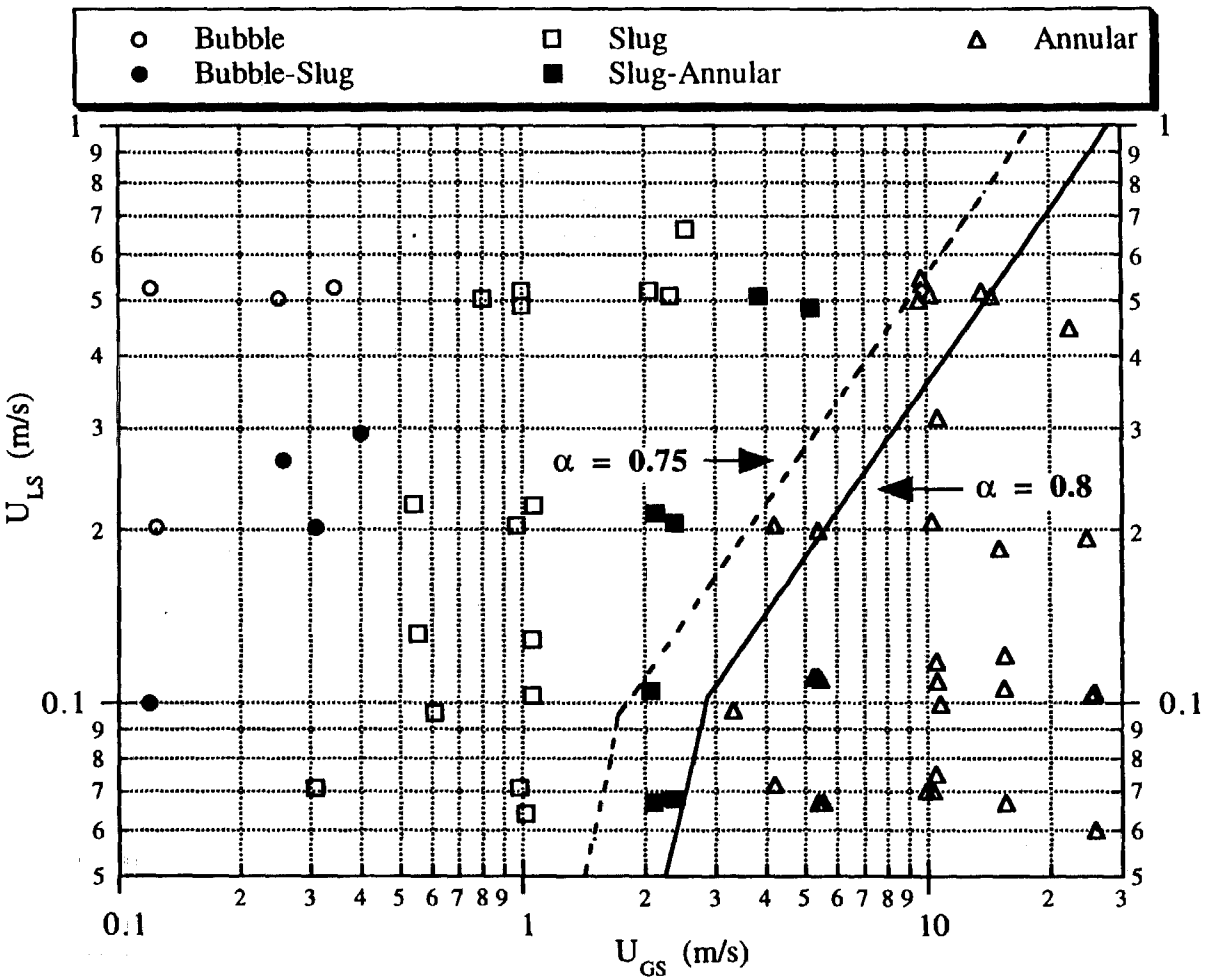

Figure 6.10 Flow Pattern Map for Air-Water/Zonyl FSP in a 12.7 mm ID Tube with Slug-Annular Transition Model

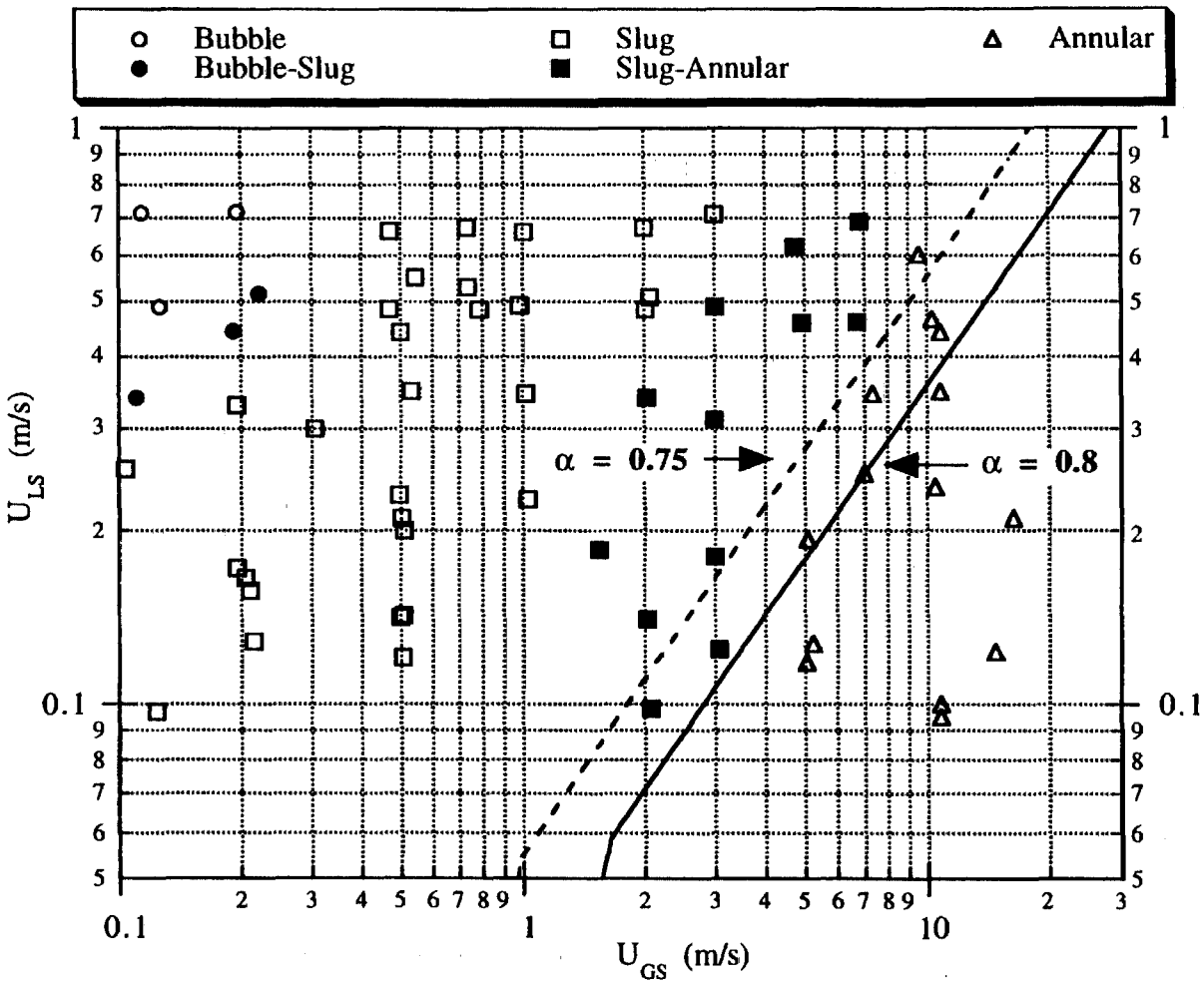

Figure 6.11 Flow Pattern Map for Air-Water in a 25.4 mm ID Tube with Slug-Annular Transition Model

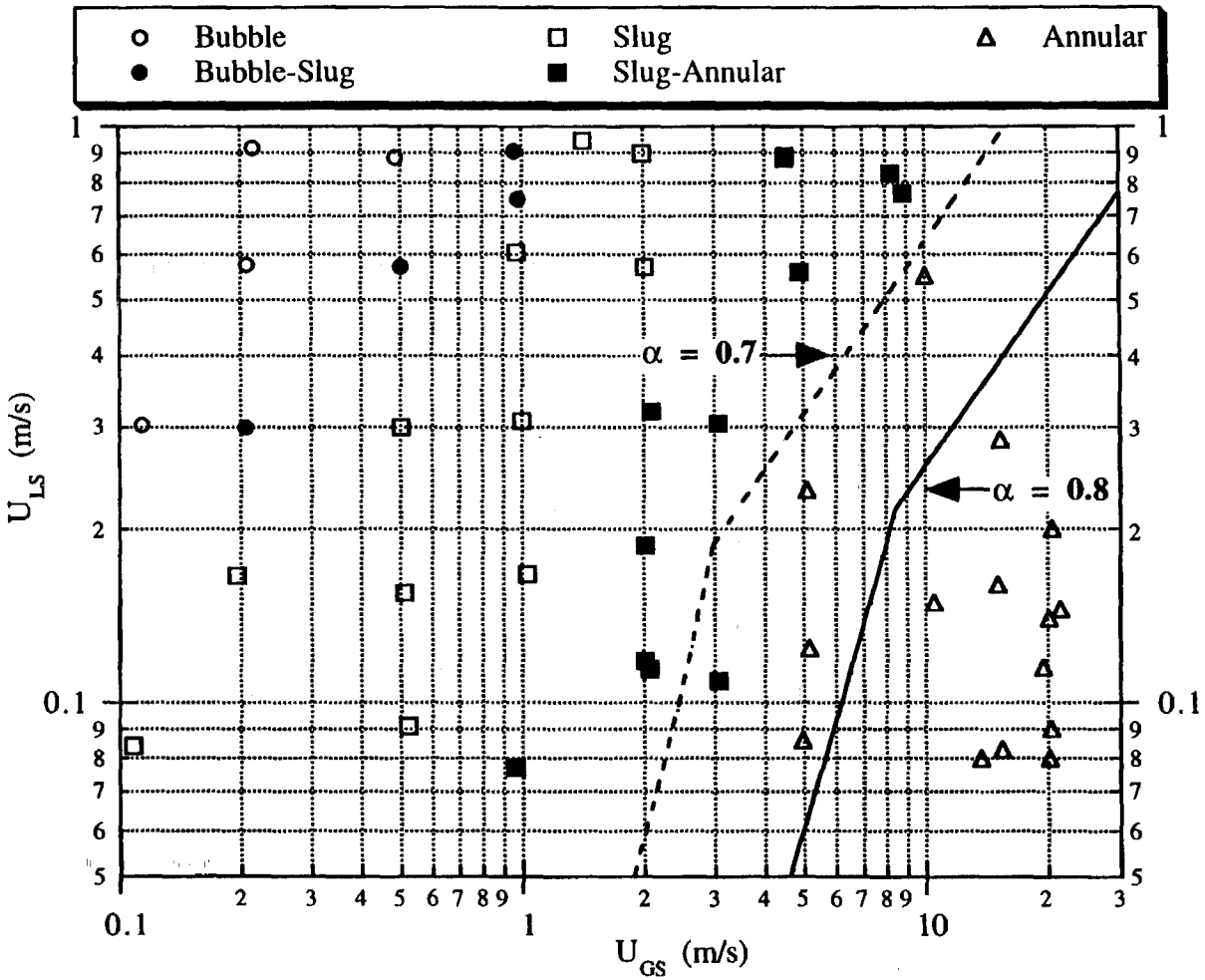

Figure 6.12 Flow Pattern Map for Air-Water/Glycerin in a 25.4 mm ID Tube with Slug-Annular Transition Model

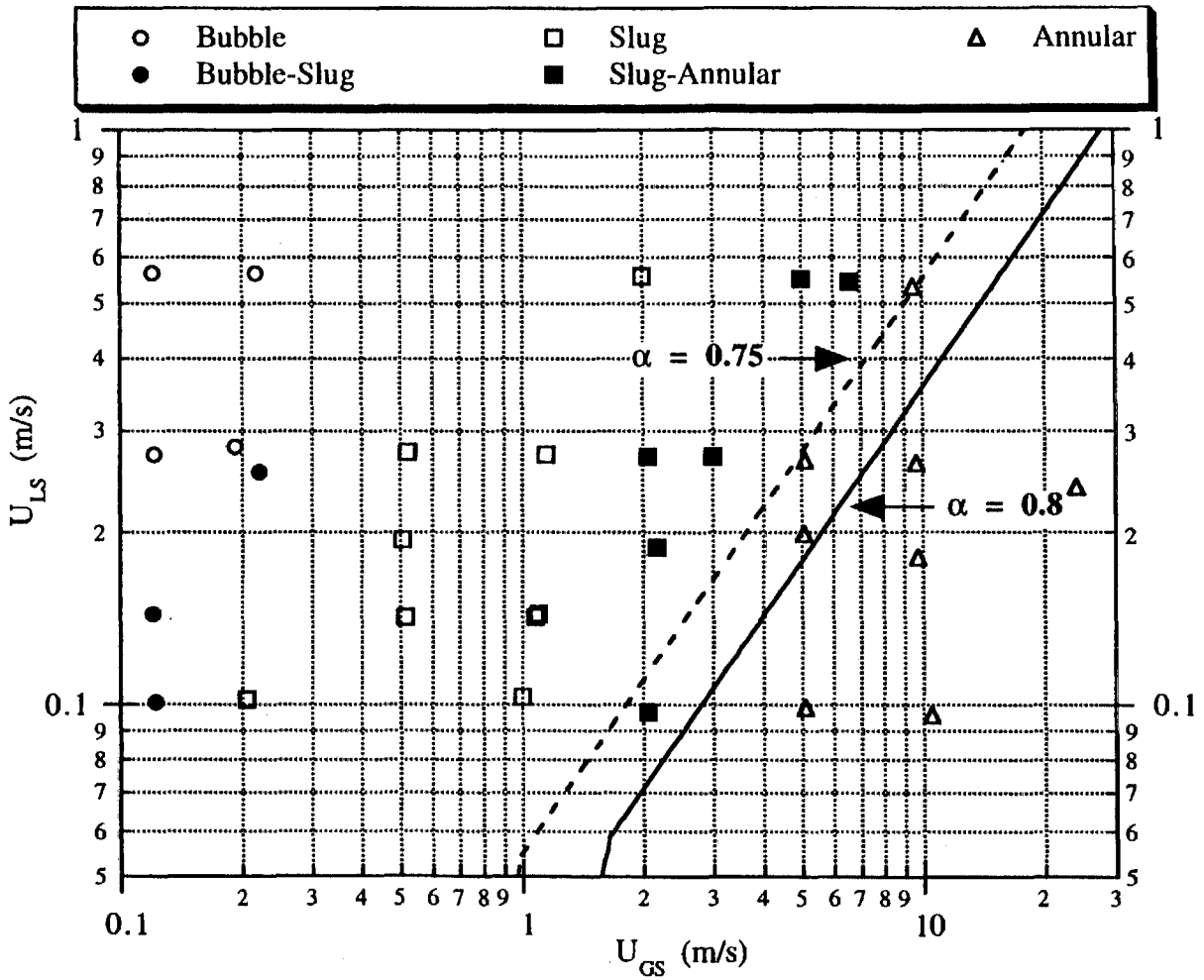

Figure 6.13 Flow Pattern Map for Air-Water/Zonyl FSP in a 25.4 mm ID Tube with Slug-Annular Transition Model

shape of the model predictions appears to be qualitatively similar to the shape of the boundary between the slug-annular and annular flow experiments.

One of the difficulties in using the void fraction to model the slug-annular transition is the sensitivity of the results to the transition void fraction value. In this region of the flow pattern map, small changes in the void fraction correspond to large changes in U_{GS}. As an example, for U_{LS} = 0.5 m/s, a void fraction of 0.75 occurs at U_{GS} = 9.0 m/s while a void fraction of 0.8 occurs at U_{GS} = 15.1 m/s. Thus small changes in the transition void fraction result in large changes in the predicted superficial velocities at the transition.

In order to produce better agreement between the transition model predictions and the experimental results, the transition void fraction was decreased. As shown in Figures 6.8, 6.10, 6.11 and 6.13 for air-water and air-water/Zonyl FSP in both tube diameters tested, a turbulent transition void fraction of 0.75 produces a better separation between the slug-annular and annular data points than did the void fraction of 0.8. This adjustment still produces discrepancies at high U_{LS}. This discrepancy could be caused by the problems encountered with flow pattern identification in this region of the maps or could indicate that the transition does not fall along a line of constant void fraction at high U_{LS}. Despite these problems, a transition criteria of $\langle\alpha\rangle$ = 0.75 does appear to provide a simple estimate of the location of the boundary between slug-annular and annular flows for both tube diameters and for high and low surface tension liquids.

Similarly, it was found that a transition void fraction of 0.7 produces better separation between the slug-annular and annular flows for the air-water/glycerin results in Figures 6.9 and 6.12. Again the poorest agreement occurs at high U_{LS} for the 12.7 mm ID tube results but the accuracy of the flow pattern identification of the experiments in that region is questionable.

The void fraction matching model for the slug-annular transition suffers from a lack of an accurate pressure drop model in the transition region and from the sensitivity of the results to small changes in the predicted void fraction. While the model predictions were disappointing, they do suggest that the void fraction is a reasonable transition criteria, even if the best value for the transition void fraction was determined empirically. The transition criteria presented in this section do provide sufficient accuracy to permit operation of two-phase annular systems in the purely annular region of the flow pattern map.

6.4 Weber Number Based Flow Pattern Transition Model

Zhao and Rezkallah, 1993, proposed an alternate flow pattern map and transition criteria for microgravity two-phase flows based on the Weber numbers for gas and liquid. The data in the present study were evaluated in terms of the Weber numbers and the approach appears to have some merit.

Based on photographic image analysis of microgravity air-water two-phase flow experiments, the Zhao and Rezkallah, 1993, suggest that the flow patterns observed in microgravity are controlled primarily by surface tension and inertial forces. The authors suggest that the bubble and slug flow patterns occur under conditions where the surface tension forces dominate while annular flow occurs under conditions where inertial forces are controlling. The slug-annular transition region represents a condition where both surface tension and inertial forces are important.

The Weber number, defined as

$$We = \frac{\rho U^2 D}{\sigma}, \tag{6.27}$$

is the ratio of inertial forces to surface tension forces and is therefore the logical group with which to test the proposed mechanism. Zhao and Rezkallah, 1993, defined the superficial Weber numbers for the gas and liquid phases by

$$We_{GS} = \frac{\rho_G U_{GS}^2 D}{\sigma} \tag{6.28}$$

and

$$We_{LS} = \frac{\rho_L U_{LS}^2 D}{\sigma} . \tag{6.29}$$

Flow pattern maps were constructed by plotting We_{GS} vs We_{LS}. Based on their flow pattern maps, the authors proposed that the boundary between the slug and slug-annular flow patterns was given by

$$We_{GS} \cong 1 , \tag{6.30}$$

while the boundary between the slug-annular and annular flow pattern was given by

$$We_{GS} \cong 20 . \tag{6.31}$$

The data presented by Zhao and Rezkallah, 1993 show these transition criteria to be approximately true although there are discrepancies. The concept of a constant Weber number transition criteria is consistent with the force controlled regions of the flow pattern map described previously.

In order to test the Weber number criteria with the present data, Weber number flow pattern maps are constructed for air-water, air-water/glycerin and air-water/Zonyl FSP in both tube diameters as shown in Figures 6.14 - 6.19. The observation put forth by Zhao and Rezkallah, 1993 that the transitions occur at constant We_{GS} is approximately true for low values of We_{LS} but deviates from this at higher We_{LS}. A similar trend can be seen in

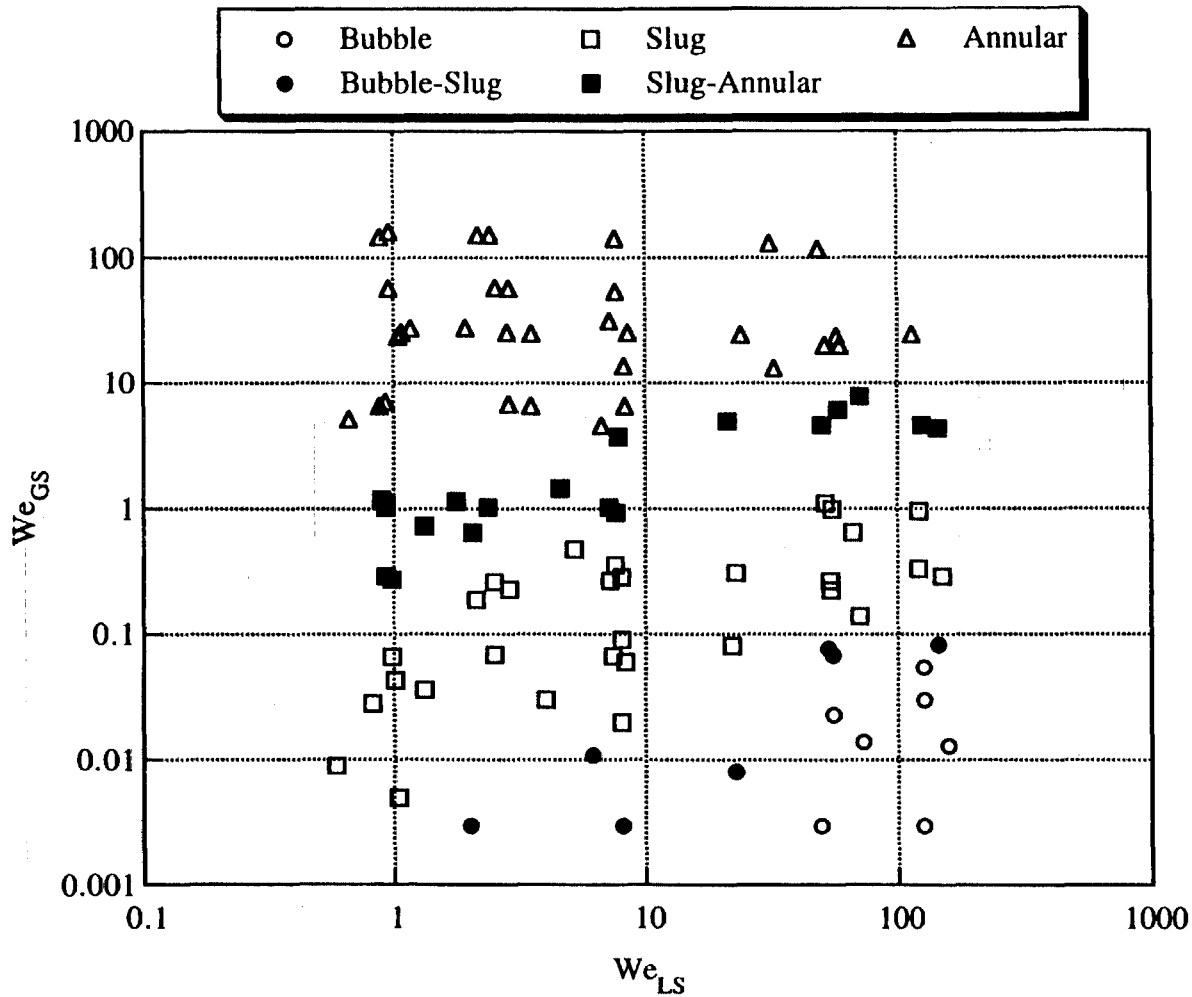

Figure 6.14 Microgravity Weber Number Flow Pattern Map for Air-Water in a 12.7 mm ID Tube

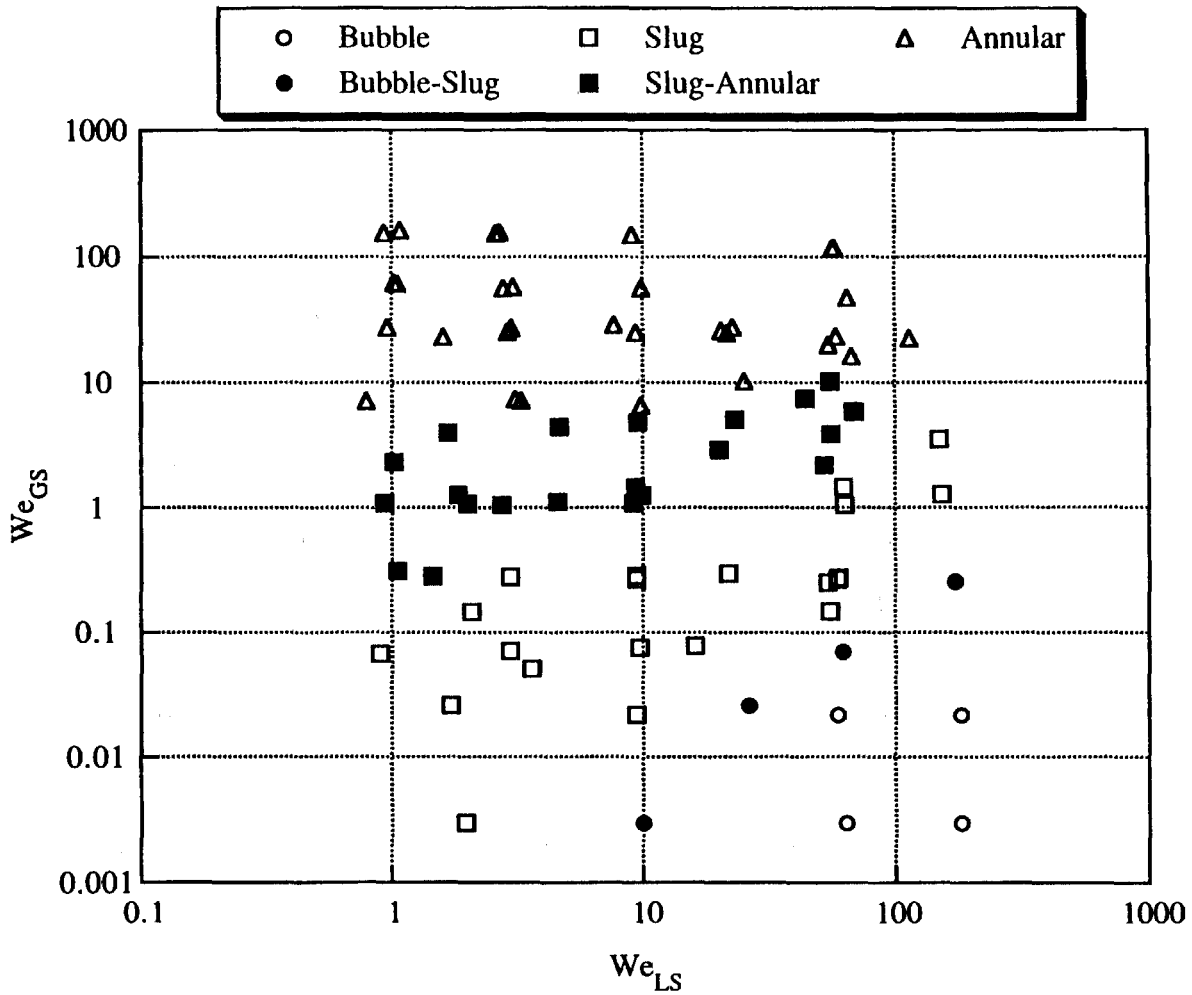

Figure 6.15 Microgravity Weber Number Flow Pattern Map for Air-Water/Glycerin in a 12.7 mm ID Tube

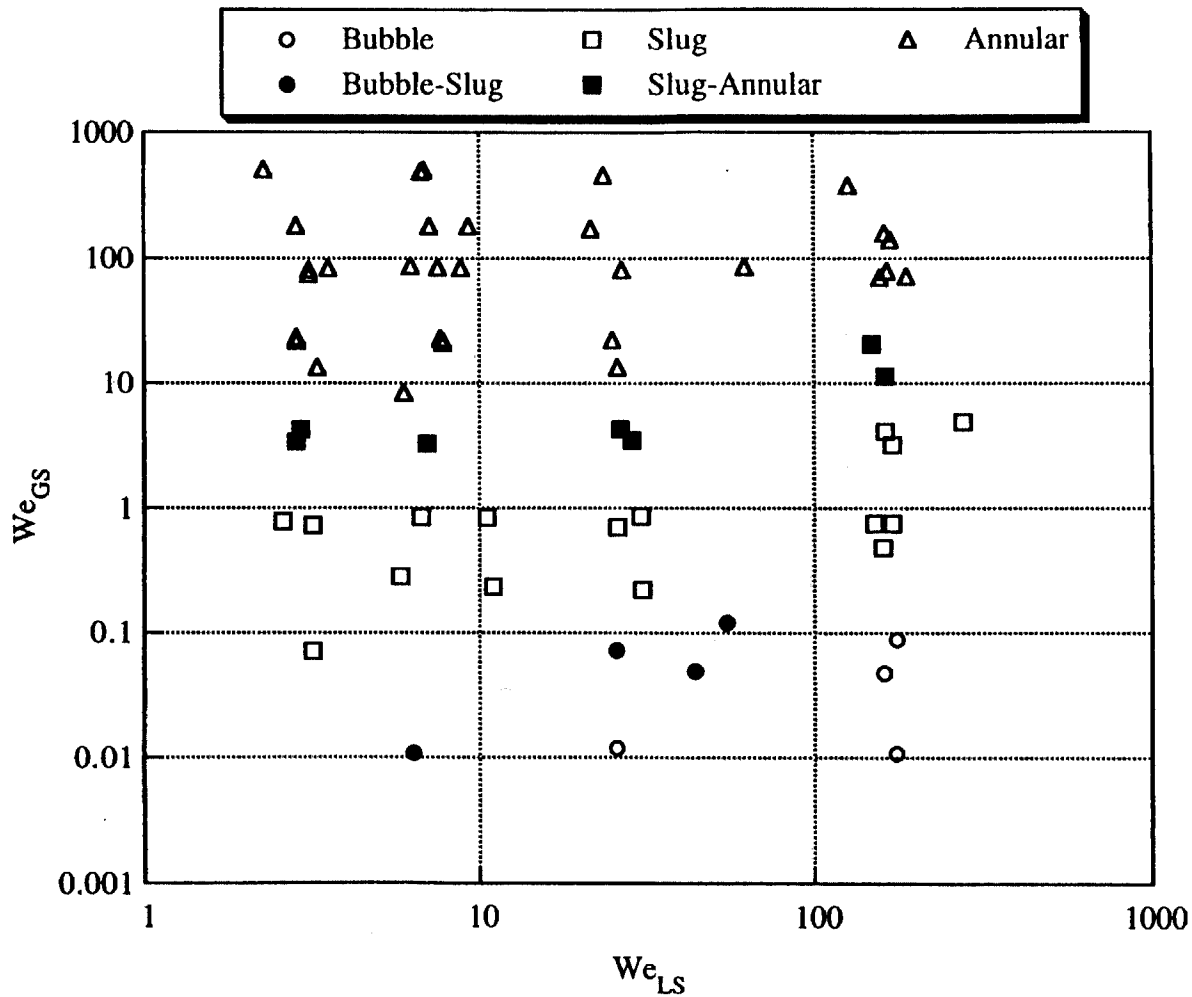

Figure 6.16 Microgravity Weber Number Flow Pattern Map for Air-Water/Zonyl FSP in a 12.7 mm ID Tube

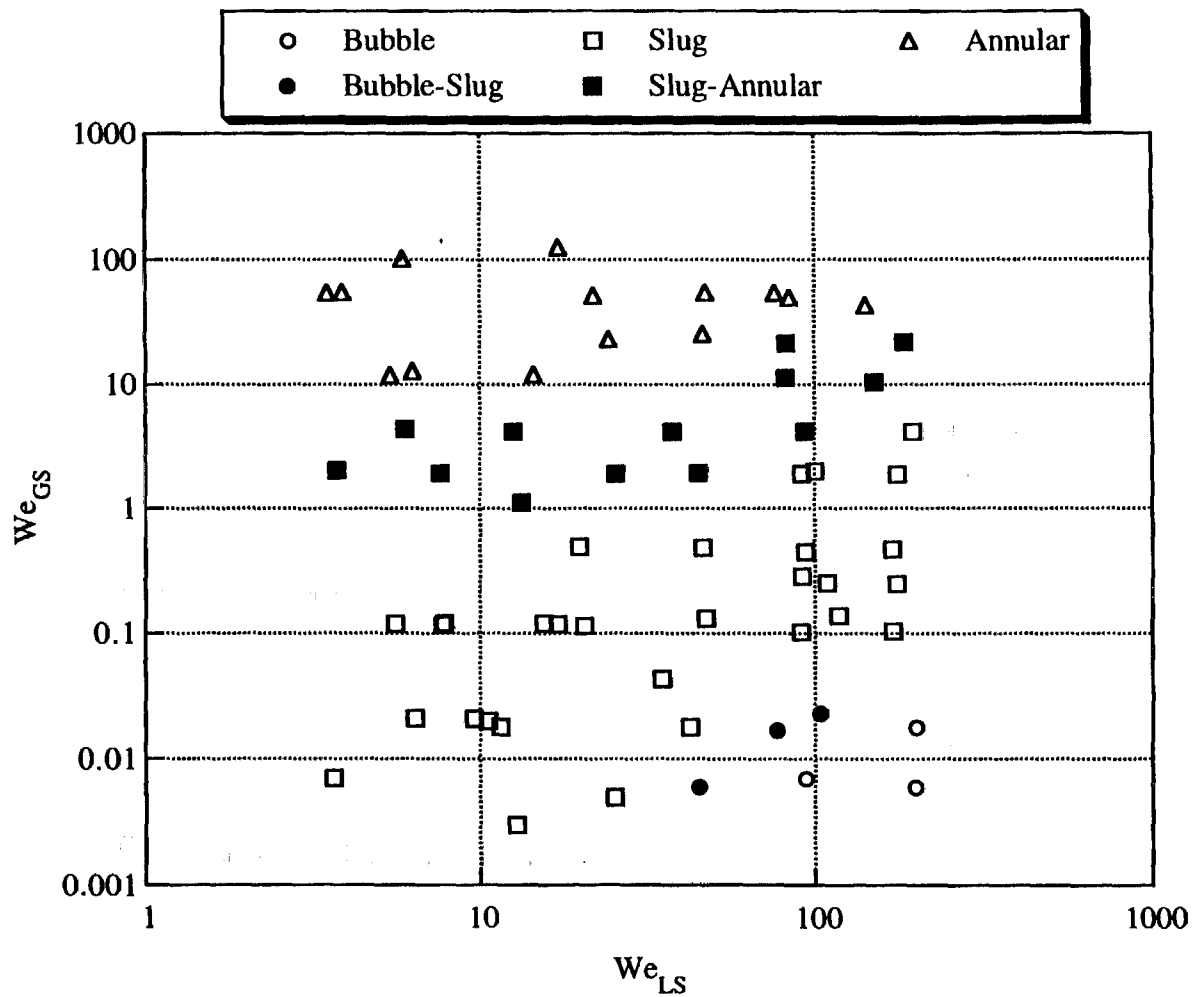

Figure 6.17 Microgravity Weber Number Flow Pattern Map for Air-Water in a 25.4 mm ID Tube

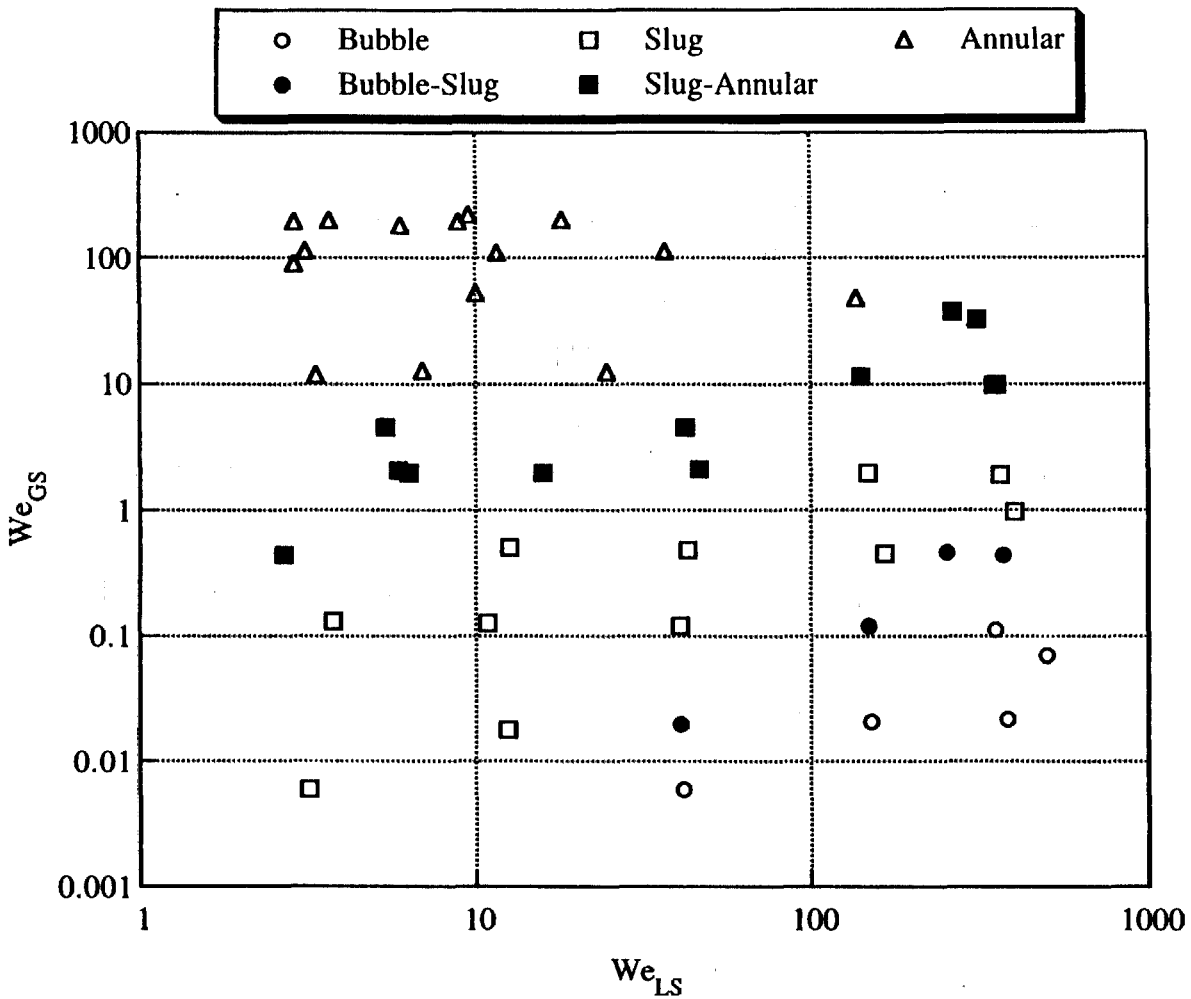

Figure 6.18 Microgravity Weber Number Flow Pattern Map for Air-Water/Glycerin in a 25.4 mm ID Tube

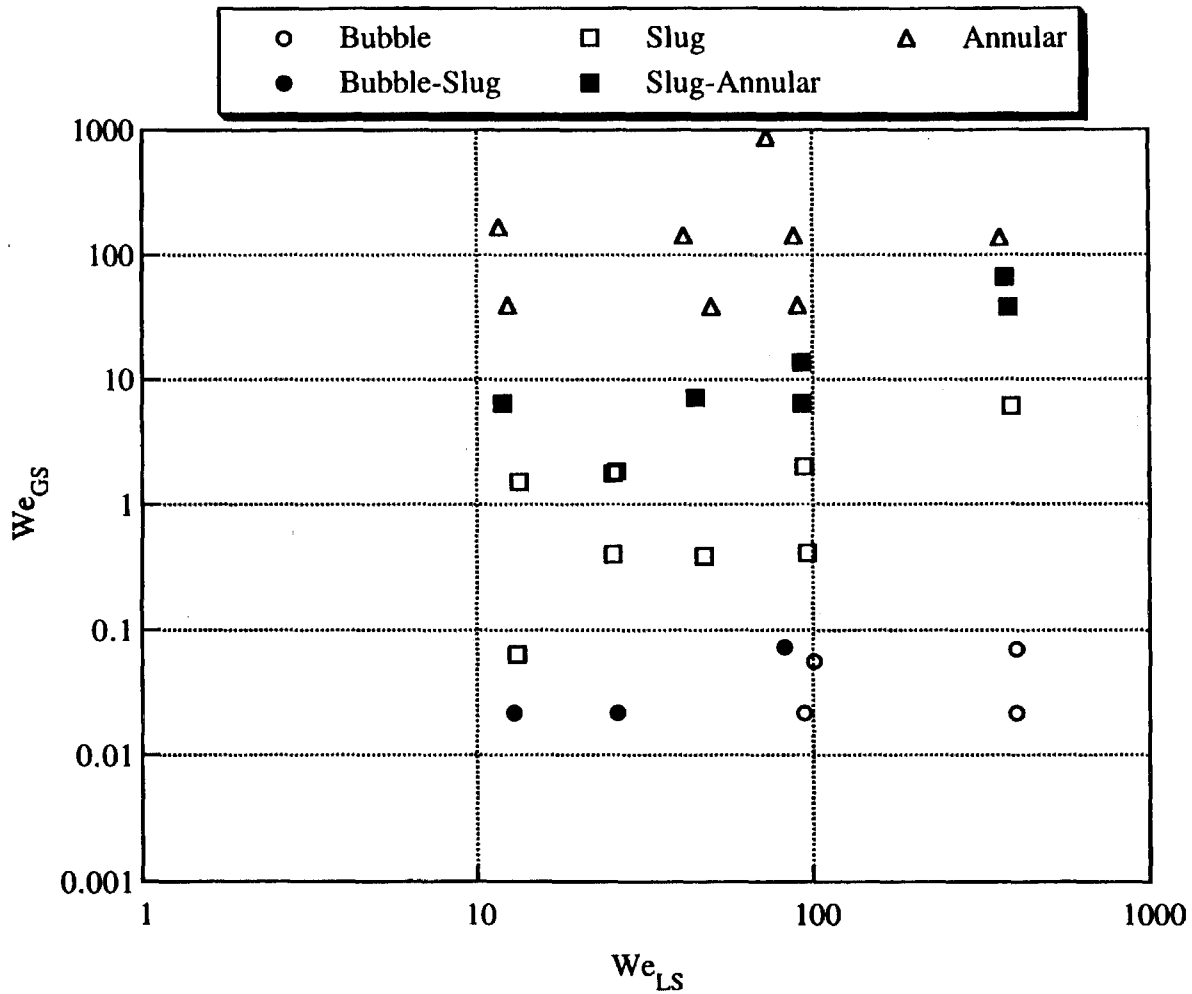

Figure 6.19 Microgravity Weber Number Flow Pattern Map for Air-Water/Zonyl FSP in a 25.4 mm ID Tube

the Weber number flow pattern maps presented by Zhao and Rezkallah, 1993, although the deviation from constant Weber number transitions is less than that of the present study.

The Weber number flow pattern maps shown in Figures 6.14-6.19 do not support the constant Weber number transition criteria over the entire parameter space. However, the flow patterns do fall into distinct zones on the flow pattern maps and the boundaries are qualitatively similar to those on the velocity based flow pattern maps. This similarity occurs because the Weber numbers defined by (6.28) and (6.29) are computed from the squares of the superficial velocities. Since a direct relation between the void fraction and superficial velocities in bubble and slug flows was demonstrated previously, the similarity between void fraction based transition criteria and Weber number based criteria is expected.

Transition models based on empirical fits of the transition boundaries in the figures would be easy to implement because the Weber numbers are easily calculated, but similar relations could be calculated in terms of superficial velocities as well. The advantages of Weber number based flow pattern maps will only be realized if a mechanistic criteria can be determined which is simpler to implement than the complex void fraction based slug-annular transition model presented previously. To accomplish this, further work into the balance between the inertial and surface tension forces, as well as any other forces affecting the flow patterns, is required.

Chapter 7 Summary, Conclusions and Recommendations

7.1 Summary of Research

The preceding text described a study of the flow patterns and properties of two-phase gas-liquid flows in microgravity. The previous work in this area has been limited primarily to photographic flow pattern identification and pressure drop, so an experimental system was developed which allowed for the reliable high-speed measurement of void fraction, liquid film thickness, propagation velocity, pressure drop and wall shear stress in addition to flow pattern identification by both photographic and electronic methods. These measurements provided the detailed knowledge needed to better understand the processes occurring in two-phase flows.

The physical properties of the fluids were known to affect the behavior of two-phase flows so three fluid systems were utilized in this study which allowed the effects of liquid viscosity and the gas-liquid surface tension to be characterized. The characterization of the effect of tube diameter was also attempted but this was limited to flow pattern identification in two tube sizes due to limited resources.

The initial experimental studies established the microgravity flow pattern maps for each fluid system and each tube diameter, showing the occurrence of the flow patterns identified in microgravity as a function of gas and liquid superficial velocities. Many of these early experimental studies led to the refinements of the measurement systems needed for more detailed measurements. The next stage of experimentation focused on obtaining measurements of void fraction, film thickness, pressure drop and propagation velocity across the gas-liquid superficial velocity parameter space. Finally, because annular flow is the most prevalent flow pattern in industrial applications, a set of experiments was focused

specifically on annular flow to obtain some of the information needed for modeling and design correlations.

Throughout the analysis of the experimental results, the commonly used 1g two-phase flow models for quantities such as void fraction and pressure drop were evaluated to gauge their suitability for microgravity two-phase flow. In addition, mechanistic models of the microgravity flow pattern transitions were developed and refined based on the findings made during this study. Finally, the analysis of the measurements and observations made during this study were used to gain a more detailed understanding of the processes occurring in microgravity two-phase flows and to suggest future work in this area.

7.2 Conclusions

A number of conclusions can be made from the results presented in this study:

1. The proper design and operation of multiphase flow measurement equipment in the microgravity aircraft environment requires special attention to details which are often insignificant in earth-based experiments. The effects of vibration, residual acceleration components in all directions, electromagnetic noise, ground loops, atmospheric pressure changes, flow development length and ease of operation in the short-duration microgravity environment must be carefully considered if the experiments are to succeed.

2. Three flow patterns (bubble flow, slug flow and annular flow) have been observed in microgravity. In addition, transitional states between bubble and slug flow and slug and annular flow have been observed. These flow patterns occur in distinct regions of the gas and liquid superficial velocity parameter space.

3. The effects of liquid viscosity on the flow pattern maps are small. The reduction in surface tension between the gas and the liquid shifts the transition from bubble to slug flow

to higher void fraction values but produces no change in the transition from slug to annular flow. Doubling the tube diameter shifts the transition from bubble to slug flow to lower values of void fraction for the air-water system only but otherwise has little effect on the flow pattern maps.

4. The void fraction and bubble propagation velocity in microgravity bubble and slug flows can be effectively modeled with the Drift-Flux model. A distribution coefficient of 1.21 has been determined from experimental measurements for low viscosity (1 cP) systems and is independent of surface tension. For the higher viscosity liquid (6 cP) system tested in this study, a distribution coefficient of 1.48 has been determined from experimental measurements.

5. Two-phase friction factors measured in this study for microgravity bubble and slug flows are not well predicted from the homogeneous friction factor model. This result may be due to the proximity of the laminar-turbulent transition for most of the experimental conditions and to insufficient test section length resulting in very small pressure gradients across the test section.

6. The liquid film in microgravity annular flow is axisymmetric in the mean but locally rough and irregular. Waves on the annular film are irregular and ring-like. The shape of the waves is in a state of continuous change.

7. An increase in the liquid viscosity causes an increase in the mean film thickness and wave amplitude at the same gas and liquid flow conditions. A decrease in the surface tension causes a decrease in the mean film thickness and wave amplitude at the same flow conditions. The ratio of wave amplitude to film substrate thickness is essentially independent of liquid viscosity and surface tension.

8. Increasing gas superficial velocity and decreasing liquid superficial velocity cause the mean film thickness and the wave amplitude to decrease. As the superficial gas velocity increases, the ratio of wave amplitude to film substrate thickness decreases linearly and is essentially independent of the liquid superficial velocity. An increase in the superficial gas velocity increases both the wave velocity and frequency.

9. The mechanistic film thickness models developed by Kosky, 1971 and Henstock and Hanratty, 1976 are in fair agreement with the experimental results for microgravity annular flow. The normalized film thickness correlates well with the liquid Reynolds number.

10. The microgravity annular flow pressure drop increases with increasing gas or liquid superficial velocity and is much greater than that of the gas flowing alone in the tube. An increase in the liquid viscosity significantly increases the annular flow pressure drop. Large changes in the surface tension did not cause a change in the annular flow pressure drop.

11. The Lockhart-Martinelli-Chisholm separated flow model for annular flow pressure drop predicts the annular flow pressure drop in microgravity with about the same accuracy as in the normal gravity environment (±20%). The Wallis interfacial friction factor pressure drop model is accurate for microgravity annular flows when the void fraction is greater than 0.8. For void fractions less than 0.8, the Wallis model significantly underpredicts the interfacial friction factor.

12. The wall shear stress profile in microgravity annular flows closely tracks the shape of the gas-liquid interface. The peak values of wall shear stress coincide with the peaks of the waves.

13. Force balances on microgravity annular flows suggest that droplet entrainment may cause a large fraction of the increased pressure drop in annular flow as compared to single-

phase gas flow. The force balances suggest that entrainment is significantly reduced as the liquid viscosity or surface tension are increased.

14. The bubble-slug flow pattern transition appears to fall along a line of constant void fraction. The transition void fraction is in the range of 0.35 - 0.45 for all fluid systems and tube diameters tested except for the air-water system in a 25.4 mm ID tube where a transition void fraction of 0.23 is reported.

15. A void fraction matching criteria for modeling the slug-annular flow pattern transition predicts that the transition falls along a line of constant void fraction of 0.8 when both the liquid and gas phases in annular flow are turbulent. This model predicts that the transition does not fall along a line of constant void fraction when the gas is turbulent and the liquid is laminar. The predicted transition void fraction of 0.8 does not provide good separation between the turbulent slug and annular flows on the flow pattern maps but a transition void fraction of 0.75 for low viscosity (1 cP) liquids and 0.7 for high viscosity (6 cP) liquids does provide an reasonable prediction of the transition on the flow pattern map.

16. Weber number flow pattern transition models in their current form do not provide a more accurate prediction of the transitions than can be predicted from the void fraction based models. The Weber number models are simpler to use.

7.3 Recommendations for Future Work

Based on the results and conclusions of this study as well as the needs of those designing and operation microgravity two-phase flow systems, the following suggestions for future research can be made:

1. Because of limited resources, many of the detailed measurements presented for microgravity two-phase flow in a 12.7 mm ID tube were not made for the 25.4 mm ID tube. While the diameter effect on the flow pattern maps was assessed in this study, the effect of diameter on other quantities of interest such as film thickness, pressure drop, velocities and wall shear stress was not quantified. A study to determine these effects should be performed while the facilities for this work still exist.

2. The pressure drop measurements for bubble and slug flows need to be repeated using a longer test section. The current experimental apparatus provide signals which were too small to be accurately measured. More accurate and reproducible measurements would lead to the development of a suitable pressure drop model for microgravity bubble and slug flows.

3. The force balance results of this study suggest that droplet entrainment and deposition may play a significant role in many of the processes occurring in microgravity annular flow. Thus measurements of the entrainment rate are an essential element in developing a more mechanistic understanding of microgravity annular flows. Such measurements will be difficult and longer duration space flight experiments will probably be required to achieve them.

4. The effort to improve the accuracy of slug-annular flow pattern transition models should continue. A better understanding of the details of the mechanism of transition will likely be required.

5. The microgravity two-phase flow investigation of Reinarts, 1993 as well as others, using Freon refrigerants shows that large changes occur in the flow pattern maps with large changes in the density of the fluids and other physical property changes. While the air-water system and similar systems have been investigated thoroughly in the present study and others, a similar level of understanding for fluid systems of industrial interest such as steam-water, ammonia and Freon refrigerants would provide a more complete foundation for the design and operation of practical microgravity two-phase flow systems.

6. The correlations for design and operation of two-phase flow systems in microgravity which are beginning to emerge are valid only for a straight, smooth tube. Actual flow systems frequently contain many bends, reductions, expansions valves and tees which could be expected to significantly effect the performance of the two-phase system. There is at present no work in the literature characterizing the effects of such components in a microgravity system.

7. The results of this study suggest that the waves on the annular film are responsible for many of the observed phenomena such as the large increases in pressure drop and wall shear stress. The detailed processes occurring in and around these waves will probably only be understood through a combined effort of gas and liquid flow field simulations and experimental measurements. Previous work in two-phase flow phenomena has been confined almost exclusively to experimental investigations but theoretical advances and simulations will likely be required before two-phase flow phenomena can be advanced to the next level of understanding.

8. The effects of entrance conditions on the microgravity two-phase flow phenomena observed in this study are not well understood. The effects of flow conditions and equipment configurations on the formation and growth of Taylor bubbles, liquid slugs and annular waves should be investigated.

9. Many space flight systems which work well on earth fail to perform as expected upon reaching the microgravity environment. With the current understanding of two-phase flow phenomena, such failures can be expected (and have already occurred) with two-phase flow systems as well. For these systems to become practical, future work must seek to define when microgravity flow systems will behave as they do on earth and when they will not. Similarly, earth-based two-phase flow models must be verified or modified for the microgravity environment prior to being implemented for design.

Notation

A	Cross-sectional tube area, m^2
A_E	Net momentum loss due to droplet entrainment and deposition, Pa/m
B	Physical property grouping for void fraction transition models, dimensionless
C	Blasius correlation constant or Chisholm model constant, dimensionless
C_o	Distribution coefficient, dimensionless
D	Tube diameter, m
E	Expectation value of a stationary process
f	Fanning friction factor, dimensionless
F	Any local quantity
Fr	Froude number, dimensionless
g	Acceleration of gravity, m/s^2
h	Liquid film thickness, mm
ID	Inside diameter of tube, mm
L	Length, m
m	Constant in distribution coefficient model, dimensionless
n	Constant in distribution coefficient model, dimensionless
N	Prandtl or Schmidt number, dimensionless
P	Pressure, Pa
r	Radial direction in cylindrical coordinates
R	Correlation coefficient for linear curve fit, dimensionless
R	Tube radius, mm
R_{12}	Cross correlation between processes 1 and 2, dimensionless
Re	Reynolds number, dimensionless
t	Time, s
u	Velocity in axial direction, m/s

U	Velocity, m/s
U_o	Bubble rise velocity in vertical flows, m/s
$U*$	Friction velocity, m/s
V	Voltage, volts
We	Weber number, dimensionless
x	Axial direction in Cartesian coordinates and nose to tail direction on the aircraft
X	Stationary process
X^2	Lockhart-Martinelli model parameter, dimensionless
y	Wing-tip to wing-tip direction on the aircraft
z	Floor to ceiling direction on the aircraft
α	Void fraction, the ratio of gas volume to total volume, dimensionless
δ	Film thickness for turbulent velocity profile, mm
Δ	Difference
ϕ	Power spectral density function
$\phi(\alpha)$	Correlation between interfacial and gas-phase friction factors
ϕ_G	Gas phase two-phase flow multiplier for the Lockhart-Martinelli-Chisholm model
Φ	Normalized power spectral density function
Γ_{LF}	Mass flow rate of liquid film
μ	Viscosity, cP
ν	Kinematic viscosity, m^2/s
ρ	Density, kg/m^3
ρ_{12}	Normalized cross-correlation of processes 1 and 2, dimensionless
θ	Time lag between two processes, s
σ	Surface tension, dyne/cm
τ	Shear stress, Pa/m
ω	Frequency, Hz

Subscripts

c	Centerline
E	Entrainment
G	Gas phase
GS	Gas phase, superficial
h	Film thickness
i	Interface
L	Liquid phase
LS	Liquid phase, superficial
M	Void fraction averaged mixture
MS	Total of gas and liquid phases, superficial
ref	Reference
T	Total
TP	Two phase
w	Wall
WF	Wall friction
τ	Wall shear stress

Superscripts

n	Reynolds number exponent for Blasius correlation
*	Dimensionless
+	Normalized

Conventions

<a>	Cross-sectional area average of quantity a
$\bar{a}$	Mean value of quantity a

References

Albers, J.A. and Macosko, R.P., "Experimental Pressure Drop Investigation of Nonwetting, Condensing Flow of Mercury Vapor in a Constant Diameter Tube in 1-G and Zero Gravity Environments", NASA TN D-2838, NASA Lewis Research Center, Cleveland, Ohio, 1965.

Ambrosini, W., Andreussi, P. and Azzopardi, B.J., "A Physically Based Correlation for Drop Size in Annular Flow", *Int. J. Multiphase Flow*, **17**, 497-507, 1991.

Anderson, J.D., Modern Compressible Flow, McGraw-Hill, New York, 1982.

Andreussi, P., Asali, J.C. and Hanratty, T.J., "Initiation of Roll Waves in Gas-Liquid Flows", *AIChE J.*, **31**, 119-126, 1985.

Asali, J.C., Entrainment in Vertical Gas-Liquid Annular Flows, Ph.D. Dissertation, University of Illinois, 1984.

Asali, J.C., Hanratty, T.J. and Andreussi, P., "Interfacial Drag and Film Height for Vertical Annular Flow", *AIChE J.*, **31**, 895-902, 1985.

Baker, O., "Simultaneous Flow of Oil and Gas", *Oil and Gas J.*, **53**, 185-195, 1954.

Baker, O., "Multiphase Flow in Pipelines", *Oil and Gas J.*, **56**, 156-167, 1958.

Barnea, D., "Transition from Annular Flow and from Dispersed Bubble Flow - Unified Models for the Whole Pipe Range of Inclinations", *Int. J. Multiphase Flow*, **12**, 733-744, 1986.

Bendat, J.S. and Piersol, A.G., Random Data: Analysis and Measurement Procedures, 2nd Ed., John Wiley and Sons, New York, 1986.

Bendickson, K.H., "An Experimental Investigation of the Motion of the Long Bubbles in Inclined Tubes", *Int. J. Multiphase Flow*, **10**, 467-483, 1984.

Bousman, W.S. and McQuillen, J.B., " Characterization of Annular Two-Phase Gas-Liquid Flows in Microgravity", Proceedings of the NASA Second Microgravity Fluid Physics Conference, NASA Lewis Research Center, Cleveland, June, 1994.

Brown, R.C., Andreussi, P. and Zanelli, S., "The Use of Wire Probes for the Measurement of Liquid Film Thickness in Annular Gas-Liquid Flows", *Can. J. Chem. Eng.*, **56**, 754-757, 1978.

Chauve, M.P. and Schiestel, R., "Influence of Weak Wall Undulations on the Structure of Turbulent Pipe Flow: An Experimental and Numerical Study", *J. Fluid Mech.*, **160**, 47-75, 1985.

Chen, I., Downing, R., Parish, R. and Keshock, E., "A Reduced Gravity Flight Experiment: Observed Flow Regimes and Pressure Drops of Vapor and Liquid Flow in Adiabatic Piping", Proceedings of the 1988 AIChE Heat Transfer Conference, **84**, 203-216, Houston, 1988.

Chu, K.J. and Dukler, A.E., "Statistical Characteristics of Thin, Wavy Films III: Structure of the Large Waves and Their Resistance to Gas Flow", *AIChE J.*, **21**, 583-593, 1975.

Colin, C., Ecoulements Diphasiques a Bulles et a Poches en Micropesanteur, M.S. Thesis, Institut de Mecaniques des Fluides de Toulouse, France, 1990.

Collins, R., de Moraes, F.F., Davidson, J.F. and Harrison, D., "The Motion of a Large Gas Bubble Rising Through Liquid Flowing in a Tube", *J. Fluid Mech.*, **89**, 497-514, 1978.

Crowley, C.J. and Sam, R.G., "Microgravity Experiments with a Simple Two-Phase Thermal System", Report No. PL-TR-91-1059, Phillips Laboratory, Kirtland Air Force Base, New Mexico, 1991.

Dukler, A.E., "The Role of Waves in Two Phase Flow: Some New Understandings", *Chem.Eng. Ed.,* 108-138, Summer, 1977.

Dukler, A.E., Fabre J.A., McQuillen, J.B. and Vernon, R., "Gas Liquid Flow at Microgravity Conditions: Flow Patterns and Their Transitions", *Int. J. Multiphase Flow*, **14**, 389-400, 1988.

Fore, L.B., Droplet Entrainment in Vertical Gas-Liquid Annular Flow, Ph.D. Dissertation, University of Houston, 1993.

Freymuth, P., "Frequency Response and Electronic Testing for Constant-Temperature Hot-Wire Anemometers", *J. Phys. E: Sci. Instr.*, **10**, 705-710, 1977.

Goldstein, R.J., ed., Fluid Mechanics Measurements, Hemisphere Publishing, New York, 1983.

Govan, A.H., Hewitt, G.F., Owen, D.G. and Burnett, G., "Wall Shear Stress Measurements in Vertical Air-Water Annular Two Phase Flow", *Int. J. Multiphase Flow*, **15**, 307-325, 1989.

Grob, B., Basic Electronics, McGraw-Hill, New York, 1977.

Henstock, W.H. and Hanratty, T.J., "The Interfacial Drag and the Height of the Wall Layer in Annular Flows", *AIChE J.*, **22**, 990-1000, 1976.

Heppner, D.B., King, C.D. and Littles, J.W., "Zero-G Experiments in Two-Phase Fluid Flow Regimes", Proceedings of the Intersociety Conference on Environmental Systems, ASME 75-ENAS-24, San Francisco, July, 1975.

Hewitt, G.F. and Hall-Taylor, N.S., Annular Two-Phase Flow, Pergamon Press, Oxford, 1970.

Hill, W.S. and Best, F.R., "Definition of Two-Phase Flow Behaviors for Spacecraft Design", Report No. PL-TR-91-1050, Phillips Laboratory, Kirtland Air Force Base, New Mexico, 1991.

Huckerby, C.S. and Rezkallah, K.S., "Flow Pattern Observations in Two-Phase Gas-Liquid Flow in a Straight Tube Under Normal and Microgravity Conditions", Proceedings of the 1992 AIChE Heat Transfer Conference, **88**, 288, 139-147, San Diego, 1992.

Janicot, A.J.P., Experimental and Theoretical Studies of Gas-Liquid Two Phase Flow at Reduced Gravity Conditions, M.S. Thesis, University of Houston, August, 1988.

Jayawardena, S.S., Turbulent Flow in the Core Region of Vertical Annular Gas-Liquid Flow, Ph.D. Dissertation, University of Houston, 1993.

Jurman, L.A., Bruno, K. and McCready, M.J., "Periodic and Solitary Waves on Thin, Horizontal, Gas-Sheared Liquid Films", *Int. J. Multiphase Flow*, **15**, 371-384, 1989.

Koestal, A. and Gutstein, M.U., "Study of Wetting and Nonwetting Mercury Condensing Pressure Drops", NASA TN D-2514, NASA Lewis Research Center, Cleveland, Ohio, 1964.

Kosky, P.G., "Thin Liquid Films Under Simultaneous Shear and Gravity Forces", *Int. J. Heat Mass Transfer*, **14**, 1220-1224, 1971.

Lacy, C.E., Flooding and Wavy Films in Vertical Annular Gas-Liquid Flows, Ph.D. Dissertation, University of Houston, 1992.

Lambert, A., KC-135 Zero Gravity Two Phase Flow Pressure Drop Experiments and Modeling, M.S. Thesis, Texas A&M University, 1990.

Laurinat, J.E., Hanratty, T.J. and Dallman, J.C., "Pressure Drop and Film Height Measurements for Annular Gas-Liquid Flow", *Int. J. Multiphase Flow*, **10**, 341-356, 1984.

Lekan, J., "Microgravity Research in NASA Ground Based Facilities", NASA Technical Memorandum 101397, 1989.

Lockhart, L.W. and Martinelli, R.C., "Proposed Correlation of Data of Isothermal Two-Phase, Two Component Flow in Pipes", *Chem. Eng. Prog.*, **45**, 39-48, 1949.

Lopes, J.C.P. and Dukler, A.E., "Droplet Entrainment in Vertical Annular Flow and Its Contribution to Momentum Transfer", *AIChE J.*, **32**, 1500-1515, 1986.

Ludwieg, H., "Instrument for Measuring the Wall Shearing Stress of Turbulent Boundary Layers", NACA Technical Memorandum 1284, Washington, D.C., May, 1950.

Mao, Z., An Investigation of Two-Phase Gas-Liquid Slug Flow, Ph.D. Dissertation, University of Houston, 1988.

McLean, J.W., "Computation of Turbulent Flow Over a Moving Wavy Boundary", *Phys. Fluids*, **26**, 2065-2073, 1983.

Miller, K.M., Ungar, E.K., Dzenitis, J.M. and Wheeler, M., "Microgravity Two-Phase Pressure Drop Data in Smooth Tubing", ASME Winter Meeting, New Orleans, Nov. 1993.

Nicklin, D.J., Wilkes, J.O.and Davidson, J.F., "Two-Phase Flow in Vertical Tubes", *Trans. Inst. Chem. Engrs. London*, **40**, 61-68, 1962.

Paras, S.V. and Karabelas, A.J., "Properties of the Liquid Layer in Horizontal Annular Flow", *Int. J. Multiphase Flow*, **17**, 439-454, 1991.

Press, W.H., Teukolsky, S.A., Vetterling, W.T. and Flannery, B.P., Numerical Recipes in Fortran, 2nd Ed., Cambridge University Press, New York, 1992.

Reinarts, T.R., Adiabatic Two Phase Flow Regime Data and Modeling for Zero and Reduced (Horizontal Flow) Acceleration Fields, Ph.D. Dissertation, Texas A&M University, 1993.

Taitel, Y. and Dukler, A.E., "A Model for Predicting Flow Regime Transitions in Horizontal and Near Horizontal Gas-Liquid Flow", *AIChE J.*, **22**, 47-55, 1976.

Thomas, J.B., Applied Probability and Random Processes, Robert E. Kreiger Publishing, Malabar, Florida, 1971.

Tse, F.S. and Morse, I.E., Measurement and Instrumentation in Engineering, Marcel-Dekker, New York, 1989.

Wallis, G.B., One Dimensional Two Phase Flow, McGraw-Hill, New York, 1969.

Wasden, F.K., Studies of Mass and Momentum Transfer in Free Falling Wavy Films, Ph.D. Dissertation, University of Houston, 1989.

Zabaras, G.J., Studies of Vertical Annular Gas-Liquid Flows, Ph.D. Dissertation, University of Houston, 1985.

Zhao, L. and Rezkallah, K.S., "Gas-Liquid Flow Patterns at Microgravity Conditions", *Int. J. Multiphase Flow*, **19**, 751-763, 1993.

Zuber, N. and Findlay, J.A., "Average Volumetric Concentration in Two Phase Flow Systems", *J. Heat Transfer*, 453-468, Nov., 1965.

Appendix A High Speed Still Photographs of Microgravity Two-Phase Flows

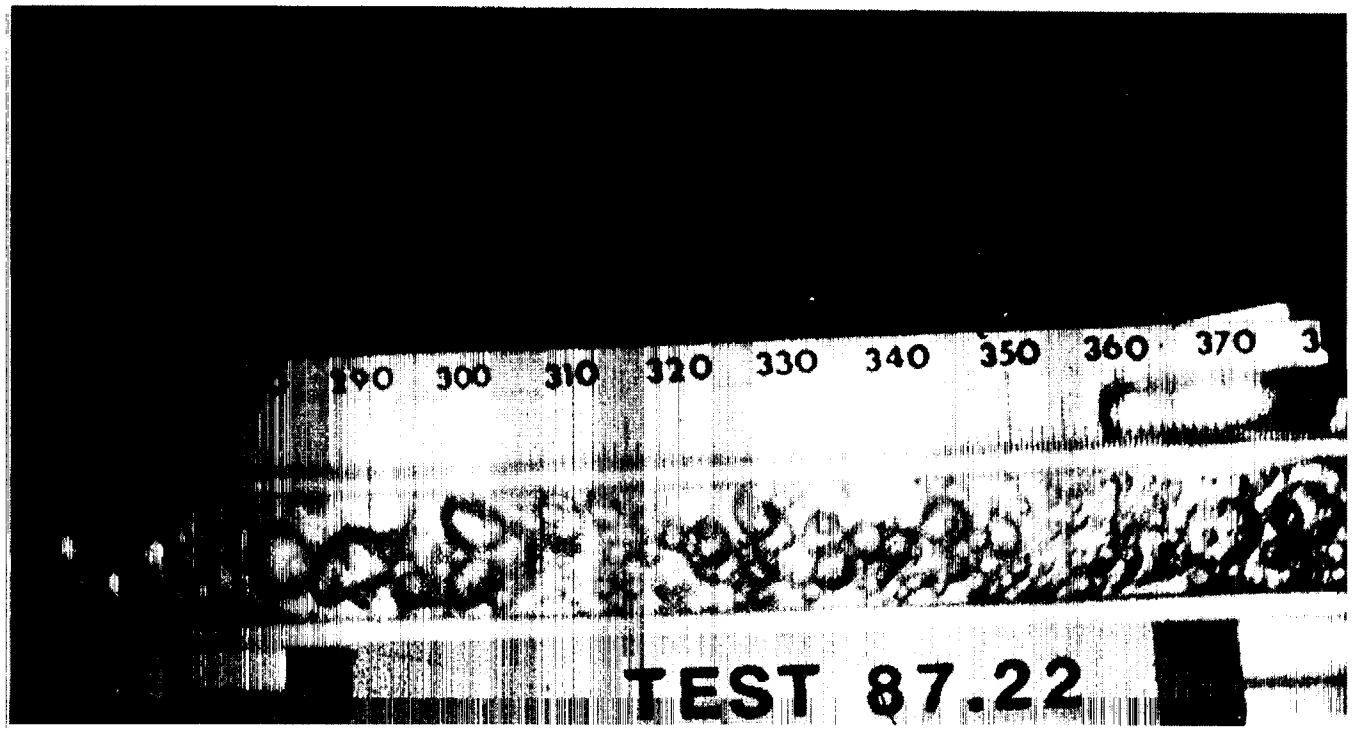

Figure A.1 Photograph of Microgravity Air-Water Bubble Flow in a 12.7 mm ID Tube

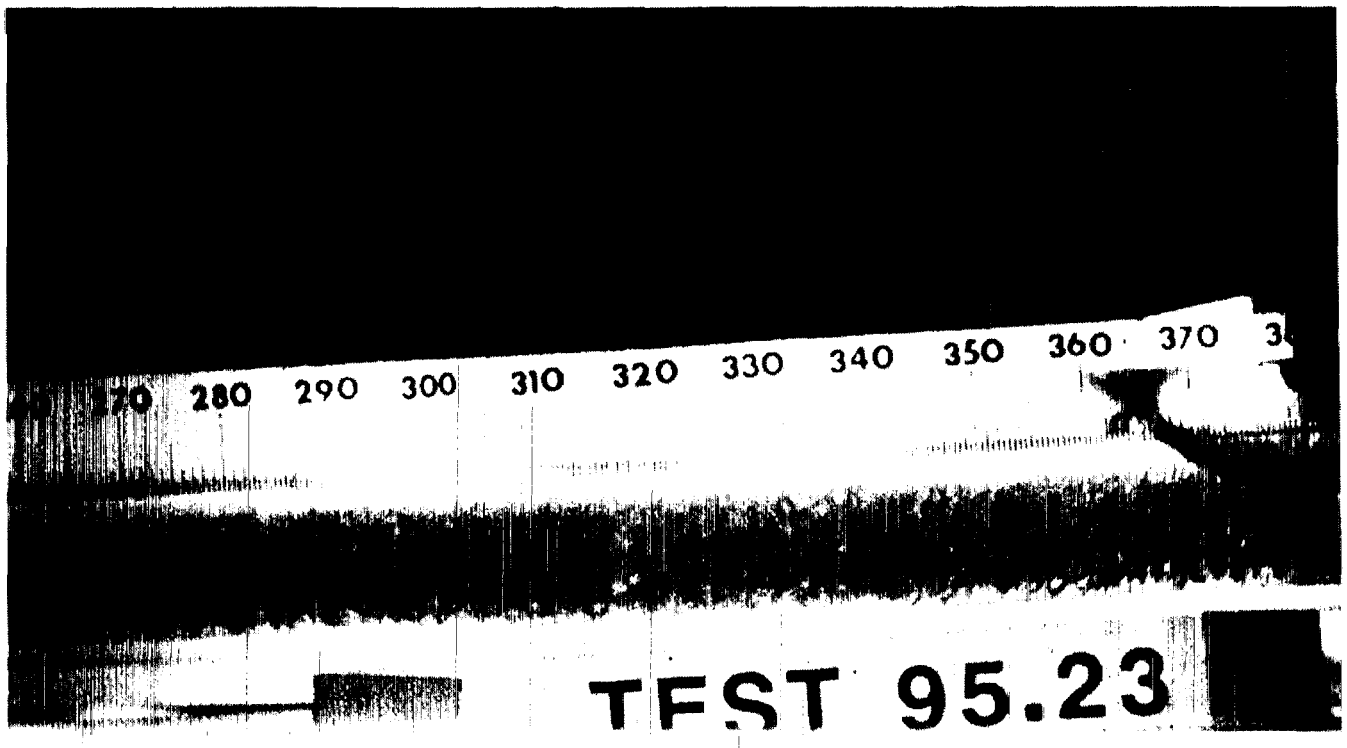

Figure A.2 Photograph of Microgravity Air-Water/Glycerin Bubble Flow in a 12.7 mm ID Tube

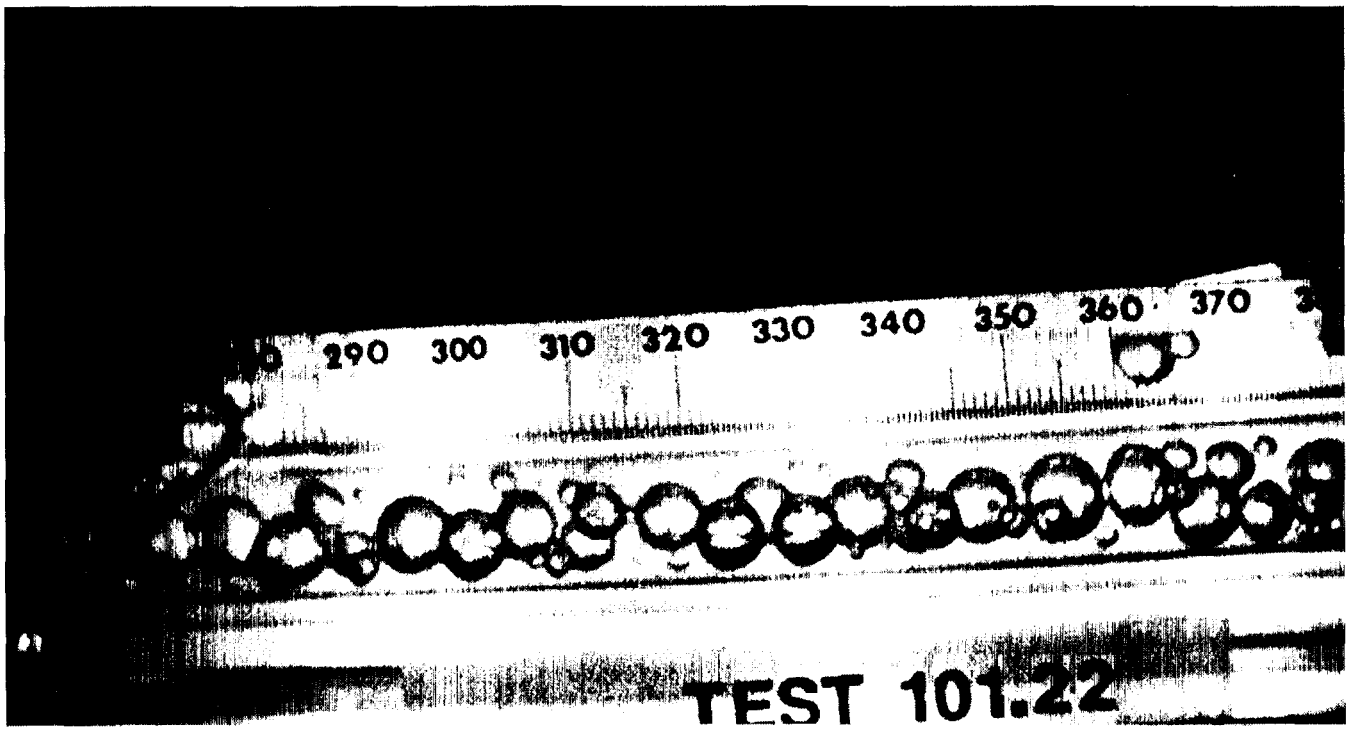

Figure A.3 Photograph of Microgravity Air-Water/Zonyl FSP Bubble Flow in a 12.7 mm ID Tube

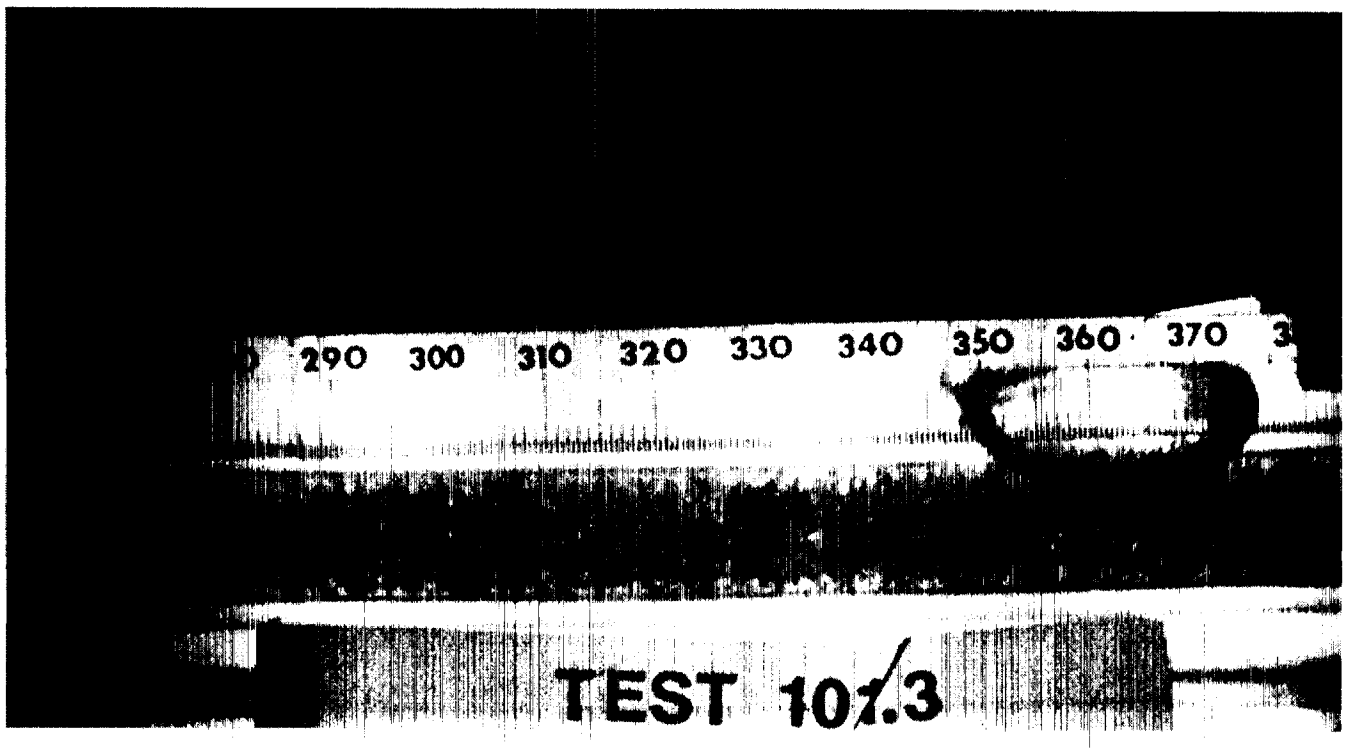

Figure A.4 Photograph of Microgravity Air-Water/Zonyl FSP Bubble Flow in a 12.7 mm ID Tube

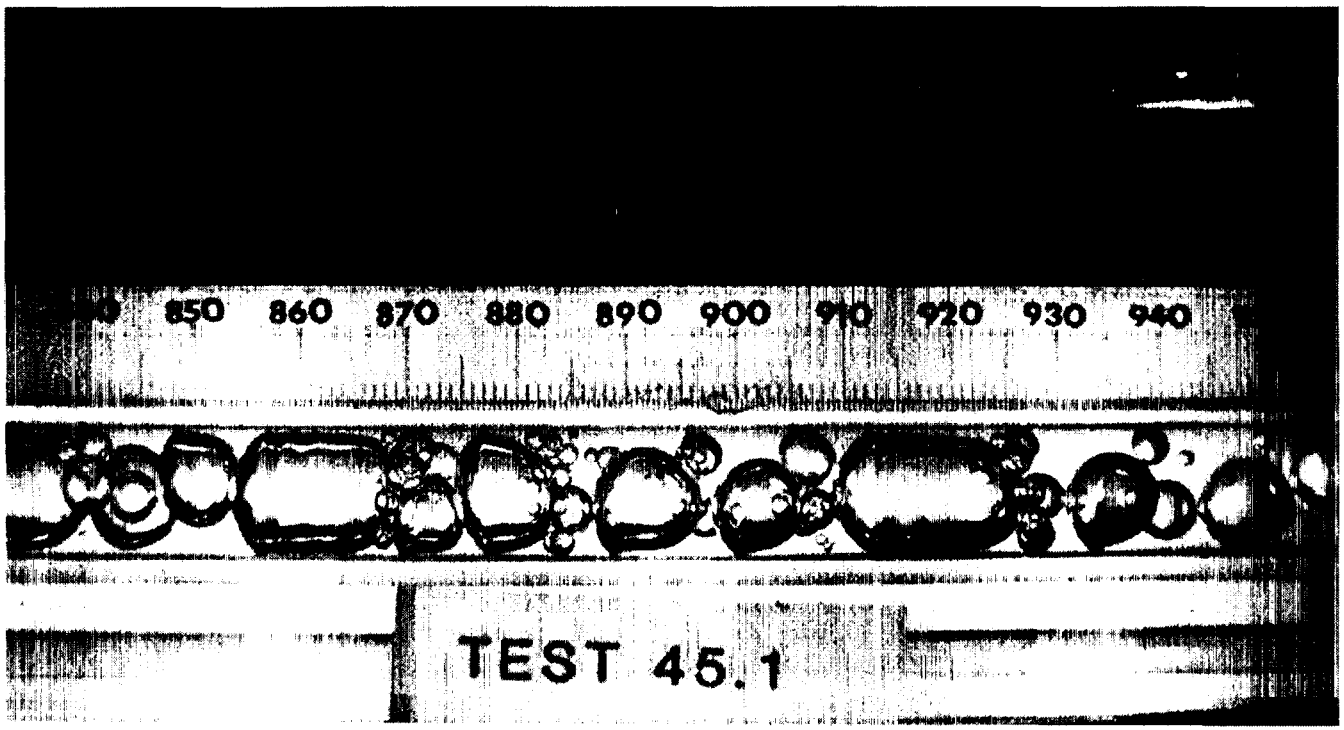

Figure A.5 Photograph of Microgravity Air-Water Bubble-Slug Transition Flow in a 12.7 mm ID Tube

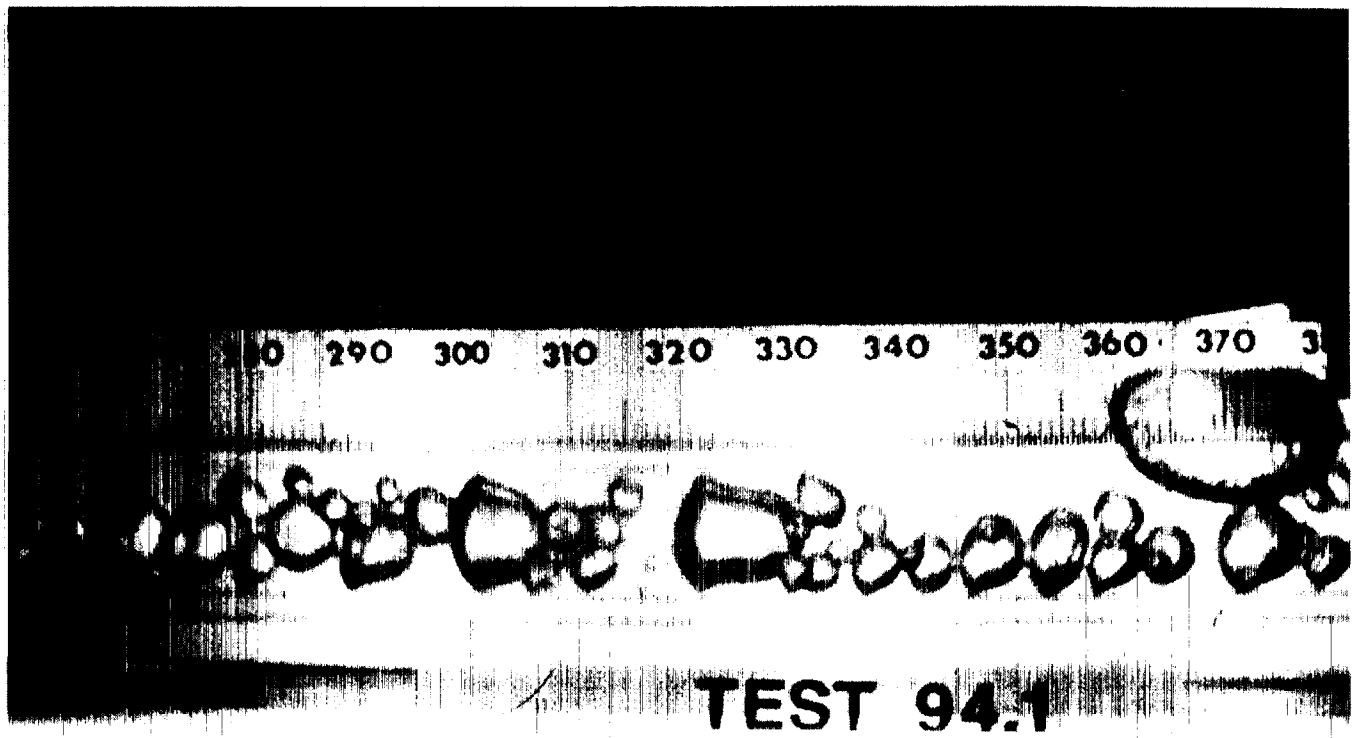

Figure A.6 Photograph of Microgravity Air-Water/Glycerin Bubble-Slug Transition Flow in a 12.7 mm ID Tube

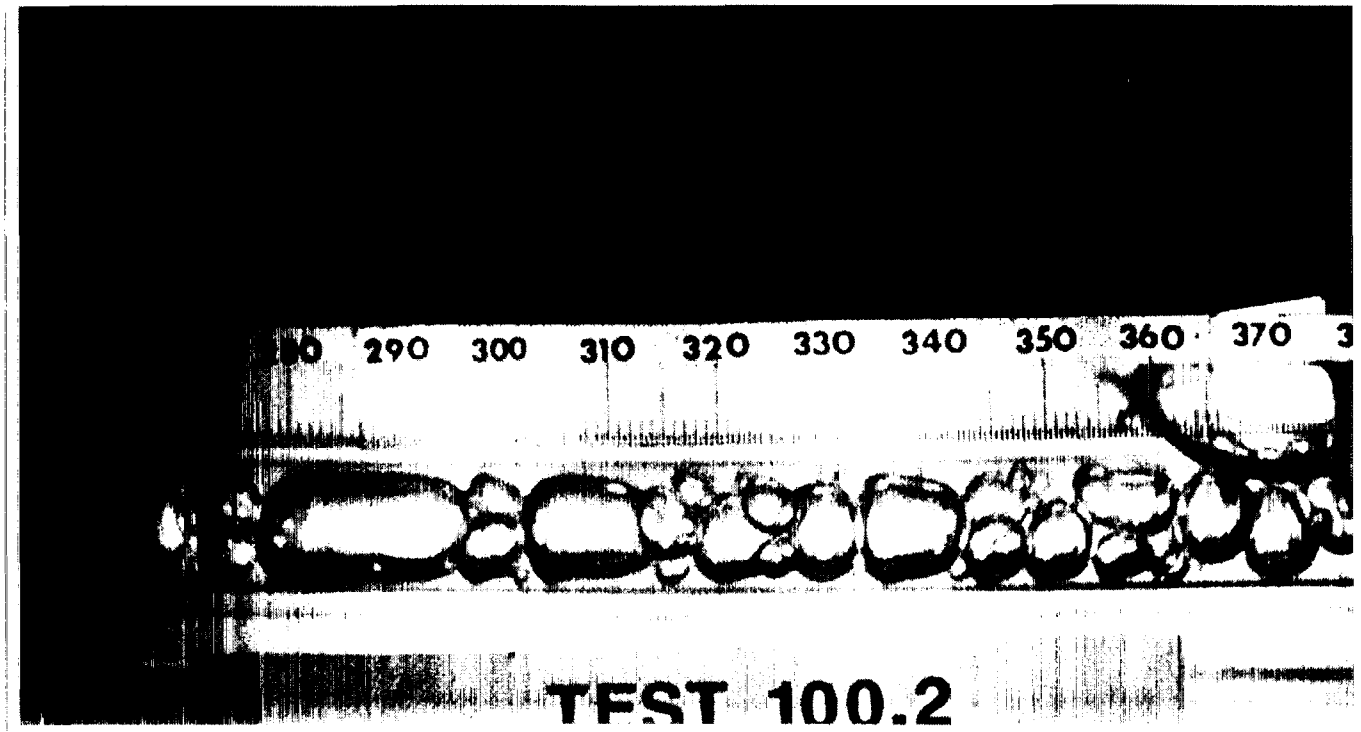

Figure A.7 Photograph of Microgravity Air-Water/Zonyl FSP Bubble-Slug Transition Flow in a 12.7 mm ID Tube

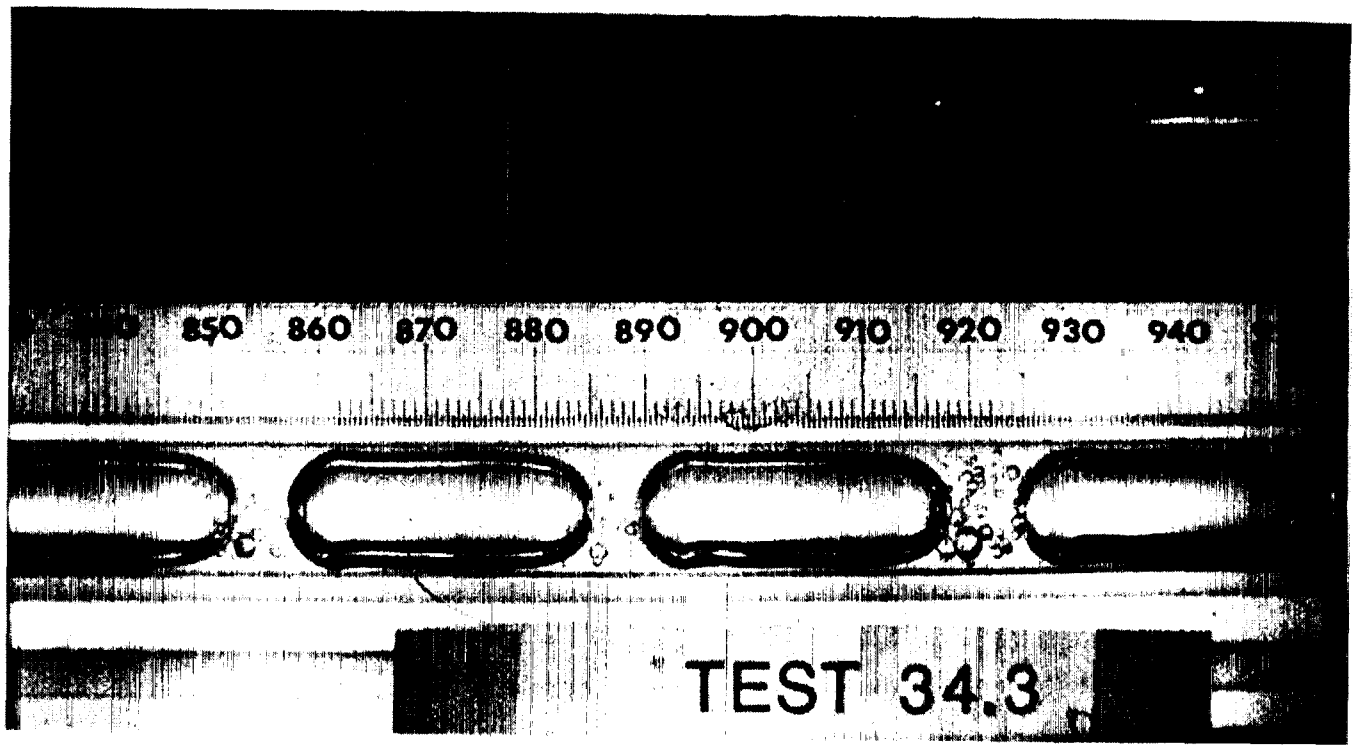

Figure A.8 Photograph of Microgravity Air-Water Slug Flow in a 12.7 mm ID Tube

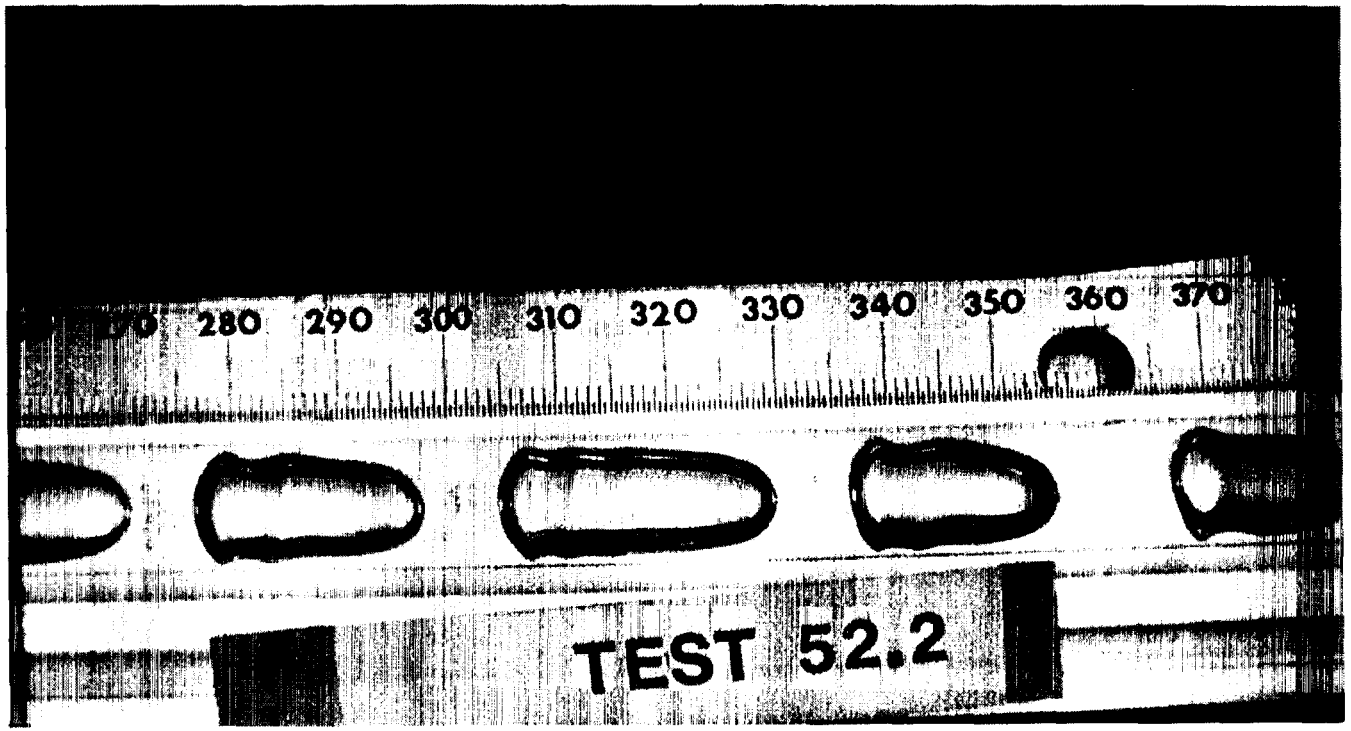

Figure A.9 Photograph of Microgravity Air-Water/Glycerin Slug Flow in a 12.7 mm ID Tube

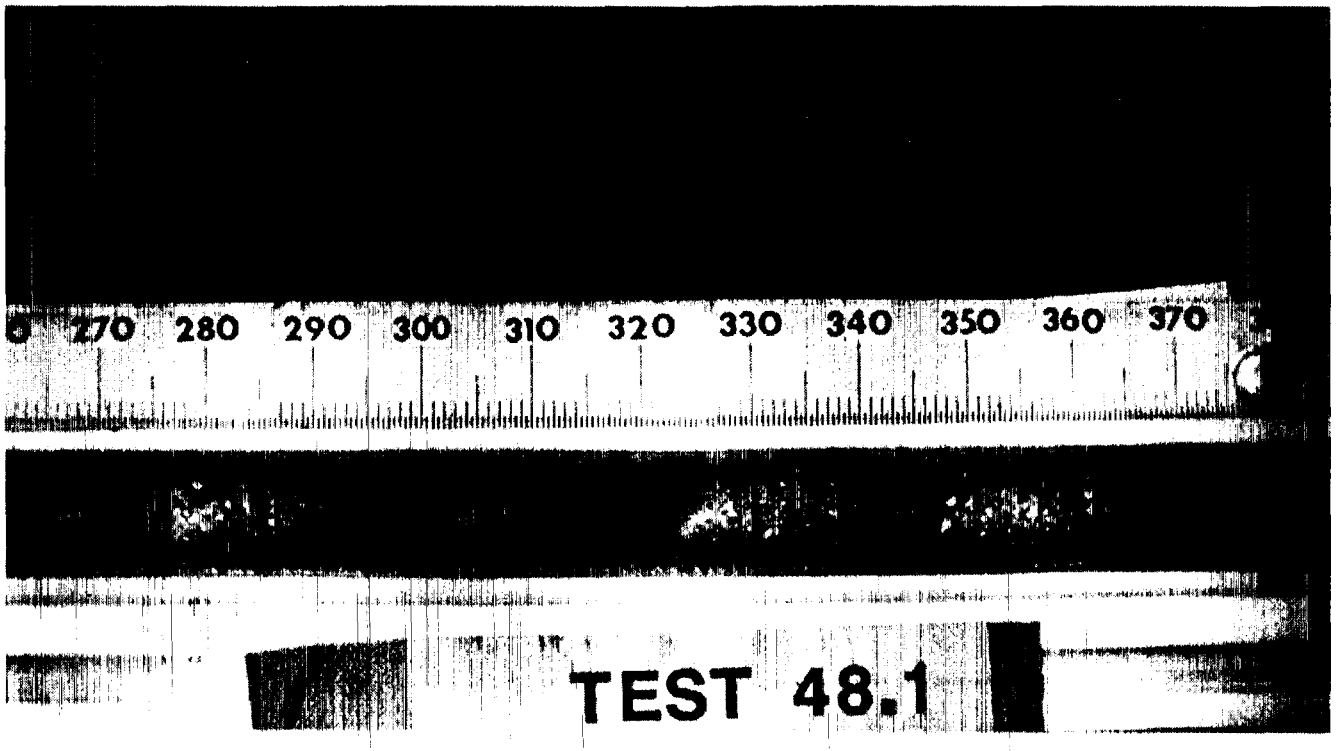

Figure A.10 Photograph of Microgravity Air-Water/Zonyl FSP Slug Flow in a 12.7 mm ID Tube

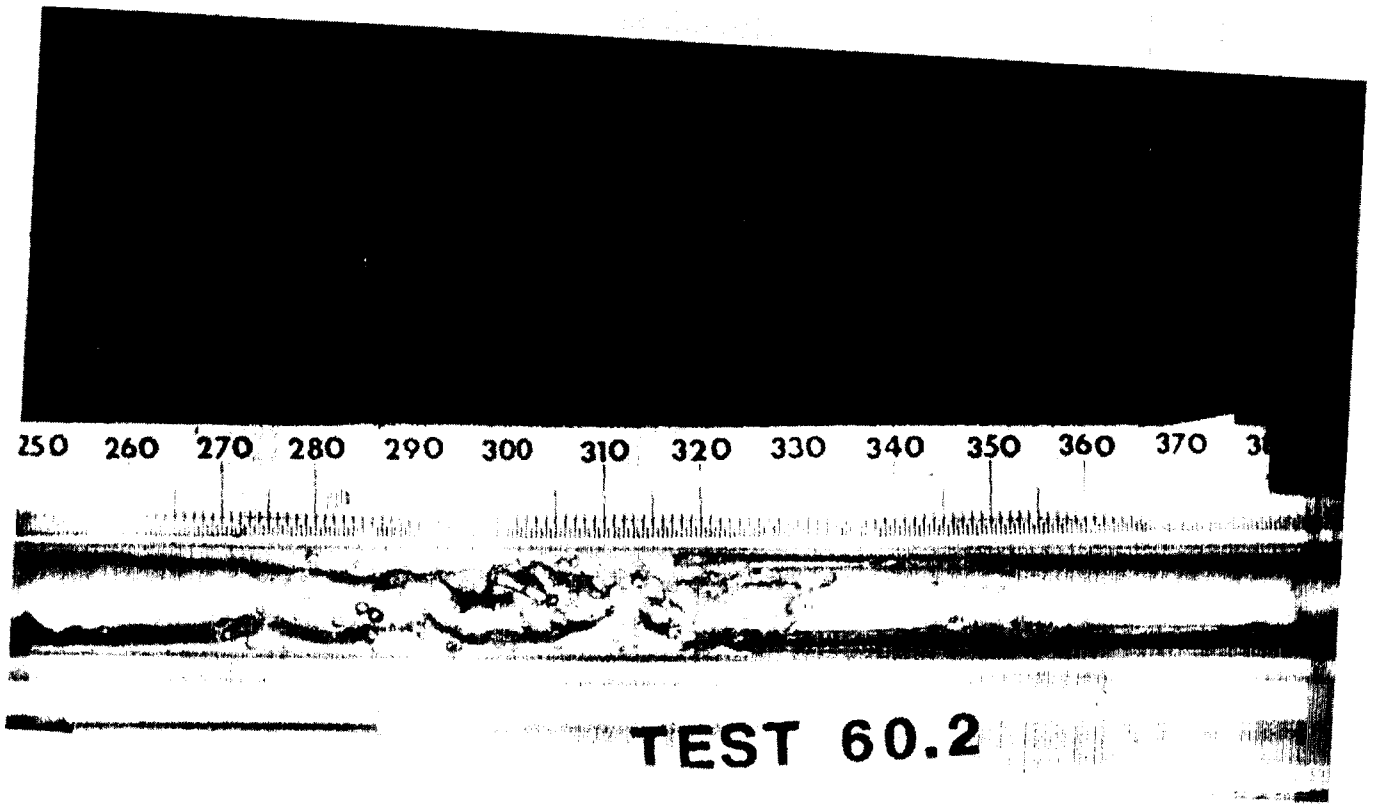

Figure A.11(a) Microgravity Air-Water Slug-Annular Transition Flow Prior to Rupture of a Liquid Slug

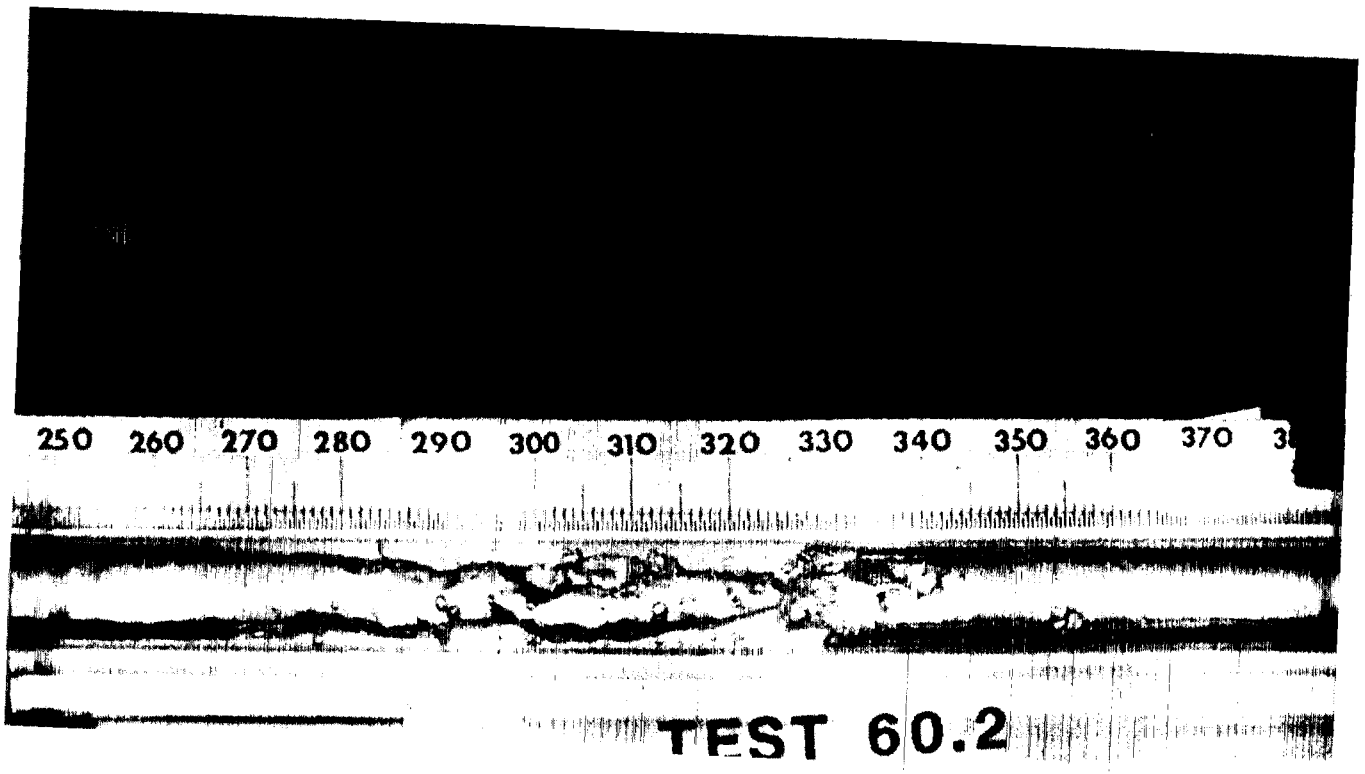

Figure A.11(b) Microgravity Air-Water Slug-Annular Transition Flow Showing Rupture of a Liquid Slug

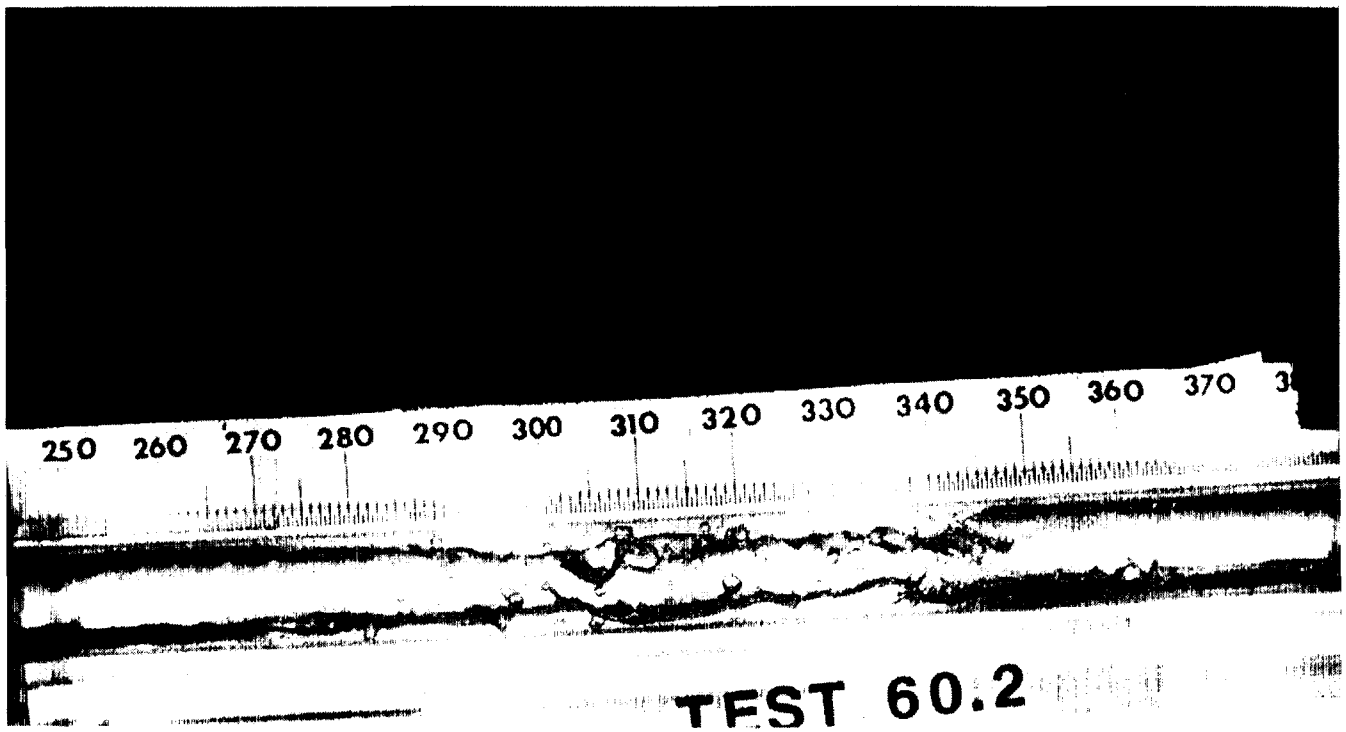

Figure A.11(c) Microgravity Air-Water Slug-Annular Transition Flow After Rupture of a Liquid Slug

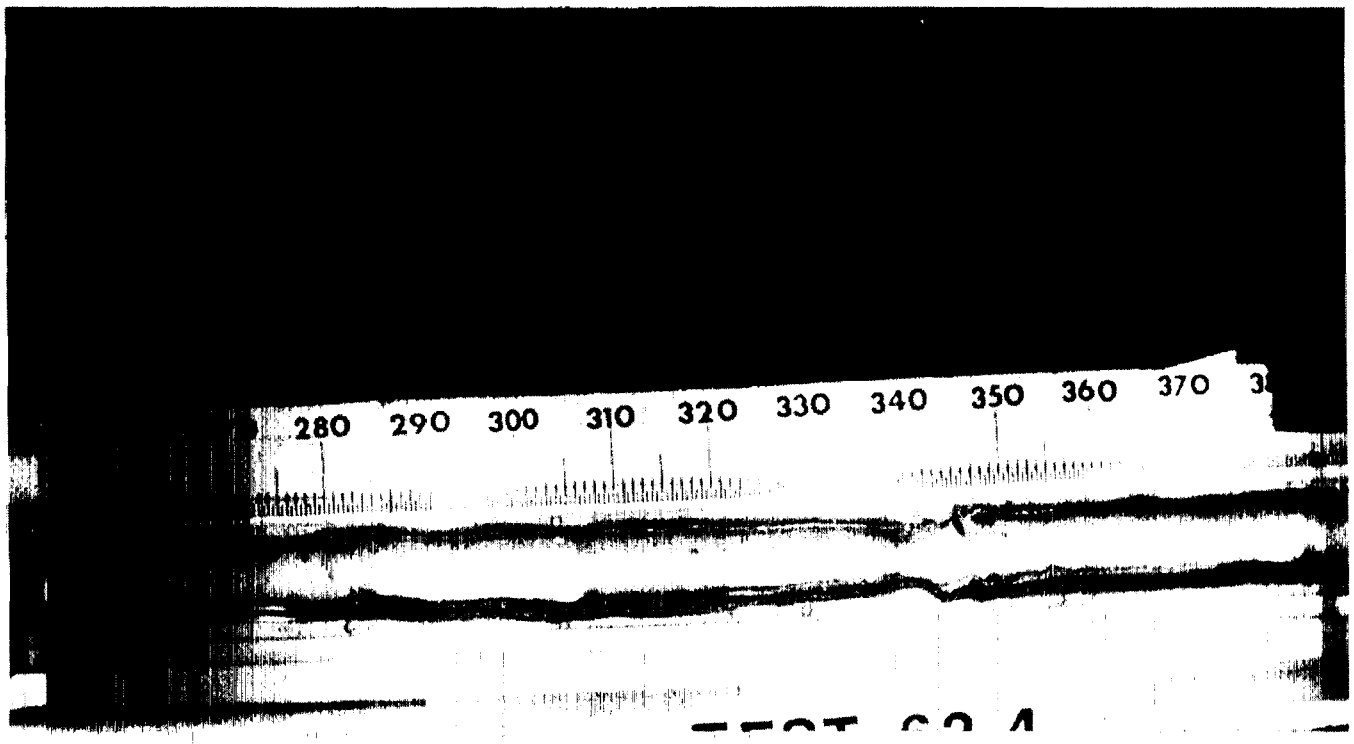

Figure A.12(a) Microgravity Air-Water/Glycerin Slug-Annular Transition Flow Prior to Bridging of the Tube

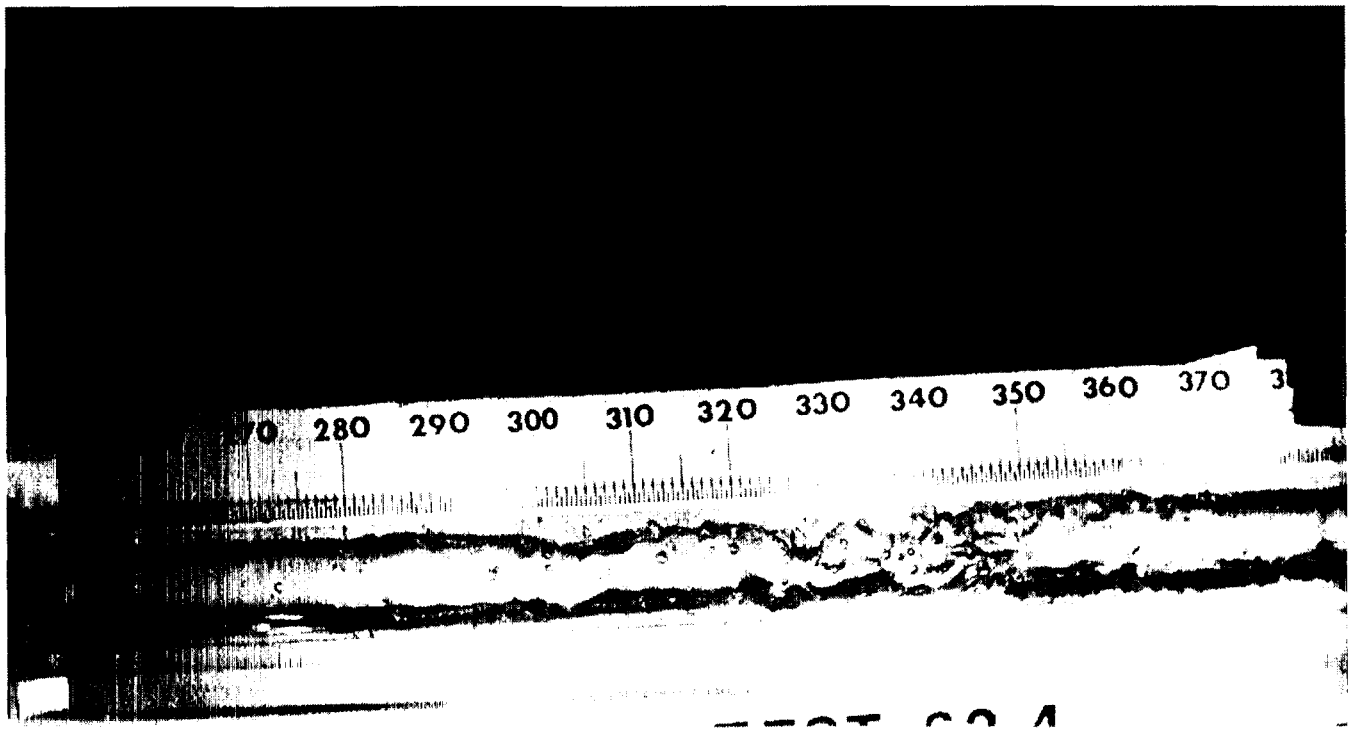

Figure A.12(b) Microgravity Air-Water/Glycerin Slug-Annular Transition Flow During Bridging of the Tube

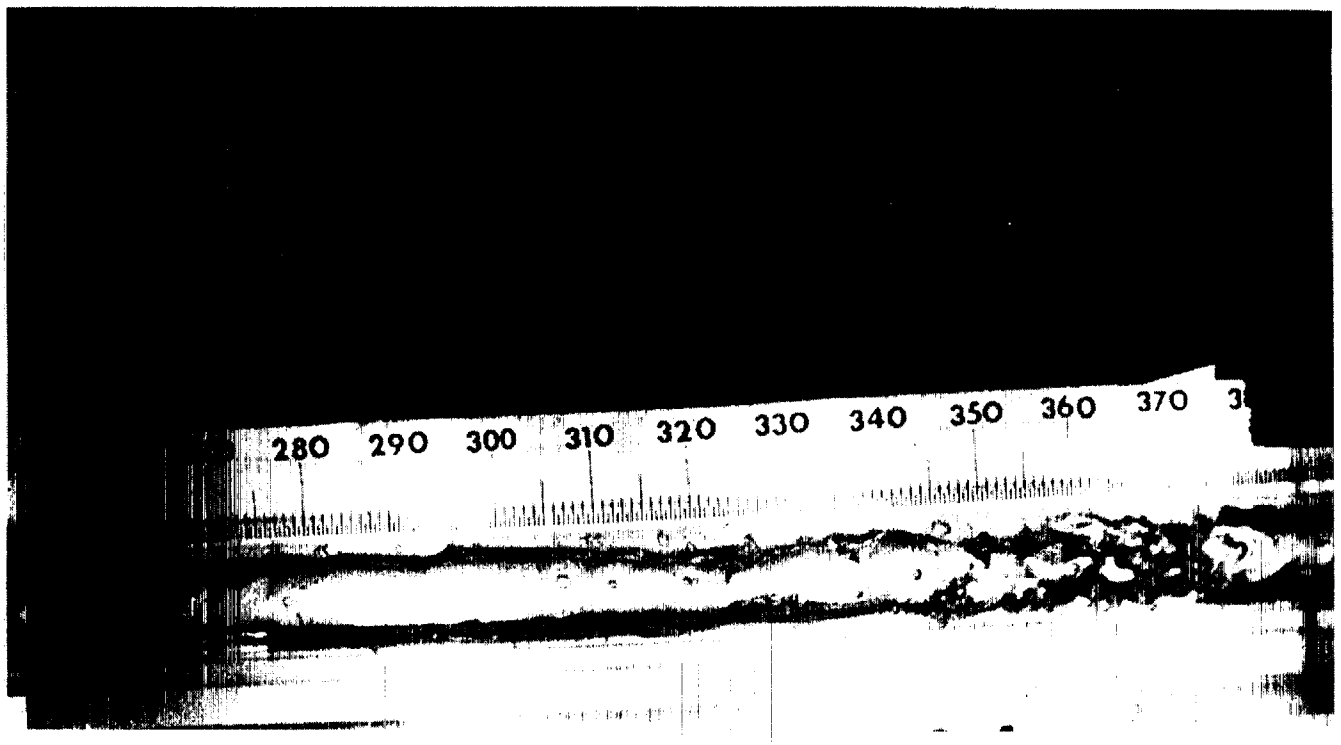

Figure A.12(c) Microgravity Air-Water/Glycerin Slug-Annular Transition Flow After Bridging of the Tube

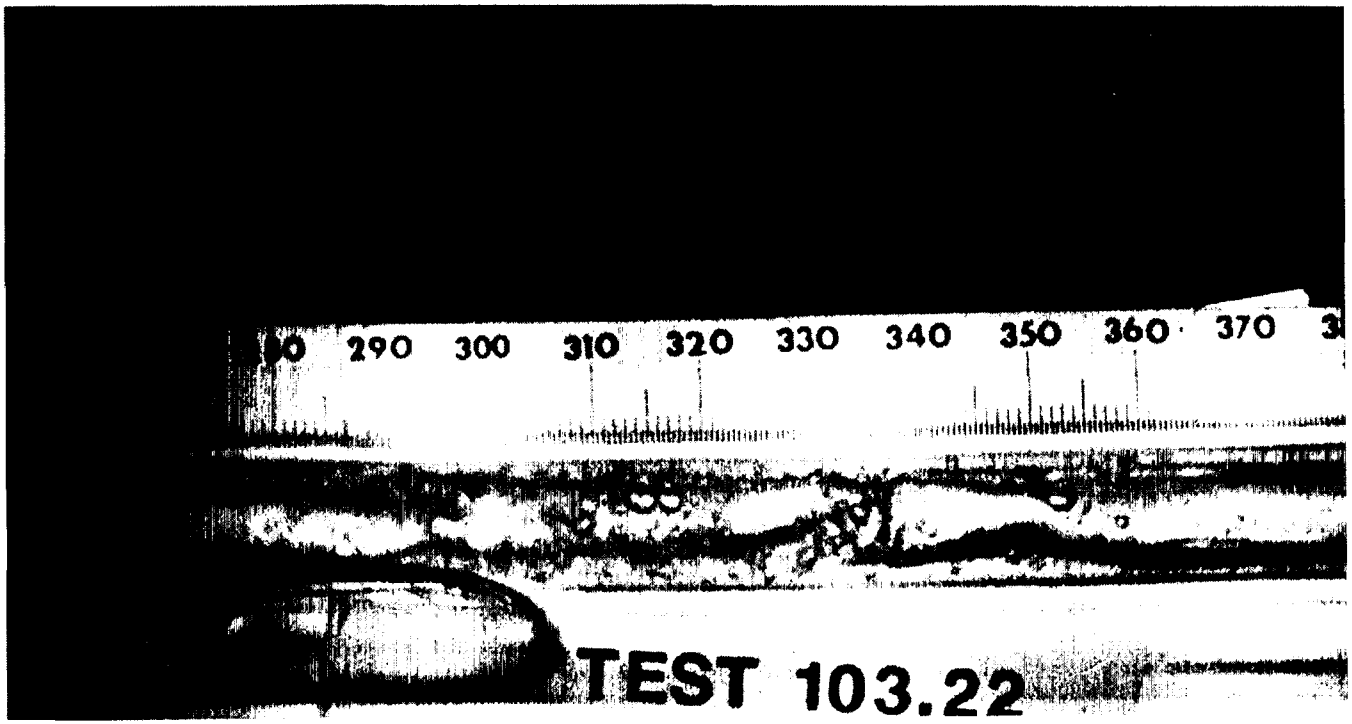

Figure A.13(a) Microgravity Air-Water/Zonyl FSP Slug-Annular Transition Flow Prior to Rupture of a Liquid Slug

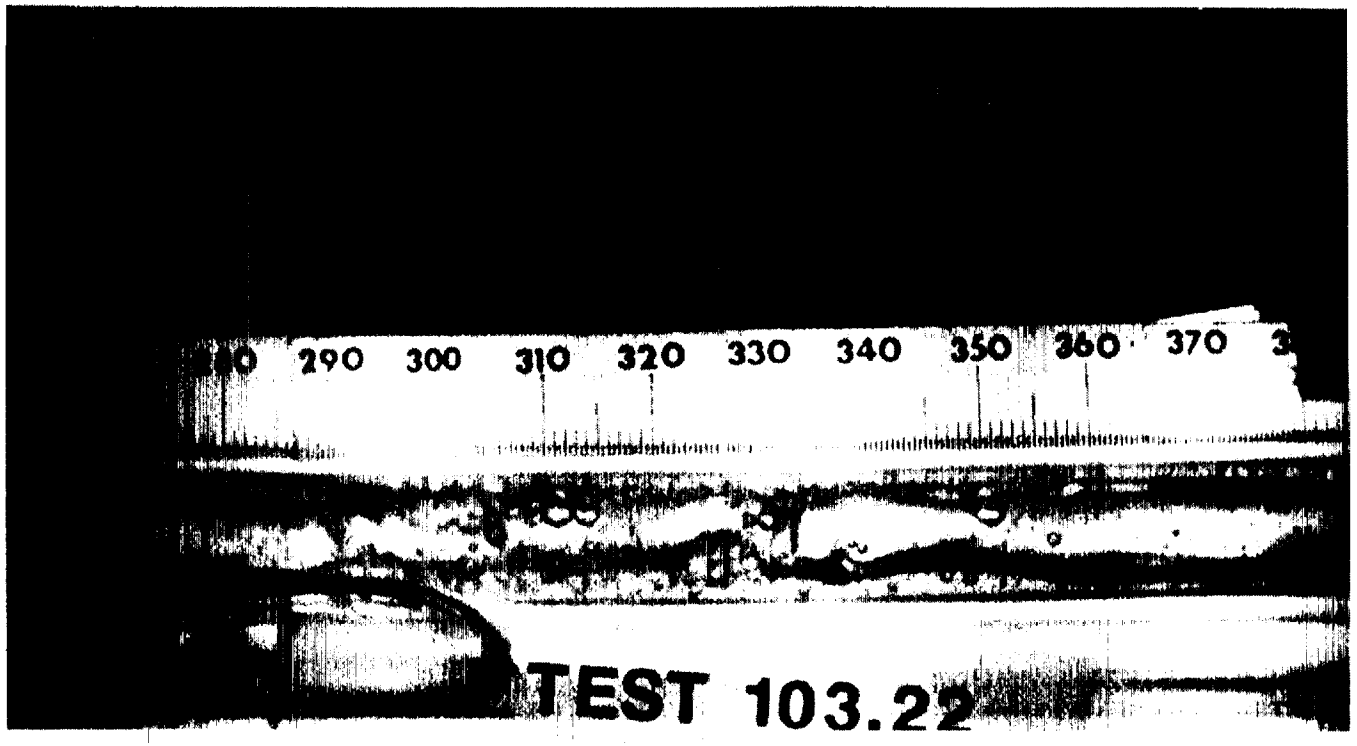

Figure A.13(b) Microgravity Air-Water/Zonyl FSP Slug-Annular Transition Flow Showing Rupture of a Liquid Slug

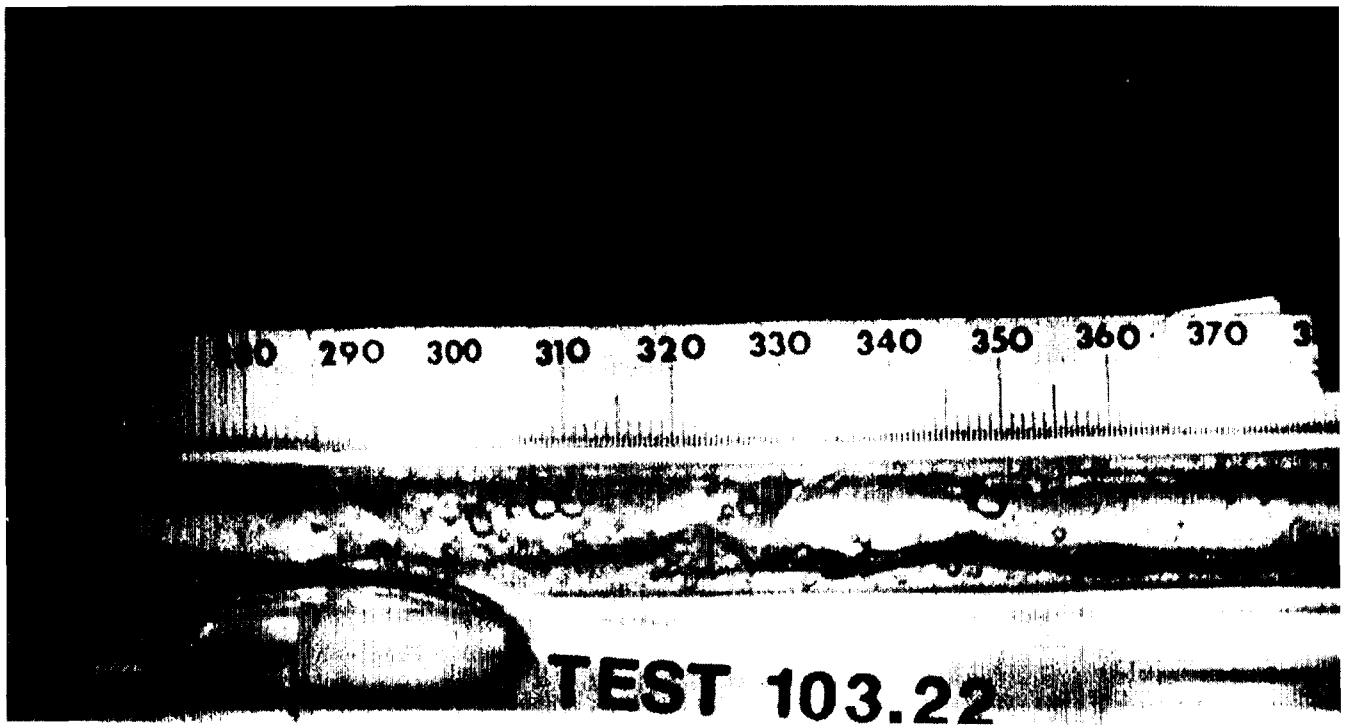

Figure A.13(c) Microgravity Air-Water/Zonyl FSP Slug-Annular Transition Flow After Rupture of a Liquid Slug

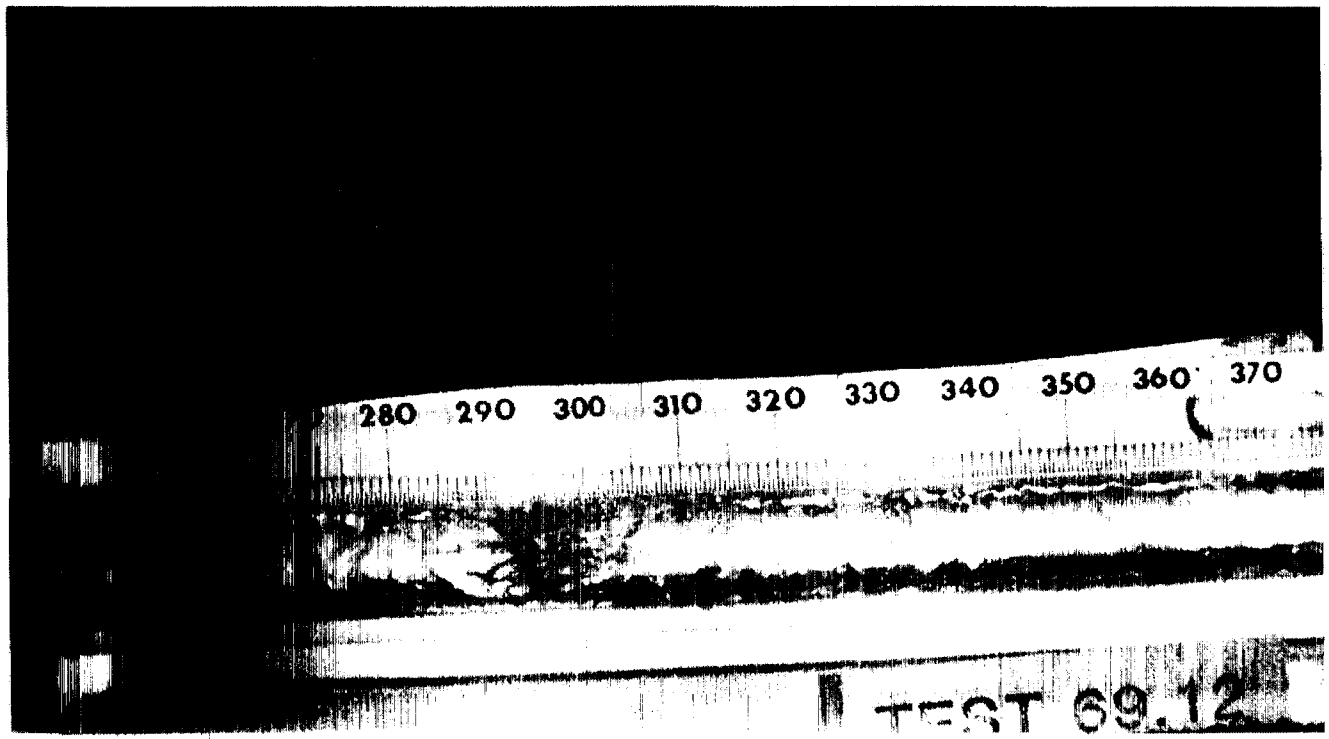

Figure A.14 Photograph of Microgravity Air-Water Annular Flow in a 12.7 mm ID Tube

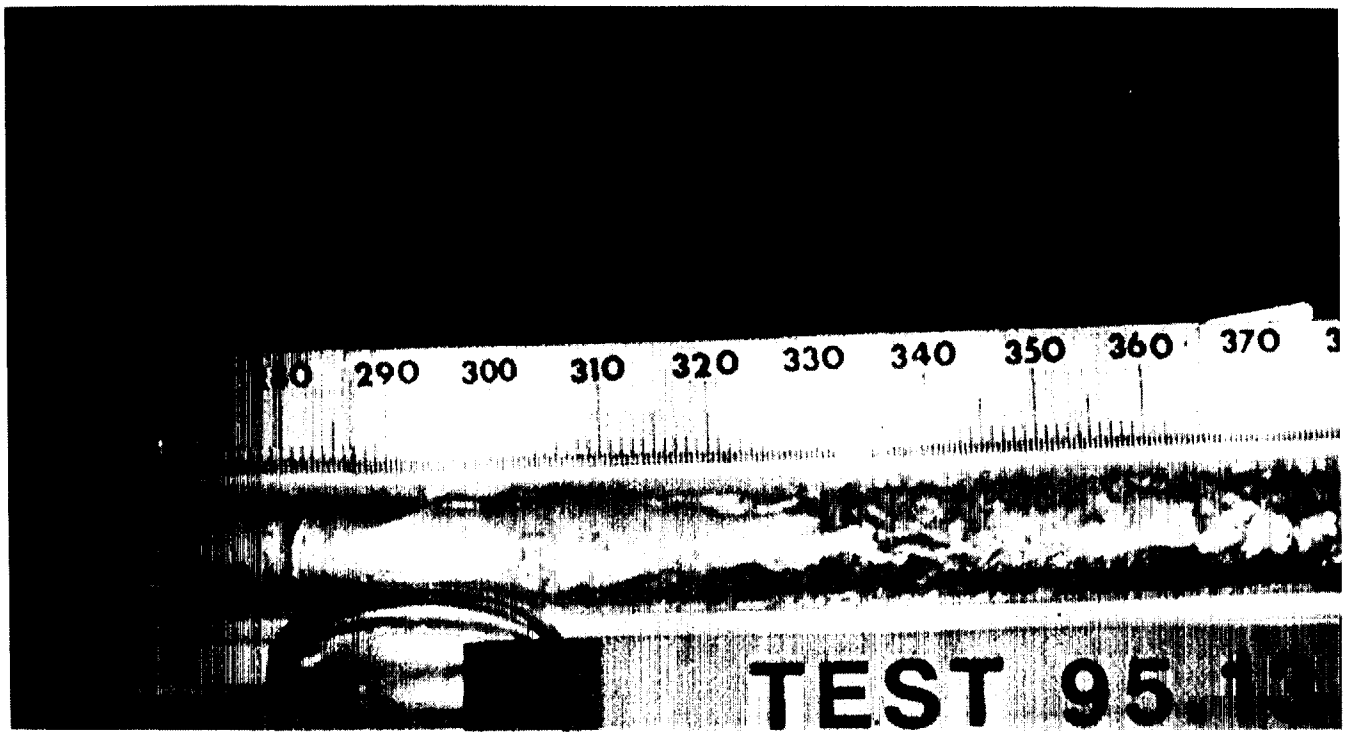

Figure A.15 Photograph of Microgravity Air-Water/Glycerin Annular Flow in a 12.7 mm ID Tube

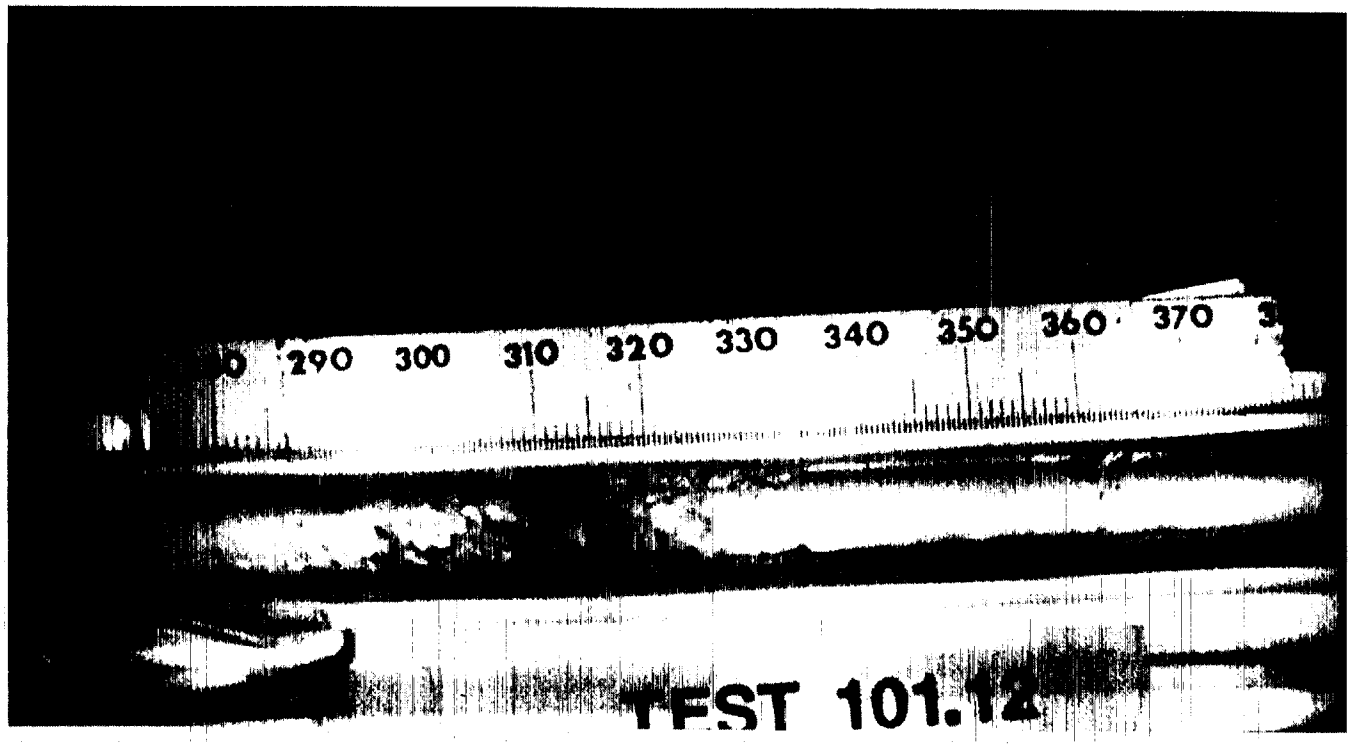

Figure A.16 Photograph of Microgravity Air-Water/Zonyl FSP Annular Flow in a 12.7 mm ID Tube

Appendix B Literature Microgravity Flow Pattern Data

Table B.1 Microgravity Flow Pattern Data from Chen et al., 1988

U_{GS} (m/s)	U_{LS} (m/s)	Flow Pattern
0.26	0.165	Bubble
0.475	0.154	Bubble
0.712	0.144	Bubble-Slug
0.953	0.134	Annular
1.31	0.12	Annular
1.85	0.094	Annular
2.32	0.07	Annular
2.72	0.058	Annular
3.65	0.021	Annular

Table B.2 Microgravity Flow Pattern Data from Dukler et al., 1988

U_{GS} (m/s)	U_{LS} (m/s)	Flow Pattern
0.09	0.478	Bubble
0.65	0.94	Bubble
0.13	0.88	Bubble
0.134	0.46	Bubble
0.61	0.084	Slug
0.22	0.076	Slug
0.64	0.08	Slug
1.09	0.46	Slug
1.75	0.45	Slug
1.9	0.92	Slug
0.7	0.08	Slug
0.65	0.45	Slug
0.16	0.079	Slug
2.22	0.079	Slug-Annular
1.8	0.079	Slug-Annular
2.99	0.438	Slug-Annular
25.32	0.08	Annular
11.44	0.451	Annular
7.97	0.082	Annular
2.22	0.079	Annular
23	0.418	Annular
11.4	0.077	Annular
10.1	0.08	Annular

Table B.3 Microgravity Flow Pattern Data from Janicot, 1988

Ugs (m/s)	Uls (m/s)	Flow Pattern
0.09	0.478	Bubble
0.65	0.94	Bubble
0.13	0.88	Bubble
0.13	0.46	Bubble
0.64	1.06	Bubble
0.2	1.09	Bubble
0.61	0.084	Slug
0.22	0.076	Slug
0.64	0.08	Slug
1.09	0.46	Slug
1.75	0.45	Slug
1.9	0.92	Slug
0.7	0.08	Slug
0.65	0.45	Slug
0.16	0.079	Slug
0.71	0.475	Slug
0.21	0.083	Slug
0.2	0.081	Slug
0.175	0.082	Slug
1.15	1.04	Slug
0.22	0.083	Slug
0.77	0.082	Slug
1.8	0.079	Slug-Annular
25.32	0.08	Annular
11.44	0.451	Annular
7.97	0.082	Annular
2.22	0.079	Annular
2.99	0.438	Annular
23	0.418	Annular
11.4	0.077	Annular
10.1	0.08	Annular
3.42	0.08	Annular
20.4	0.08	Annular
19.7	0.46	Annular
3.4	0.477	Annular

Table B.4 Microgravity Flow Pattern Data from Colin, 1990

Ugs (m/s)	Uls (m/s)	Flow Pattern
0.08	0.494	Bubble
0.123	0.551	Bubble
0.159	0.531	Bubble
0.044	0.692	Bubble
0.114	0.653	Bubble
0.159	0.627	Bubble
0.193	0.61	Bubble
0.246	0.591	Bubble
0.054	0.881	Bubble
0.116	0.845	Bubble
0.174	0.819	Bubble
0.247	0.766	Bubble
0.086	1.104	Bubble
0.153	1.058	Bubble
0.191	1.001	Bubble
0.274	0.971	Bubble
0.045	0.331	Bubble
0.063	0.306	Bubble
0.052	0.309	Bubble
0.065	0.319	Bubble
0.124	0.313	Bubble
0.049	0.448	Bubble
0.06	0.418	Bubble
0.159	0.881	Bubble
0:047	0.268	Bubble
0.059	0.256	Bubble
0.047	0.489	Bubble
0.05	0.958	Bubble
0.067	0.931	Bubble
0.128	0.954	Bubble
0.219	0.937	Bubble
0.129	0.336	Bubble
0.129	0.865	Bubble
0.128	0.839	Bubble
0.129	0.835	Bubble
0.13	0.822	Bubble
0.132	0.809	Bubble
0.061	0.938	Bubble
0.06	0.918	Bubble
0.058	0.902	Bubble
0.058	0.888	Bubble
0.057	0.878	Bubble
0.056	0.865	Bubble
0.123	1.485	Bubble
0.038	0.243	Bubble

Table B.4 Microgravity Flow Pattern Data from Colin, 1990 (continued)

Ugs (m/s)	Uls (m/s)	Flow Pattern
0.021	0.233	Bubble
0.021	0.263	Bubble
0.024	0.251	Bubble
0.015	0.241	Bubble
0.108	0.381	Bubble
0.11	0.257	Bubble
0.11	0.408	Bubble
0.037	0.965	Bubble
0.045	0.994	Bubble
0.039	0.992	Bubble
0.11	0.887	Bubble
0.05	0.854	Bubble
0.043	0.839	Bubble
0.125	0.793	Bubble
0.134	0.757	Bubble
0.062	0.448	Bubble
0.076	0.445	Bubble
0.069	0.883	Bubble
0.093	0.872	Bubble
0.092	0.862	Bubble
0.127	0.84	Bubble
0.164	0.834	Bubble
0.165	0.833	Bubble
0.215	0.54	Bubble
0.217	0.535	Bubble
0.132	0.468	Bubble
0.124	0.862	Bubble
0.223	0.842	Bubble
0.377	0.815	Bubble
0.47	0.803	Bubble
0.564	0.821	Bubble
0.563	0.804	Bubble
0.624	0.806	Bubble
0.178	0.673	Bubble
0.281	0.682	Bubble
0.47	0.668	Bubble
0.455	0.665	Bubble
0.192	0.486	Slug
0.301	0.292	Slug
0.292	0.555	Slug
0.323	0.487	Slug
0.226	0.304	Slug
0.466	0.284	Slug
0.485	0.29	Slug
0.23	0.304	Slug

Table B.4 Microgravity Flow Pattern Data from Colin, 1990 (continued)

Ugs (m/s)	Uls (m/s)	Flow Pattern
0.121	0.278	Slug
0.201	0.271	Slug
0.436	0.278	Slug
0.065	0.475	Slug
0.124	0.46	Slug
0.353	0.914	Slug
0.55	0.952	Slug
0.127	0.258	Slug
0.128	0.33	Slug
0.128	0.304	Slug
0.129	0.469	Slug
0.129	0.461	Slug
0.129	0.46	Slug
0.129	0.543	Slug
0.097	0.244	Slug
0.209	0.322	Slug
0.125	0.441	Slug
0.124	0.438	Slug
0.188	0.43	Slug
0.188	0.427	Slug
0.19	0.41	Slug
0.231	0.467	Slug
0.229	0.464	Slug
0.231	0.462	Slug
0.284	0.448	Slug
0.252	0.539	Slug
0.319	0.528	Slug
0.137	0.214	Slug
0.136	0.216	Slug
0.206	0.204	Slug
0.292	0.205	Slug
0.387	0.206	Slug
0.305	0.184	Slug
0.258	0.174	Slug
0.176	0.467	Slug
0.23	0.469	Slug
0.318	0.464	Slug
0.414	0.457	Slug

Table B.5 Microgravity Flow Pattern Data from Huckerby and Rezkallah, 1992

Ugs (m/s)	Uls (m/s)	Flow Pattern
0.1808	0.087	Bubble
0.251	0.288	Bubble
0.1533	0.312	Bubble
0.222	0.714	Bubble
0.274	0.75	Bubble
0.275	0.8246	Bubble
0.3299	1.66	Bubble
0.115	3.2	Bubble
0.641	2.02	Bubble-Slug
0.521	2.17	Bubble-Slug
0.489	0.624	Bubble-Slug
0.3046	0.6607	Bubble-Slug
0.522	1.313	Bubble-Slug
0.4135	2.1198	Bubble-Slug
0.373	2.861	Bubble-Slug
1.72	0.13	Slug
1.035	0.138	Slug
1.152	0.167	Slug
0.753	0.232	Slug
0.7465	0.2377	Slug
2.46	0.28	Slug
0.488	0.294	Slug
2.984	0.324	Slug
5.945	0.355	Slug
4.95	0.388	Slug
1.892	0.4465	Slug
1.894	0.48	Slug
0.6926	0.5178	Slug
0.5314	0.5433	Slug
3.978	0.6118	Slug
1.428	0.6346	Slug
1.987	0.648	Slug
1.922	0.69	Slug
2.425	0.85356	Slug
1.077	0.973	Slug
1.063	0.98795	Slug
0.973	1.112	Slug
0.786	1.31	Slug
0.718	2.39	Slug
0.8149	2.1676	Slug
4.91	0.24	Slug-Annular
3.89	0.283	Slug-Annular
5.78	0.308	Slug-Annular
4.82	0.373	Slug-Annular
5.89	0.374	Slug-Annular
2.93	0.409	Slug-Annular
2.95	0.477	Slug-Annular
2.978	0.817	Slug-Annular
3.928	1.055	Slug-Annular

Table B.6 Microgravity Flow Pattern Data from Zhao and Rezkallah, 1993

Ugs (m/s)	Uls (m/s)	Flow Pattern
0.3	2.27	Bubble
0.29	3.46	Bubble
0.48	3.53	Bubble
0.66	3.45	Bubble
0.75	3.73	Bubble
1	3.71	Bubble
0.47	0.92	Slug
0.72	0.89	Slug
0.95	0.95	Slug
1.56	0.86	Slug
2.76	0.88	Slug
0.42	2.39	Slug
0.65	2.26	Slug
0.81	2.35	Slug
1.13	2.33	Slug
2.49	2.33	Slug
2.42	3.34	Slug
0.33	0.09	Slug
0.53	0.09	Slug
0.67	0.09	Slug
0.39	0.13	Slug
0.47	0.11	Slug
0.66	0.12	Slug
1.05	0.13	Slug
1.41	0.13	Slug
0.14	0.21	Slug
0.21	0.21	Slug
0.27	0.21	Slug
0.65	0.2	Slug
0.97	0.2	Slug
1.82	0.2	Slug
0.5	0.3	Slug
0.57	0.3	Slug
0.77	0.3	Slug
1.75	0.3	Slug
0.54	0.09	Slug
0.81	0.09	Slug
1.26	0.09	Slug
0.37	0.09	Slug
0.71	0.09	Slug
1.05	0.09	Slug
0.37	0.45	Slug
0.42	0.43	Slug
0.52	0.43	Slug
1.06	0.4	Slug

Table B.6 Microgravity Flow Pattern Data from Zhao and Rezkallah, 1993 (continued)

Ugs (m/s)	Uls (m/s)	Flow Pattern
2.02	0.44	Slug
2.58	0.5	Slug
0.4	0.47	Slug
0.64	0.44	Slug
0.71	0.47	Slug
1.04	0.47	Slug
1.93	0.46	Slug
5.36	0.92	Slug-Annular
7.5	0.85	Slug-Annular
9.95	0.9	Slug-Annular
12.25	0.85	Slug-Annular
14.97	1.02	Slug-Annular
11.53	0.56	Slug-Annular
13.22	1.38	Slug-Annular
4.9	1.97	Slug-Annular
6.72	2.18	Slug-Annular
9.08	2.13	Slug-Annular
10.46	2.08	Slug-Annular
4.65	3.06	Slug-Annular
6.62	2.83	Slug-Annular
8.56	2.59	Slug-Annular
10.42	2.39	Slug-Annular
1.26	0.09	Slug-Annular
1.68	0.09	Slug-Annular
2.63	0.09	Slug-Annular
4.1	0.09	Slug-Annular
6.58	0.09	Slug-Annular
8.96	0.09	Slug-Annular
12.48	0.09	Slug-Annular
2.63	0.13	Slug-Annular
3.85	0.13	Slug-Annular
6.51	0.13	Slug-Annular
8.99	0.13	Slug-Annular
12.29	0.13	Slug-Annular
3.15	0.2	Slug-Annular
5.53	0.2	Slug-Annular
9.11	0.19	Slug-Annular
11.89	0.21	Slug-Annular
3.14	0.29	Slug-Annular
5.43	0.29	Slug-Annular
7.35	0.29	Slug-Annular
9.98	0.3	Slug-Annular
12.37	0.29	Slug-Annular
1.91	0.09	Slug-Annular
2.26	0.09	Slug-Annular

Table B.6 Microgravity Flow Pattern Data from Zhao and Rezkallah, 1993 (continued)

Ugs (m/s)	Uls (m/s)	Flow Pattern
3.39	0.09	Slug-Annular
4.58	0.09	Slug-Annular
6.42	0.09	Slug-Annular
8.9	0.09	Slug-Annular
12.52	0.09	Slug-Annular
1.6	0.09	Slug-Annular
2.2	0.09	Slug-Annular
3.21	0.09	Slug-Annular
4.58	0.09	Slug-Annular
6.46	0.09	Slug-Annular
8.81	0.09	Slug-Annular
12.37	0.09	Slug-Annular
13.8	0.14	Slug-Annular
15.02	0.2	Slug-Annular
4.36	0.43	Slug-Annular
7.51	0.42	Slug-Annular
10.15	0.42	Slug-Annular
12.01	0.42	Slug-Annular
3.81	0.38	Slug-Annular
7.44	0.38	Slug-Annular
9.74	0.36	Slug-Annular
11.96	0.36	Slug-Annular
16.51	0.33	Slug-Annular
4.61	0.3	Slug-Annular
6.69	0.41	Slug-Annular
13.39	0.09	Annular
16.37	0.09	Annular
18.95	0.09	Annular
21.51	0.09	Annular
23.31	0.09	Annular
14.26	0.09	Annular
16.39	0.09	Annular
18.86	0.09	Annular
19.14	0.09	Annular
22.35	0.09	Annular
16.74	0.13	Annular
19.31	0.13	Annular
19.9	0.14	Annular
23.02	0.13	Annular
17.1	0.2	Annular
19.66	0.17	Annular
19.72	0.19	Annular
18.73	0.19	Annular
22.66	0.19	Annular
27.86	0.14	Annular
32.17	0.11	Annular

Table B.7 Microgravity Flow Pattern Data for 4.7 mm ID Tube from Reinarts, 1993

Ugs (m/s)	Uls (m/s)	Flow Pattern
1.922	0.546	Annular
2.456	0.413	Annular
2.434	0.400	Annular
2.799	0.341	Annular
3.007	0.327	Annular
2.829	0.311	Annular
3.528	0.282	Annular
6.685	0.071	Annular
6.761	0.070	Annular
6.740	0.064	Annular
2.853	0.197	Annular
2.359	0.424	Annular
2.461	0.416	Annular
2.897	0.308	Annular
3.711	0.305	Annular
2.510	0.258	Annular
4.530	0.254	Annular
2.463	0.153	Annular
2.498	0.102	Annular
2.657	0.076	Annular
6.128	0.089	Annular
2.205	0.044	Annular

Table B.8 Microgravity Flow Pattern Data for 10.5 mm ID Tube from Reinarts, 1993

Ugs (m/s)	Uls (m/s)	Flow Pattern
0.054	0.456	Bubble
0.060	0.387	Bubble-Slug
0.148	0.393	Bubble-Slug
0.129	0.474	Bubble-Slug
0.261	0.076	Slug
0.290	0.078	Slug
0.106	0.378	Slug
0.125	0.331	Slug
0.115	0.188	Slug
0.128	0.094	Slug
0.141	0.092	Slug
0.138	0.019	Slug
0.157	0.019	Slug
0.127	0.017	Slug
0.213	0.355	Slug
0.055	0.186	Slug
0.075	0.185	Slug
0.077	0.097	Slug
0.069	0.097	Slug
0.062	0.022	Slug
0.057	0.009	Slug
0.057	0.006	Slug
0.133	0.009	Slug
0.115	0.024	Slug
0.135	0.100	Slug
0.597	0.156	Slug-Annular
0.589	0.161	Slug-Annular
0.486	0.116	Slug-Annular
0.328	0.083	Slug-Annular
0.453	0.039	Slug-Annular
0.685	0.166	Slug-Annular
0.470	0.121	Slug-Annular
0.472	0.118	Slug-Annular
0.396	0.105	Slug-Annular
0.384	0.165	Slug-Annular
0.623	0.044	Slug-Annular
0.614	0.043	Slug-Annular
0.568	0.164	Slug-Annular
0.666	0.161	Slug-Annular
0.666	0.162	Slug-Annular
0.589	0.167	Slug-Annular
0.353	0.069	Slug-Annular
0.347	0.068	Slug-Annular
0.245	0.017	Slug-Annular
0.228	0.024	Slug-Annular

Table B.8 Flow Pattern Data for 10.5 mm ID Tube from Reinarts, 1993 (continued)

Ugs (m/s)	Uls (m/s)	Flow Pattern
0.170	0.005	Slug-Annular
0.174	0.005	Slug-Annular
2.106	0.201	Annular
3.828	0.094	Annular
1.459	0.060	Annular
2.254	0.039	Annular
2.878	0.068	Annular
3.666	0.007	Annular
3.466	0.033	Annular
2.482	0.027	Annular
0.976	0.025	Annular
1.386	0.017	Annular
3.164	0.011	Annular
0.898	0.009	Annular
0.597	0.376	Annular
0.606	0.362	Annular
2.472	0.120	Annular
2.286	0.061	Annular
1.247	0.060	Annular
2.957	0.056	Annular
1.765	0.075	Annular
0.505	0.029	Annular
2.381	0.030	Annular
1.365	0.015	Annular
0.817	0.506	Annular
1.228	0.176	Annular
1.210	0.176	Annular
1.361	0.109	Annular
1.747	0.046	Annular
1.265	0.040	Annular
1.565	0.016	Annular
0.559	0.018	Annular
1.607	0.002	Annular
1.082	0.010	Annular
2.938	0.118	Annular
1.395	0.110	Annular
2.900	0.096	Annular
1.115	0.062	Annular
1.282	0.030	Annular
2.306	0.018	Annular
1.752	0.020	Annular
2.874	0.007	Annular
2.965	0.056	Annular
1.250	0.030	Annular
0.814	0.016	Annular

Table B.8 Flow Pattern Data for 10.5 mm ID Tube from Reinarts, 1993 (continued)

Ugs (m/s)	Uls (m/s)	Flow Pattern
0.807	0.015	Annular
2.840	0.012	Annular
2.844	0.011	Annular
1.650	0.016	Annular
3.171	0.006	Annular
0.844	0.005	Annular
1.415	0.382	Annular
1.720	0.260	Annular
0.950	0.145	Annular
1.470	0.094	Annular
1.385	0.084	Annular
1.043	0.048	Annular
3.007	0.015	Annular
3.046	0.015	Annular
1.296	0.024	Annular
3.286	0.022	Annular
3.153	0.011	Annular
3.191	0.010	Annular
1.087	0.002	Annular

Appendix C Microgravity Flow Pattern Data

Table C.1 Microgravity Flow Pattern Data for Air-Water, 12.7 mm ID Tube

Run	U_{GS} (m/s)	U_{LS} (m/s)	Pattern
64.32	0.234	0.9	Bubble
68.2	0.249	0.608	Bubble
83.32	0.487	0.805	Bubble
85.2	0.109	0.504	Bubble
87.22	0.312	0.532	Bubble
87.3	0.362	0.807	Bubble
90.2	0.118	0.806	Bubble
45.1	0.22	0.177	Bubble-Slug
60.1	0.114	0.101	Bubble-Slug
64.2	0.182	0.34	Bubble-Slug
65.3	0.597	0.861	Bubble-Slug
81.12	0.118	0.204	Bubble-Slug
89.1	0.576	0.519	Bubble-Slug
155.6	0.543	0.53	Bubble-Slug
32.1	0.43	0.072	Slug
34.3	0.147	0.073	Slug
58.1	1.11	0.203	Slug
58.22	0.396	0.082	Slug
59.2	0.506	0.207	Slug
65.1	0.36	0.143	Slug
65.2	0.589	0.335	Slug
66.2	1.154	0.341	Slug
66.13	1.433	0.163	Slug
67.12	0.9	0.104	Slug
67.2	0.202	0.055	Slug
67.3	1.118	0.878	Slug
68.3	0.77	0.601	Slug
69.32	1.674	0.581	Slug
81.32	0.981	0.527	Slug
83.22	0.291	0.203	Slug
84.12	0.345	0.065	Slug
85.3	2.034	0.792	Slug
86.12	1.244	0.197	Slug
86.22	0.624	0.203	Slug
86.32	1.205	0.789	Slug
91.1	2.18	0.515	Slug
144.5	0.987	0.121	Slug
155.4	0.533	0.071	Slug
155.5	1.071	0.526	Slug
156.2	1.075	0.193	Slug
156.3	0.536	0.195	Slug
156.4	1.064	0.113	Slug
156.5	0.546	0.113	Slug
156.6	2.059	0.53	Slug
31.1	2.194	0.069	Slug-Annular
33.1	1.773	0.082	Slug-Annular
60.2	1.666	0.102	Slug-Annular

Table C.1 Microgravity Flow Pattern Data for Air-Water, 12.7 mm ID Tube (continued)

Run	U_{GS} (m/s)	U_{LS} (m/s)	Pattern
66.3	4.294	0.861	Slug-Annular
68.1	2.208	0.095	Slug-Annular
69.2	4.595	0.328	Slug-Annular
70.12	2.486	0.153	Slug-Annular
70.3	5.784	0.603	Slug-Annular
82.22	1.116	0.069	Slug-Annular
83.12	2.251	0.068	Slug-Annular
84.22	4.426	0.506	Slug-Annular
85.1	2.01	0.198	Slug-Annular
89.2	4.433	0.8	Slug-Annular
90.1	3.987	0.2	Slug-Annular
143.6	5.106	0.545	Slug-Annular
155.1	2.099	0.11	Slug-Annular
155.2	2.103	0.069	Slug-Annular
155.3	1.089	0.071	Slug-Annular
156.1	2.1	0.192	Slug-Annular
35.2	5.302	0.067	Annular
36.1	4.403	0.185	Annular
37.22	7.503	0.407	Annular
38.1	11.567	0.192	Annular
59.1	7.672	0.206	Annular
69.12	10.828	0.099	Annular
70.2	10.138	0.349	Annular
81.22	9.23	0.514	Annular
82.12	10.067	0.073	Annular
87.1	4.685	0.058	Annular
88.2	10.238	0.765	Annular
141.1	24.75	0.197	Annular
141.2	10.825	0.077	Annular
141.3	10.395	0.12	Annular
141.4	10.325	0.209	Annular
141.5	15.665	0.121	Annular
141.6	9.264	0.549	Annular
142.1	15.655	0.07	Annular
142.2	15.68	0.114	Annular
142.3	15.179	0.198	Annular
142.4	10.299	0.134	Annular
142.5	5.278	0.134	Annular
142.6	22.43	0.498	Annular
143.1	26.183	0.07	Annular
143.2	25.5	0.105	Annular
143.3	5.476	0.069	Annular
143.4	5.378	0.121	Annular
143.5	5.285	0.207	Annular
144.1	25.079	0.067	Annular
144.2	25.453	0.111	Annular
144.3	23.517	0.399	Annular
144.4	10.441	0.074	Annular
144.6	10.008	0.542	Annular

Table C.2 Microgravity Flow Pattern Data for Air-Water/Glycerin, 12.7 mm ID Tube

Run	U_{GS} (m/s)	U_{LS} (m/s)	Pattern
94.3	0.303	0.509	Bubble
95.23	0.119	0.529	Bubble
95.33	0.119	0.894	Bubble
96.32	0.3	0.896	Bubble
62.2	0.332	0.34	Bubble-Slug
94.1	0.114	0.21	Bubble-Slug
97.22	1.034	0.873	Bubble-Slug
157.6	0.542	0.522	Bubble-Slug
52.2	0.12	0.093	Slug
53.13	0.784	0.492	Slug
54.2	0.781	0.096	Slug
55.2	1.107	0.31	Slug
71.12	0.571	0.266	Slug
71.22	0.463	0.126	Slug
73.3	1.022	0.487	Slug
92.12	0.332	0.087	Slug
92.2	0.306	0.204	Slug
93.1	1.082	0.08	Slug
93.2	1.049	0.204	Slug
93.3	3.799	0.816	Slug
97.13	1.053	0.509	Slug
98.1	2.46	0.525	Slug
98.2	2.302	0.823	Slug
157.4	0.534	0.063	Slug
157.5	1.067	0.513	Slug
158.2	1.087	0.204	Slug
158.3	0.559	0.207	Slug
158.4	1.074	0.114	Slug
158.5	0.544	0.114	Slug
158.6	2.089	0.526	Slug
53.2	2.111	0.094	Slug-Annular
54.1	3.02	0.48	Slug-Annular
62.32	2.157	0.142	Slug-Annular
62.4	4.285	0.143	Slug-Annular
63.1	3.471	0.297	Slug-Annular
71.32	2.28	0.209	Slug-Annular
71.42	5.551	0.44	Slug-Annular
72.1	3.113	0.067	Slug-Annular
72.2	4.562	0.319	Slug-Annular
72.3	6.515	0.492	Slug-Annular
93.1	1.082	0.08	Slug-Annular
96.1	4.041	0.086	Slug-Annular
96.22	4.46	0.205	Slug-Annular
99.12	2.304	0.09	Slug-Annular
99.22	2.46	0.203	Slug-Annular
99.3	3.994	0.496	Slug-Annular

Table C.2 Flow Pattern Data for Air-Water/Glycerin, 12.7 mm ID Tube (continued)

Run	U_{GS} (m/s)	U_{LS} (m/s)	Pattern
147.6	4.892	0.551	Slug-Annular
148.6	4.948	0.548	Slug-Annular
157.1	2.089	0.11	Slug-Annular
157.2	2.131	0.064	Slug-Annular
157.3	1.134	0.068	Slug-Annular
158.1	2.135	0.201	Slug-Annular
52.1	10.12	0.308	Annular
52.12	10.35	0.3	Annular
62.1	6.496	0.333	Annular
63.2	8.202	0.544	Annular
73.1	10.934	0.184	Annular
73.2	10.665	0.316	Annular
92.32	9.641	0.71	Annular
94.2	9.093	0.489	Annular
95.13	9.773	0.084	Annular
145.1	25.195	0.107	Annular
145.2	10.274	0.113	Annular
145.3	10.189	0.203	Annular
145.4	5.523	0.117	Annular
145.5	5.212	0.208	Annular
145.6	9.8	0.506	Annular
146.1	25.417	0.109	Annular
146.2	24.858	0.2	Annular
146.3	15.444	0.116	Annular
146.4	15.284	0.209	Annular
146.5	5.457	0.12	Annular
146.6	13.968	0.533	Annular
147.1	25.358	0.064	Annular
147.2	16.016	0.067	Annular
147.3	10.711	0.065	Annular
147.4	5.433	0.059	Annular
147.5	22.111	0.502	Annular
148.1	15.289	0.111	Annular
148.2	10.637	0.115	Annular
148.3	25.984	0.069	Annular
148.4	15.947	0.068	Annular
148.5	22.021	0.499	Annular

Table C.3 Microgravity Flow Pattern Data for Air-Water/Zonyl FSP, 12.7 mm ID Tube

Run	U_{GS} (m/s)	U_{LS} (m/s)	Pattern
50.1	0.251	0.505	Bubble
100.4	0.344	0.527	Bubble
101.22	0.124	0.202	Bubble
101.3	0.12	0.526	Bubble
47.22	0.119	0.1	Bubble-Slug
49.1	0.399	0.294	Bubble-Slug
61.3	0.258	0.264	Bubble-Slug
100.2	0.31	0.202	Bubble-Slug
48.1	0.802	0.504	Slug
48.2	0.609	0.096	Slug
61.1	1.062	0.103	Slug
61.4	2.534	0.664	Slug
100.1	0.307	0.071	Slug
101.4	1	0.52	Slug
102.3	0.982	0.071	Slug
102.4	0.968	0.203	Slug
103.42	2.325	0.508	Slug
153.3	1.019	0.064	Slug
153.5	1	0.49	Slug
154.2	1.068	0.22	Slug
154.3	0.539	0.221	Slug
154.4	1.057	0.129	Slug
154.5	0.554	0.132	Slug
154.6	2.053	0.521	Slug
47.1	5.185	0.485	Slug-Annular
102.2	3.868	0.508	Slug-Annular
103.22	2.356	0.068	Slug-Annular
103.32	2.371	0.205	Slug-Annular
153.1	2.107	0.067	Slug-Annular
153.2	2.068	0.105	Slug-Annular
154.1	2.134	0.213	Slug-Annular
49.2	10.63	0.313	Annular
50.22	3.317	0.097	Annular
61.2	10.745	0.0994	Annular
100.3	9.626	0.5	Annular
101.12	9.917	0.07	Annular
102.12	4.2	0.072	Annular
103.13	4.208	0.203	Annular
149.1	24.578	0.193	Annular
149.2	10.505	0.075	Annular
149.3	10.521	0.118	Annular
149.4	10.307	0.206	Annular
149.5	15.459	0.121	Annular
149.6	9.73	0.547	Annular
150.1	15.526	0.067	Annular
150.2	15.426	0.106	Annular
150.3	15.068	0.185	Annular

Table C.3 Flow Pattern Data for Air-Water/Zonyl FSP, 12.7 mm ID Tube (continued)

Run	U_{GS} (m/s)	U_{LS} (m/s)	Pattern
150.4	10.574	0.109	Annular
150.5	5.246	0.111	Annular
150.6	22.389	0.447	Annular
151.1	25.858	0.06	Annular
151.2	25.668	0.104	Annular
151.3	5.545	0.067	Annular
151.4	5.46	0.11	Annular
151.5	5.402	0.199	Annular
151.6	13.616	0.517	Annular
152.1	25.367	0.103	Annular
152.2	5.365	0.067	Annular
152.3	5.366	0.111	Annular
152.4	10.302	0.07	Annular
152.5	10.221	0.511	Annular
152.6	14.45	0.507	Annular

Table C.4 Microgravity Flow Pattern Data for Air-Water, 25.4 mm ID Tube

Run	U_{GS} (m/s)	U_{LS} (m/s)	Pattern
1413	0.195	0.717	Bubble
1415	0.114	0.715	Bubble
1507	0.126	0.49	Bubble
1118	0.192	0.444	Bubble-Slug
1408	0.11	0.34	Bubble-Slug
1502	0.221	0.516	Bubble-Slug
1102	0.47	0.663	Slug
1103	2	0.674	Slug
1105	1.01	0.662	Slug
1108	0.124	0.097	Slug
1113	0.506	0.12	Slug
1115	0.215	0.128	Slug
1120	0.984	0.492	Slug
1124	2.07	0.508	Slug
1125	0.5	0.141	Slug
1135	0.104	0.255	Slug
1136	0.196	0.172	Slug
1138	0.509	0.2	Slug
1139	1.03	0.226	Slug
1402	0.533	0.349	Slug
1405	1.02	0.345	Slug
1410	0.195	0.33	Slug
1412	0.305	0.3	Slug
1414	2.98	0.71	Slug
1417	0.732	0.673	Slug
1418	0.738	0.53	Slug
1420	2.02	0.485	Slug
1421	0.468	0.484	Slug
1504	0.786	0.485	Slug
1506	0.545	0.55	Slug
1513	0.509	0.142	Slug
1515	0.205	0.165	Slug
1519	0.497	0.23	Slug
1521	0.211	0.157	Slug
1523	0.085	0.182	Slug
1525	0.503	0.21	Slug
1107	4.74	0.623	Slug-Annular
1111	2.08	0.098	Slug-Annular
1123	4.92	0.459	Slug-Annular
1133	2.02	0.256	Slug-Annular
1403	2.03	0.34	Slug-Annular
1409	2.99	0.311	Slug-Annular
1416	6.83	0.69	Slug-Annular
1503	3	0.49	Slug-Annular
1505	6.74	0.46	Slug-Annular
1511	2.03	0.14	Slug-Annular
1516	1.55	0.185	Slug-Annular

Table C.4 Flow Pattern Data for Air-Water, 25.4 mm ID Tube (continued)

Run	U_{GS} (m/s)	U_{LS} (m/s)	Pattern
1518	3.06	0.124	Slug-Annular
1524	3	0.18	Slug-Annular
1104	9.57	0.604	Annular
1112	10.8	0.1	Annular
1114	14.7	0.123	Annular
1116	5.04	0.118	Annular
1117	10.8	0.442	Annular
1128	10.8	0.095	Annular
1132	10.5	0.237	Annular
1140	5.07	0.193	Annular
1404	10.8	0.348	Annular
1411	7.35	0.345	Annular
1425	16.35	0.21	Annular
1501	10.3	0.465	Annular
1514	5.23	0.127	Annular
1522	7.02	0.25	Annular

Table C.5 Microgravity Flow Pattern Data for Air-Water/Glycerin, 25.4 mm ID Tube

Run	U_{GS} (m/s)	U_{LS} (m/s)	Pattern
1202	0.383	1.052	Bubble
1208	0.215	0.92	Bubble
1221	0.486	0.884	Bubble
1234	0.114	0.303	Bubble
1246	0.207	0.576	Bubble
1205	0.959	0.908	Bubble-Slug
1210	0.98	0.749	Bubble-Slug
1236	0.205	0.3	Bubble-Slug
1241	0.5	0.572	Bubble-Slug
1203	1.42	0.945	Slug
1213	0.522	0.091	Slug
1215	0.196	0.166	Slug
1217	0.108	0.084	Slug
1223	1.99	0.899	Slug
1225	0.512	0.155	Slug
1238	0.502	0.3	Slug
1239	1	0.308	Slug
1242	2.02	0.571	Slug
1244	0.971	0.605	Slug
1250	1.03	0.167	Slug
1204	8.25	0.83	Slug-Annular
1207	4.5	0.88	Slug-Annular
1211	2.07	0.114	Slug-Annular
1212	0.957	0.077	Slug-Annular
1218	3.07	0.109	Slug-Annular
1219	8.85	0.765	Slug-Annular
1222	4.52	0.889	Slug-Annular
1224	2.02	0.187	Slug-Annular
1233	2.09	0.32	Slug-Annular
1240	3.07	0.305	Slug-Annular
1245	4.89	0.559	Slug-Annular
1247	2.02	0.118	Slug-Annular
1214	13.7	0.08	Annular
1216	4.97	0.086	Annular
1226	15.1	0.16	Annular
1229	5.14	0.124	Annular
1230	10.5	0.149	Annular
1231	5.1	0.233	Annular
1235	15.3	0.285	Annular
1243	10	0.55	Annular
1249	15.4	0.083	Annular
1252	19.5	0.115	Annular
1253	21.5	0.145	Annular
1254	20.2	0.08	Annular
1255	20.4	0.09	Annular
1256	20.5	0.2	Annular
1257	20.2	0.14	Annular

Table C.6 Microgravity Flow Pattern Data for Air-Water/Zonyl FSP, 25.4 mm ID Tube

Run	U_{GS} (m/s)	U_{LS} (m/s)	Pattern
1308	0.121	0.273	Bubble
1310	0.192	0.282	Bubble
1326	0.12	0.565	Bubble
1328	0.217	0.565	Bubble
1315	0.221	0.255	Bubble-Slug
1319	0.12	0.144	Bubble-Slug
1335	0.122	0.101	Bubble-Slug
1302	0.52	0.276	Slug
1305	1.15	0.273	Slug
1313	0.505	0.194	Slug
1317	1.08	0.142	Slug
1320	1.1	0.144	Slug
1321	0.515	0.142	Slug
1324	2	0.557	Slug
1334	0.999	0.103	Slug
1336	0.205	0.102	Slug
1303	2.06	0.271	Slug-Annular
1309	3	0.271	Slug-Annular
1311	2.17	0.188	Slug-Annular
1323	5	0.551	Slug-Annular
1329	6.6	0.545	Slug-Annular
1333	2.06	0.097	Slug-Annular
1301	24	0.24	Annular
1304	9.66	0.264	Annular
1307	5.1	0.267	Annular
1312	9.7	0.181	Annular
1316	5.05	0.199	Annular
1325	9.51	0.536	Annular
1331	5.1	0.099	Annular
1332	10.5	0.096	Annular

Appendix D Microgravity Bubble and Slug Flow Data

Table D.1 Microgravity Bubble and Bubble-Slug Flow Data, 12.7 mm ID Tube

Run	Fluids	Pattern	U_{GS} (m/s)	U_{LS} (m/s)	U_{MS} (m/s)	U_{GS}/U_{MS}	$\langle U_G \rangle$ (m/s)	$\langle \alpha \rangle$	dP/dx (Pa/m)	Re_{TP}	f_{TP}
83.32	AW	B	0.487	0.805	1.292	0.377	1.54	0.303	2434	11420	0.0133
85.2	AW	B	0.109	0.504	0.613	0.178	0.67	0.162	752	6512	0.0152
87.22	AW	B	0.312	0.532	0.844	0.370	0.91	0.313	1215	7353	0.0158
87.3	AW	B	0.362	0.807	1.169	0.310	1.30	0.283	2037	10629	0.0132
90.2	AW	B	0.118	0.806	0.924	0.128	-	0.113	1237	10390	0.0104
45.1	AW	B-S	0.22	0.177	0.397	0.554	0.36	0.402	-	-	-
60.1	AW	B-S	0.114	0.101	0.215	0.530	0.61	0.431	-	-	-
64.2	AW	B-S	0.182	0.34	0.522	0.349	0.61	0.297	-	-	-
65.3	AW	B-S	0.597	0.861	1.458	0.409	1.81	0.375	-	-	-
81.12	AW	B-S	0.118	0.204	0.322	0.366	0.37	0.312	388	2809	0.0346
89.1	AW	B-S	0.576	0.519	1.095	0.526	1.24	0.488	2009	7114	0.0208
94.3	AWG	B	0.303	0.509	0.812	0.373	1.10	0.291	2495	1372	0.0301
95.23	AWG	B	0.119	0.529	0.648	0.184	-	0.137	1384	1332	0.0216
95.33	AWG	B	0.119	0.894	1.013	0.117	-	0.079	2238	2222	0.0134
96.32	AWG	B	0.3	0.896	1.196	0.251	-	0.172	2674	2359	0.0127
62.2	AWG	B-S	0.332	0.34	0.672	0.494	1.06	0.420	-	-	-
94.1	AWG	B-S	0.114	0.21	0.324	0.352	0.39	0.304	852	537	0.0658
97.22	AWG	B-S	1.034	0.873	1.907	0.542	2.82	0.430	-	-	-
50.1	AWZ	B	0.251	0.505	0.756	0.332	0.98	0.320	-	-	-
100.4	AWZ	B	0.344	0.527	0.871	0.395	0.98	0.271	993	8051	0.0114
101.22	AWZ	B	0.124	0.202	0.326	0.380	0.37	0.350	609	2688	0.0561
101.3	AWZ	B	0.12	0.526	0.646	0.186	0.74	0.150	668	6961	0.0120
47.22	AWZ	B-S	0.119	0.1	0.219	0.543	0.28	0.466	-	-	-
49.1	AWZ	B-S	0.399	0.294	0.693	0.576	0.91	0.512	-	-	-
61.3	AWZ	B-S	0.258	0.264	0.522	0.494	0.64	0.382	-	-	-
100.2	AWZ	B-S	0.31	0.202	0.512	0.605	-	0.528	547	3067	0.0281

Table D.2 Microgravity Slug Flow Data for Air-Water in a 12.7 mm ID Tube

Run	Fluids	U_{GS} (m/s)	U_{LS} (m/s)	U_{MS} (m/s)	U_{GS}/U_{MS}	$\langle U_G \rangle$ (m/s)	$\langle \alpha \rangle$	dP/dx (Pa/m)	Re_{TP}	f_{TP}
32.1	AW	0.43	0.072	0.502	0.857	0.52	0.617	-	-	-
58.1	AW	1.11	0.203	1.313	0.845	1.81	0.660	-	-	-
58.22	AW	0.396	0.082	0.478	0.828	0.53	0.652	-	-	-
59.2	AW	0.506	0.207	0.713	0.710	0.85	0.610	-	-	-
65.1	AW	0.36	0.143	0.503	0.716	0.64	0.554	-	-	-
65.2	AW	0.589	0.335	0.924	0.637	1.16	0.506	-	-	-
66.2	AW	1.154	0.341	1.495	0.772	2.03	0.600	-	-	-
67.12	AW	0.9	0.104	1.004	0.896	1.41	0.652	-	-	-
67.2	AW	0.202	0.055	0.257	0.786	0.32	0.546	-	-	-
67.3	AW	1.118	0.878	1.996	0.560	2.54	0.491	-	-	-
68.3	AW	0.77	0.601	1.371	0.562	1.81	0.497	-	-	-
69.32	AW	1.674	0.581	2.255	0.742	3.39	0.586	-	-	-
81.32	AW	0.981	0.527	1.508	0.651	1.81	0.600	2683	7659	0.0187
83.22	AW	0.291	0.203	0.494	0.589	0.56	0.504	584	3109	0.0307
84.12	AW	0.345	0.065	0.410	0.841	0.46	0.677	-	-	-
85.3	AW	2.034	0.792	2.826	0.720	3.39	0.603	4099	14246	0.0082
86.12	AW	1.244	0.197	1.441	0.863	1.75	0.690	954	5677	0.0094
86.22	AW	0.624	0.203	0.827	0.755	0.92	0.704	411	3111	0.0129
86.32	AW	1.205	0.789	1.994	0.604	2.42	0.552	2386	11339	0.0085
91.1	AW	2.18	0.515	2.695	0.809	3.91	0.668	-	-	-
144.5	AW	0.987	0.121	1.108	0.891	1.19	0.728	559	3826	0.0106
155.1	AW	2.099	0.110	2.209	0.950	2.50	0.760	465	6743	0.0025
155.2	AW	2.103	0.069	2.172	0.968	-	0.770	284	6371	0.0017
155.3	AW	1.089	0.071	1.160	0.939	1.19	0.674	234	4805	0.0034
155.4	AW	0.533	0.071	0.604	0.882	0.71	0.705	119	2268	0.007
155.5	AW	1.071	0.526	1.597	0.671	1.85	0.618	1973	7755	0.0128
155.6	AW	0.543	0.530	1.073	0.506	1.19	0.509	1453	6682	0.0163

Table D.2 Microgravity Slug Flow Data for Air-Water in a 12.7 mm ID Tube (continued)

Run	Fluids	U_{GS} (m/s)	U_{LS} (m/s)	U_{MS} (m/s)	U_{GS}/U_{MS}	$\langle U_G \rangle$ (m/s)	$\langle \alpha \rangle$	dP/dx (Pa/m)	Re_{TP}	f_{TP}
156.1	AW	2.1	0.192	2.292	0.916	1.72	0.727	1068	7963	0.0047
156.2	AW	1.075	0.193	1.268	0.848	1.19	0.708	684	4709	0.0092
156.3	AW	0.536	0.195	0.731	0.733	0.76	0.648	413	3264	0.014
156.4	AW	1.064	0.113	1.177	0.904	1.22	0.741	355	3879	0.0063
156.5	AW	0.546	0.113	0.659	0.829	0.67	0.703	123	2485	0.0061
156.6	AW	2.059	0.530	2.589	0.795	2.27	0.667	3385	10954	0.0096

Table D.3 Microgravity Slug Flow Data for Air-Water/Glycerin in a 12.7 mm ID Tube

Run	Fluids	U_{GS} (m/s)	U_{LS} (m/s)	U_{MS} (m/s)	U_{GS}/U_{MS}	$\langle U_G \rangle$ (m/s)	$\langle \alpha \rangle$	dP/dx (Pa/m)	Re_{TP}	f_{TP}
52.2	AWG	0.12	0.093	0.213	0.563	0.30	0.434	-	-	-
53.13	AWG	0.784	0.492	1.276	0.614	2.12	0.458	-	-	-
54.2	AWG	0.781	0.096	0.877	0.891	1.27	0.621	-	-	-
55.2	AWG	1.107	0.31	1.417	0.781	2.12	0.574	-	-	-
71.12	AWG	0.571	0.266	0.837	0.682	1.16	0.526	-	-	-
71.22	AWG	0.463	0.126	0.589	0.786	0.91	0.548	-	-	-
73.3	AWG	1.022	0.487	1.509	0.677	2.42	0.609	-	-	-
92.12	AWG	0.332	0.087	0.419	0.792	0.00	0.539	349	461	0.0243
92.2	AWG	0.306	0.204	0.510	0.600	0.64	0.546	1029	552	0.0491
93.1	AWG	1.082	0.08	1.162	0.931	1.49	0.703	532	824	0.0075
93.2	AWG	1.049	0.204	1.253	0.837	1.59	0.652	1029	1040	0.0106
97.13	AWG	1.053	0.509	1.562	0.674	2.21	0.558	3681	1646	0.0192
98.1	AWG	2.46	0.525	2.985	0.824	4.23	0.657	4629	2443	0.0085
98.2	AWG	2.302	0.823	3.125	0.737	4.62	0.594	8015	3026	0.0114
157.1	AWG	2.089	0.110	2.199	0.950	2.27	0.719	1171	1476	0.0048
157.2	AWG	2.131	0.064	2.195	0.971	1.72	0.727	694	1430	0.003
157.3	AWG	1.134	0.068	1.202	0.943	1.39	0.706	524	843	0.007
157.4	AWG	0.534	0.063	0.597	0.894	0.75	0.610	-	-	-
157.5	AWG	1.067	0.513	1.580	0.675	2.00	0.547	3267	1708	0.0163
157.6	AWG	0.542	0.522	1.064	0.509	1.22	0.418	2406	1476	0.0206
158.1	AWG	2.135	0.201	2.336	0.914	2.78	0.708	2033	1628	0.0072
158.2	AWG	1.087	0.204	1.291	0.842	1.56	0.682	1214	979	0.0129
158.3	AWG	0.559	0.207	0.766	0.730	0.86	0.597	842	736	0.0201
158.4	AWG	1.074	0.114	1.188	0.904	1.32	0.694	745	867	0.0097
158.5	AWG	0.544	0.114	0.658	0.827	0.77	0.627	397	585	0.0139
158.6	AWG	2.089	0.526	2.615	0.799	2.63	0.651	4992	2179	0.0118

Table D.4 Microgravity Slug Flow Data for Air-Water/Zonyl FSP in a 12.7 mm ID Tube

Run	Fluids	U_{GS} (m/s)	U_{LS} (m/s)	U_{MS} (m/s)	U_{GS}/U_{MS}	$\langle U_G \rangle$ (m/s)	$\langle \alpha \rangle$	dP/dx (Pa/m)	Re_{TP}	f_{TP}
48.1	AWZ	0.802	0.504	1.306	0.614	1.69	0.578	-	-	-
48.2	AWZ	0.609	0.096	0.705	0.864	0.91	0.680	-	-	-
61.1	AWZ	1.062	0.103	1.165	0.912	1.41	0.685	-	-	-
61.4	AWZ	2.534	0.664	3.198	0.792	4.23	0.647	-	-	-
100.1	AWZ	0.307	0.071	0.378	0.812	0.45	0.678	274	1547	0.0378
101.4	AWZ	1	0.52	1.520	0.658	1.81	0.596	1936	7797	0.0132
102.3	AWZ	0.982	0.071	1.053	0.933	1.30	0.744	274	3429	0.0061
102.4	AWZ	0.968	0.203	1.171	0.827	1.37	0.711	881	4302	0.0141
103.42	AWZ	2.325	0.508	2.833	0.821	3.63	0.672	2547	11806	0.0061
154.1	AWZ	2.134	0.213	2.347	0.909	2.38	0.740	1315	7751	0.0058
154.2	AWZ	1.068	0.220	1.288	0.829	1.52	0.706	814	4807	0.0106
154.3	AWZ	0.539	0.221	0.760	0.709	0.88	0.623	591	3642	0.0172
154.4	AWZ	1.057	0.129	1.186	0.891	1.39	0.738	510	3947	0.0088
154.5	AWZ	0.554	0.132	0.686	0.808	0.78	0.690	354	2704	0.0154
154.6	AWZ	2.053	0.521	2.574	0.798	2.94	0.649	3328	11465	0.0091

Appendix E Microgravity Annular Flow Data

Table E.1 Microgravity Annular Flow Data for Air-Water, 12.7 mm ID Tube

Run	Fluids	U_{GS} (m/s)	U_{LS} (m/s)	h Mean (mm)	h Std. Dev. (mm)	U (m/s)	PSD Mode (Hz)	dP/dx Mean (Pa/m)	dP/dx Std. Dev. (Pa/m)	Tau Wall Mean (Pa)	Tau Wall Std. Dev. (Pa)
87.1	AW	4.69	0.06	0.64	0.26	-	-	-	-	-	-
143.3	AW	5.48	0.07	0.68	0.35	1.09	1.95	810	668	9.37	9.77
82.12	AW	10.07	0.07	0.51	0.23	-	-	-	-	-	-
144.4	AW	10.44	0.07	0.50	0.21	1.56	5.37	1566	604	4.51	1.38
141.2	AW	10.83	0.08	0.50	0.19	1.56	8.30	1774	504	5.03	3.51
142.1	AW	15.66	0.07	0.41	0.13	1.85	11.72	2411	558	4.30	1.35
144.1	AW	25.08	0.07	0.31	0.07	2.63	17.58	4769	763	5.71	3.66
143.1	AW	26.18	0.07	0.25	0.04	2.50	16.60	4884	1968	5.53	3.42
142.5	AW	5.28	0.13	0.82	0.43	1.52	2.44	1346	979	6.14	5.20
143.4	AW	5.38	0.12	0.74	0.39	1.56	3.42	1270	993	8.11	8.73
142.4	AW	10.30	0.13	0.59	0.26	1.79	8.30	2349	778	4.56	1.70
141.3	AW	10.40	0.12	0.66	0.23	1.72	7.81	2321	714	4.36	1.15
141.5	AW	15.67	0.12	0.53	0.15	2.17	15.62	3638	731	4.87	2.39
142.2	AW	15.68	0.11	0.46	0.16	2.17	16.11	3307	758	4.65	1.98
144.2	AW	25.45	0.11	0.35	0.08	2.94	21.00	6507	1044	7.93	5.86
143.2	AW	25.50	0.11	0.29	0.06	2.78	20.51	6578	1292	7.55	5.41
90.1	AW	3.99	0.20	0.92	0.46	-	-	-	-	-	-
143.5	AW	5.29	0.21	0.91	0.44	1.85	4.88	2028	1387	4.85	2.15
141.4	AW	10.33	0.21	0.77	0.27	2.00	8.79	3513	1045	4.75	1.98
142.3	AW	15.18	0.20	0.58	0.19	2.38	13.67	4854	1106	6.21	3.69
141.1	AW	24.75	0.20	0.41	0.07	3.33	23.93	9716	1419	9.61	6.10
143.6	AW	5.11	0.55	1.10	0.54	2.78	5.86	8096	3181	7.43	4.79
81.22	AW	9.23	0.51	0.88	0.35	-	-	-	-	-	-
141.6	AW	9.26	0.55	-	-	2.94	8.79	5434	3863	8.91	5.37
144.6	AW	10.01	0.54	0.86	0.32	3.13	16.11	-	-	10.49	6.29
142.6	AW	22.43	0.50	0.55	0.15	4.17	20.02	7629	3205	20.56	10.82
144.3	AW	23.52	0.40	0.50	0.12	3.85	31.25	17194	2996	17.85	9.95

Table E.2 Microgravity Annular Flow Data for Air-Water/Glycerin, 12.7 mm ID Tube

Run	Fluids	U_{GS} (m/s)	U_{LS} (m/s)	h Mean (mm)	h Std. Dev. (mm)	U (m/s)	PSD Mode (Hz)	dP/dx Mean (Pa/m)	dP/dx Std. Dev. (Pa/m)	Tau Wall Mean (Pa)	Tau Wall Std. Dev. (Pa)
147.4	AWG	5.43	0.06	0.78	0.37	0.93	1.95	1278	690	6.11	2.12
147.3	AWG	10.71	0.07	0.64	0.27	1.67	6.35	2272	715	5.75	2.47
148.4	AWG	15.95	0.07	0.50	0.15	2.00	4.39	3414	783	7.10	4.23
147.2	AWG	16.02	0.07	0.50	0.18	2.38	9.76	3454	817	7.17	4.47
147.1	AWG	25.36	0.06	0.40	0.08	2.50	12.21	6073	847	11.25	6.87
148.3	AWG	25.98	0.07	0.38	0.08	2.38	13.18	6213	922	11.54	7.11
146.5	AWG	5.46	0.12	0.87	0.34	1.72	3.91	1995	1407	6.53	3.47
145.4	AWG	5.52	0.12	-	-	1.72	4.88	1886	1326	6.46	3.26
145.2	AWG	10.27	0.11	0.77	0.30	1.85	5.86	2884	1219	6.82	4.21
148.2	AWG	10.64	0.12	0.66	0.29	2.17	6.35	3191	1298	7.08	4.52
148.1	AWG	15.29	0.11	0.57	0.21	2.50	10.25	4552	1208	8.98	6.61
146.3	AWG	15.44	0.12	0.55	0.15	2.08	6.35	4756	1224	9.47	7.22
145.1	AWG	25.20	0.11	0.48	0.10	2.63	14.16	7899	1421	15.02	11.06
146.1	AWG	25.42	0.11	0.41	0.08	2.63	13.67	8237	1559	15.60	11.49
145.5	AWG	5.21	0.21	1.28	0.51	2.27	3.91	3153	2639	7.93	5.70
145.3	AWG	10.19	0.20	0.89	0.33	2.38	6.84	4832	2323	9.56	7.32
146.4	AWG	15.28	0.21	0.61	0.16	2.63	10.74	7215	2384	14.52	12.14
146.2	AWG	24.86	0.20	0.46	0.09	3.13	16.11	12182	2394	23.22	17.16
147.6	AWG	4.89	0.55	1.22	0.74	5.56	5.37	8280	7556	16.67	17.27
148.6	AWG	4.95	0.55	1.09	0.70	5.56	5.37	8178	7651	16.11	16.89
94.2	AWG	9.09	0.49	0.97	0.37	-	-	-	-	-	-
145.6	AWG	9.80	0.51	1.17	0.44	4.17	7.32	11070	6937	22.42	18.89
146.6	AWG	13.97	0.53	0.77	0.21	3.85	12.21	15631	7755	31.71	24.87
148.5	AWG	22.02	0.50	0.55	0.21	5.56	14.65	21802	7043	44.37	31.26
147.5	AWG	22.11	0.50	0.61	0.22	5.56	14.65	22386	6958	48.34	33.73

Table E.3 Microgravity Annular Flow Data for Air-Water/Zonyl FSP, 12.7 mm ID Tube

Run	Fluids	U_{GS} (m/s)	U_{LS} (m/s)	h Mean (mm)	h Std. Dev. (mm)	U (m/s)	PSD Mode (Hz)	dP/dx Mean (Pa/m)	dP/dx Std. Dev. (Pa/m)	Tau Wall Mean (Pa)	Tau Wall Std. Dev. (Pa)
102.12	AWZ	4.20	0.07	0.62	0.26	-	-	-	-	-	-
152.2	AWZ	5.37	0.07	0.53	0.29	1.52	3.52	915	654	9.90	5.12
151.3	AWZ	5.55	0.07	0.49	0.24	1.32	1.46	919	681	8.60	4.19
101.12	AWZ	9.92	0.07	0.48	0.16	-	-	-	-	-	-
152.4	AWZ	10.30	0.07	0.41	0.17	1.72	4.39	1555	564	5.42	1.53
149.2	AWZ	10.51	0.08	0.46	0.14	1.56	5.37	1619	637	4.66	1.12
150.1	AWZ	15.53	0.07	0.33	0.08	2.08	3.42	2483	749	4.18	1.11
151.1	AWZ	25.86	0.06	0.22	0.04	2.63	8.30	4707	835	4.04	1.27
150.5	AWZ	5.25	0.11	0.63	0.32	1.56	3.91	1352	959	6.55	3.10
152.3	AWZ	5.37	0.11	0.55	0.32	1.61	2.44	1242	912	8.11	4.28
151.4	AWZ	5.46	0.11	0.55	0.29	1.52	3.91	1289	977	6.38	2.93
149.3	AWZ	10.52	0.12	0.51	0.16	1.61	4.39	2272	812	4.36	1.07
150.4	AWZ	10.57	0.11	0.47	0.17	1.79	5.86	2295	862	4.54	1.17
150.2	AWZ	15.43	0.11	0.38	0.10	2.17	11.72	3361	996	4.25	1.27
149.5	AWZ	15.46	0.12	0.39	0.10	2.00	7.32	3526	1003	4.58	1.91
152.1	AWZ	25.37	0.10	0.23	0.11	3.57	11.72	6418	1063	4.21	1.31
151.2	AWZ	25.67	0.10	0.25	0.04	2.78	8.79	6488	1228	4.22	1.28
151.5	AWZ	5.40	0.20	0.63	0.34	1.79	4.88	2049	1406	5.00	1.86
149.4	AWZ	10.31	0.21	0.58	0.18	1.85	7.32	3451	1376	4.56	1.64
150.3	AWZ	15.07	0.19	0.44	0.13	2.38	7.81	4972	1327	4.94	2.27
149.1	AWZ	24.58	0.19	0.33	0.06	3.13	11.23	9141	1771	8.22	4.63
100.3	AWZ	9.63	0.50	0.66	0.29	-	-	-	-	-	-
149.6	AWZ	9.73	0.55	-	-	2.63	6.84	8137	4313	7.41	4.26
152.5	AWZ	10.22	0.51	0.65	0.32	3.85	14.16	8162	3922	6.12	3.22
151.6	AWZ	13.62	0.52	0.54	0.17	3.33	11.23	10505	4288	6.68	3.49
152.6	AWZ	14.45	0.51	0.53	0.27	4.55	15.62	10870	3844	7.55	4.06
150.6	AWZ	22.39	0.45	0.41	0.08	3.85	24.90	17911	3404	12.01	6.17

REPORT DOCUMENTATION PAGE

Form Approved
OMB No. 0704-0188

1. AGENCY USE ONLY (*Leave blank*)	2. REPORT DATE	3. REPORT TYPE AND DATES COVERED
	February 1995	Final Contractor Report

4. TITLE AND SUBTITLE

Studies of Two-Phase Gas-Liquid Flow in Microgravity

5. FUNDING NUMBERS

WU-963-25-0A
G-NAG3-510

6. AUTHOR(S)

William Scott Bousman

7. PERFORMING ORGANIZATION NAME(S) AND ADDRESS(ES)

University of Houston
Department of Chemical Engineering
Houston, Texas 77204

8. PERFORMING ORGANIZATION REPORT NUMBER

E-9445

9. SPONSORING/MONITORING AGENCY NAME(S) AND ADDRESS(ES)

National Aeronautics and Space Administration
Lewis Research Center
Cleveland, Ohio 44135-3191

10. SPONSORING/MONITORING AGENCY REPORT NUMBER

NASA CR-195434

11. SUPPLEMENTARY NOTES

This report was submitted as a dissertation in partial fulfillment of the requirements for the degree Doctor of Philosophy in Chemical Engineering to the University of Houston, Houston, Texas, December 1994. Project Manager, John B. McQuillen, Space Experiments Division, NASA Lewis Research Center, organization code 6712, (216) 433-2876.

12a. DISTRIBUTION/AVAILABILITY STATEMENT

Unclassified - Unlimited
Subject Category 34

This publication is available from the NASA Center for Aerospace Information, (301) 621-0390.

12b. DISTRIBUTION CODE

13. ABSTRACT (*Maximum 200 words*)

Two-phase gas-liquid flows are expected to occur in many future space operations. Due to a lack of buoyancy in the microgravity environment, two-phase flows are known to behave differently than those in earth gravity. Despite these concerns, little research has been conducted on microgravity two-phase flow and the current understanding is poor. This dissertation describes an experimental and modeling study of the characteristics of two-phase flows in microgravity. An experiment was operated onboard NASA aircraft capable of producing short periods of microgravity. In addition to high speed photographs of the flows, electronic measurements of void fraction, liquid film thickness, bubble and wave velocity, pressure drop and wall shear stress were made for a wide range of liquid and gas flow rates. The effects of liquid viscosity, surface tension and tube diameter on the behavior of these flows were also assessed. From the data collected, maps showing the occurrence of various flow patterns as a function of gas and liquid flow rates were constructed. Earth gravity two-phase flow models were compared to the results of the microgravity experiments and in some cases modified. Models were developed to predict the transitions on the flow pattern maps. Three flow patterns, bubble, slug and annular flow, were observed in microgravity. These patterns were found to occur in distinct regions of the gas-liquid flow rate parameter space. The effect of liquid viscosity, surface tension and tube diameter on the location of the boundaries of these regions was small. Void fraction and Weber number transition criteria both produced reasonable transition models. Void fraction and bubble velocity for bubble and slug flows were found to be well described by the Drift-Flux model used to describe such flows in earth gravity. Pressure drop modeling by the homogeneous flow model was inconclusive for bubble and slug flows. Annular flows were found to be complex systems of ring-like waves and a substrate film. Pressure drop was best fitted with the Lockhart-Martinelli model. Force balances suggest that droplet entrainment may be a large component of the total pressure drop.

14. SUBJECT TERMS	15. NUMBER OF PAGES
Two-phase flow; Microgravity; Voids; Film thickness; Pressure drop; Bubbles; Annular flow	313
	16. PRICE CODE: A14

17. SECURITY CLASSIFICATION OF REPORT	18. SECURITY CLASSIFICATION OF THIS PAGE	19. SECURITY CLASSIFICATION OF ABSTRACT	20. LIMITATION OF ABSTRACT
Unclassified	Unclassified	Unclassified	